CRANFIELD UNIVERSITY

Wenjing Wei

Biomimetic Polymer Reactor: Design and Modulation of Novel Tandem Catalysts

School of Aerospace, Transport and Manufacturing
PhD in Manufacturing

PhD
Academic Years: 2017 - 2021

Supervisor: Dr Iva Chianella
Associate Supervisor: Professor Vijay Kumar Thakur
Professor Krzysztof Koziol

September 2021

CRANFIELD UNIVERSITY

School of Aerospace, Transport and Manufacturing
PhD in Manufacturing

PhD

Academic Years 2017 - 2021

Wenjing Wei

Biomimetic Polymer Reactor: Design and Modulation of Novel Tandem Catalysts

Supervisor: Dr Iva Chianella
Associate Supervisor: Professor Vijay Kumar Thakur
Professor Krzysztof Koziol
September 2021

This thesis is submitted in partial fulfilment of the requirements for the degree of PhD

ABSTRACT

Tandem catalysis can perform multi-step catalytic reactions in one-pot sequentially, which not only improves the efficiency of reactions significantly, but also decreases time, energy and the amounts of reagents needed. However, as there is always more than one active site (catalyst) in tandem reactors, it is critical to separate different sites and ensure each step is conducted individually. Moreover, it is often challenging to control the whole reaction processes due to the complexity of the systems. In this research, several bio-inspired catalytic reactors were proposed and developed to address the two challenges of site separation and smart control of tandem catalysis.

First of all, the goal of sites separation has been achieved in this work through an enzyme-inspired molecularly imprinted polymer reactor MIP-Au-NP-BNPC and a core-shell structure catalytic nanoreactor AMPS@AM-Ag. Two molecularly imprinted cavities were created in MIP-Au-NP-BNPC. The different channels of the two catalytic sites in the reactor enabled different catalytic reactions to occur in different regions, resulting in the process of tandem reactions. As a result of the radial distribution of catalytic sites and mass transfer, the core-shell structure of AMPS@AM-Ag enabled the nanoreactor to perform different catalytic processes sequentially. Hence, the nanoreactor demonstrated the ability to conduct tandem catalysis with successful site separation.

Then a biomimetic switch was introduced into the reactor to achieve the smart control of the catalytic process. Firstly, a new type of catalytic reactor consisting of a three-layer mussel-inspired polymer, MIP-AgPRS, was developed. The smart switchable layer composed of mussel-inspired self-healing copolymer was prepared between two MIP layers. This middle smart layer was able to react to different temperatures, permitting either simple or tandem reactions by closing and opening the access of the intermediate products.

Secondly, a bilayer polymer reactor, DPR, composed of two different temperature-sensitive polymer layers was prepared. The two functional layers were not only able to respond to different specific temperatures, but each also

contained different catalytic sites. Because of the two different phase transition processes of the two layers, the polymer reactor demonstrated to be able to perform simple/tandem catalysis in different temperature regions. As a result, this new type of bilayer polymer reactor was capable of achieving smart control of the tandem reactions.

Finally, a three-layer switchable polymer reactor, PRS, with two MIP layers and a PNIPAM-PAM switchable layer in the middle was prepared. In an aqueous environment, when the temperature was low (lower than 47 °C), it exhibited an open access (hydrophilic condition), while when the temperature was high (higher than 47 °C), it became closed (hydrophobic condition). Furthermore, a comonomer (AM) was introduced in the middle layer with different ratios to adjust the responsive temperature range, enabling a more comprehensive range of practical uses. Therefore, a fast responsive and stable polymer reactor with self-controlled catalytic property was obtained.

By preparing different types of new catalytic reactors, the research carried out here has shown the ability to achieve a smart control of the tandem catalysis while separating the catalytic sites effectively. Therefore, this study has highlighted new solutions to address the challenges present in tandem catalysis and has provided novel inspiration on how to exploit functional polymers while performing complicated catalytic reactions.

Keywords:

tandem catalysis; sites separation; bio-inspired polymer; smart catalytic reactor

ACKNOWLEDGEMENTS

Firstly, I want to express my sincere gratitude to all my supervisors for providing me with lots of supports and helps during my PhD study. I want to thank Dr Iva Chianella for her supervision. Iva helped me a lot to make me familiar with the labs quickly when I came. She gave me valuable suggestions about my research progress and always been a great friend to support me when I faced challenges. I am also deeply grateful to professor Songjun Li, my supervisor in China. He taught me how to conduct research in the very beginning. I learnt a lot about how to analyse the experiments and write papers from him. I also want to thank Professor Vijay Kumar Thakur for his kind helps and constant supports. He is a very good supervisor and also a nice friend.

Many thanks are also expressed to the Dual PhD Degree Programme between Cranfield University and Jiangsu University. It is an exceptional and beneficial experience for me to study in both the two universities. It gave me the chance to communicate with different researchers and learn novel research methods. It also gave me a chance to see new sceneries, meet new friends and experience a new adventure in my life.

I want to thank Mr Jim Hurley, Dr David Ayre, Dr Christopher Shaw, Dr Edith Rogers, Professor Krzysztof Koziol and other people who offered me kind helps and great supports during my research.

My special thanks go to my lovely friends Shuyang, Shouqi, Shuang, Danning, Sid, Adam and Dengdeng, who always encouraged and supported me during a hard time. I also want to thank my roommates Minfeng, Guokang and Shaowei. There are lots of challenges for me to come to a new university in a new country. Because of the company of my friends, my research life is not lonely any more. I want to thank my research group members in China. I always remember the time we were together to do the research and solve the challenges.

Last but not least, I would like to thank my father, mother, brother and all my families. Without your understanding and encouragement, I am not able to be the person I am today. Also, I want to thank my best friend Xiang Chen. Thank you

for always being there. Your constant belief and unconditional supports mean a lot to me.

TABLE OF CONTENTS

LIST OF FIGURES

LIST OF TABLES

LIST OF EQUATIONS

LIST OF ABBREVIATIONS

AIBN	2,2'-Azobis(2-methylpropionitrile)
AM	Acrylamide
AMPS	2-Acrylamido-2-Methylpropane Sulfonic Acid
AP	4-Aminophenol
APS	Ammonium Persulfate
BNPC	Bis (4-Nitrophenyl) Carbonate
DAPO	Bis (2,4-Diaminophenyl) Oxalate
DLS	Dynamic Light Scattering
DMSO	Dimethyl Sulfoxide
DNPO	Bis (2,4-Dinitrophenyl) Oxalate
DOPA	3,4-Dihydroxy-L-phenylalanine
DPA	Dopamine Methacrylamide
DPR	Double-responsive Polymer Reactor
DSC	Differential Scanning Calorimetry
EDS	Energy Dispersive X-ray Spectroscopy
FTIR	Fourier Transform Infrared Spectrometer
GAC	Guaiacol Carbonate
HPR	High-temperature Responsive Polymer Reactor
LCST	Lower Critical Solution Temperature
MBA	N, N'-Methylene Bisacrylamide
MIP	Molecularly Imprinted Polymer
MPR	Moderate-temperature Responsive Polymer Reactor
NIPAM	N-isopropylacrylamide
NMA	N-(Hydroxymethyl) Acrylamide
NP	4-Nitrophenol
NPA	4-Nitrophenyl Acetate
PAM	Polyacrylamide
PAMPS	Poly-2-Acrylamido-2-Methylpropane Sulfonic Acid
PDPA	Polydopamine Acrylamide
PNAGA	Poly-N-Acryloyl Glycine
PNIPAM	Poly-N-Isopropylacrylamide
PTFE	Polytetrafluoroethylene

PTFMA	Poly-2-Trifluoromethacrylic Acid
PS	Polystyrene
PVI	Poly-1-Vinlylimidazole
SEM	Scanning Electron Microscope
SPR	Surface Plasmon Resonance
TEM	Transmission Electron Microscope
TFMA	2-Trifluoromethacrylic Acid
TPD	Temperature Programmed Desorption
UCST	Upper Critical Solution Temperature
UV	Ultraviolet
VI	1-Vinlylimidazole
XRD	X-ray Diffraction

Chapter 1 Introduction

1.1 Brief background

A tandem reaction means a process where two or more independent reactions proceed one by one in a one-pot system. Compared with the common multi-step reactions, the tandem reaction does not need to deal with intermediate products during the reaction process, saving additional separation and purification steps. This process not only reduces the reaction steps, minimising the waste generation and energy consumption, but also saves large amounts of solvents and reactants [1]. This results in a significant improvement of the reaction efficiency, and it is incredibly beneficial for the environment. Tandem catalysis defines a process in which tandem reactions are achieved through catalytic systems containing single or multiple active sites. Similar to enzymatic reactions in biological systems, by catalysing a series of complex compounds concisely and efficiently in the same environment, tandem catalysis allows to simplify the processing steps of intermediate products and to optimise complex reaction processes, hence expanding its exploitation in a wide variety of chemical synthesis and other fields [2, 3].

1.2 Tandem catalysis

The tandem catalytic system is an independent reaction system composed of a single or a combination of multiple sites, which aims to complete a multi-step reaction sequentially in a stable environment, saving operation steps and optimising the reaction process. Transforming simple precursors into complex target molecules through different methods has always been a desired and challenging outcome in the area of organic chemistry. Although the development of transition metals has revolutionised organic synthesis, the capabilities of this method are limited by the requirement of performing the entire chemical process into multiple separate steps. Therefore, researchers have become increasingly

more interested in the "one-pot method" reaction process. The "one-pot method" refers to the completion of multiple catalytic conversions in the same system after a single preparation stage [4]. Based on the need to save costs and reduce external control, the requirements for high selectivity and high conversion rate catalysis processes are increasing, which promotes the continuous development of this type of reaction. At the same time, a large number of research articles on coupling reactions have emerged [5-7], such as the use of Pd to catalyse the formation of carbon-carbon bonds [8], exchange coupling [9] or hydroformylation catalysis [10, 11], enzymes [12, 13] or Ni-catalysed domino reaction [14], as well as multi-functional [15, 16] or multi-component [17] catalysis, and some processes involving stoichiometric series or cascade reactions [18, 19]. The multi-step or tandem reaction that can be carried out by the "one-pot method" generally means the continuous transformation of two or more individual steps based on a single initial preparation [20]. In this chapter, according to the different properties of the catalytic process and the catalytic reactor, the concept of tandem reaction is further clarified through a simple classification of multi-step and tandem reactions.

The first type is multi-step reactions. A multi-step reaction is a reaction system that contains different reaction processes in the same environment, but it is not necessarily a tandem reaction. There are two main categories of multi-step reactions. The first category is a one-pot reaction consisting of several independent catalytic processes. The second catalyst needs to be added after finishing the first catalytic conversion process in this type of reaction, so it is not a tandem catalytic reaction. The second category is a domino reaction (cascade reaction), which means that the substrate has experienced two or more different conversions. The multiple conversion process consists of a single catalytic conversion mechanism and continuous changes in stoichiometric ratio. The continuous reaction carried out here generally involves only one catalyst, and subsequent reactions are based on the same reaction mechanism. Tietze [21] defines it as when two or more bond transitions occur under the same conditions, there is no need to add additional reagents or catalysts, and the following reactions are derived from the results of the previous step. In this process, the

continuous steps can be intramolecular processes (including intermediate products produced in the catalytic cycle) [22], or intermolecular processes (as shown in **Figure 1-1**).

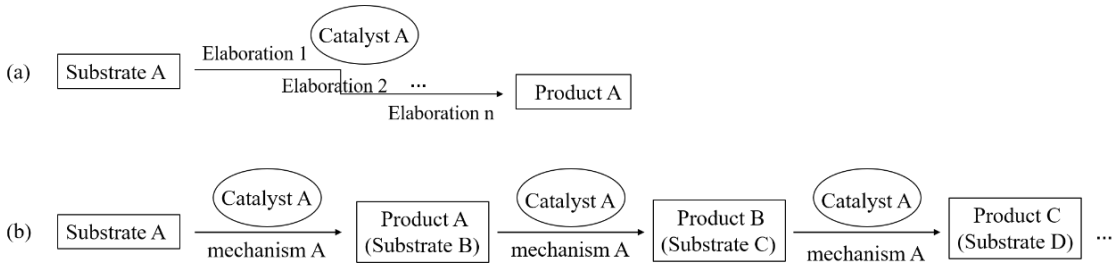

Figure 1-1 Domino catalysis scheme: (a) intramolecular; (b) intermolecular.

The second type is tandem reactions. Compared with the multi-step reaction mentioned above, the tandem reaction has two apparent differences. The first difference is that all catalysts are added to the system in the preparation stage of the reaction, and no additional catalyst is required during the catalysis process. The second difference is that the reaction contains more than one reaction mechanism. The word “tandem” in the tandem reaction contains two meanings: the first is that two different mechanisms work together; the second is that the reactions proceed one after another in succession [23]. Tandem reaction is mainly divided into three different categories according to the different mechanisms:

The first category is the auto tandem catalytic reaction, which refers to a spontaneous reaction of a precursor catalysed by a single catalyst. The reaction process contains two or more different mechanisms. At the beginning of the reaction, all the materials needed for the reaction (catalyst, initiate substrate, additional reagents) are added at first. Then the reaction proceeds spontaneously one by one without adding additional reagents during the reaction. Although the two reaction cycles are catalysed by the same catalyst, the intermediate products are completely different in each cycle. As shown in **Figure 1-2**, initial substrate A is firstly converted into product A through catalyst A, and then product A is used as substrate B to enter the next reaction, then product B is obtained through

catalyst A. Under ideal circumstances, this self-tandem process is carried out sequentially according to the conversion of substrate molecules. Still, they are generally parallel in a macroscopic perspective, which means cycle B and cycle A are carried out at the same time after product A is produced. When the reaction system reaches an equilibrium, the auto tandem catalytic processes can achieve a very high reaction efficiency. Therefore, it has applications in various reactions [24], such as the conversion of aldehydes obtained by the hydroformylation of α-olefins into other functional groups and the conversion to alcohols by hydrogenation and conversion to carboxylic acids by oxidation [25].

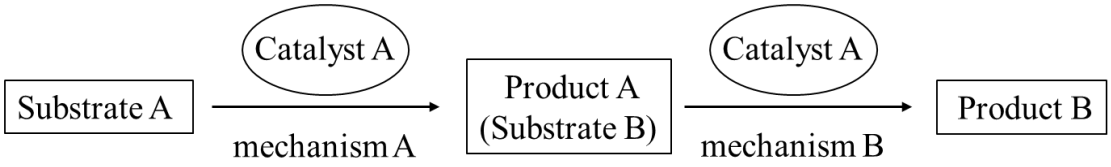

Figure 1-2 Auto tandem catalysis scheme.

The second category is assisted tandem catalysis. In this catalytic process, other reagents are added to initiate the change of the reaction mechanism, which can further expand the scope, selectivity and performance of the catalytic process with only single catalyst. As shown in **Figure 1-3**, catalyst A firstly catalyses a reaction. Then it is transformed into catalyst B (usually by directly regulating the active sites), and catalyst B directly catalyses the initial reaction product. Different from the auto tandem catalysis, since two catalysts cannot exist at the same time, the two reactions cannot proceed at the same time [26]. The main limitation of assisted tandem catalysis comes from the conditions of assisted intervention. Compared with auto tandem catalysis, assisted tandem catalysis cannot happen spontaneously, and the process must be monitored to confirm the completion time of the first reaction process, avoiding the premature triggering of the second process. The control of the intervention time and method is of great significance to improve the assisted tandem catalysis. The key point of assisted tandem reaction is to ensure that the reaction can proceed in sequence, which means that the sequential reactions involved in the system always require adding

additional reagents or change the reaction conditions. The advantage of assisted tandem reaction is that the reaction can be carried out in a single reaction system, and there is no need to conduct additional purification between different steps.

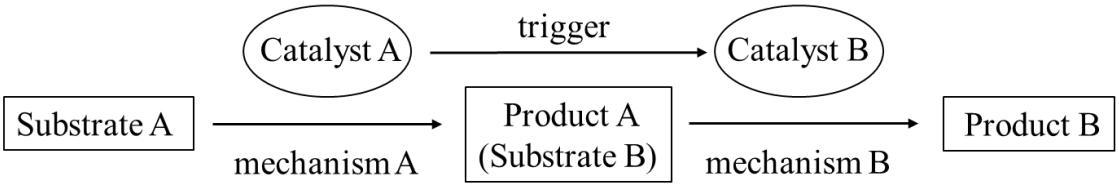

Figure 1-3 Assisted tandem catalysis scheme.

The third category is orthogonal tandem catalysis. The characteristic of orthogonal reactions is that they are independent of each other, and the orthogonal catalysis process generally involves two or more catalysts with different functions. These catalysts are added to the system from the beginning of the reaction. **Figure 1-4** shows that the organic initial substrate A first reacts with the catalyst A to obtain the product A. At this time, the product A acts as the substrate B for the next reaction and is catalysed by the catalyst B to be converted into product B. In orthogonal tandem catalysis, once substrate B is produced, the two catalytic processes will proceed simultaneously. Compared with the auto tandem reaction, the orthogonal tandem catalysis contains more than one catalyst, further expanding the range of practical applications. In addition, compared with the assisted tandem reaction, the orthogonal tandem reaction does not need additional controls by real-time observation and detection process, so it can be spontaneously carried out with simpler operation properties. Hence, it is suitable for a wide range of practical uses in the field of organic synthesis [27], for example the upgrading of alkanes or alkenes (**Figure 1-5**) [28, 29]. Without specific mention, the tandem catalysis in the following parts of the thesis generally refers to orthogonal tandem catalysis.

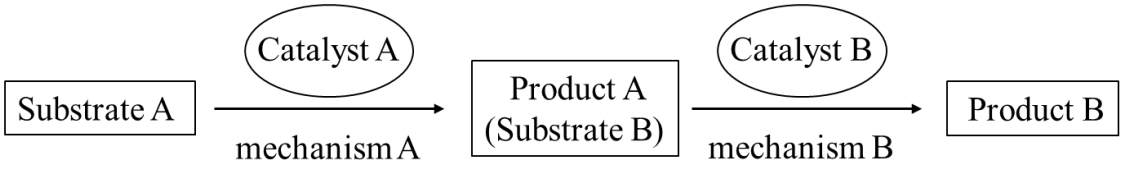

Figure 1-4 Orthogonal tandem catalysis scheme.

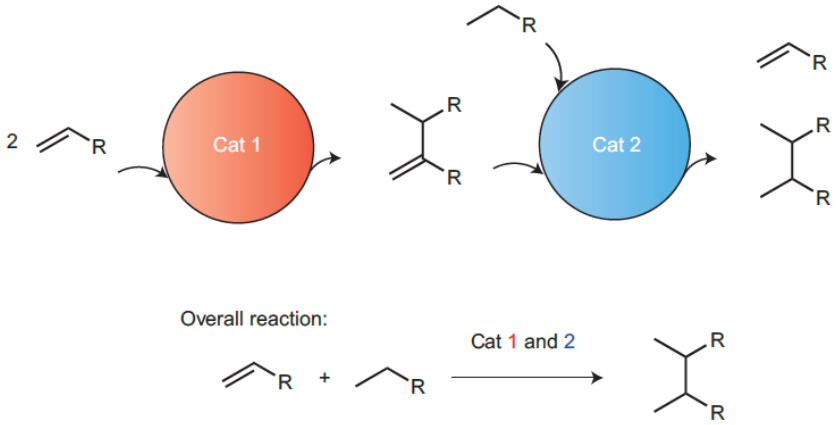

Figure 1-5 Tandem catalysts: alkene dimerization/transfer hydrogenation and then hydrogenation to produce a new alkane mixture [30]

1.3 The challenges of tandem catalysts

Tandem catalyst refers to a catalytic system formed by a combination of active catalytic sites. The tandem catalyst allows multiple continuous reactions to be carried out in a simple reaction system under similar conditions, reducing separation steps of intermediate products, saving time and raw materials, and improving reaction efficiency [31, 32]. Due to the different mechanisms between the reactions, two or more different kinds of active sites are generally involved in tandem catalysis. The most commonly used active sites are acidic sites, basic sites, and metal sites [33, 34]. Because of the different characteristics of different sites, sometimes there will be incompatibility or even mutual reactions between the two sites (such as acidic and basic sites, oxidants and reducing agents, etc.) [35]. Therefore, to selectively catalyse tandem reactions, the distribution of active sites must be determined according to the type of reaction, and the compatibility

of catalysts, solvents, and additives must be further considered. In this way, different catalytic sites can be separated, so that each step of the reaction can proceed independently in order, and the mutual interference between different reactions can be reduced. In recent years, several studies have made important breakthroughs in this field, mainly by setting up physical barriers or loading active sites on different solid phases, including stepwise separation of tandem reactions [36], a one-pot synthesis of Pickering emulsion reaction and so on.

Xue [37] et al. proposed an enhanced Pickering emulsion to achieve the coexistence of acid and base active sites in tandem catalysts. In the experiment, an inorganic shell layer was formed around the droplets through the cross-linking of the emulsifier particles, which strengthened the structure of the water-in-oil Pickering emulsion. Acidic or basic sites were added to the water phase before preparing Pickering emulsion. In the process of the emulsion formation, a protective layer can be covered on the outside of the acidic or basic droplets to achieve the coexistence effects of acid-base active catalytic sites. The experiment completed the deacetalization-Knoevenagel tandem reaction through this coexistence system. Although this Pickering emulsion realised the separation of incompatible acidic and basic sites, the reaction orientation could not be guaranteed in the tandem reaction since the two catalysts were dispersed in the same continuous phase.

Yang [38] et al. prepared a layered Pickering emulsion for tandem reactions. Firstly, two basic Pickering emulsions were prepared. In one of the emulsions, the acid catalysts were dissolved in the dispersed water phase droplets, and then the droplets were dissolved in the continuous oil phase. Similarly, in another emulsion, the basic catalysts were dispersed in the water phase droplets, and then the droplets were dispersed in the oil phase. Then the two Pickering emulsions were brought into contact with each other, mixed and layered (**Figure 1-6**), and finally two emulsions separated layer by layer were obtained. The layered structure dispersed the emulsion droplets in different areas, avoiding direct contact. As a result, the aqueous phase droplets separated the acidic and basic catalysts in zones during the reaction process, so the two catalysts could

coexist. At the same time, due to the layer-by-layer structure, the reactants located in the oil phase could diffuse freely. They were catalysed by acid sites to the intermediate products, and then catalysed by basic sites to the final products, completing directional catalysis in a desired direction. This tandem catalytic system was capable of completing the directional catalytic reaction process as well as disperse the catalytic sites, but the preparation process required fine control and the steps were relatively complicated and time-consuming.

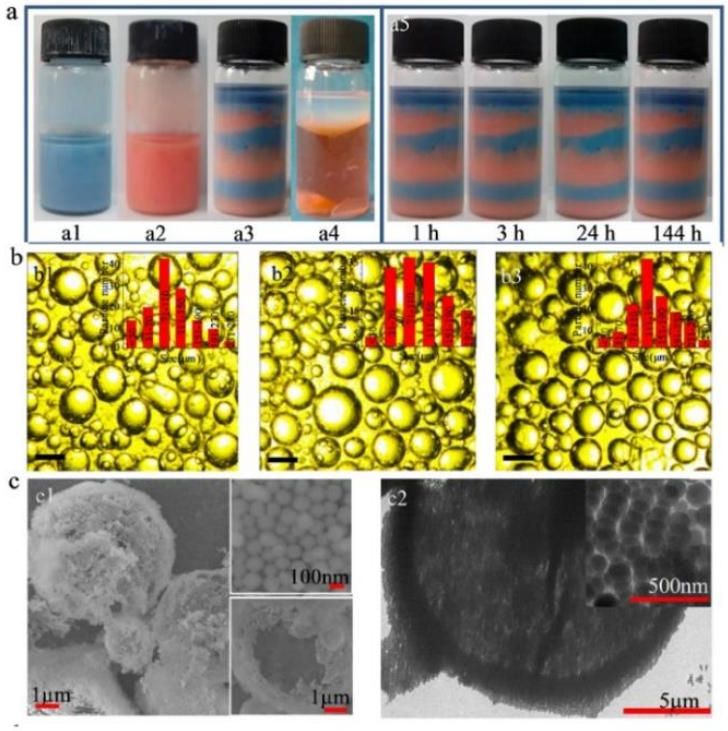

Figure 1-6 Formation of the layered Pickering emulsions with the existence of Congo Red (a); Optical microscopy images (b); SEM and TEM images of emulsion droplets (c) [38]

Although the current research has greatly promoted the development of the site separation in tandem catalysts, there are still some challenges. Some catalysts enable the separation of different sites, but the reaction order cannot be controlled, causing other side reactions and by-products. Other tandem catalysts can separate sites effectively and carry out sequential reactions, but they usually require highly complex synthesis steps, which makes the

practical application of the catalysts still limited. Therefore, simpler and more effective preparation methods are needed to separate the catalytic sites to further promote the study of tandem catalysts.

In addition, the regulation of the catalytic process has always been one of the key challenges for catalytic reactions. The use of self-controlled catalysts enables chemical reactions to respond to specific internal or external stimuli in the reaction system, thereby increasing the adaptability and practical application ranges of the catalysts. Researchers have achieved the control of the substrate channel through precise adjustment of the structure-activity relationship of the catalyst or the phase transition of the catalytic system, thereby realising the smart controls of the catalytic processes. Currently in several studies, many new catalysts have been proposed [39, 40] to realise this goal.

Song et al. [41] designed a yolk-shell structure nanoreactor, which consisted of coating the temperature-sensitive polymer PNIPAM loaded with Au nanoparticles on the outer pores of mesoporous hollow silica spheres (PNIPAM/Au@meso-SiO_2) **Figure 1-7**). The nanoreactor had significant catalytic activity when the temperature was below the LCST (Lower Critical Solution Temperature) of PNIPAM (such as 30 °C). When the temperature reached 50 °C (higher than the LCST), the polymer experienced a phase change to become a hydrophobic film on the SiO_2 surface and block the mesopores, resulting in low catalytic activity. Further tests showed that the catalytic activity could be switched on and off repeatedly by controlling the temperature. Kinetic studies showed that the phase change behaviour of PNIPAM controlled the diffusion of the catalyst in the mesopores, thereby controlling the reaction process.

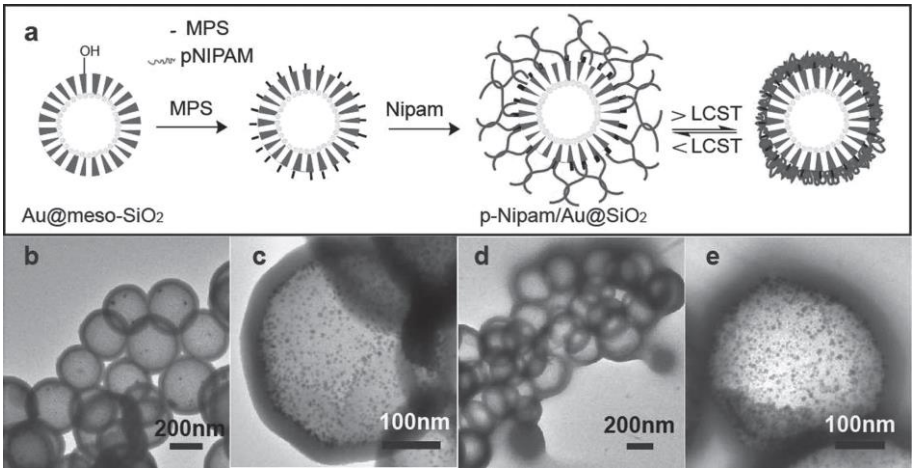

Figure 1-7 The synthesis process of the core-shell nanoreactor (a); TEM image of Au@meso-SiO_2 composite (b, c); TEM image of PNIPAM/Au@meso-SiO_2 composite (d, e) [41]

Li et al. [42] prepared a temperature-responsive nanoreactor in which the catalytic activity improved with increasing temperature. The nanoreactor was composed of functionalised polyacrylamide (PAM) and 2-acrylamide-2-methyl propane sulfonic acid (PAMPS) copolymer composite with silver nanoparticles encapsulated in it. At a relatively low temperature (lower than its responsive temperature) (for example 20 °C), the polymer channels were closed because of the intermolecular force between PAM and PAMPS, preventing the contact between metal nanoparticles and the reaction substrate, causing relatively low reactivity of the reaction. At relatively high temperatures (higher than its responsive temperature) (such as 40 °C), the intermolecular force between PAM and PAMPS of the nanoreactor dissociated, so that the substrate channels opened and the reaction substrate could get into contact with the silver nanoparticles, thus showing significant catalytic activity (**Figure 1-8**).

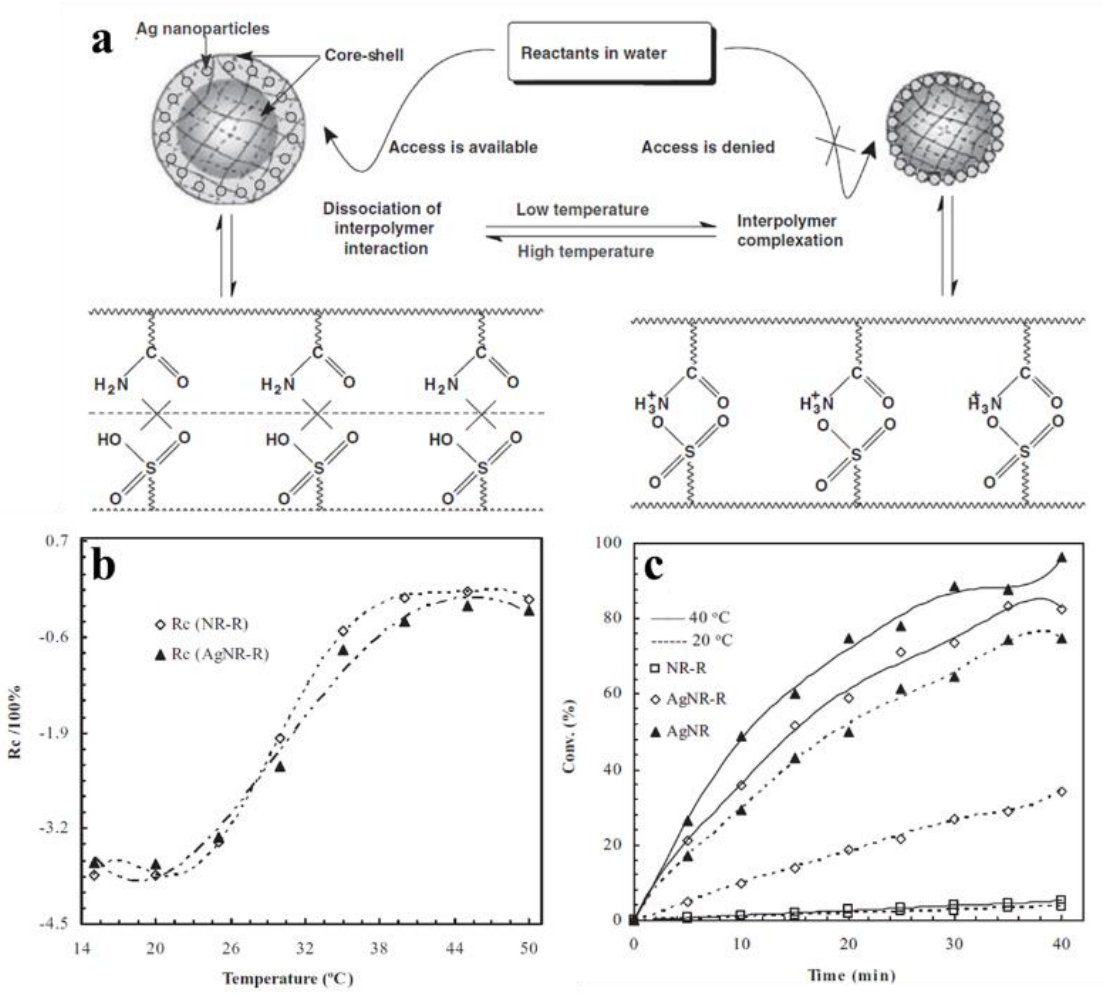

Figure 1-8 The mechanism of thermosensitive nanoreactor (a); DLS curves of nanoreactor (b); Catalytic activity of nanoreactor for reduction of 4-nitrophenol [42]

Although significant progress has been made to effectively regulate the catalytic processes, the practical application of smart catalysts is still very limited. One of the important reasons lies in the complexity and diversity of the reaction process and catalytic mechanism in the practical catalytic processes. Many reactions often include simple single-step reactions and complex multi-step reactions (tandem reactions) [43]. In order to realise the smart control of complex reactions, exploring new methods, technologies and preparing smart reactors that can be applied in the field of tandem reactions are also of great significance in the field of catalysis for future research.

1.4 The biomimetic polymer as carriers of tandem catalytic reactors

In order to solve the challenges of site separation and the control of complex reaction processes mentioned above, the concept of a biomimetic tandem catalytic reactor was introduced in this study to solve these problems from a bionic perspective. It has been known that the development of highly efficient and complex reaction processes similar to the synthesis of compounds in organisms has always been one of the goals in the field of biosynthesis. For example, enzymatic reactions have high atomic efficiency, high chemical and stereo selectivity. In enzymatic reactions, only a few steps are needed to selectively generate complex structures with multiple stereo centres starting from simple reactants. Enzymatic processes usually involve domino reactions [21, 44], multi-component reactions [45, 46] and other processes, showing extremely high reaction efficiency. Therefore, they have been attracting more and more attention from researchers in the field of complex reactions [47, 48]. In recent years, the introduction of diversity-oriented synthesis (DOS) [49] and biology-oriented synthesis (BIOS) [50] have created conditions to realise this goal. Unlike organic synthesis, enzymatic reactions are highly adaptive and are often activated or inhibited by specific conditions, ensuring the depletion of one substrate resulting in the synthesis of a specific product.

The highly efficient and complex reactions of biological systems in nature can provide plenty of inspiration for the study of tandem reactions. Several studies have designed a biomimetic multi-component tandem catalytic reaction system to enable the efficient and straightforward synthesis of complex products with different structures. In this thesis, the combination of the biomimetic polymer and the active sites has permitted the tandem reaction to be carried out sequentially, reducing side and interference reactions and improving the overall reaction efficiency. On the other hand, the introduction of smart polymers is also being used to improve the controllability of the reaction so that catalytic processes can be switched between simple catalysis and tandem catalysis according to the

external environment, which provides a new solution for the study of tandem reaction. The next part of this thesis briefly introduces several biomimetic polymers used in novel tandem catalysts.

1.4.1 Molecularly imprinted polymers

The first type of biomimetic polymers described in this thesis is the molecularly imprinted polymer (MIP). Because of its unique molecular recognition function, MIP can be applied to the field of tandem catalysis to increase the selectivity of the catalyst. Several classic substances are capable of molecular recognition in biological systems, such as enzymes, antibodies, receptors, and particle channels. They mainly complete complex tandem reactions selectively through precise molecular recognition reactions. The molecular recognition abilities of these highly specific macromolecules are mainly produced via an exquisite three-dimensional structure, which provides binding sites for the target molecules. There are several different interactions within the binding site, such as hydrogen bonding, hydrophobic, electrostatic, and other intermolecular interactions. The complex recognition systems have excellent performance and fine structure, enabling many important applications in different fields. However, as essentially derived from biological tissues, they always show instability to the environmental conditions such as acid/base pH, high temperatures and organic solvents, limiting the practical application ranges. In addition, the need for immobilisation and the requirement for coating on surfaces also brings new challenges for researchers. At the same time, these biomaterials are generally costly and have complicated preparation processes. Due to these limitations of the practical use, researchers have been trying to develop a synthetic macromolecule with molecular recognition properties by mimicking biomolecules [51-53].

Wulff et al. [54] first proposed the concept of molecular imprinting technology in 1972, which meant a technical method for preparing artificial receptors. Molecularly imprinted polymer (MIP) refers to a polymer showing selective recognition properties for a target compound. Such molecular recognition is obtained by including in the pre-polymerization mixed system a template

molecule, which can be either the target compound itself or one of its closely related analogues [55]. Because of the presence of the template, the polymer will generate recognition cavities with the template during the polymerisation reaction. Then the imprinting cavities can be obtained by washing off part or all of the template [56, 57]. Generally, the preparation method of MIP includes three main procedures (**Figure 1-9**). The first procedure is the complexation of the target compound (template) with one or more functional monomers, where the functional monomers contain functional groups that can form either a covalent bond or a non-covalent bond with the target molecule in the system. In this step, binding sites are mainly formed around the template and functional monomers. In the second procedure, the crosslinking agent is added to the solvent to polymerise the functional monomer into a highly crosslinked polymer network, thereby firmly supporting and fixing the binding site structure of the prepolymer. The third procedure is removing of the template, creating complementary binding sites and imprinting cavities. The template is usually completely removed by repeated washing with organic solvents, often with the addition of bases and acids. The position and alignment of the functional groups of the cavity are generated for the template (i.e., "tailor-made" binding sites). Compared with analogues with similar structures, these imprinted cavities will preferentially bind to target substrate, mainly because of the influence of shape, size, corresponding bond formation and selective conformation of surface chemistry [58]. In this way, the resulted MIP is equipped with the recognition abilities toward specific templates. The mechanism of MIP is comparable to the commonly mentioned "lock and key" concept of the specific interactions between proteins and their substrates or receptors, such as the interactions between antibodies and their antigens [59, 60].

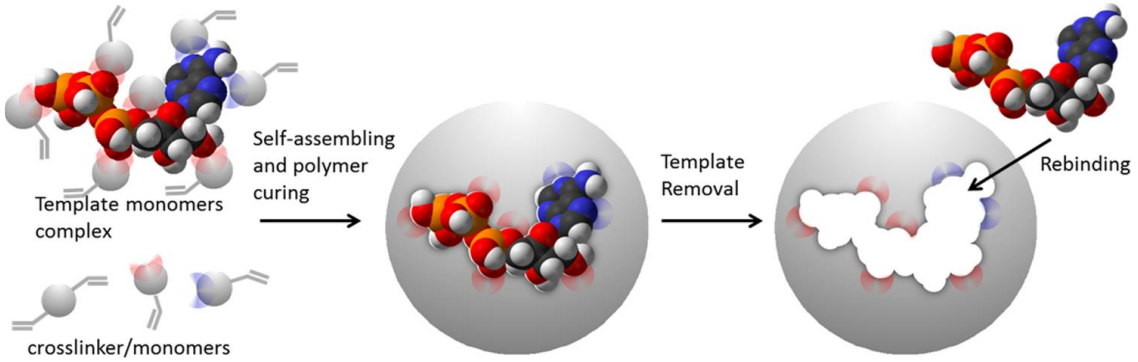

Figure 1-9 The preparation process of the molecular imprinted polymer [55].

The methods for preparing molecularly imprinted polymers can be divided into two types: covalent and non-covalent processes, which are mainly judged by the type of the interactions between the target template and the functional monomers. Among them, the covalent type proposed by Wulff in 1972 [54], involves the covalent bond between the functional monomer and the corresponding target template during the pre-polymerisation process. After the polymerisation, the template is removed by chemical cleavage of the covalent complex. The same covalent bond is formed in the subsequent application process to make the MIP bind to the target compound. In a covalent system, the interaction between the templates and the monomers is formed through reversible covalent bonds, such as esters, ketals, and Schiff bases. By stably maintaining the covalent interactions between the template and the monomer during the imprinting process, the imprinted polymers obtained have high specificity. The covalent system has great advantages in recognition specificity, but it also has several disadvantages. For example, because the system contains covalent bonds which is stable, it might be difficult to perform chromatographic separation. Moreover, as the covalent bond between the template and the monomer is not easy to break, it must always be formed through a reversible reaction, limiting the practical applications.

Therefore, the second method, non-covalent interaction, has been proposed and used in the presented work. Non-covalent bonds are generally formed through ‘weak’ interactions such as hydrogen bonds, electrostatic interactions,

hydrophobic interactions, and metal coordination bonds. Compared with covalent imprinting, non-covalent imprinting has a wider application range and more compounds can be imprinted. At the same time, the imprinting process is simpler and easier, as the template is mixed with the functional monomer to complete the complexation step and after polymerisation the template can be easily removed via simple methods. However, the forces of the non-covalent bond are relatively weak and the formation of the complex is mainly controlled by the balance of the reaction. Therefore, to form the complexation between the template and the monomer completely, and to maintain the stability of the complex, an excess of functional monomer is necessary. At present, non-covalent imprinting becomes the most widely used technology and has become a general synthetic method to prepare MIP [61].

Unlike antibodies in nature, MIP is easy to prepare and has a low cost as well as high stability and good mechanical abilities. Molecular imprinting technology can be applied to a wide range of analytes, including small molecules (drugs, pesticides, carbohydrates, etc.), organic macromolecules and biological cells (growth hormone, tumour cells, immunoglobulins, etc.) [52, 62]. In addition, MIP can be used to prepare tailor-made polymers under a variety of environmental conditions which bioreceptors cannot adapt to. Due to its excellent performance and wide range of applications, researchers have applied MIP to a variety of fields such as biomolecular recognition [63, 64], protein detection [65, 66], chromatographic separation [67, 68], hazardous, radioactive waste capture [69], solid-phase extraction [70, 71] element identification in electrochemical sensors [72, 73], catalysis and drug delivery [74, 75], etc, all exhibiting great potentials.

Biomimetic catalysts that mimic enzymes are also an important application area. When the chemical structure of the template is strategically designed to be similar to the transition state or the intermediate product of the reaction, the method of molecular imprinting has been proven to form a three-dimensional cavity in the polymer matrix, which exhibits enzyme-like catalytic activity. As early as the late 1980s, molecularly imprinted polymers made significant progress in the field of catalysis. Damen et al. [76, 77] published ground-breaking articles on stereo

control of chemical reactions and Wulff et al. [78] studied its application to enantioselective synthesis. Leohardt et al. [79] demonstrated the effect of substrate analogues on the imprinting. In 1989, Robinson et al. [80] published the first example of polymer imprinting using transition state analogues. In the subsequent years, researchers explored different methods of preparing imprinted synthetase. At the same time, they also studied its application in various chemical reactions, such as dehydrofluorination [81], β-elimination [82], type II aldolase [83], Diels-Alder reaction [84], phosphate hydrolysis [85] and so on. During the past decade, the development of MIP catalysts has flourished. Because its mechanism is similar to enzymes, its application in selective catalysis is one of the main directions of molecularly imprinted polymer catalysts [56].

1.4.2 Mussel-inspired smart polymers

The second type of biomimetic polymers described in this thesis is the mussel-inspired smart polymers. Because of its excellent adhesion and good self-healing ability, it can anchor active sites as carriers and provide smart switchable components for catalysts. The mussel-inspired materials have been developed to mimic the strong adhesion of mussels to gravel, rocks and ships in the sea. Studies found that the strong adhesion of mussels is mainly derived from the adhesion proteins in the mussel silk feet. These adhesion proteins can be solidified in a short time, so that mussels adhere firmly to the surface of various matrix materials in an aqueous environment [86, 87]. The critical component of mussel adhesion protein is 3,4-dihydroxy-L-phenylalanine (DOPA). The catechol group contained in DOPA is the main reason for its adhesion. Catechol has a strong surface affinity so that mussels can cross-link and bond with its adhesion surface. This cross-linking originates from various interactions such as metal chelation, hydrogen bonding, and free radical coupling, exhibiting good adhesion and self-healing effects [88-90]. Various factors, such as pH in the solution, amino compounds, metal ions, etc., may affect this adhesion properties. Because of its superior performance, several researchers have started studying and preparing

mussel-inspired polymers and then applying them to various fields such as chemistry, biology, and medicine.

Tang et al. [91] added Zn^{2+} to the vulcanisation reaction of butadiene-styrene-vinylpyridine rubber (VPR) and found that it formed a pyridine-Zn^{2+}-pyridine cross-linked network structure (**Figure 1-10**). This preparation method mainly reduced the stress in synthetic rubber by simulating the reversible bonds in mussels. The prepared sample can quickly return to its original shape when it was heated to 60°C. As for this system, the initial shape was controlled by the covalent network, and the transient network performed as a switch to fix the temporary shape.

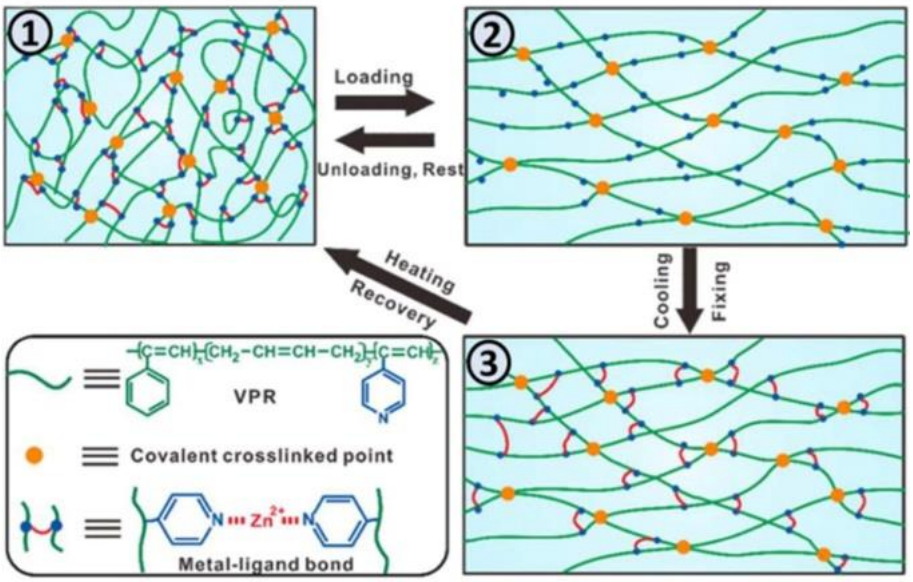

Figure 1-10 The shape-fixing mechanism of the VPR containing both covalent and metal-ligand cross-links [91].

To achieve the same purpose, Zhang et al. [92] introduced Fe^{3+} to coordinate with 6 oxygen atoms to form a metal complex to enhance the mechanical properties of epoxidized natural rubber (ENR). Researchers used zinc acrylate to cure ENR at the existence of $FeCl_3$, resulting in a network structure containing

covalent and metal supramolecular crosslinks. Through the cyclic tensile experiment, the dissociation behaviour of the Fe^{3+}-O bond under stress was studied and the expected hysteresis was obtained. At the same time, the influence of the coordination bond on the toughness was also proved. Coexisting networks (covalent and supramolecular networks) can enable the prepared materials two shape-setting conditions. As a result, a new triple shape memory property was produced in a simple polymer. The original shape was formed at 100 °C. The second shape was fixed when it was cooled to 43 °C from 100 °C and then the third shape fixed at 0 °C after being deformed at 43 °C. At the same time, it is possible to adjust the triggering temperatures with different contents of ferric.

In addition to adjusting the mechanical properties of the samples, the materials developed to mimic the mussels and their viscous proteins have also shown high potentials in self-healing properties [93]. Kollbe et al. prepared a material containing polyacrylate and polymethacrylate that mimicked mussels and confirmed its self-healing property in an aqueous solution [94]. The reason came from the hydrogen bonds formed between the catechol molecules at the interface, which accelerated the self-healing processes of the broken part of the polymer. When these non-covalent effects existed on the subsurface, this process could be further accelerated. The sample after repairing showed similar mechanical properties to the original sample (**Figure 1-11**), proving that the material can achieve a complete self-repairing process. Similarly, in addition to marine organisms like mussels, other organisms in nature also exhibit similar adhesion capabilities. For example, snails can secrete a kind of mucus so that they can maintain close adhesion to various surfaces such as rough rocks. Based on this feature, Cho et al. [95] synthesised a reversible superglue hydrogel that could be reversibly transformed for dehydration and hydration. This hydrogel showed a strong adjustment effect on the near-surface elastic modulus. The adjustment range was from 180 kPa (water state) to 2.3 GPa (dry state), which is similar to the transformation of snail's own structure from mucus to epiphragm.

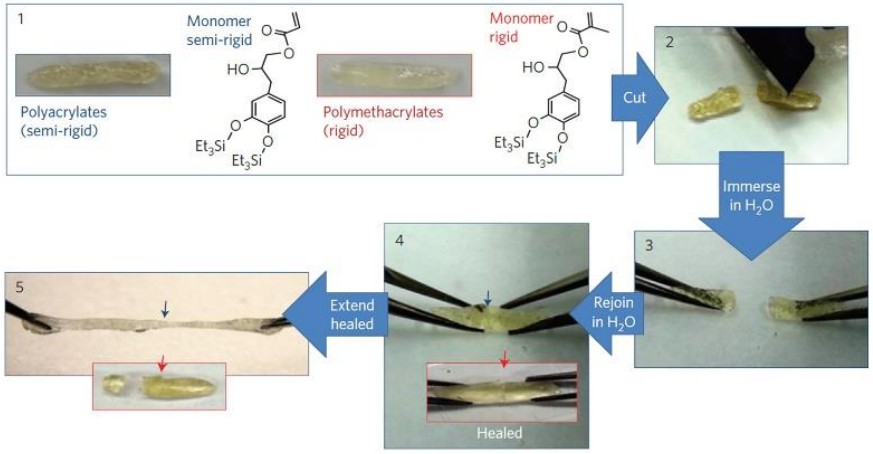

Figure 1-11 The self-healing process for polyacrylate materials [94].

1.4.3 Temperature-responsive polymers

The third type of biomimetic material described here is temperature-responsive polymers. Considering its sensitive properties toward different temperatures, the introduction of temperature-responsive polymers will enable the switchable control of catalyst. Stimulus-responsive polymers refer to the polymers that experience a series of conformational changes under external stimuli (i.e., temperature, pH, radiation, light). Many different research directions have been derived based on stimulus-responsive polymers, such as stimulus-responsive biofilms, films, capsules, and polymer brushes [96]. Stimuli-responsive polymers have also found applications in the development of fields such as drug release, catalysis, and sensors. Compared with other stimulus conditions (such as pH, light), the control of temperature is easier to realise and observe, and the operation of equipment is simpler. Therefore, temperature-responsive polymer has attracted the attention of several researcher groups worldwide. Temperature-responsive polymer (temperature-sensitive polymer) means that the polymer exhibits response behaviours controlled by the changes of external temperature.

Temperature-sensitive polymers can be divided into two types, namely polymers with the lower critical solution temperature and polymers with the upper critical solution temperature. Some polymers will undergo phase separation when the

temperature is higher than a specific temperature. This temperature is called the Lower Critical Solution Temperature (LCST). When the temperature in the solvent is lower than the LCST, the polymer chains and solvent molecules are in a homogeneous phase. However, when the temperature is higher than the LCST, the polymer and the solvent will undergo phase separation.

Poly-N-isopropylacrylamide (PNIPAM) is one of the most widely reported temperature-responsive polymers [97-99]. The LCST in its aqueous solution is between 31 °C-33 °C, which is close to human body temperature. The polymer structure of PNIPAM has repetitive hydrophobic and hydrophilic units. Hence, the polymer solution will change from water-soluble to insoluble states according to its degree of order with different temperatures. When the temperature in the solution is higher than 32°C, the polymer chains of PNIPAM change from a stretched arbitrary coil condition (dissolved) to a compact globule conformation (insoluble). This phase separation phenomenon is caused by the interactions between the polymer backbone and the non-polar functional groups on the side chains. Specifically, below its LCST, the PNIPAM chain exists in the form of coils due to the hydrogen bonding of the amide group and water. Above its LCST, when the kinetic energy of the molecule is greater than the energy of the hydrogen bond between water molecules, the interaction of the hydrogen bond is destroyed. As a result, the hydrophobic interaction between the hydrophobic backbone and the isopropyl group becomes the dominant one [100], and then the polymer conformation changes from a linear and flexible chain to a collapsed globule shape due to the aggregation of hydrophobic molecules inside or between molecules. The interactions between the polymer and the aqueous solution and between the polymer groups are the main factors that determines the specific behaviour changes of the LCST.

As for individual polymer chains, this conformational transition can be changed by adjusting the composition of the polymer [101], such as by copolymerising with another hydrophilic or hydrophobic monomer to increase or decrease the LCST [102, 103]. The LCST changes due to structural factors that affect the interactions between the polymer and water. In addition to PNIPAM, some of other classic

LCST polymers include poly-N-[2-(diethylamine) acrylamide] (PDEAEAM) [104], poly N-dimethylaminoethyl methacrylate (PDMAEMA) [105, 106], poly-N-diethylamine ethyl methacrylate (PDEAEMA) and poly-N, N-diethyl acrylamide (PDEAAM) [107, 108].

The Upper Critical Solution Temperature (UCST) is the opposite to LCST. It refers to the critical temperature from phase separation to homogeneous phase. The difference between the two is shown in **Figure 1-12**. For UCST polymers, the temperature-sensitive response mainly relies on the side chains between the different polymers or the strong molecular force between the polymer and the solvent. This effect can be hydrogen bonds, such as in poly-N-acryloyl glycine (PNAGA) (**Figure 1-13**), or it can be the electrostatic force between zwitterionic polymers.

PNAGA is a non-ionic polymer with UCST effect in the water. Seuring et al. [109-111] reported that the temperature response of PNAGA mainly came from the hydrogen bonds between polymer side-chain functional groups. Results indicated that the UCST of PNAGA changed to a lower temperature until there was no obvious UCST by continuously adding sodium thiocyanate to the PNAGA solution. The fundamental reason behind this was that the hydrogen bonds in the solution were destroyed. In addition, in their research, the introduction of hydrophobic monomers for copolymerisation, such as butyl acrylate or styrene [112], would also affect the cloud point, causing it to shift to higher temperatures. Mäkinen et al. [113] also obtained similar results when preparing triblock copolymers of PNAGA, PNIPAM and polyethylene oxide (PEO). The research results demonstrated that the block formation of PNAGA and PNIPAM changed their response temperatures respectively. At the same time, it showed that the different arrangement order of the blocks in the block copolymer also had influences on the temperature-sensitive behaviours of the copolymer.

In addition to the UCST of the polymer itself, there are also cases where the UCST effect is produced by the interactions between the polymer groups through the copolymerisation of two or more polymers. For example, in a copolymer of acrylamide and acrylonitrile, the UCST increases as the content of acrylonitrile

increases, and it was also found that the response temperature was related to the monomer ratio. Moreover, there are urea-based copolymers that also show response temperature, which is mainly because of the large number of hydrogen bonds in the copolymers of polyallylamine and polyallylurea as well as a series of their derivatives. In addition, since the copolymer structure is resonance stable, hydrogen bonding and possible π-π bonding could be enhanced. Further studies have found that its UCST would increase due to the increase of urea group content, while it would decrease due to the rise of molecular weight [114].

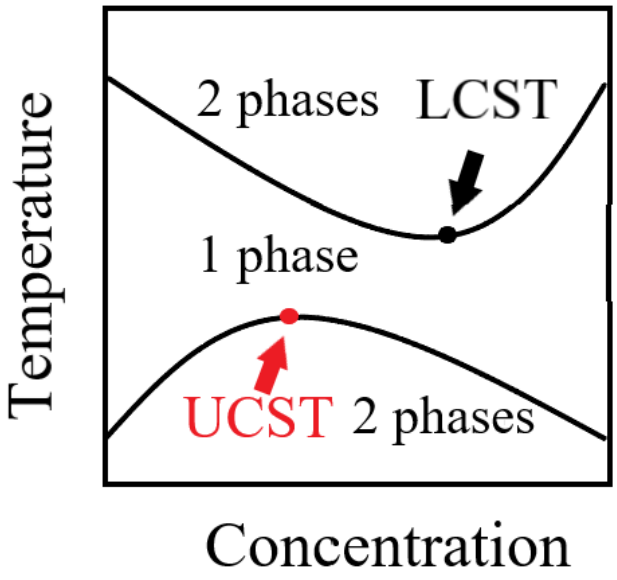

Figure 1-12 A phase diagram of the differences of UCST and LCST for a thermo-responsive polymer.

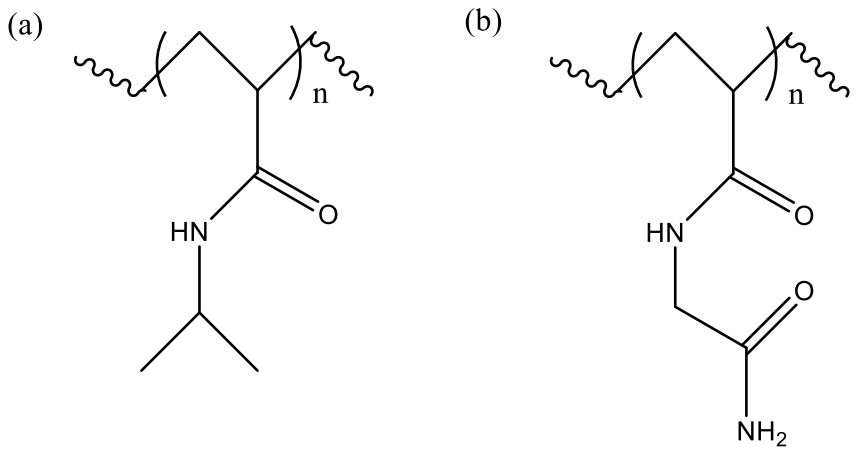

Figure 1-13 Structure schemes of LCST polymer PNIPAM (a) and UCST polymer PNAGA (b).

Based on the unique temperature sensitivity of LCST and UCST polymers themselves, a series of in-depth studies have been conducted. Further control of the responsive temperatures has broadened the temperature range of their applications, promoting the development for practical uses.

1.5 Aims and objectives

The overall aim of this project was to propose, develop and synthesis novel polymeric catalytic reactors to obtain an efficient, spatially separated and easily controllable tandem catalysis. In order to solve the two challenges of site separation and smart control, the project aim has been achieved through the following objectives:

-Development of molecularly imprinted polymer as the tandem catalyst allowing separation of each step in the reactions.

-Development of nanoreactor with core–shell structures as spatiotemporal compartments for “undisturbed” tandem catalysis.

-Development of novel polymer-based solutions that allow temperature-controlled access to the multiple MIP based catalytic sites during tandem

catalysis using mussel-like, self-healing polymers and temperature responsive polymers.

-Discussion of temperature responsive behaviours of smart polymers and adjustment of the responsive temperature ranges.

1.6 Thesis structure and published work

1.6.1 Thesis structure

The author of the thesis has taken part in the Dual PhD Degree Programme between Cranfield University (UK; 30/09/2019 to 30/09/2021) and Jiangsu University (China; 10/09/2017 to 30/09/2019) for PhD study. The content of this thesis based on the research in the two universities.

The structure of this thesis is formatted as journal papers and written based on the published papers. There are seven main chapters in the thesis. The section below will briefly introduce the contents of different chapters and the published work-related.

Chapter 1 contained a background introduction and a brief literature review. In this chapter, the background information and definition about tandem catalysis were introduced. Then the challenges of the tandem catalysis were discussed. The Chapter also shows some catalytic reactors presented in the literatures, analysing their advantages and disadvantages. Furthermore, the Chapter reports a literature review on the different smart polymers which have been used in the subsequent experimental sections.

Chapter 2 to chapter 6 mainly discussed five novel polymer reactors prepared to address the challenges of active sites separation and smart control of the catalysts. In chapter 2, an enzyme-like molecularly imprinted tandem catalytic reactor was introduced. Inspired by the ability of intracellular enzymatic reactions that can recognise different reaction substrates, in this experiment a novel imprinted polymer reactor was prepared, which contained acidic sites and metal nanoparticles as catalytic sites for catalytic reduction and hydrolysis. By

imprinting the initial product and the intermediate product, the two catalytic sites, like the compartments of the enzyme reaction in the cell, catalysed different reactions respectively, thereby completing the entire tandem reaction process. In some functional polymer reactors, tandem catalysis is mainly carried out through precise control of catalytic sites and artificial isolation. However, the novel catalytic reactor in this experiment proceeded the tandem catalysis in sequence naturally with different catalytic sites through the imprinting process, which simplifies the synthesis steps and improves the potential applications.

In chapter 3, a core-shell tandem nanoreactor was introduced. A variety of complex and multi-step reactions can be carried out in a cell without interference, as there are different compartments separated spatiotemporally in the cell. These compartments can ensure that each reaction step is carried out independently in different environments, even with varying values of pH, salt concentrations, etc. Inspired by the separated areas in the cell, a core-shell polymer reactor was synthesised in this experiment, in which the core and shell regions contained different catalytic sites, responsible for catalysing different reactions respectively. Due to the effect of mass transfer and the radial distribution of reaction sites, this structure enabled this nanoreactor to separate different reaction processes from each other spatiotemporally. Therefore, this nanoreactor could complete tandem reactions sequentially, minimising the occurrence of any side reactions. Common nanoreactors and dual-function catalysts often involve competition or cross-reactions during tandem processes. This new type of nanoreactor has shown the ability to perform the entire reaction process in the desired direction, improving the overall reaction efficiency and the output of the target product. This has provided new ideas for the application of functional catalysts in the field of tandem catalysis.

In chapter 4, mussel-inspired "sandwich" switchable smart tandem catalytic reactor was introduced. The previous two experiments were mainly designed for the challenge of separating different catalytic sites. Based on the site separation properties, this experiment introduced mussel-inspired smart polymers to control the catalytic processes so that the tandem reaction process could be adjusted

under different conditions. Inspired by the high-efficiency adhesion and self-healing properties of mussels, a mussel-like smart layer was prepared as the switch of a multi-layer polymer reactor, which could control the opening and closing of the channel for the substrates, thereby controlling the whole tandem reaction. The catalytic reactor consisted of two functional catalytic layers and a smart switchable layer. The top and bottom layers were composed of molecularly imprinted polymers and active sites (acidic components and metal nanoparticles). The intermediate layer was prepared by copolymerisation of polydopamine acrylamide (PDPA) and polyacrylamide, which can act as a switch, allowing or inhibiting the passing of substrate molecules under low or high temperature conditions. At low temperature, the channel of intermediate products was blocked because of the closed condition of middle layer, so that only simple reactions could happen. At high temperature, the intermediate channel was opened, conducting the whole tandem reactions. Therefore, the tandem catalytic reactor achieved the control of the tandem reaction processes as well as the separation of catalytic sites.

In chapter 5, a dual-responsive bilayer polymer reactor was introduced. The biological systems realise the self-regulation of the complex reaction process mainly through their soft changeable shapes and their freely changing stack structure. They can accurately transport the reactants through the channels to different catalytic components, achieving self-control performance from simple reactions to complex tandem reactions. Inspired by this, a novel dual responsive bilayer polymer reactor was prepared. The reactor was capable of changing its shape through the different responsive abilities of each layer when exposed to different temperatures, completing catalytic processes from simple reactions to complex reactions at low, medium and high temperatures. The smart catalytic reactor had two different temperature-sensitive layers, and the two layers contained acidic and metal catalytic sites respectively for different catalytic reactions. The first layer was the PAMPS-PAM copolymer, which could respond to medium temperature due to the weak hydrogen bonds between the two polymers. At medium temperature the hydrogen bonds were broken and the reaction channel opened, thereby catalysing the hydrolysis reaction. The second

layer was composed of PTFMA-PVI containing Au nanoparticles, which had strong electrostatic effects. At high temperature, due to the dissociation of the effects, the channel opened and the tandem reaction from hydrolysis to reduction was carried out. In this way, the reactor allowed the regulation of simple/tandem reaction processes.

In chapter 6, a self-regulating catalytic polymer reactor PRS was prepared. Such reactor was composed of two layers of molecularly imprinted polymer and an intermediate temperature response layer. The top and bottom layers of molecularly imprinted polymers contained two different catalytical active sites for two consecutive steps in tandem catalysis. The molecularly imprinted properties of the polymer also improved the selectivity of the reaction. The middle switchable layer was composed of PNIPAM and PAM and was responsible for the control of the tandem catalytic processes thanks to its behaviours at different temperatures. When the temperature was lower than the LCST of the copolymer, the intermediate layer was open, allowing the reactants to pass through, so that the tandem catalysis from hydrolysis to reduction could be carried out. When the temperature rose above the LCST, the intermediate layer was closed, inhibiting the entry of intermediates, so that only the hydrolysis reaction could proceed. Therefore, PRS permitted to control the catalytic process. In addition, by adding an appropriate proportion of copolymer acrylamide (AM), the adhesion and mechanical properties of the intermediate layer significantly improved. As a result, PRS could carry out the repeatedly switchable catalysis process stably with high efficiency.

Chapter 7 comprises a brief conclusion about the several experiments. By analysing and comparing the results of different experiments, this chapter confirmed that these novel polymer reactors were able to achieve the smart tandem processes effectively as expected. Moreover, it further discussed the directions of the future work based on the presented work and put forward ideas that can further optimise the polymer reactors.

1.6.2 Published work

The thesis was written based on several published papers of the thesis author as the first author. The specific published papers and corresponding chapters are as follows:

Wei, W., Zhou T., Wu S., Shen X., Zhu M., Li S. and Turner A. P. F. (2019) 'Biomimetic polymer reactors and their applications in self-ruled catalysis', Chapter 1, *Smart Polymer Catalysts and Tunable Catalysis*, 2019, 1-31. Elsevier. (Chapter 1)

Wei W., Zhu M., Wu S., Shen X. and Li S. (2020) 'Stimuli-responsive biopolymers: An inspiration for synthetic smart materials and their applications in self-controlled catalysis', *Journal of Inorganic and Organometallic Polymers and Materials*, 30, pp. 69-87. (Chapter 1)

Wei, W., Zhou T., Wu S., Shen X., Zhu M. and Li S. (2018) 'An enzyme-like imprinted-polymer reactor with segregated quantum confinements for a tandem catalyst', *RSC Advances*, 8, pp.1610-1620. (Chapter 2)

Wei, W., Zhou T., Wu S., Shen X., Zhu M. and Li S. (2019) 'Nanoreactor with core-shell architectures used as spatiotemporal compartments for "undisturbed" tandem catalysis', *Journal of Inorganic and Organometallic Polymers and Materials*, 29, pp.1235-1242. (Chapter 3)

Wei W., Xiao P., Thakur V. K., Chianella I. and Li S. (2020) 'Smart bilayer polymer reactor with cascade/non-cascade switching catalyst characteristics', *Materials Today Chemistry*, 17, 100279. (Chapter 4)

Wei W., Thakur V. K., Chew Y. M. J. and Li S. (2020) 'Towards next generation "smart" tandem catalysts with sandwiched mussel-inspired layer switch', *Materials Today Chemistry*, 17, 100286. (Chapter 5)

Wei W., Thakur V. K., Li S., Chianella I., (2021) 'Self-switchable polymer reactor with PNIPAM-PAm smart switch capable of tandem/simple catalysis', *Polymer*, 235, 124265. (Chapter 6)

Chapter 2 Dual-template molecularly imprinted polymer MIP-Au-NP-BNPC and its site separation tandem catalysis

2.1 Introduction

Enabling complex chemical reactions sequentially in one-pot, tandem catalysis not only simplifies synthesis, separation and purification steps, but also reduces the use of solvents and ingredients. Tandem catalysis is environmentally friendly, convenient and efficient, drawing extensive attention in lots of related areas. Among the existing tandem catalytic reactors, the most common type is the functional reactor consisting of different sites [115, 116]. For example, in the initial research on functional reactors, researchers prepared a reactor containing both acid and base catalytic sites [117, 118], in which acidic catalytic sites were responsible for catalysing one reaction and basic catalytic sites catalysed another reaction. Thus, this functional reactor completed the entire tandem process. However, the system always required precise site control to prepare the functional tandem reactors [119-121] to avoid incompatible reactions and cross-reactions, resulting in high cost and complex synthesis processes. Therefore, this type of reactor does not seem to be suitable yet for practical applications and further improvements of the structures are needed to make it cheaper and easier to synthesise. In future research on functional tandem reactors, it is necessary to further develop new types of reactors that are easy to prepare and can perform tandem reactions while avoiding unnecessary side and unwanted reactions.

In the development process of materials, researchers have obtained a lot of inspiration from nature. The way of complex continuous reactions occurred in cells provides new ideas for solving the problems in tandem catalysis [38, 122]. In the process of evolution, cells in organisms face challenges to synthesise the required final products from available primary molecules through irreversible multistep reactions. After millions of years of evolution, the cell finally achieved the ultimate goal by dividing the main enzymatic reaction chamber for reactions

[123,124]. In this process, the required multi-step reactions are carried out in separate areas in a simplified way, avoiding unexpected reactions due to the specificity of the enzymatic reaction. Enzymes can be used as a streamlined scaffold to regulate the sequence of tandem catalysis, thus saving the steps of additional regulation of catalytic sites. Although the specific reaction mechanism still needs to be further clarified, there has been explanation of these separated regions for catalysis in microscopic quantum mechanics theories [125,126]. The results showed that the success of the tandem reaction mainly depends on the interactions of different kinds of catalytic sites and substrates. The tandem reaction process with specific recognition properties generally includes two parts: the available channels and the continuous catalysis. The former enables the target reaction to occur, and the latter controls the progress of the tandem catalytic process. Therefore, the cell as a reactor can complete a variety of specific tandem reactions in sequence.

Inspired by this delicate structure, in this experiment, an enzyme-like molecularly imprinted polymer (MIP) was prepared to solve the current challenges in tandem reactors. The polymer reactor consisted of two parts: a MIP containing acidic sites to catalyse hydrolytic reactions; gold nanoparticles encapsulated inside the polymer to catalyse reductive reactions (**Figure 2-1**). The functional MIPs were prepared by imprinting two types of substrates. Herein, two compounds, bis(4-nitrophenyl) carbonate (BNPC) and 4-nitrophenol (NP), were chosen as two substrates as they can be well coupled to acidic catalytic sites and metal catalytic sites [127, 128]. BNPC can be catalytically hydrolysed to NP through acidic sites, and then NP is further catalysed by reductive metal nanoparticles to obtain the final product 4-aminophenol (AP). In this way, this MIP reactor is able to complete the tandem catalysis. Because of the existence of two imprinted parts, the reactor can be divided into two separate microscopic regions and each one is responsible for a separate reaction. Moreover, the two active sites enable the process of tandem catalysis. The recognitive imprinted parts and two corresponding active sites make the tandem catalysis proceeding in the expected direction without additional control and manual separation of different active sites.

To simplify the description of the experiment and analysis part, the polymer reactor is named as MIP-Au-NP-BNPC. To study the performance of the imprinted part of the reactor on the tandem catalysis, three controls were also prepared: two samples containing only a single template (BNPC or NP) and one sample without template (MIP-Au-BNPC, MIP-Au-NP, NIP-Au, respectively). This research aims at using the novel MIP reactor to achieve the tandem catalysis with recognitive separation regions of catalytic sites, so as to provide inspiration for functional catalysts that can be applied to complex chemical reactions in the future.

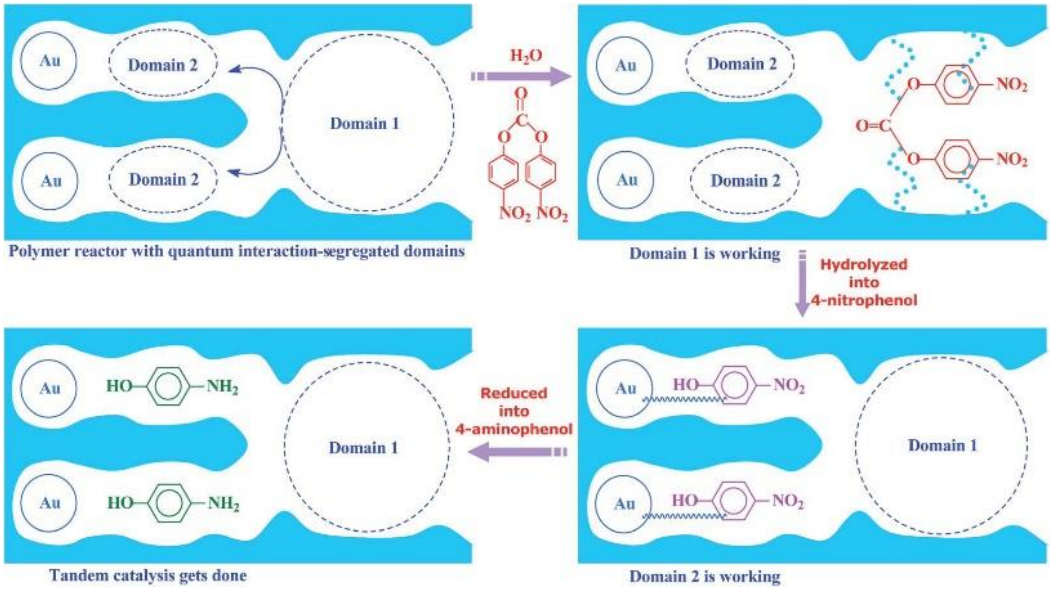

Figure 2-1 The tandem catalysis mechanism for the enzyme-like imprinted-polymer reactor.

2.2 Experimental section

2.2.1 Experimental materials and equipment

The chemicals and equipment used in the experiment are shown in **Table 2-1** and **Table 2-2** below:

Table 2-1 Experimental materials

Chemicals	Purity	Company
2,2'-Azobis(2-methylpropionitrile) (AIBN)	98.0%	Sigma-Aldrich Ltd
N, N'-Methylene bisacrylamide (MBA)	99.0%	Sigma-Aldrich Ltd
Dimethyl sulfoxide (DMSO)	≥99.9%	Sigma-Aldrich Ltd
Sodium borohydride ($NaBH_4$)	≥98.0%	Sigma-Aldrich Ltd
2-Acrylamido-2-methylpropane sulfonic acid (AMPS)	99.0%	Sigma-Aldrich Ltd
Acrylamide (AM)	≥99.0%	Sigma-Aldrich Ltd
Gold (III) chloride trihydrate ($HAuCl_4 \cdot 3H_2O$)	≥99.9%	Sigma-Aldrich Ltd
4-Nitrophenol (NP)	≥99.0%	Sigma-Aldrich Ltd
Bis (4-nitrophenyl) carbonate (BNPC)	≥99.0%	Sigma-Aldrich Ltd
Acetic acid	≥99.7%	Sigma-Aldrich Ltd
Methanol	≥99.9%	Sigma-Aldrich Ltd

Table 2-2 Experimental equipment

Equipment	Company	Model
Vacuum oven	Yiheng Instrument, China	DHG-9145A
Constant temperature water bath	Sanfa Scientific Instruments, China	HH-S4
Electronic balance	Sartorius, Germany	BS-210S
Electrochemical workstation	Chenhua instruments, China	CHI760E
UV-visible spectrophotometer	Shimadzu corporation, Japan	UV-2800
Transmission electron microscope	Hitachi, Japan	JEM-2100
Scanning electron microscope	JEOL, Japan	JSM-7800F
Fourier Transform Infrared Spectrometer	Thermo Fisher Scientific Inc., US	Nicolet MX-1E
Zetasizer	Malvern Panalytical, UK	Nano ZS90
BET surface area and porosity analyser	Kantar Corporation, US	NOVA2000
Temperature-programmed desorption device	Fantai, China	FINESORB-3010

2.2.2 The preparation of the polymer reactor

The polymer reactor was prepared by the classical molecular imprinting synthesis method (**Figure 2-2**) [129]. Firstly, chloroauric acid (78.8 mg; 0.2 mmol) was added to the dimethyl sulfoxide solution of one template NP (0.4 mmol ml^{-1}; 5 ml) to obtain the $[Au\ (NP)_2]^{3+}$ complex [130, 131]. Then another template BNPC (30.4 mg; 0.1 mmol), functional monomer (2-acrylamide-2-methylpropanesulfonic acid (AMPS); 0.21 g, 1.0 mmol), crosslinking agent (N, N'-methylene bisacrylamide (MBA); 0.54 g, 3.5 mmol) and initiator (AIBN; 0.2 g) were added to the mixed solution. After complete ultrasonic dispersion and nitrogen deoxygenation, the mixed solution system was put under ultraviolet radiation (365nm; 24h) to polymerise completely, forming the precursor of the molecularly imprinted polymer. After the polymerisation, an excess of sodium borohydride solution (10 times the content of Au ions; 2 h) was used to further reduce the Au ions to the Au nanoparticles. Then the obtained polymer sample was washed repeatedly with 500 mL mixed solution of acetic acid and methanol (methanol: 10%) (36 hours, the solution was changed every 12 hours), and the finally obtained sample was dried in a vacuum oven and further grounded to a size of 60 mesh for the next test.

Considering the necessity of Au nanoparticles for the entire catalytic process, the other three controls (MIP-Au-BNPC, MIP-Au-NP, NIP-Au) also contained Au and were synthesised under the same conditions. The control groups only contained a single template or no template, and therefore only a single selective channel or non-selective channel was included in the polymer network of the sample.

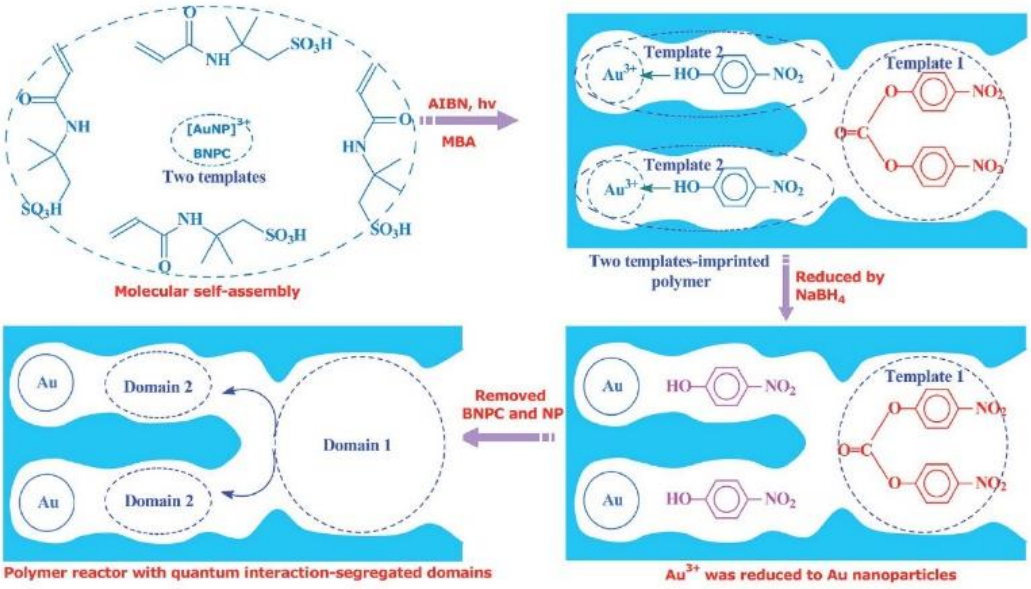

Figure 2-2 The preparation process of the enzyme-like imprinted-polymer reactor.

2.3 Tests and characterisation

2.3.1 Scanning electron microscope (SEM) and Energy-dispersive X-ray spectroscopy (EDS) tests

After grinding to the size of 60 mesh, a small amount of the polymer reactor sample (10 mg) was sticked on the conductive carbon adhesive tapes. Then the morphologies of the samples were observed by scanning electron microscope (SEM) after gold-spraying treatment. At the same time, the type and content of elements contained in the sample were analysed by energy-dispersive X-ray spectroscopy (EDS).

2.3.2 Transmission electron microscope (TEM) tests

The grounded polymer reactor sample (10 mg) was added to the solvent ethanol (4 mL) and completely dispersed by ultrasound. Then the dispersive solution was added dropwise (2-3 drops) onto the TEM copper mesh (carbon film) and dried for the tests. The size and distribution of Au nanoparticles in the sample and the control group were observed by TEM.

2.3.3 BET surface area and porosity analyser tests

The powder samples (0.1 g) of the sample and two controls were dried overnight, weighed, and placed in a long-necked flask for testing. The specific surface area and the specific pore size distribution were obtained by BET tests to confirm the existence of molecular imprinting components in different samples.

2.3.4 Fourier transform infrared spectrometer (FTIR) test

The polymer reactor sample powder was mixed with potassium bromide (KBr) powder (1/100-1/50) and grounded uniformly. Then it was dried with an infrared lamp and tested as a thin tablet. The FTIR tests were used to show the different functional groups of the samples and the template removing processes to study the structure and composition of the polymer reactor. The scanning range was 4000 to 400cm^{-1}.

2.3.5 Surface plasmon resonance (SPR) tests

SPR tests were used to characterise the characteristic absorption peaks of metal nanoparticles to figure out the type of it. A small amount of dry sample powder (20 mg) was pressed into a mould containing barium sulphate ($BaSO_4$) for the tests with UV-vis spectrophotometer.

2.3.6 Temperature programmed desorption (TPD) tests

TPD tests can be used to clarify the interactions between the samples and the corresponding substrates to further study the molecular imprint recognition performance [132, 133]. Compared with the control reactor lacking the imprinted components, the samples with the corresponding imprinted parts have stronger interactions with the substrate.

The powder samples (10 mg) were put into a U-shaped tube (inner diameter: 4mm) and 10 μl of the corresponding substrate (concentration: 0.05 μmol/mL acetonitrile solution) was added for complete adsorption. Then the sample was heated at the rate of 10 °C/min in a nitrogen gas until the substrate was desorbed from the samples. The final desorbing spectra were recorded and analysed by the data processing system.

2.3.7 Catalytic tests

The tandem catalysis tests were consisted of two reaction processes: hydrolysis and reduction. The specific catalysis process was tested by UV-vis spectrophotometer every 10 minutes until the completion of the tests. Each test result was obtained by averaging three times. The initial concentration of BNPC was 0.2 μmol/mL (10 mL PBS; pH 7.0) and the polymer reactor concentration of each test group was 1.0 mg/mL. The reducing agent $NaBH_4$ was added to the system simultaneously with content four times of BNPC. Moreover, due to the self-hydrolysis of the initial substrate NPA that existed in the tests, the conversion rate without the catalyst was tested at the same condition for each test and then deducted to obtain the conversion contributed only by catalysts [134].

2.3.8 Electrochemical tests

An electrochemical workstation was used to further determine the interactions between the imprinted parts of the prepared reactor and the substrates [135]. The workstation was a traditional three-electrode structure (Au plate working electrode, Pt wire counter electrode, and Ag/AgCl reference electrode). The polymer reactor powder (10 mg) pre-soaked and with 2 μmol template solution fully adsorbed was put into an electrolytic cell (electrolyte: 10 mL PBS; pH 7.0). The sample was scanned continuously until a stable cyclic voltammetry curve was reached (scan range: -0.3 to -1 V; scan rate: 1 mV/s).

2.4 Results and analysis

2.4.1 The analysis of the composition and morphology of the polymer reactor

As mentioned in the preparation section, the polymer reactor MIP-Au-NP-BNPC contained two templates: BNPC and NP. The molecularly imprinted cavities were obtained by washing these two templates repeatedly during the synthesis (**Figure 2-2**). First of all, the main functional groups of the polymer reactors and the process of molecular imprinting were studied by FTIR spectroscopy (**Figure 2-3**).

There were four main absorption peaks appearing in the figure: the O-H/N-H stretching vibration absorption peaks appearing at 3000-3750 cm^{-1}, the C=O absorption peaks appearing at 1600-1800 cm^{-1}, the S=O absorption peaks appearing at 1300-1550 cm^{-1} and the absorption peak of C-N/C-C at 1000-1300 cm^{-1} [136, 137]. To further confirm the composition of the reactor, the figure also showed the spectra of the other three control groups.

To further confirm the complete removal of the templates, the spectra of the two templates (BNPC and NP) and the precursor of the MIP-Au-NP-BNPC sample (the sample before the templates washing processes) were also compared in the figure. The figure showed that the polymer precursor contained two characteristic peaks of the template around 3400 and 1750 cm^{-1}. When the template BNPC and NP were removed, the spectrum of the polymer reactor became similar to that of the other reactor without template. Combined with the specific reaction process (**Figure 2-1**), the presence of imprinted components can be confirmed by the results (the presence of imprinted components was further discussed in section 2.3.3 and 2.3.4).

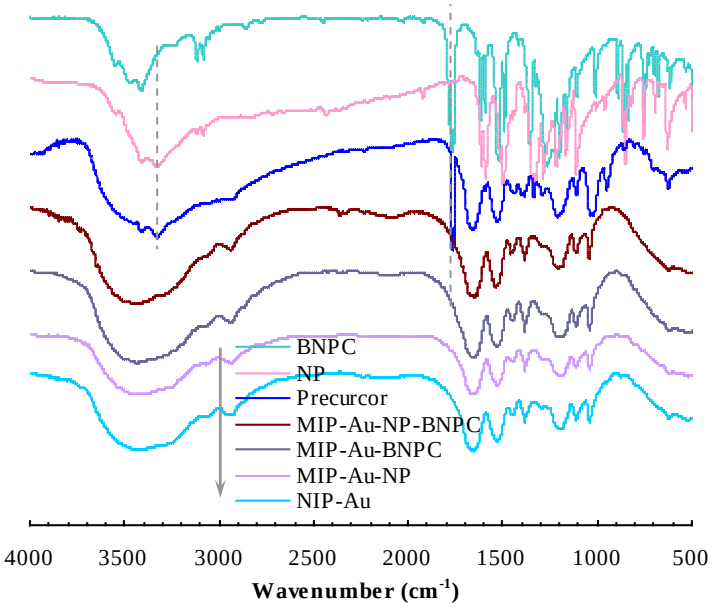

Figure 2-3 FTIR spectra of the prepared polymer reactors.

Figures 2-4 and **Figure 2-5** showed the SEM and TEM images, showing the morphology of the polymer reactor and the distribution of metal nanoparticles contained in the polymer carrier respectively. It is shown in the SEM image in Figure 2-4 that the surface was rough and porous, which resulted from repeated washing preparation processes of the molecularly imprinted parts. It can be seen from the TEM image in Figure 2-5 that the metal nanoparticles distributed on the several reactors were uniformly distributed with a similar particle size of about 15 nm.

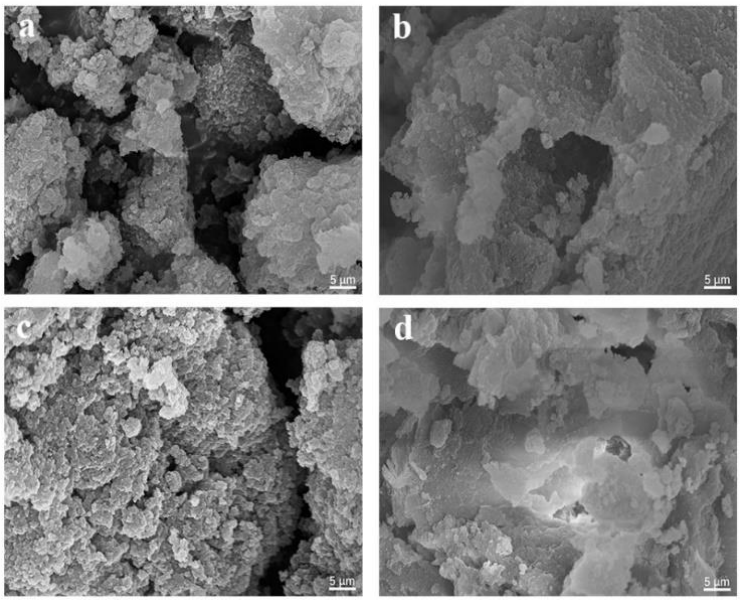

Figure 2-4 SEM images of the polymer reactors (a) MIP-Au-NP-BNPC; (b) MIP-Au-BNPC; (c) MIP-Au-NP; and (d) NIP-Au.

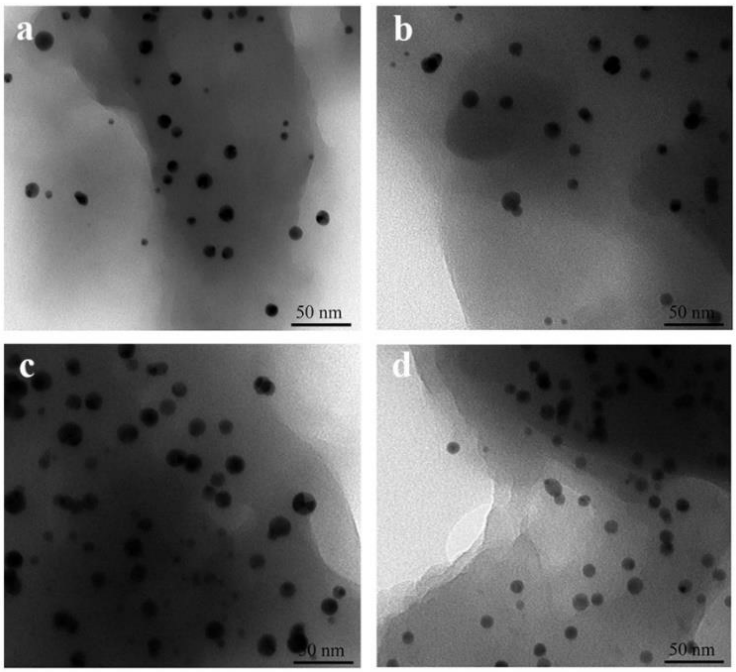

Figure 2-5 TEM images of the polymer reactors (a) MIP–Au–NP–BNPC; (b) MIP–Au–BNPC; (c) MIP–Au–NP; and (d) NIP–Au.

2.4.2 The analysis of the elements in the polymer reactor

The type of metal nanoparticles and other elements in the polymer reactor were further studied through SPR and EDS tests. When light reaches the metal surface, the delocalised electrons on the metal surface will resonate due to the vibration of the light wave, thus generating plasma waves. As for metal nanoparticles, due to the decrease in the number of electrons, the resonance frequency reaches the range of visible light, forming surface plasmon resonance (SPR). Different types of metal nanoparticles have specific SPR peak ranges, so that the SPR tests can be used to determine the type of metal nanoparticles. **Figure 2-6** shows the SPR spectra of the polymer reactor MIP-Au-BNPC-NP and three control samples. All four reactors showed the characteristic peaks of Au nanoparticles at about 520-540 nm.

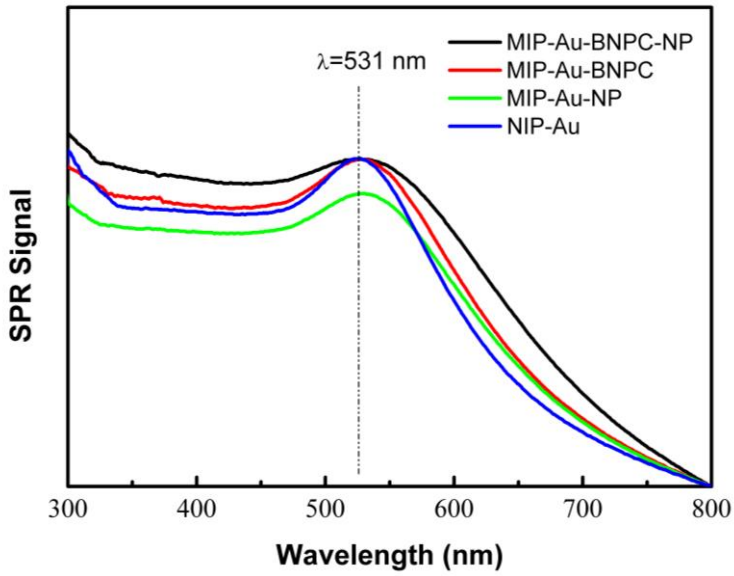

Figure 2-6 SPR spectra of the polymer reactors.

The metal nanoparticles and other elements contained in the polymer reactor were further characterised by the EDS tests in **Figure 2-7**. Several groups of samples showed similar elemental composition: C, N, O, S and Au. The content of Au was about 3.9% wt. The elements in different nanoreactors were consistent with the compositions. The results of SPR and EDS tests demonstrated that the basic composition of the polymer reactor MIP-Au-BNPC-NP was as expected.

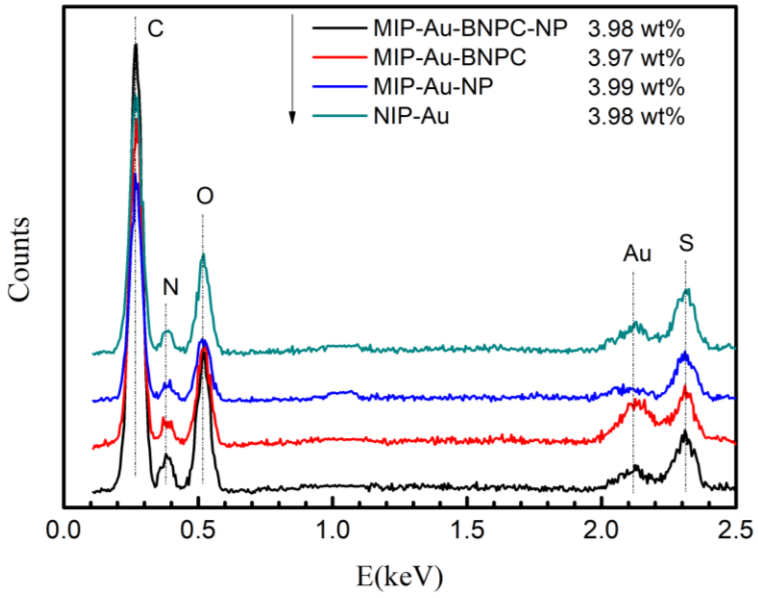

Figure 2-7 EDS spectra of the polymer reactors.

2.4.3 The analysis of BET surface areas and pore size distribution

Figure 2-8 presents the specific surface area and pore size distribution of the reactor MIP-Au-BNPC-NP and controls evaluated by BET tests. It was shown that the imprinted polymer reactor had a hysteresis loop under the condition of P/P0 <0.35, while the sample without the imprinted parts NIP-Au did not. In addition, MIP-Au-NP-BNPC showed two different pore size (<10 nm) distribution peaks at around 4 nm and 6 nm [138], while MIP-Au-BNPC and MIP-Au-NP had only one pore size distribution (6 nm / 4 nm). As for the non-imprinted polymer NIP-Au, there was no obvious pore size distribution. The results corresponding to the existence of the imprinting template cavity contained in different polymer reactors, confirming the imprinting process of the polymer reactor as expected.

Meanwhile, the specific surface areas and pore volume of the three layers of the samples are presented in **Table 2-3**. Compared with the control sample NIP-Au without imprinted components, the other three polymer reactors all showed relatively larger specific surface area and pore volume. MIP-Au-BNPC-NP with two templates exhibited higher surface area (142.7 m^2/g) and pore volume (63.9 µL/g) compared to the one template reactors MIP-Au-BNPC and MIP-Au-NP. These results were ascribed to the influence of template imprinting and washing processes during polymerisation. BET tests demonstrated the existence of molecularly imprinted parts and the influence on the morphologies of the polymer reactors.

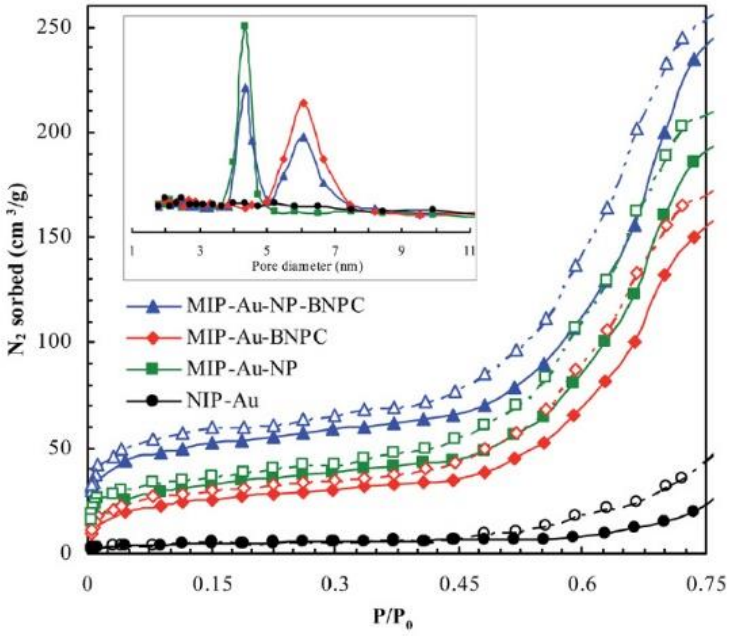

Figure 2-8 BET sorption isotherms of the polymer reactors (closed symbols: nitrogen adsorption; hollow symbols: nitrogen desorption).

Table 2-3 BET analysis of the prepared reactors

Polymer reactors	Surface area（m^2g^{-1}）	Pore volume（μLg^{-1}）
MIP-Au-NP-BNPC	142.7	63.9
MIP-Au-BNPC	108.2	59.8
MIP-Au-NP	114.6	61.2
NIP-Au	21.9	48.3

2.4.4 The analysis of the interactions between the substrates and polymer reactors by TPD tests

TPD tests were used to study the interactions between the polymer reactors and the imprinting substrates. Generally, the substrates are more difficult to desorb from the reactors when the interactions between the polymer reactor and the

substrate are stronger, therefore exhibiting the higher desorption temperature. As shown in **Figure 2-9**, the temperature when the template molecule NP was desorbed from the four samples MIP-Au-NP-BNPC, MIP-Au-BNPC, MIP-Au-NP, and NIP-Au were 268 °C, 201 °C, 270 °C and 199 °C, respectively. Compared with the two reactors without NP template (MIP-Au-BNPC and NIP-Au), the two reactors containing NP template (MIP-Au-NP-BNPC and MIP-Au-NP) both showed stronger interactions with NP. The same results also appeared in the tests of different polymer reactors desorbing from template BNPC. Both polymer reactors containing BNPC imprinted components showed higher temperatures with BNPC (367 °C and 368 °C respectively). In contrast, the other two polymer reactors that did not contain the corresponding components exhibited relatively lower desorbing temperature (262 °C and 260 °C, respectively), proving the stronger interactions of BNPC toward BNPC-containing reactors. Combined with FTIR and BET tests, the existence of imprinted parts in the polymer reactors was confirmed. Since the polymer molecular recognition properties are mainly derived from the results of molecular imprinting (i.e., imprinting of template molecules) processes in the preparation stage, polymer reactors with corresponding imprinted components will exhibit stronger interactions.

It can be seen from the test that the dual-template reactor MIP-Au-NP-BNPC demonstrated stronger interactions with the two corresponding templates, proving the higher selectivity to the corresponding substrate as a catalytic reactor. As explained in the preparation process Figure 2-1, the dual-template polymer reactor was imprinted with two template molecules BNPC and NP during preparation, and the others were imprinted with only one template or no imprinted templates. This result confirmed that the imprinted part of the template molecule can accommodate the corresponding substrate molecule, and only specific substrate molecules are able to enter its corresponding imprinted area.

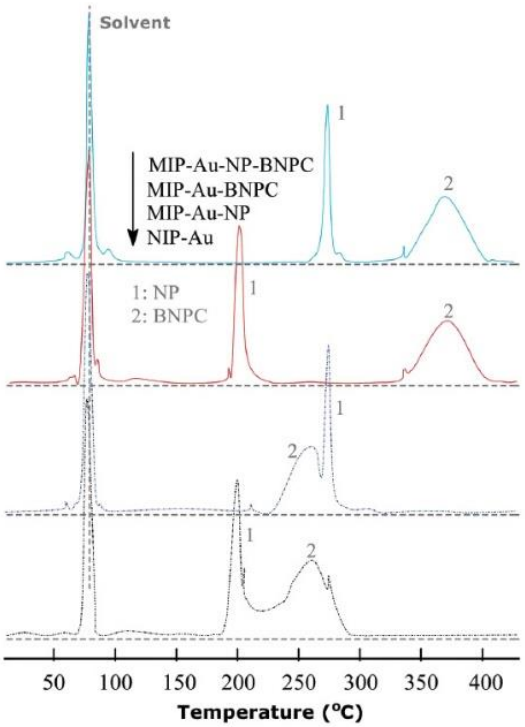

Figure 2-9 TPD profiles for the desorption of NP and BNPC from the polymer reactors.

2.4.5 The analysis of catalytic tests

The tandem catalytic process consisted of two consecutive reaction processes: hydrolysis and reduction. First of all, the catalytic efficiency of hydrolysis reaction was studied through the catalytic tests (**Figure 2-10**). To further study the influence of different active sites on the reaction, a non-acidic dual-template polymer reactor with acrylamide as the functional monomer was prepared as a control group to observe the hydrolysis behaviours of BNPC. Compared to the non-acidic control group, other polymer reactors containing acidic sites all showed higher catalytic reactor efficiency because the acidic sites were the catalysts for the hydrolysis of BNPC.

On the other hand, it can be seen that the two polymer reactors containing BNPC imprinted components all showed higher catalytic efficiency than the other two reactors without BNPC imprinted components, confirming that the presence of

the imprinted component BNPC increased the hydrolysis efficiency of the substrate. After subtracting the catalytic effect of MIP-Au-NP from MIP-Au-NP-BNPC and subtracting the corresponding catalytic effect of NIP-Au from the catalytic efficiency of MIP-Au-BNPC, the specific impact of BNPC imprinted component in the polymer reactors to the catalytic hydrolysis processes can be obtained (**Figure 2-11**). It can be seen from the results that the effects of BNPC imprinting components in the two reactors MIP-Au-NP-BNPC and MIP-Au-BNPC, were very similar. As a result, the imprinted parts of BNPC in the two reactors can be regarded as an independent area to accommodate the hydrolysis of BNPC. To further prove this conclusion, another analogue, guaiacol carbonate (GAC), was selected as a control group for further comparison. The two polymer reactors containing BNPC imprinted components had a degree of catalytic efficiency for the analogue GAC, but the catalytic efficiency was relatively low.

The comparison in Figure 2-11 indicated that both reactors showed a preference to BNPC. The results strongly confirmed that the imprinted components can regulate the reaction process and improve the selectivity toward templates in tandem reactions. Combined with the TPD tests, it was concluded that the polymer reactor could carry out the recognition and selectivity of the two templates of BNPC and NP, achieving the tandem catalysis from hydrolysis to reduction, promoting the reactions in the expected directions. Moreover, the imprinted components improved the efficiency of the reactions as the reactions happened in the corresponding cavities.

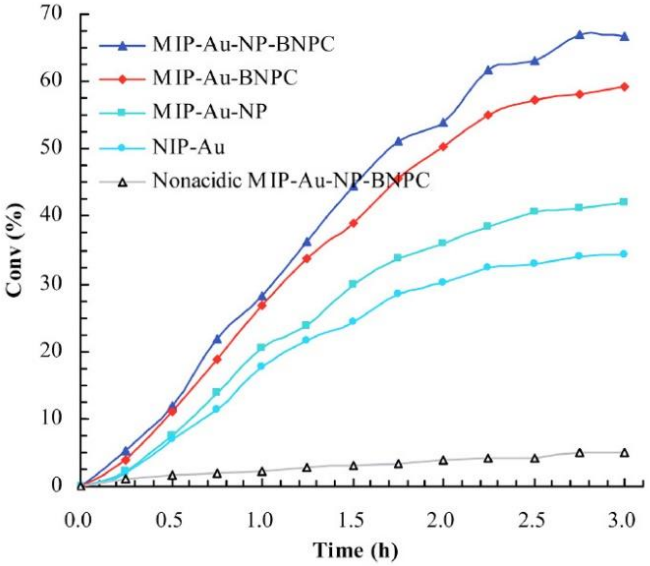

Figure 2-10 Catalytic performance for the hydrolysis of BNPC at different polymer reactors.

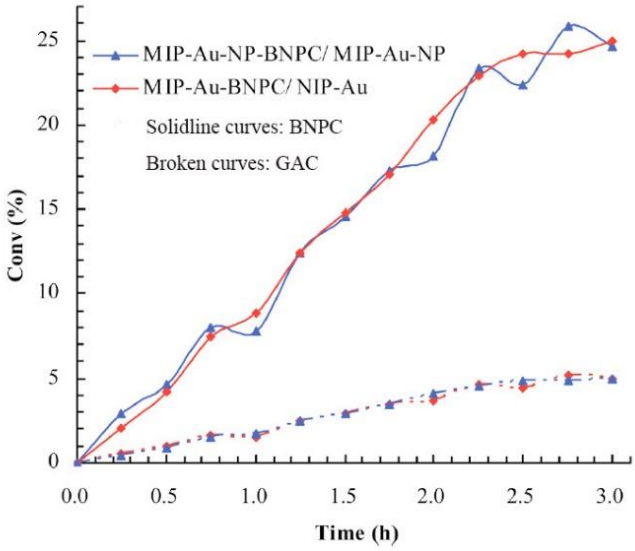

Figure 2-11 Contribution of the BNPC-imprinted components in MIP-Au-NP-BNPC and MIP-Au-BNPC to the selective catalysis

In order to study the whole catalytic process, UV spectroscopy was used to record the tandem catalytic process of BNPC at the existence of reducing agent $NaBH_4$. As shown in **Figure 2-12a**, for the non-imprinted reactor NIP-Au, there was a

decrease in 272 nm (initial substrate: BNPC) and an increase in 400 nm (hydrolytic product: NP), only performing the catalytic hydrolysis from BNPC to NP. Due to the absence of imprinted channels in NIP-Au, it was difficult for NP to contact metal nanoparticles, preventing the complete tandem catalytic processes. As shown in **Figure 2-12b**, for the dual-substrate polymer reactor MIP-Au-NP-BNPC, the decrease of the peak of BNPC (272 nm) resulted in an increase of the final product AP (297 nm), while the intermediate product NP (400 nm) increased firstly and then decreased. The whole changes indicated the tandem processes from hydrolysis to reduction, which was due to the existence of contact channels between the intermediate product NP and metal nanoparticles in the reactor MIP-Au-NP-BNPC, promoting the reactions as expected.

A similar reaction process occurred in the single-template reactor MIP-Au-NP (**Figure 2-12c**). The initiate product BNPC experienced a tandem process from hydrolysis to reduction to the final product AP. The difference was that the peak of the final product AP was smaller than that of the dual-template reactor, which was because MIP-Au-NP-BNPC contained the BNPC imprinted parts and improved the hydrolytic efficiency. As for the sample MIP-Au-BNPC, in addition to the formation of NP, the substrate also converted to bis (4-nitrophenyl) carbonate (BAPC; 320 nm) (**Figure 2-12d**), which came from the direct reduction of BNPC to BAPC. The emergence of direct reduction products was mainly due to the existence of the imprinted cavity BNPC. As mentioned above, the imprinted polymer can accommodate the corresponding substrate molecules, and only the corresponding substrate molecules can enter the channel in this area. Therefore, the MIP-Au-BNPC with the BNPC imprinted component provided the substrate BNPC with a channel to contact the metal nanoparticles, thereby obtaining the direct reduction product of BNPC.

As demonstrated in the catalytic process of MIP-Au-NP-BNPC and other controls, in the whole tandem processes, two different catalytic sites were responsible for the tandem reactions. At the same time, the imprinted parts provided the necessary channels for substrates, enabling the reactions in desired directions.

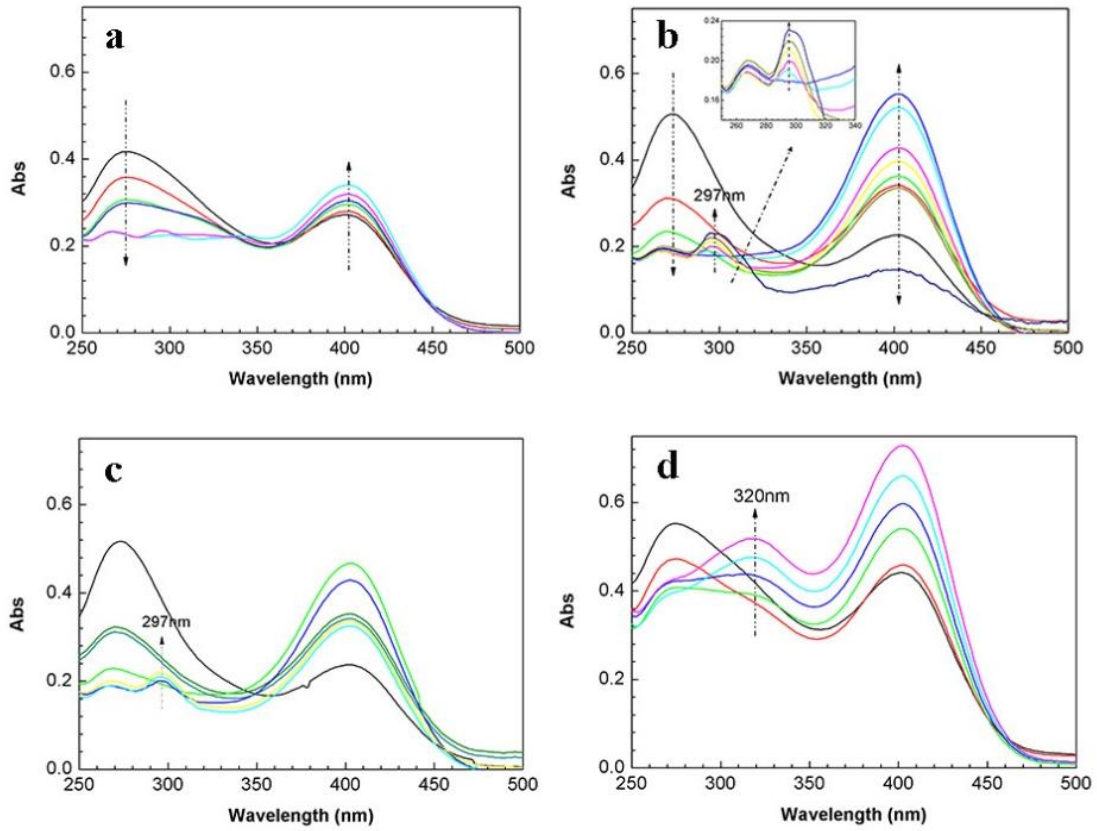

Figure 2-12 UV spectrum of BNPC at the polymer reactors (a) NIP-Au; (b) MIP-Au-NP-BNPC; (c) MIP-Au-NP; and (d) MIP-Au-BNPC.

2.4.6 The analysis of electrochemistry tests

Electrochemical tests were used to further study the interactions between the polymer reactors and the substrates [135]. It is known that the ability to reduce or oxidise binding molecules depends on the strength of the binding. A stronger bond requires more energy to open and therefore exhibits a more significant redox potential. As shown in the **Figure 2-13**, in the whole electrochemical process, the substrate molecule D experiences three processes: desorption, diffusion, and electrochemical reaction.

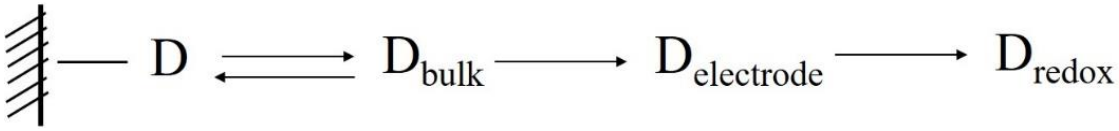

Figure 2-13 Electrochemical process of the substrate D.

In the whole electrochemical processes, the influence of the diffusion can be offset by applying ultrasound, so the electrochemical reaction of the substrate mainly depends on desorption. According to the theory of thermodynamics, the potential of the substrate in the bulk solution can be written as：

$$\mu_b = \mu^{\varphi} + RTln\frac{C_1}{C^{\varphi}} \quad \textbf{(2-1)}$$

Where μ^{φ} represents the standard chemical potential of the substrate, C^{φ}represents the corresponding standard concentration, C_1represents the actual concentration, R is the gas constant (8.314J $mol^{-1}K^{-1}$), and T is the reaction temperature. Connecting this equation (2-1) with the adsorption and desorption equilibrium of the substrate, the following equation is further obtained:

$$\begin{aligned} \mu_b &= \mu_n \\ &= \mu^n + RTln\frac{C_1}{C^n} \\ &= -RTlnK + RTln\frac{C_1}{C^n} \end{aligned} \quad \textbf{(2-2)}$$

In this equation, subscript n stands for polymer reactor. K is the equilibrium constant of the substrate adsorbed by the reactor, which relates to the affinity of the polymer to the substrate. Thermodynamic theory is used to discuss the role of the substrate in the working electrode, the equation (2-3) is finally obtained:

$$\begin{aligned} \mu_e &= \mu^e + RTln\frac{C_2}{C^e} \\ &= nEF + RTln\frac{C_2}{C^e} \end{aligned} \quad \textbf{(2-3)}$$

In equation (2-3), n represents the moles of electrons transferred in the redox process, E represents the redox potential of the substrate, and F is the Faraday

constant (96485 C mol^{-1}). C^e is the standard concentration of the substrate on the surface of the working electrode, and C_2 is the corresponding actual concentration. Equation (2-4) can be further obtained by subtracting equation (2-3) from (2-2):

$$lnK = (\frac{nF}{RT})E + \frac{\mu_e - \mu_n}{RT} - ln\frac{C_n C_2}{C^e C_1} \quad \textbf{(2-4)}$$

After eliminating the concentration gradient of the substrate in the solution by ultrasound, the stable redox condition is finally obtained by continuously scanning with a lower and constant cyclic voltammetry. Equation (2-5) is obtained:

$$lnK = \left(\frac{nF}{RT}\right)E + \frac{\Delta\mu}{RT} - ln\delta\frac{C^n}{C^e} \equiv aE + b \quad \textbf{(2-5)}$$

In equation (2-5), δ represents the ratio of C_2/C_1 when the substrate reaches the equilibrium of desorption and redox, and a, b are two quantitative constants. Under the same conditions, the interactions between the substrates, polymer reactors and the controls can be represented by equation (2-6):

$$\Delta lnK = a\Delta E \quad \textbf{(2-6)}$$

In this equation, K represents the strength of the binding force between the polymer reactors and the substrates, a is a constant, and E is the redox potential. In this way, the binding force between the polymer reactor and the catalytic substrate is directly related to the redox potential in the tests. A stronger binding force between the two will cause a larger redox potential. Therefore, the electrochemical desorption tests can be used to investigate the interactions of the dual-template polymer reactor to the substrates in tandem catalysis.

Figure 2-14 shows the desorption-reduction potentials of two substrates BNPC and NP desorbing, from the polymer reactor MIP-Au-NP-BNPC and the three controls. The peaks of BNPC desorbing from the catalytic reactor MIP-Au-NP-BNPC and the three control groups (MIP-Au-BNPC, MIP-Au-NP, NIP-Au) occurred at -806, -801, -768, -763 mV (Figure 2-14 (a-d)). In the results, the two reactors MIP-Au-NP-BNPC and MIP-Au-BNPC that contained the BNPC imprinted components showed stronger interactions on BNPC. In comparison,

the other two reactors without the BNPC imprinting components exhibited weaker interactions. The other substrate NP also showed similar results. As shown in Figure 2-14 (e-h), compared with the two reactors MIP-Au-BNPC and NIP-Au without NP imprinted components (-769, -766 mV), the two reactors MIP-Au-NP-BNPC and MIP-Au-NP containing NP imprinted components showed higher desorbing values toward NP (-788, -782 mV), proving that the two reactors had stronger interactions to NP. The results confirmed that the reactors had stronger interactions and higher selectivity toward the corresponding templates, which is consistent with TPD results. Combined with the analysis of UV catalytic tests, it can be concluded that the reactor MIP-Au-NP-BNPC is able to complete the tandem catalysis in desired directions with high catalytic efficiency.

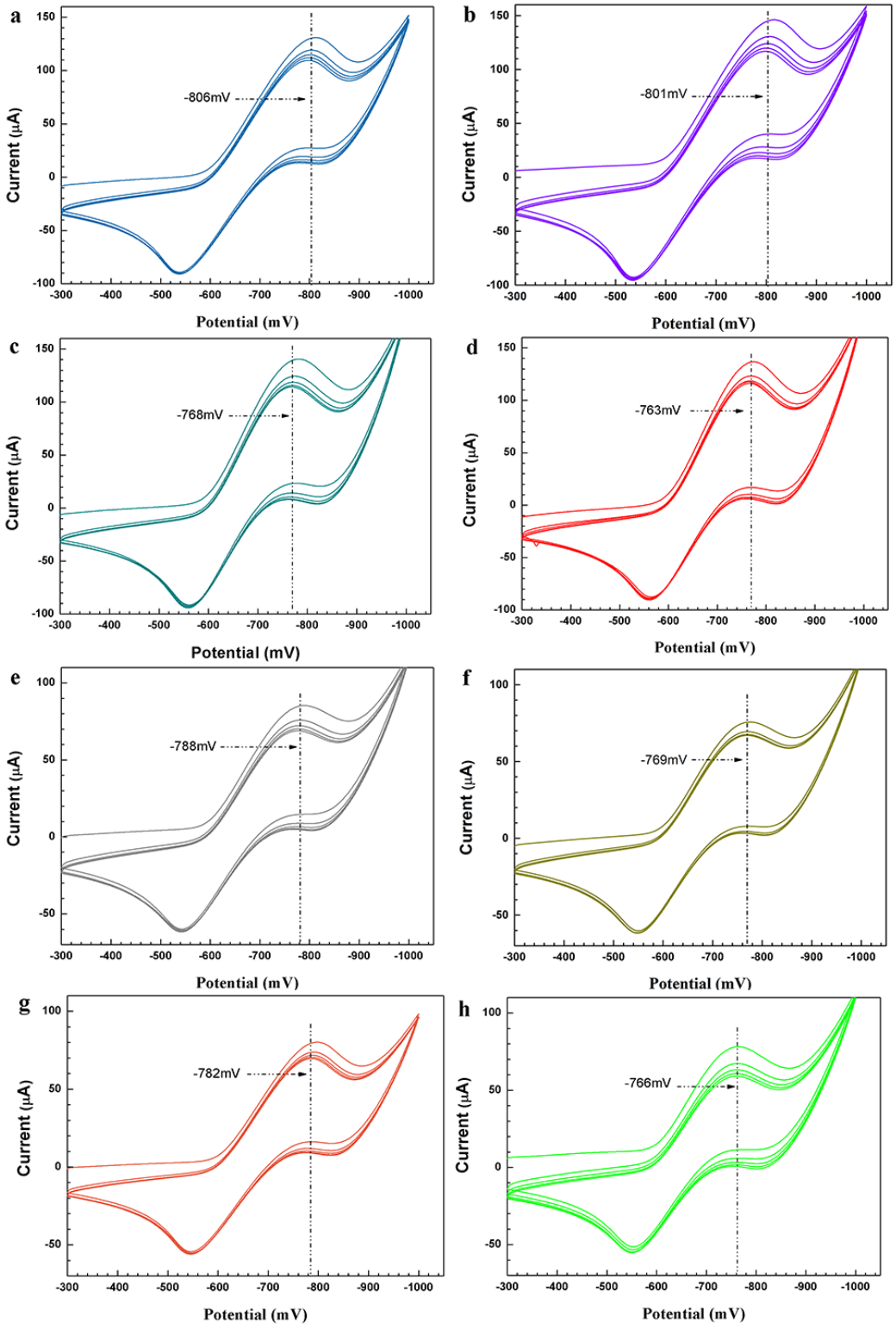

Figure 2-14 The desorption-reduction profiles of BNPC (a-d) and NP (e-h) at the prepared reactors (a) and (e) MIP-Au-NP-BNPC; (b) and (f) MIP-Au-BNPC; (c) and (g) MIP-Au-NP; (d) and (h) NIP-Au.

2.5 Interpretation of the tandem catalysis process by quantum mechanics

It is known that Schrödinger's equation solves the basic theory of microscopic particles and their motion under the potential field [139]:

$$\left[-\frac{\hbar^2}{2m}\nabla^2 + V(r)\right]\varphi(r) = E\varphi(r)\ (Time\ independent)$$

$$i\hbar\frac{\partial}{\partial t}\Psi(r,t) = \left[-\frac{\hbar^2}{2m}\nabla^2 + V(r)\right]\Psi(r,t)\ (Time\ dependent) \quad \textbf{(2-7)}$$

In this equation, $\hbar$ is the reduced Planck constant (1.05457*10^{-34}J s), i is the imaginary unit, φ (or Ψ) is the wave function of the quantum system (a function of position r or time t), E is the total energy of the quantum state, and V is the potential energy. Usually, time-independent functions are used for more convenient calculations. After calculating the time-independent function, the time-dependent function can also be further obtained by directly multiplying the exponential function exp(-iEt/$\hbar$) [140].

Due to the various changes of particle motion in practical applications and the complexity of the actual potential field, a series of simplified models need to be adopted in the practical calculation. The specific quantum mechanical behaviour is more complicated since the tandem catalytic system generally contains multiple active catalytic sites. In the dual-template tandem catalytic reactor, two different catalytic sites respectively catalyse one of the reactions. Due to the presence of the imprinted template, the two catalytic sites have specific substrate channels to promote the continuous reaction, which can further simplify the quantum mechanical behaviours in the tandem catalytic system.

In this experiment, the coupled BNPC and its hydrolytic product NP were selected as a set of imprinted templates to prepare the dual-template reactor MIP-Au-NP-BNPC. BNPC can be hydrolysed to NP firstly due to the presence of acidic sites, and then NP can be further reduced to AP by the metal nanoparticles. However, the other control groups contained only one template (BNPC or NP) or no template, so the polymer network contained only one or no accessible channels.

As a result, there was no tandem reaction occurred in the other control groups. Kronecker deltas ($\delta_{mm'}$; 1 or 0) and Dirac functions (δ (r); 0 or ∞) are used to summarise the different mechanical behaviours between the dual template polymer reactor and other controls. According to **Figure 2-15**, a simplified model can be obtained to describe the quantum mechanical behaviours in the polymer reactor (equation 2-8):

$$V(r) = -\frac{h^2\Omega}{m}\left[\delta_{m_1 m}\cdot\delta(r) + \delta_{m_2 m}\cdot\delta(r-b)\right] \quad \textbf{(2-8)}$$

In this equation, the interactions between the substrate molecules and two different "imprinted components" (BNPC (m1) and NP (m2) imprinted network) are considered as the potential well of the two processes in the tandem reaction (Ω represents the size of the potential well). The Kronecker deltas is based on the following conditions: the polymer network of these reactors contains ($\delta_{mm} = 1$) or lacks ($\delta_{mm'} = 0$) the corresponding "imprints". The reactor containing imprinted components will have strong interactions with the corresponding substrate molecules (V~- ∞), while the polymer reactor without imprinted components will not participate in the interaction with the substrate molecule (V~0). In this way, the Schrödinger equation for the entire tandem reaction can be expressed as:

$$\begin{aligned} &-\frac{h^2}{2m}\frac{d^2\varphi(r)}{dr^2} - \frac{h^2\Omega}{m}[\delta_{m_1 m}\cdot\delta(r) + \delta_{m_2 m}\cdot\delta(r-b)]\varphi(r) = E\varphi(r) \\ &\frac{d^2\varphi(r)}{dr^2} - k^2\varphi(r) = -2\Omega\left[\delta_{m_1 m}\cdot\delta(r) + \delta_{m_2 m}\cdot\delta(r-b)\right]\varphi(r) \end{aligned} \quad \textbf{(2-9)}$$

In this equation, $k \equiv \sqrt{-2mE/h^2}$ (The bound motion of the substrate molecules in the polymer reactor requires energy E<0). In order to further solve the equation (2-9), considering the complexity of the mathematical operations, the Fourier transform method is adopted. The Fourier transform of equation (2-9) is as follows:

$$\begin{aligned} &-\omega^2\psi(\omega) - k^2\psi(\omega) \\ &\qquad = -2\Omega\int_{-\infty}^{+\infty}\left[\delta_{m_1 m}\cdot\delta(r) + \delta_{m_2 m}\cdot\delta(r-b)\right]\varphi(r)e^{-i\omega r}dr \end{aligned} \quad \textbf{(2-10)}$$

$$= -2\Omega[\delta_{m_1 m}\varphi(0) + \delta_{m_2 m}\varphi(b)e^{-iwb}]$$

Therefore, it reads:

$$\psi(\omega) = \frac{2\Omega\left[\delta_{m_1 m}\varphi(0) + \delta_{m_2 m}\varphi(b)e^{-iwb}\right]}{k^2 + \omega^2} \quad \textbf{(2-11)}$$

In this equation, $\psi(\omega) = \int_{-\infty}^{+\infty} \varphi(r)e^{-i\omega r}dr$ (Fourier transform of $\varphi(r)$). The transformation in equation (2-11) shows that the wave function of the substrate molecule in the tandem system is as follows:

$$\varphi(r) = \frac{\Omega}{k}[\delta_{m_1 m}\varphi(0)e^{-k|r|} + \delta_{m_2 m}\varphi(b)e^{-k|r-b|}] \quad \textbf{(2-12)}$$

In equation (2-12), when r=0 and r=b, $\varphi(r)$ is written as:

$$\varphi(0) = \frac{\Omega}{k}[\delta_{m_1 m}\varphi(0) + \delta_{m_2 m}\varphi(b)e^{-kb}]$$
$$\varphi(b) = \frac{\Omega}{k}[\delta_{m_1 m}\varphi(0)e^{-kb} + \delta_{m_2 m}\varphi(b)] \quad \textbf{(2-13)}$$

In this way, it reads:

$$-\Omega\delta_{m_2 m}e^{-kb}\varphi(b) = \left(\Omega\delta_{m_1 m} - k\right)\varphi(0)$$
$$\left(\Omega\delta_{m_2 m} - k\right)\varphi(b) = -\Omega\delta_{m_1 m}e^{-kb}\varphi(0) \quad \textbf{(2-14)}$$

Dividing one relationship by the other in equation (2-14) will give:

$$\Omega^2\delta_{m_1 m}\delta_{m_2 m}e^{-2kb} = (\Omega\delta_{m_1 m} - k)(\Omega\delta_{m_2 m} - k) \quad \textbf{(2-15)}$$

Equation (2-15) provides a formula that includes energy, because k is a function of E. A value of zero in any Kronecker deltas will cause $k \equiv 0$ (hence $E \equiv 0$). As a result, the non-bound motions of the substrate molecules in the two potential wells makes it impossible to complete the whole tandem process (as shown in other control reactors, the entire tandem reaction process cannot be successfully completed due to the lack of necessary "imprints"). As for MIP-Au-NP-BNPC, the entire catalytic process can be completed with:

$$e^{-kb} = \pm(1 - \frac{k}{\Omega}) \tag{2-16}$$

In order to solve the final E, a simpler notation needs to be adopted.

$$X \equiv kb = b\sqrt{-\frac{2mE}{h^2}}\ and\ \sigma \equiv \frac{1}{b\Omega} \tag{2-17}$$

Therefore, equation (2-17) can be written as:

$$\begin{aligned} e^{-X} &= \pm(1 - \sigma X) \\ &= y^{\pm}(X) \end{aligned} \tag{2-18}$$

This is a transcendental equation of X (and therefore the transcendental equation of E). This equation can be obtained by drawing the equations of e^{-X} and $\pm(1 - \sigma X)$ in the same grid and finding the intersection point (**Figure 2-16**). The number of intersections is determined by the magnitude of σ (more or less than 1). There may be one or two. In this experiment, the imprinted cavity of BNPC allowed the channel of substrate BNPC for hydrolytic catalysis. Then the intermediate product NP can be contacted with Au nanoparticles for the next catalytic reduction process. It is unrealistic for two different types of reactions to obtain the same energy in two potential wells with different functions (corresponding to the single intersection in Figure 2-16b). Therefore, the tandem catalytic process can be carried out when $\sigma < 1$.Thus, the two intersection points in Figure 2-16a shows the prerequisites for the completion of the tandem catalytic processes of the polymer reactor MIP-Au-NP-BNPC (the separated quantum regions necessary for the tandem catalysis):

$$E_n = -\frac{h^2 X_n^2}{2b^2 m_n}(n = 1,2) \tag{2-19}$$

The separated quantum region in the polymer reactor is composed of two independent quantum domains, leading to the whole tandem catalysis. Therefore, once the initial substrate contacts the polymer reactor, the substrate molecules can contact the corresponding two quantum separation regions, one of which is

responsible for catalysing the hydrolysis, and the other is responsible for the subsequent reduction.

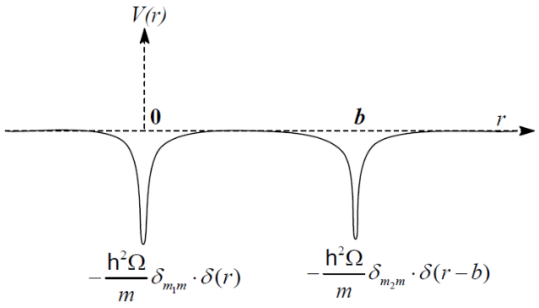

Figure 2-15 Suggested tandem δ potential-wells.

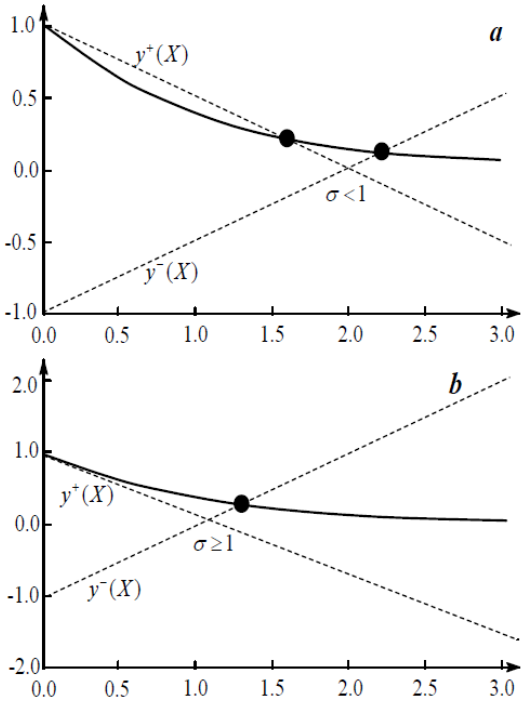

Figure 2-16 Schematically graphic solutions to Equation (2-18).

2.6 Conclusion

In this chapter, the experiments and findings mainly have shown to be a solution to the current multi-site separation challenge in tandem catalysis by preparing an enzyme-inspired dual-template imprinted polymer reactor MIP-Au-NP-BNPC. The polymer reactor consisted of two parts: a functional molecularly imprinted polymer and two active sites (acid sites and Au nanoparticle sites). The acidic catalytic sites were responsible for the catalytic hydrolysis of the initial substrates, while the Au nanoparticles were responsible for the catalytic reduction of intermediate products so that the two sites could perform the whole tandem catalysis. At the same time, the two imprinted components in the reactor provided the corresponding channels to the initial and intermediate substrates, improving the selectivity and ensuring the expected tandem reactions. Like the enzymatic reactions, the imprinted cavities in the reactor provided a separate reaction area for each step of the reaction, thereby avoiding the occurrence of side reactions.

Several different kinds of tests and characterisations were used to study the composition and catalytic properties of MIP-Au-NP-BNPC. FTIR, TEM, SPR and EDS tests were conducted to confirm the structure and composition of the reactor, as well as the existence and distribution of metal nanoparticles. Meanwhile, SEM, BET and TPD tests were used to investigate the molecularly imprinted morphologies, pore size and the interactions between the sample and the substrate. The results clarified that the reactor had lager surface areas, pore volume than the non-imprinted polymer reactor and also proved the reactor had specific recognition to the two substrates BNPC and NP. Electrochemical tests were used to further confirm that there were strong interactions between the imprinted area and the substrates. Then UV catalytic tests proved that MIP-Au-NP-BNPC was able to complete the whole tandem catalysis and it also achieved high efficiency and selectivity toward substrates. Moreover, the specific tandem catalytic mechanism and conditions were explained in detail from the perspective of microscopic quantum theories. As for some existing tandem catalytic reactors, the structural design mainly relies on precise control and artificial separation of different catalytic components. In contrast, this experimental design depends on

the imprinted separation area to complete the separation of different sites, thereby completing the expected tandem processes.

Chapter 3 Core-shell nanoreactor AMPS@AM-Ag and its "non-interference" tandem catalysis

3.1 Introduction

Because of significantly reducing the steps of synthesis and separation, as well as improving the efficiency of reactions, tandem catalysis has attracted intensive attention from researchers worldwide. In the tandem catalysis process, a series of different reactions can be carried out sequentially so that the entire system can complete in one-pot effectively [43, 34]. During the reaction process, two independent catalytic reactions can be effectively combined by finely controlling the dispersion of different active sites in different spatial structures or accurately combining two or more sites. Although a series of progress has been made in this area [142-144], there are still many challenges in practical applications. One of the biggest challenges is that there is always mutual interference occurred during the multistep tandem processes. A simply combination of two different catalytic reactions cannot achieve the expected one-pot process as a lower reaction efficiency is observed, because of temporal misalignments that often appear in the reaction, resulting in the failure of sequential reactions. During such a process, one reaction may not necessarily result in the next reaction process. In fact, mutual interference of different reactions and other side reactions always take place along with the main reactions. Therefore, it is crucial to explore novel catalytic reactors for practical applications.

Nature provides many inspirations for researchers to solve complex problems. Because of their perfect functionality and autonomy, biological systems have given us many directions and references in the progress of new materials, for example, the complex tandem catalytic materials [145, 146]. The cells in a biological system have shown perfect efficiency and coordination when catalysing multiple internal reactions, during which the multistep reactions proceed sequentially, and there is no mutual interference between different reactions. The main reason behind this is that the main enzymatic reactions occur

in compartments separated in time and space [147, 148]. The specific isolation method is to divide different small areas (such as normalised reaction site distribution). Therefore, although different tandem processes occur under different environmental conditions (pH, salt concentration, hydrophilicity and hydrophobicity), they can all be successfully carried out in separate spaces [149]. Meanwhile, due to the limiting factors of intracellular mass transfer, the tandem catalysis will not interfere with each other. As a result, biological systems, including cells, can complete complex tandem catalytic reactions with high efficiency and high yield.

Inspired by the cell reaction mechanism, researchers have proposed many new structures for tandem catalysis, including the partitioning strategy of immobilised enzymes [122], the gradual separation of tandem reactions [36], the one-step synthesis of Pickering emulsion [37, 38], the orthogonal design of tandem catalysis [150] and the double-layer structure of coupled catalysis [151], etc. These methods propose either temporal or spatial separation methods, which provide important research clues for the further research of tandem catalysis. Because the preparation of these reactor usually involves a very complicated synthesis process, it takes a lot of time and the cost is relatively high. Therefore, it is essential to further explore simple solutions for synthesis.

In this chapter, a new core-shell structure tandem nanoreactor was proposed to carry out the reduction and hydrolysis tandem reactions without interference. This tandem reactor separated acidic poly-2-acrylamide-2-methylpropane sulfonic acid (PAMPS) sites and reductive Ag nanoparticle catalytic sites through a core-shell structure. The shell layer containing Ag nanoparticles can be used to catalyse a precursor reaction (typical reactions such as the catalytic reduction of nitro groups [152]), and the core layer containing acidic sites can be used to catalyse the next reaction (typical reactions such as the catalytic hydrolysis of ester groups [153]). As different catalytic sites were separated in different spatial areas of the nanoreactor, reactions can proceed without interference. Previous studies have reported some core-shell nanoreactors in which the core-shell structure is prepared by the direct combination of different sites, so it is hard to

achieve the complete separation of them [119, 120]. In this prepared nanoreactor, different catalytic sites are respectively distributed in the polymer core layer and shell layer to achieve better separation. In addition, due to the restriction of mass transfer and the radial distribution of active sites, the reaction process can be driven by time and space to achieve sequential catalysis (detailed explanation of the mass transfer process discussed in section 3.5). As a result, the nanoreactor permits to achieve a "no interference" tandem catalytic process.

In order to further investigate the specific tandem reaction process, as shown in **Figure 3-1**, bis(2,4-dinitrophenyl) oxalate (DNPO) was selected as an example of the initial template in the experiment. This reactant can be catalytic reduced to the intermediate bis(2,4-diaminophenyl) oxalate (DAPO) (A-B) by Ag nanoparticles in the shell, and then DAPO can be hydrolysed to the final product 2,4-bisaminophenol (DAP) (B-E) by acidic sites in the core [124, 154]. Hence, this nanoreactor realises the complete tandem catalytic process from reduction to hydrolysis. This research aims to study and prove that this new core-shell nanoreactor allows to perform interference-free tandem reactions to provide inspiration for future research in the field of tandem catalysis.

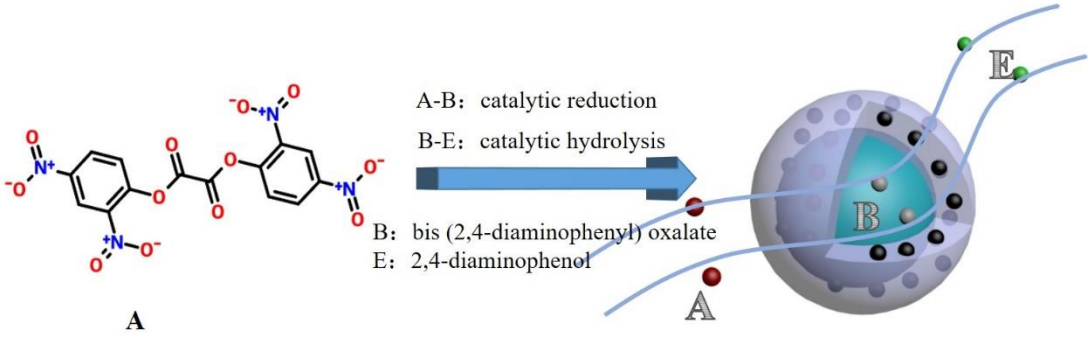

Figure 3-1 Tandem catalytic process of the core-and-shell nanoreactor.

3.2 Experimental section

3.2.1 Experimental materials and equipment

The chemicals and equipment used in the experiment are shown in **Table 3-1** and **Table 3-2** below:

Table 3-1 Experimental materials

Chemicals	Purity	Company
Bis(2,4-dinitrophenyl) oxalate (DNPO)	98%	Sigma-Aldrich Ltd
Ammonium persulfate (APS)	≥98.0%	Sigma-Aldrich Ltd
N, N'-Methylene bisacrylamide (MBA)	99.0%	Sigma-Aldrich Ltd
Span 80		Sigma-Aldrich Ltd
Tween 80		Sigma-Aldrich Ltd
Cyclohexane	≥99.0%	Sigma-Aldrich Ltd
Sodium borohydride ($NaBH_4$)	≥98.0%	Sigma-Aldrich Ltd
2-Acrylamido-2-methylpropane sulfonic acid (AMPS)	99.0%	Sigma-Aldrich Ltd
Acrylamide (AM)	≥99.0%	Sigma-Aldrich Ltd
Silver nitrate ($AgNO_3$)	≥99.0%	Sigma-Aldrich Ltd
N-(hydroxymethyl) acrylamide solution	48.0%	Sigma-Aldrich Ltd
Ethanol	≥99.8%	Sigma-Aldrich Ltd

Table 3-2 Experimental equipment

Equipment	Company	Model
Vacuum oven	Yiheng Instrument, China	DHG-9145A
Electronic balance	Sartorius, Germany	BS-210S
Constant temperature water bath	Sanfa Scientific Instruments, China	HH-S4
Electrochemical workstation	Chenhua instruments, China	CHI760E
UV-visible spectrophotometer	Shimadzu corporation, Japan	UV-2800
Transmission electron microscope	Hitachi, Japan	JEM-2100
Scanning electron microscope	JEOL, Japan	JSM-7800F
Fourier Transform Infrared Spectrometer	Thermo Fisher Scientific Inc., US	Nicolet MX-1E
Zetasizer	Malvern Panalytical, UK	Nano ZS90
X-ray diffractometer	Bruker Corporation, Germany	D8 discover

3.2.2 The preparation of core-shell nanoreactor

The core-shell nanoreactor was synthesised by continuous inverse emulsion polymerisation [155, 156]. Firstly, the PAMPS core layer was prepared, and then the shell layer monomers were added dropwise gradually to form the final core-shell structure nanoreactor.

In detail, as shown in **Figure 3-2**, firstly, 2-acrylamido-2-methylpropanesulfonic acid (AMPS; 2.9 g) was added to a 7 ml water solution. After ultrasonic dispersion, the mixed solution was added to the oil phase system cyclohexane (55 ml). Then the crosslinking agent N, N'-methylene bisacrylamide (MBA; 0.18 g), initiator ammonium persulfate (60 mg), and mixed emulsifier system Span 80 (2.35 g)-Tween 80 (0.45 g) were added to the solution. The mixed solution was transferred to a three-neck flask and put on a magnetic stirrer for stirring. The whole reaction process proceeded on the magnetic stirrer. The solution system was heated to 70 °C and reacted for 1 h to form the core layer. In the next step, the continuous phase shell monomers acrylamide (AM; 2.9 g), silver nitrate (1.63 g), and crosslinker MBA (0.18 g) were dissolved in 5ml aqueous solution and added dropwise to the core layer solution in 30 minutes. Then the whole mixed solution was heated at 70 °C for 3 h to react completely. After the reaction, an excess of reductive agent NaBH4 was used to reduce the Ag nanoparticles in the shell layer (10 times the content of Ag ions; overnight). The obtained product was repeatedly washed with ethanol and water to remove $NaBH_4$ and unreacted monomers to get the final product (named "AMPS@AM-Ag").

In order to conduct a comparative study, another two control samples (AMPS@AM and NMA@AM-Ag) were synthesised under the same conditions in this experiment (**Figure 3-3**). The two controls also had a core-shell structure. Among them, the sample AMPS@AM had the same core layer composed of PAMPS, but the shell layer did not have Ag nanoparticles, so it cannot conduct the reductive catalysis. The sample NMA@AM-Ag had the same shell structure containing metal nanoparticles, but the core layer was made of neutral N-(hydroxymethyl) acrylamide (NMA) without acidic sites, so it cannot complete the hydrolytic catalysis. The two control samples contained only a single catalytic site,

so that both of them can only catalyse once simple reaction. In this way, the tandem catalytic behaviour of AMPS@AM-Ag was discussed by comparing with the two controls.

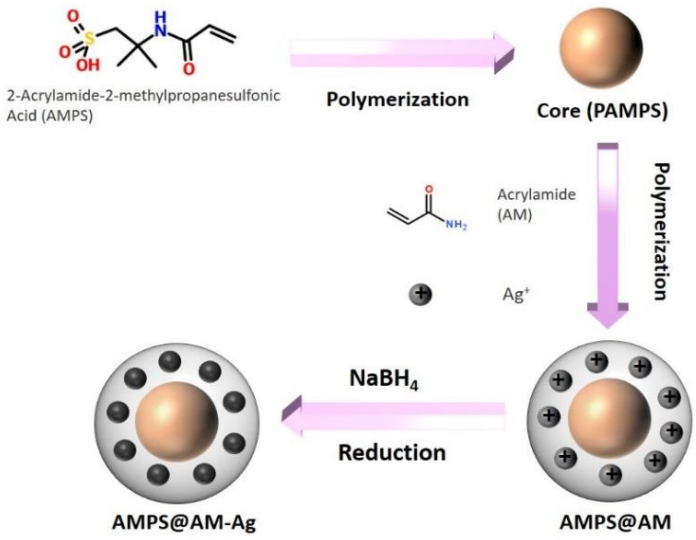

Figure 3-2 Preparation process scheme of core-shell nanoreactor AMPS@AM-Ag.

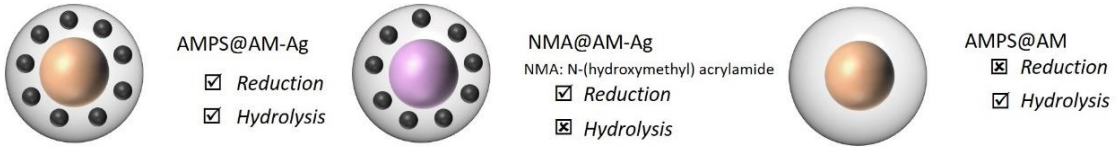

Figure 3-3 Core-shell nanoreactor AMPS@AM-Ag and two controls.

3.3 Tests and characterisation

3.3.1 Transmission electron microscope (TEM) tests

The core-shell nanoreactor emulsion was prepared by inverse emulsion polymerisation, and the final sample was diluted (10-30 times) by cyclohexane. Then the diluted solution was added dropwise (2-3 drops) onto the TEM copper mesh (carbon film) and dried for the tests. TEM tests were used to further

determine the core-shell structure of the polymer reactor, the distribution and size of metal nanoparticles.

3.3.2 Scanning electron microscope (SEM) tests

The final nanoreactor emulsion was diluted with cyclohexane (10-30 times) and then added 2 drops onto the silicon wafer. The silicon wafer was placed on the sample stage for gold spray treatment. Then the core layer and shell layer of polymer reactor and controls were characterised by SEM.

3.3.3 Dynamic light scattering (DLS) tests

The particle size analyser was used to measure the particle size at different stages of the nanoreactor to determine the core-shell structure. The prepared emulsion was diluted 10 times for tests. All samples were kept at a specific temperature for 10 minutes to reach equilibrium before measuring the particle size. Each sample was tested three times to obtain an average size.

3.3.4 Fourier transform infrared spectrometer (FTIR) tests

FTIR was used to characterise the composition of functional groups contained in samples and controls. The prepared emulsion samples (1 drop) were used for the tests. The scanning range was from 4000 to 400 cm^{-1}.

3.3.5 Surface plasmon resonance (SPR) and Energy-dispersive X-ray spectroscopy (EDS) tests

The UV-vis spectrophotometer was used to study the type of metal nanoparticles based on the metal resonance peak. A small amount of sample (10-20 mg) was mixed with barium sulphate ($BaSO_4$) for the tests. The wavelength scan range was between 300-600 nm. The EDS tests were used to compare the element composition and content in different polymer samples.

3.3.6 X-ray diffraction (XRD) tests

XRD spectroscopy was used to further confirm the existence and types of metal nanoparticles. Samples were tested as powder (0.1 g). Measurements were

performed with an acceleration voltage of 40 KV, a scanning range of 5-90° and a scanning speed of 10°/min.

3.3.7 Catalytic tests

The tandem catalytic processes of the polymer reactors were recorded over time [157]. The initial concentration of DNPO was 0.1 μmol/mL (3 mL PBS; pH 7.0). The amount of reducing agent $NaBH_4$ was ten times that of DNPO. The content of the nanoreactor in different tests was 0.9 mg/mL. The catalytic process of the reaction was measured every 5 minutes for 90 minutes in total by the UV-vis spectrophotometer and the results recorded at each time interval were averaged through three measurements. Taking into account the influence of self-reaction (such as self-hydrolysis) in the catalytic process, the self-hydrolysis process of DNPO under the condition of a non-catalytic reactor was measured and deducted from the catalytic reaction to obtain the influence of catalytic reactor.

3.3.8 Electrochemical tests

The electrochemical workstation was used to further study the interaction between the core/core-shell parts of the preparation reactor and the substrate [157-159]. The workstation was a traditional three-electrode configuration (Au plate working electrode, Pt wire counter electrode, and Ag/AgCl reference electrode). The polymer reactor powder (10 mg) pre-soaked with 2 μmol template solution absorbed was put into an electrolytic cell (electrolyte: 10 mL PBS; pH 7.0). The sample was scanned continuously until a stable cyclic voltammetry curve was reached (scan range: 0.4 to -0.6 V; scan rate: 1 mV/s).

3.4 Results and analysis

3.4.1 The analysis of TEM tests

The preparation processes showed that the polymer nanoreactor AMPS@AM-Ag had a double-layer core-shell structure and the shell contained Ag nanoparticles. TEM tests were used to study the size change and the dispersion of metal nanoparticles. **Figure 3-4** shows the core layer structure of the polymer

reactor and two controls. The core layer of the three nanoreactors exhibited similar size and good dispersion. The particle size was around 50 nm. **Figure 3-5** shows the final prepared core-shell nanoreactors with a particle size of about 100 nm. The apparent size increases from core to core-shell proved the successful preparation of the core-shell structures. Meanwhile, from Figure 3-5a and b, we can see that Ag nanoparticles with good dispersion were distributed on the nanospheres, while the control AMPS@AM did not contain Ag nanoparticles. TEM results demonstrated that the core-shell structure of the polymer nanoreactor was as expected.

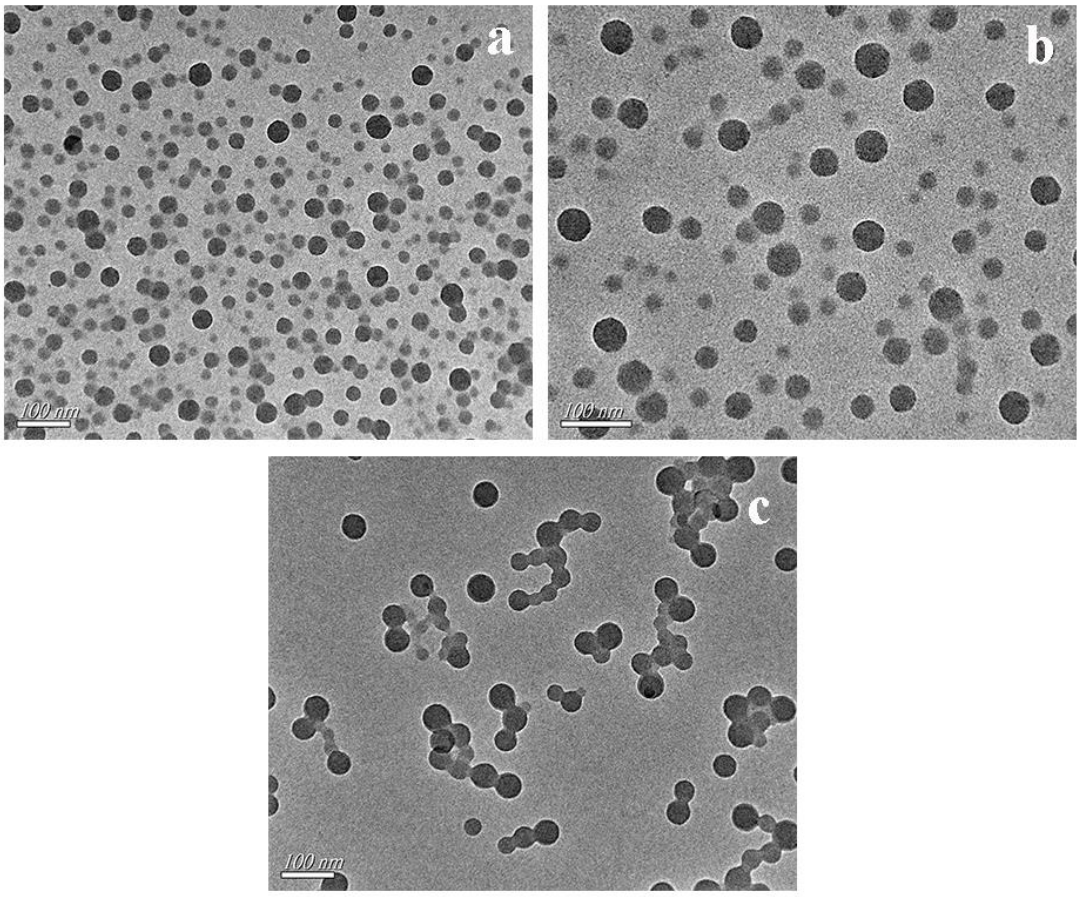

Figure 3-4 TEM images of the core part of the polymer nanoreactors (a AMPS@AM-Ag; b NMA@AM-Ag; c AMPS@AM)

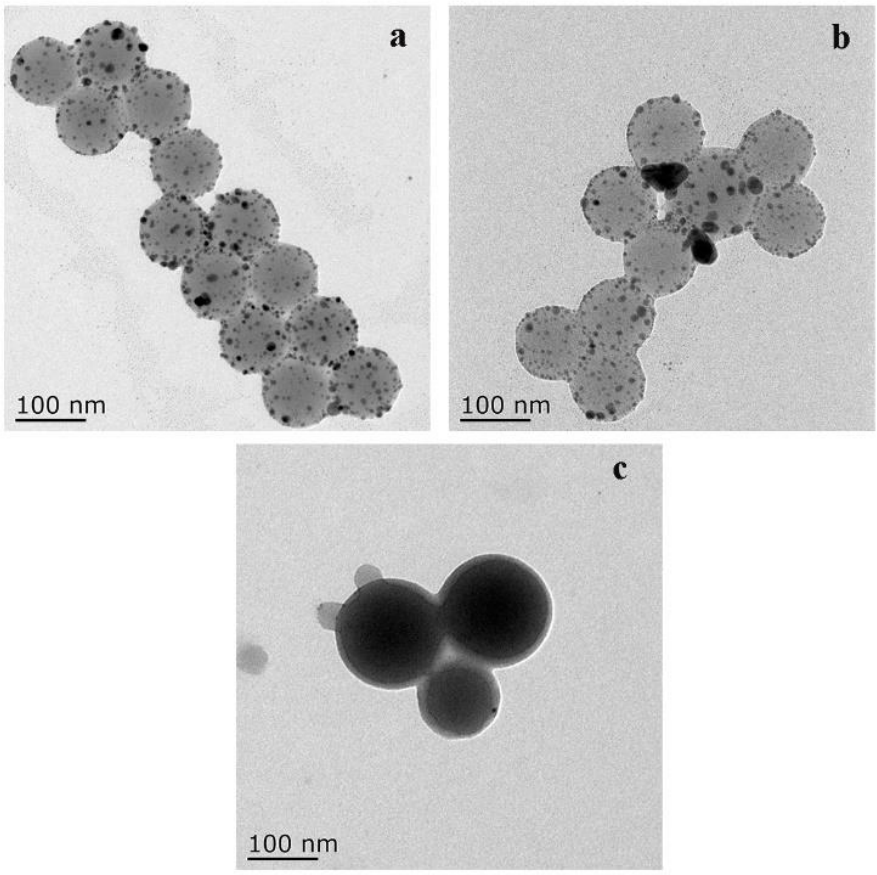

Figure 3-5 TEM images of the core-shell structure of the polymer nanoreactors (a AMPS@AM-Ag; b NMA@AM-Ag; c AMPS@AM)

3.4.2 The analysis of SEM tests

In order to further confirm the particle size of the prepared polymer reactor and the particle size change from core to core-shell structure, the surface morphology of the sample was observed by SEM. It can be seen from **Figure 3-6** that the core layer of the three polymer reactors showed a comparable particle size and uniform distribution, with a size of about 50 nm. **Figure 3-7** shows the core-shell images of three polymer reactors with the size about 100 nm. The SEM test results were consistent with the TEM, confirming the changing structure of the prepared nanoreactor from the core layer to the core-shell layer as expected.

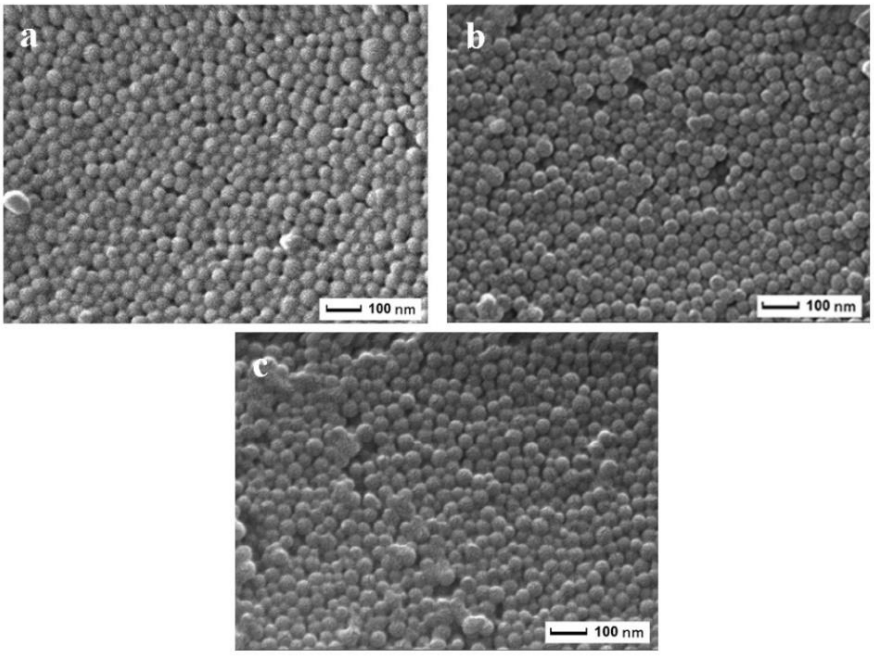

Figure 3-6 SEM images of the core part of the polymer nanoreactors (a AMPS@AM-Ag; b NMA@AM-Ag; c AMPS@AM)

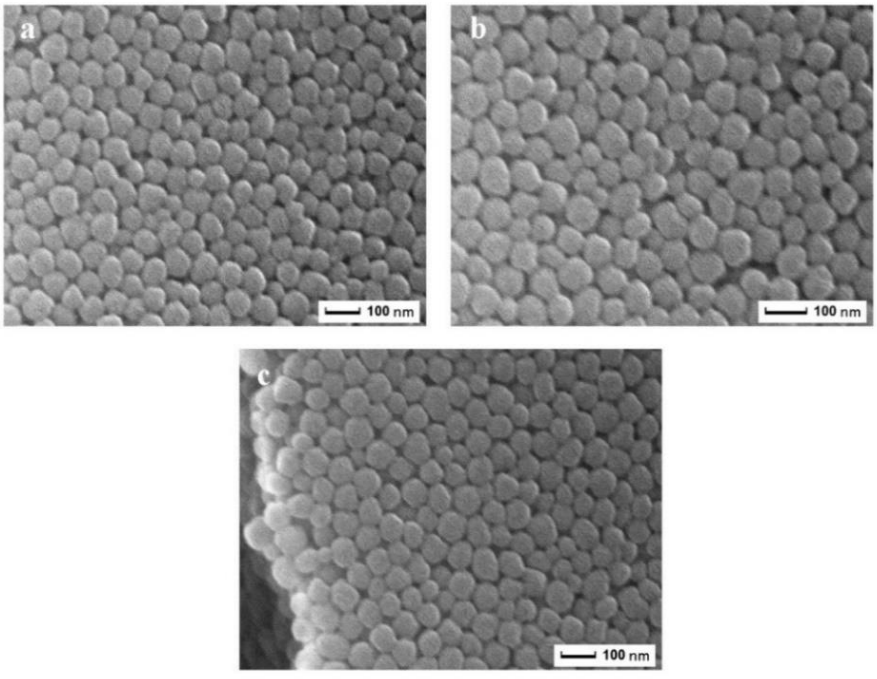

Figure 3-7 SEM images of the core-shell structure of the polymer nanoreactors (a AMPS@AM-Ag; b NMA@AM-Ag; c AMPS@AM)

3.4.3 The analysis of DLS tests

To accurately measure the change of the particle size of the polymer reactor during the polymerization process, the particle size of the nanoreactors at the different stage was measured by a dynamic light scattering analyser. It can be seen from **Figure 3-8** that the particle size-changing trends of the polymer reactor AMPS@AM-Ag were consistent with the other two groups. The particle size increased from about 50 nm in the core layer to about 100 nm in the core-shell layers. Also, the narrow particle size distribution range showed the uniform size of the nanoreactors. Combined with the results of TEM and SEM tests, it can be confirmed that the polymer reactor has experienced a process of increasing particle size from the core layer to the core-shell structure as expected.

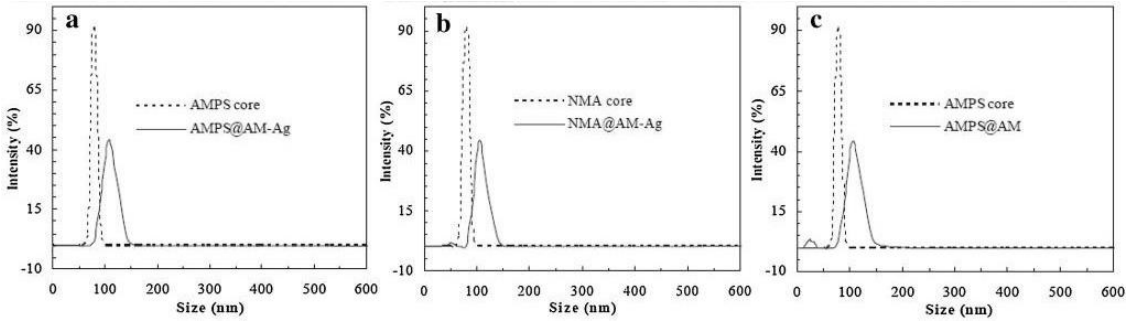

Figure 3-8 Particle distributions of the polymer nanoreactors (a AMPS@AM-Ag; b NMA@AM-Ag; c AMPS@AM)

3.4.4 The analysis of FTIR tests

The functional groups contained in several groups of polymer reactors were analysed through FTIR tests. The prepared reactor AMPS@AM-Ag consisted of a PAMPS core and a PAM-Ag shell. One control AMPS@AM had similar composition but without Ag, and the other control NMA@AM-Ag had the same shell layer but the core layer was composed of NMA. As shown in **Figure 3-9**, AMPS@AM-Ag and the two control groups all showed similar vibration peaks ranges. These peaks were distributed in 2950-3700, 1550-1800, 1300-1500 and 900-1200 cm^{-1}, which correspond to O-H/N-H, C=O, S=O, C-N/C-C bond [135, 160].

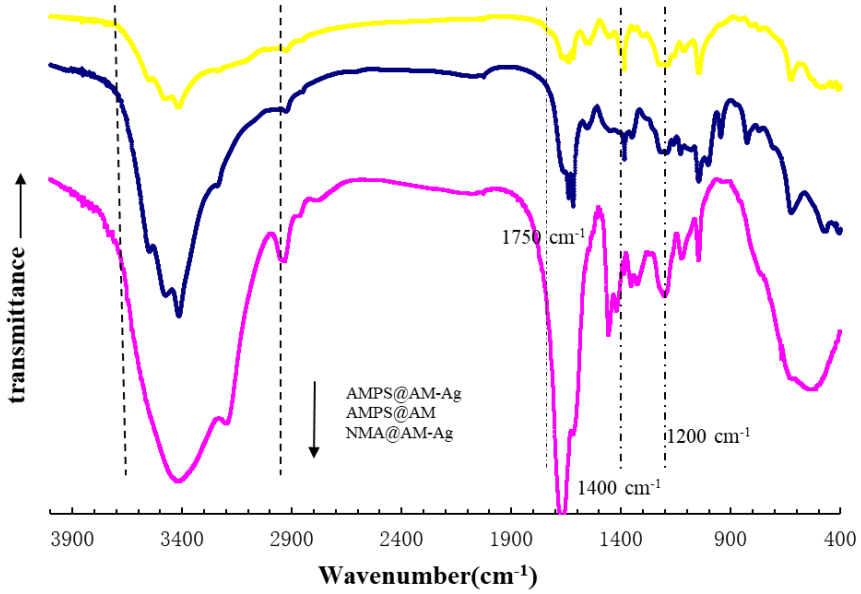

Figure 3-9 FTIR spectra of the polymer nanoreactors.

3.4.5 The analysis of SPR and EDS tests

Different types of metal nanoparticles have specific SPR peak ranges. Hence the SPR tests can be used to determine the type of metal nanoparticles. **Figure 3-10** shows the SPR spectra of the polymer reactor AMPS@AM-Ag and two control samples. The two reactors containing Ag nanoparticles, AMPS@AM-Ag and NMA@AM-Ag, all showed the characteristic peaks of Ag nanoparticles at 400nm [161], while the other group of control groups AMPS@AM did not show corresponding characteristic peaks.

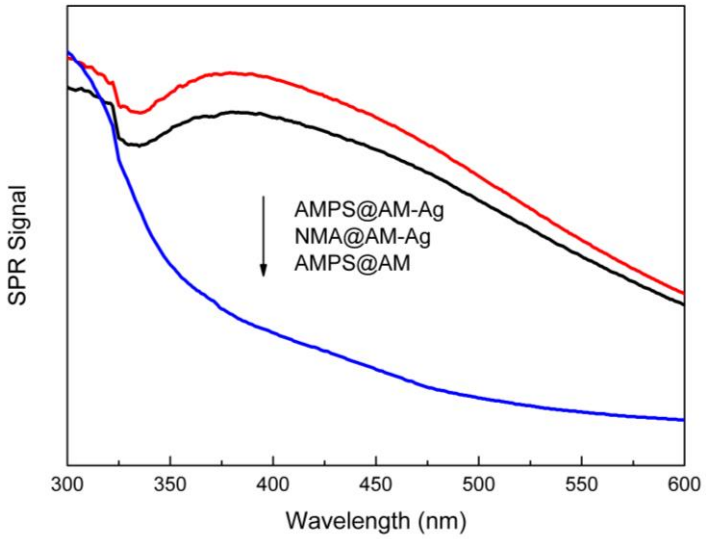

Figure 3-10 SPR spectra of the polymer nanoreactors.

The metal nanoparticles and other elements contained in the polymer reactor were further characterised by the EDS tests. As shown in **Figure 3-11**, reactor AMPS@AM-Ag contained the elements of C, N, O, S and Ag with the loading amount of Ag nanoparticles 10.76 wt%. The control AMPS@AM showed the elements C, N, O and S but without Ag because of the lack of metal nanoparticles sites. The other control NMA@AM-Ag contained the elements of C, N, O and Ag without S element because the PAMPS core was replaced with PNMA, and the loading amount of Ag nanoparticles was 10.77 wt%, which was similar to AMPS@AM-Ag. Moreover, the loading amount of S element in AMPS@AM-Ag and AMPS@AM are also similar (4.39 wt% and 4.39 wt%). The elements in different nanoreactors were consistent with the compositions.

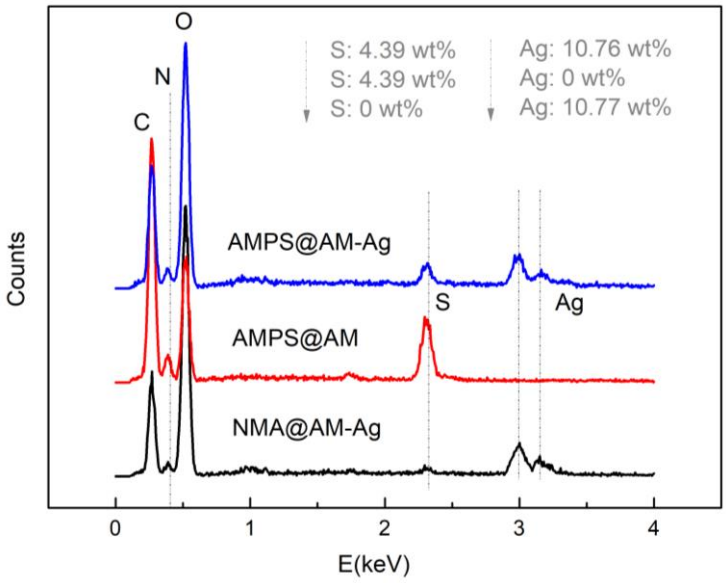

Figure 3-11 EDS spectra of the polymer nanoreactors.

3.4.6 The analysis of X-ray diffraction (XRD) tests

In this experiment, the Ag nanoparticles in the polymer reactor were further analysed by X-ray diffraction (XRD) tests (**Figure 3-12**). The figure showed that the nanoreactors AMPS@AM-Ag and NMA@AM-Ag contained the characteristic peaks of Ag nanoparticles corresponding to the standard XRD patterns. The corresponding 2θ were 38.1, 44.3, 64.4, 77.5, and 81.6 respectively, confirming the existence of Ag nanoparticles. As for the other control AMPS@AM, there was only the peak appearing at 20° in the spectra due to the polymer composition, which also appeared in the other two reactors. The combination of the above EDS and SPR results has confirmed that the prepared nanoreactors contained the corresponding elements as expected.

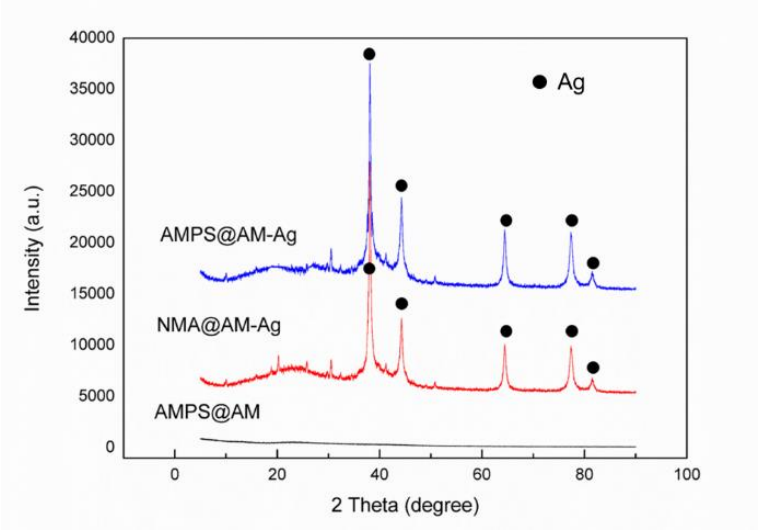

Figure 3-12 XRD spectra of the prepared nanoreactors.

3.4.7 The analysis of UV catalytic tests

In order to study the catalytic performance in the core-shell nanoreactor, the specific reaction processes were further tracked by UV spectrophotometer. As shown in **Figure 3-13**, although the polymer reactor and its control sample contained different active sites (acidic sites or reductive sites), they all showed high catalytic reduction or hydrolysis efficiency for the substrate DNPO.

Figure 3-13a showed the catalytic spectrum of polymer reactor NMA@AM-Ag over time. It can be seen that the decrease of DNPO at 360 nm resulted in an increase of DAPO at 298 nm, indicating the reductive process from DNPO to DAPO. The band change exhibited at 385-440 nm was caused by the dynamic superposition of these two compounds, resulting in accompanying peaks at 393 and 440 nm. The control NMA@AM-Ag can only catalyse the simple reductive reactions as it only contains the Ag nanoparticles sites. As for another control AMPS@AM, which only contained the acidic sites (Figure 3-13b), there was a decrease of DNPO and the increase of the hydrolytic product 2,4-dinitrophenol (DNP) at 263 nm, completing the simple hydrolysis reaction from DNPO to DNP. As for both controls, they can only conduct a simple one-step reaction as they contain a single active site.

As for the reactor AMPS@AM-Ag that contained both acidic and reductive sites, as shown in Figure 3-13c, the decrease of the initial substrate DNPO (360 nm) caused the increase of final product DAP (250 nm) at last. Along with the increase and decrease of the intermediate product DAPO (298 nm), it showed the tandem reactions from reduction (DNPO to DAPO) to hydrolysis (DAPO to DAP). It can be seen from the figure that in this catalytic process, there was no hydrolytic product DNP obtained in the system, which means no mutual interference between reactions in the process of continuous catalytic reactions. Therefore, these results show that the polymer reactor AMPS@AM-Ag can carry out an interference-free tandem reaction process from hydrolysis to reduction. The results were mainly due to the spatial separation brought by the core-shell structure of the catalytic reactor itself, which enabled the tandem reaction process to proceed in sequence (the specific spatiotemporal kinetic theory was explained in detail in section 3.5). Through a series of repeated cycle tests on AMPS@AM-Ag, it was found that its catalytic activity did not significantly decrease after the cycle, proving that the polymer reactor had good catalytic stability for practical applications.

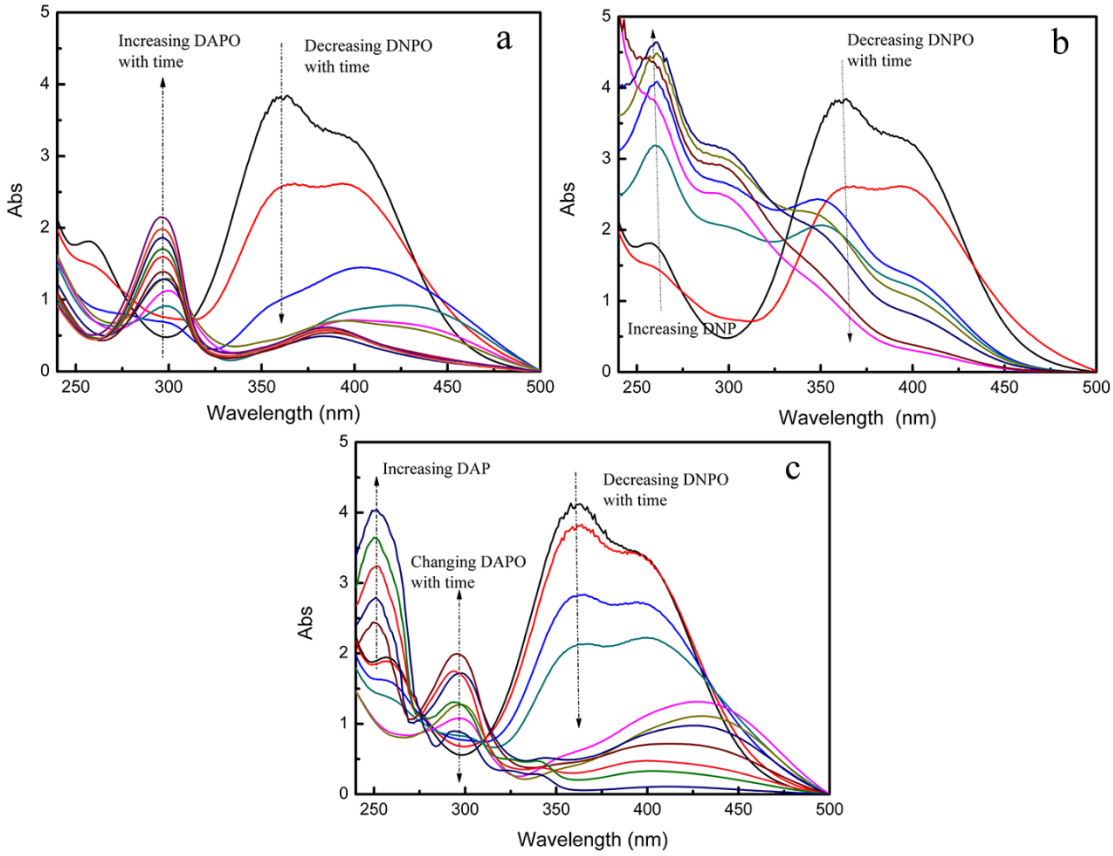

Figure 3-13 The changing UV spectra of DNPO in the polymer nanoreactors (a NMA@AM-Ag; b AMPS@AM; c AMPS@AM-Ag)

3.4.8 The analysis of electrochemistry tests

Considering the mass transfer mechanism of the polymer nanoreactor (discussed in detail in section 3.5), the critical point of the catalytic reaction is mainly the interaction between the nanoreactor and the substrate [42]. Therefore, clarifying the interactions can further explain the mass transfer process and the corresponding catalytic mechanism. Hence, in the experiment, the interactions between the reactors and the substrate were studied through the electrochemical desorption reactions [162]. In the electrochemical desorption reaction, the potential to reduce or oxidise an absorbed molecule depends on the binding force. Relatively strong interaction requires more energy to complete the desorption, causing a greater redox potential. The specific theory was discussed in detail in section 2.4.4. As shown in **Figure 3-14** [158, 159], the substrate molecules in the

electrochemical system usually experience three processes: desorption, diffusion to the electrode surface, and the final oxidation-reduction reaction. The diffusion process can be eliminated by applying ultrasound, so the desorption behaviour of the final absorbed substrate mainly depends on the redox potential.

Figure 3-14 Scheme of the desorbing electrochemical process with an absorbed molecule B.

In order to prevent the interference of the catalytic reactions to the mass transfer process in the nanoreactor, in the electrochemical tests, p-nitrophenol (PNP) was selected as a substitute for the substrate for further study. **Figure 3-15** showed the desorption and reduction potentials of substrate PNP from the core, shell, and core-shell structures of the polymer reactor AMPS@AM-Ag respectively. Comparing these different potential values, the desorption-reduction potential of the core-shell structure showed to be higher than the values of both core and shell, which means the result was not a simple superposition of core and shell potential values with an intermediate potential between them. The conclusion indicated that there was a stronger interaction in the mass transfer process of the core-shell structure than that of a single core layer or shell layer. Combined with the previous catalytic results, it was demonstrated that there was a spatiotemporal separation in this core-shell catalytic reactor AMPS@AM-Ag, inhibiting the unexpected reactions and improving the efficiency of the tandem catalysis.

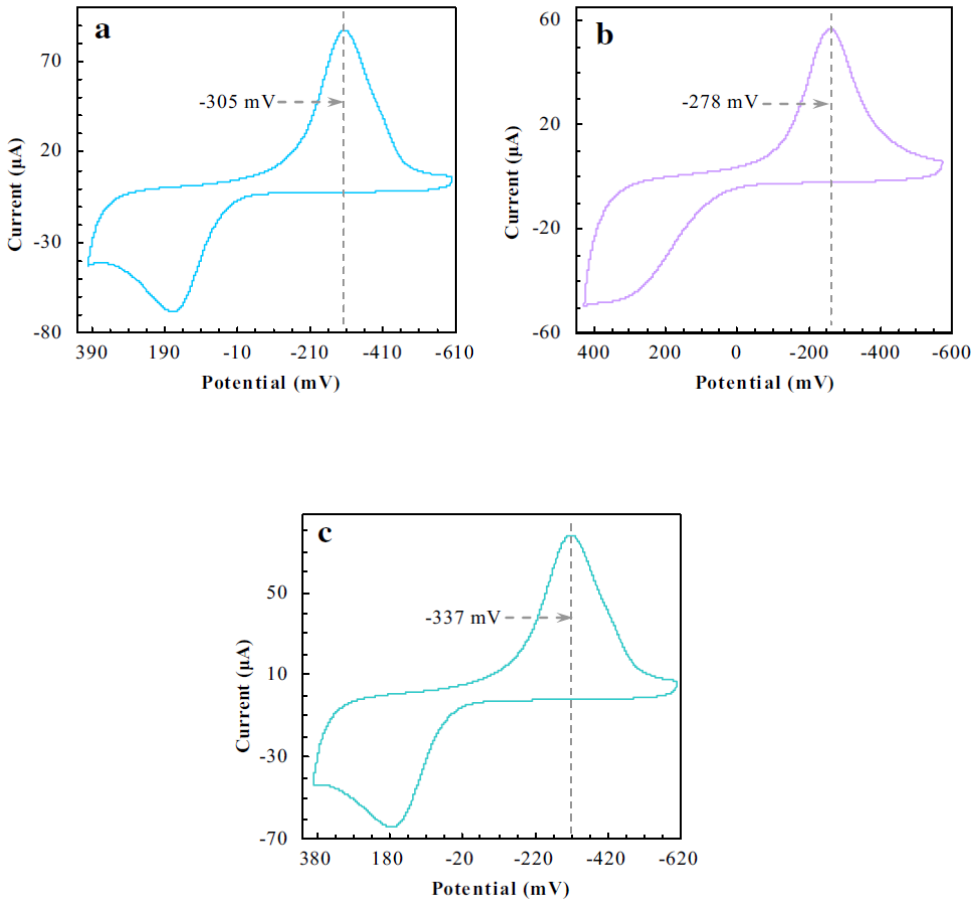

Figure 3-15 Reduction profiles of PNP desorbing from AMPS@AM-Ag (a core; b shell; c core-shell).

To further clarify the interactions, **Table 3-3** showed the potential of PNP desorbing from the prepared nanoreactor and the control groups. It can be seen from the table that the control group AMPS@AM exhibited the potential values similar to that of the polymer reactor AMPS@AM-Ag, which confirmed that the mass transfer process was mainly determined by the polymer structures of the reactor. At the same time, in the three nanoreactors, both the single core or shell structure showed a lower potential than the core-shell structure, proving that the core-shell nanostructure was the basic cause of the spatiotemporal separation effects. In this way, the nanoreactor AMPS@AM-Ag was able to achieve a non-interference tandem catalysis.

Table 3-3 Reduction potentials of PNP desorbing from all the polymer nanoreactors

Nanoreactor	Desorption-reduction potential (mV)		
	Core	Shell	Core-shell
AMPS@AM-Ag	-305	-278	-337
AMPS@AM	-307	-276	-336
NMA@AM-Ag	-283	-278	-287

3.5 The analysis of mass transfer and spatiotemporal kinetics

The conversion efficiency of the catalytic process is shown in **Figure 3-16**. Considering the complexity of dynamic conversion and superposition in the tandem catalysis process, it was difficult to analyse all the participating components quantitatively. In the experiment, DNPO was selected as the initial substrate, and then the conversion efficiency in the catalytic reaction process was studied by analysing the changing absorbance of DNPO with time in the UV tests. The figure indicated that the concentration of DNPO gradually decreased with time, and it showed an effective catalytic conversion rate for the polymer reactor and the control group (Figure 3-16a) as it experienced either catalytic hydrolysis or reduction. Compared with NMA@AM-Ag containing reductive catalytic sites and AMPS@AM containing acidic catalytic, the polymer reactor AMPS@AM-Ag with both catalytic sites exhibited a higher conversion rate. The two catalytic sites in the reactor performed the catalytic reactions together, which was different from the simple combination of two independent reactions. The DNPO conversion in AMPS@AM-Ag was lower than the sum of the conversions of NMA@AM-Ag and AMPS@AM (Figure 3-16b), which was because the spatiotemporal separation properties in AMPS@AM-Ag limited the direction of tandem catalysis.

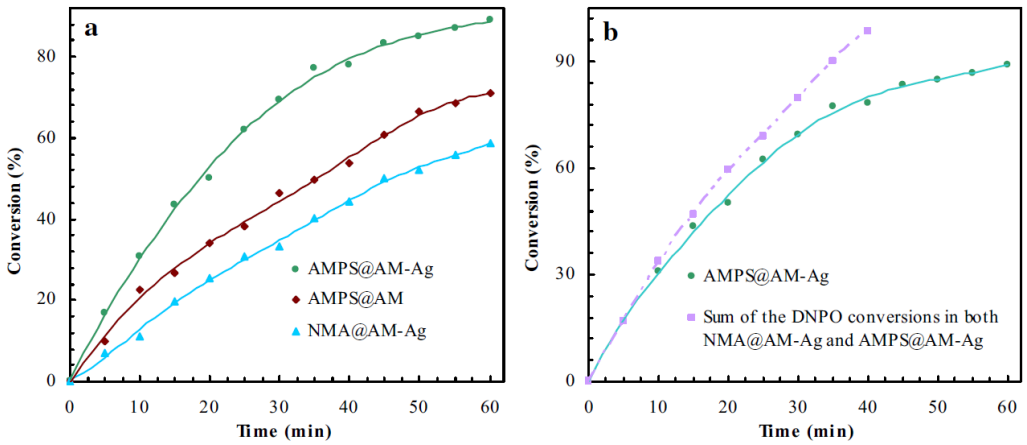

Figure 3-16 Catalytic activity of the polymer nanoreactors of DNPO (a direct comparison; b indirect comparison).

In order to further study the spatiotemporal separation effects, the kinetic theory is introduced to analyse the tandem process. As mentioned above, the nanoreactor was composed of the polymeric core layer containing acid sites and the polymeric shell layer containing Ag nanoparticles. The shell layer can complete the precursor reaction (catalytic reduction), and the core layer was responsible for the subsequent reaction (catalytic hydrolysis). According to the tandem process shown in Figure 3-1, it can be seen that the initial substrate bis(2,4-bisnitrophenyl) oxalate (DNPO) was first reduced to bis(2,4-diaminophenyl) oxalate (DAPO) by the Ag nanoparticles in the shell. Then the intermediate product DAPO was further hydrolysed by the acidic core layer to obtain the final product 2,4-diaminophenol (DAP). Due to the restriction of mass transfer and the radial distribution of reaction sites, the core-shell structure of the nanoreactor successfully separated each step of the catalytic reaction, realising the non-interfering tandem catalytic processes.

Understanding the mass transfer of catalytic materials is the basis to clarify the catalytic mechanism. For linear matrices, there have been many descriptions and theories about microscopic mechanical processes [163-165]. The common basis of these theories lies in Fick's law (Fick's first law and second law):

$$\begin{cases} J = \dfrac{dm}{dt} = -DA\dfrac{dC}{dx}; First\ law \\ \dfrac{\partial C}{\partial t} = D\dfrac{\partial^2 C}{\partial X^2}; \text{Second law} \end{cases} \quad \textbf{(3-1)}$$

In equation 3-1, J is the diffusion flux of the reaction substrate through the specified interface, A is the cross-sectional area of the interface, and D is the diffusion coefficient. C is the substrate concentration, which is related to both time t and position x. In general, Fick's first law mainly solves the relationship between mass transfer (dm/dt) and concentration gradient, while Fick's second law is mainly used to express the relationship between the rate of changing concentration and the diffusion flux related to location in unit volume. As for the spherical model (**Figure 3-17**), the mass transfer process can be evaluated by combining two laws:

$$\begin{aligned} \frac{\partial C}{\partial t} &= \frac{\left[-4\pi r^2 D\left(\frac{dC}{dr}\right)_r + 4\pi(r+dr)^2 D\left(\frac{dC}{dr}\right)_{r+dr}\right]}{4\pi r^2 dr} \\ &= \frac{\left(-4\pi r^2 D\left(\frac{dC}{dr}\right)_r + 4\pi(r+dr)^2 D\left[\left(\frac{dC}{dr}\right)_r + \left(\frac{d^2C}{dr^2}\right)dr\right]\right)}{4\pi r^2 dr} \\ &= \frac{4\pi r^2 D\frac{d^2C}{dr^2}dr + 8\pi r D\frac{dC}{dr}dr}{4\pi r^2 dr} \\ &= D[\frac{\partial^2 C}{\partial r^2} + \frac{2}{r}(\frac{\partial C}{\partial r})] \end{aligned} \quad \textbf{(3-2)}$$

Herein, r is the radius of radiation starting from the centre of the spherical model.

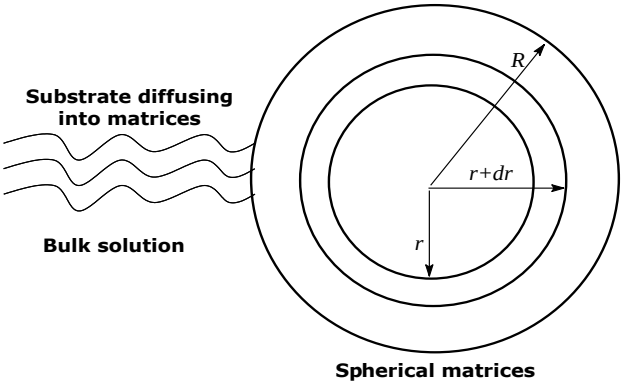

Figure 3-17 Schematic presentation of the mass transfer occurred in a spherical matrix.

The catalytic rate in the reaction mainly depends on the concentration of the substrate at different positions of the reaction, so understanding the mass transfer process in the catalytic reactor plays a decisive role in studying the catalytic mechanism. Therefore, because the catalytic conversion process will reduce the net flux, the mass balance of the substrate needs to be considered when using equation (3-2) in the nanoreactor. In this way, combining the equation (3-2) with the catalytic conversion rate as the radius changes, equation (3-3) is obtained (Figure 3-17):

$$\begin{cases} \dfrac{\partial C(r,t)}{\partial t} = D\left[\dfrac{\partial^2 C(r,t)}{\partial r^2} + \dfrac{2}{r}\left(\dfrac{\partial C(r,t)}{\partial t}\right)\right] - kC(r,t) \\ C(r,0) = u(r-R)\cdot C_0; \quad u(r-R) = \begin{cases} 0, & r-R<0 \\ 1, & r-R\geq 0 \end{cases} \end{cases} \tag{3-3}$$

In the equation, k is the catalytic rate constant, and C_0 is the initial concentration of the substrate in the bulk solution. u(r-R) is the switchable coefficient (0 or 1), which is mainly used to indicate the different concentrations inside or outside the polymer when t = 0. The establishment of this formula is mainly based on the following assumption: the participating catalytic process is regarded as a first-order kinetic process (which often occurs in the catalytic reduction of nitro compounds and the catalytic hydrolysis of ester compounds [166, 167]). After replacing k with an average rate constant, this equation can be used in a continuous catalysis process, in which the participating reactions and first-order kinetic processes are carried out at the same time (such as the tandem reaction

in this experiment). To further solve this problem, equation (3-3) is simplified by replacing C (r, t) with $\varphi(r,t)\cdot\exp(-kt)/r$ to obtain the equation (3-4):

$$\begin{cases} \dfrac{\partial\varphi(r,t)}{\partial t} = D\dfrac{\partial^2\varphi(r,t)}{\partial r^2} \\ \varphi(r,0) = u(r-R)\cdot r\cdot C_0; \quad u(r-R) = \begin{cases} 0, r-R<0 \\ 1, r-R\geq 0 \end{cases} \end{cases} \tag{3-4}$$

Equation (3-4) can be further re-written into equation (3-5) by Fourier transform:

$$\begin{cases} \dfrac{\partial\bar{\varphi}(\omega,t)}{\partial t} = -D\omega^2\bar{\varphi}(\omega,t) \\ \bar{\varphi}(\omega,0) = \displaystyle\int_{-\infty}^{+\infty}\varphi(r,0)e^{-i\omega r}dr = C_0\int_{-\infty}^{+\infty}u(r-R)\cdot\gamma\cdot e^{-i\omega r}dr \end{cases} \tag{3-5}$$

In this equation, ω is the complex variable in the transformation. The following relationship (3-6) is obtained by solving equation (3-5):

$$\bar{\varphi}(\omega,t) = \bar{\varphi}(\omega,0)\exp(-D\omega^2 t) \tag{3-6}$$

The use of the inverse Fourier transformation in (3-6) would get (3-7):

$$\begin{aligned} \varphi(r,t) &= F^{-1}\lfloor\bar{\varphi}(\omega,0)\ exp(-D\omega^2\ t)\rfloor \\ &= 2\pi F^{-1}\lfloor\bar{\varphi}(\omega,0)\rfloor * F^{-1}\lfloor exp(-D\omega^2 t)\rfloor \\ &= \frac{1}{2\pi}\varphi(r,0) * \left[\int_{-\infty}^{+\infty} exp(-D\omega^2 t)\, e^{i\omega r}d\omega\right] \\ &= \frac{1}{2\pi}\varphi(r,0) * \sqrt{\frac{\pi}{Dt}}exp\left(-\frac{r^2}{4Dt}\right) \\ &= \frac{1}{2\sqrt{\pi Dt}}\int_{-\infty}^{+\infty}\varphi\,(\delta,0)exp\,[-\frac{(r-\delta)^2}{4Dt}]d\delta \\ &= \frac{C_0}{2\sqrt{\pi Dt}}\int_{-\infty}^{+\infty}u\,(\delta-R)\cdot\delta\cdot exp\,[-\frac{(r-\delta)^2}{4Dt}]d\delta \end{aligned} \tag{3-7}$$

which accordingly gives:

$$C(r,t) = \frac{C_0\exp(-kt)}{2r\sqrt{\pi Dt}}\int_{-\infty}^{+\infty}u(\delta-R)\cdot\delta\cdot\exp\,[-\frac{(r-\delta)^2}{4Dt}]d\delta \tag{3-8}$$

Applying the nanoreactor boundary condition r=R to equation (3-8), the changing concentration of the substrate in the bulk solution (C_b(t)) is obtained:

$$C_b(t) = C(R,t)$$

$$= \frac{C_0 \exp(-kt)}{2R\sqrt{\pi Dt}} \int_{-\infty}^{+\infty} u(r-R) \cdot r \cdot \exp\left[-\frac{(R-r)^2}{4Dt}\right] dr$$

$$= \frac{C_0 \exp(-kt)}{2R\sqrt{\pi Dt}} \int_{-\infty}^{+\infty} \underbrace{u(r-R)}_{=0, r-R<0} \cdot (r-R)$$

$$\cdot \exp\left[-\frac{(R-r)^2}{4Dt}\right] d(r-R)$$

$$+ \frac{C_0 \exp(-kt)}{2R\sqrt{\pi Dt}} \int_{-\infty}^{+\infty} u(r-R) \cdot R \cdot \exp\left[-\frac{(R-r)^2}{4Dt}\right] d(r$$

$$- R) = \frac{C_0 \exp(-kt)}{2R\sqrt{\pi Dt}} \int_{r-R=0}^{+\infty} \underbrace{(r-R)}_{X}$$

$$\cdot \exp\left[-\frac{(r-R)^2}{4Dt}\right] d(r-R)$$

$$+ \frac{C_0 \exp(-kt)}{2\sqrt{\pi Dt}} \int_{r-R=0}^{+\infty} \exp\left[-\frac{(r-R)^2}{4Dt}\right] d(r-R) \qquad \textbf{(3-9)}$$

$$= \frac{C_0 \exp(-kt)}{2R\sqrt{\pi Dt}} \int_{-\infty}^{+\infty} X \cdot \exp\left(-\frac{X^2}{4Dt}\right) dX$$

$$+ \frac{C_0 \exp(-kt)}{2\sqrt{\pi Dt}} \int_{0}^{+\infty} \exp\left(-\frac{X^2}{4Dt}\right) dX$$

$$= -\sqrt{\frac{Dt}{\pi}} \frac{C_0 \exp(-kt)}{R} \int_{0}^{+\infty} \exp\left(-\frac{X^2}{4Dt}\right) d\left(-\frac{X^2}{4Dt}\right)$$

$$+ \frac{C_0 \exp(-kt)}{\sqrt{\pi}} \int_{0}^{+\infty} \exp\left(-\frac{X^2}{4Dt}\right) d\left(\frac{X}{2\sqrt{Dt}}\right)$$

$$= \sqrt{\frac{Dt}{\pi}} \frac{C_0 \exp(-kt)}{R} + \frac{C_0 \exp(-kt)}{2}$$

$$= C_0 \exp(-kt)\left(\sqrt{\frac{Dt}{\pi R^2}} + \frac{1}{2}\right)$$

It can be seen from the above equation that the change of the substrate concentration in the bulk solution is related to both the time t and the radius R. In addition, the actual spatiotemporal effects in the nanoreactor can be ignored

when $\sqrt{Dt/\pi R^2} \ll 1/2$. At this time, the actual kinetic process will be a quasi-first-order kinetic process (generally common simple process):

$$C_b(t) = \frac{C_0}{2} \cdot \exp(-kt) \quad \textbf{(3-10a)}$$

When $\sqrt{Dt/\pi R^2} \gg 1/2$, the spatiotemporal effects become the main effect. At this time, the practical kinetic process would show the spatiotemporal track in a form of Equation (3-10b):

$$C_b = C_0\sqrt{D/\pi R^2} \cdot t^{\frac{1}{2}} \exp(-kt) \quad \textbf{(3-11b)}$$

The linearisation of Equation (10a) and Equation (10b) would allow one to evaluate the catalytic mechanisms in these nanoreactors, by plotting ln(1-x) vs. t or a t-function (where x is the conversion of the initial substrate, $(C_0\text{-}C_b(t)/C_0)$:

$$\ln(1-x) = -kt - ln2 \quad \textbf{(3-12a)}$$

$$\ln(1-x) = \underbrace{-kt + lnt^{1/2}}_{t-function} + ln\sqrt{\frac{D}{\pi R^2}} \quad \textbf{(3-13b)}$$

In order to use equation (3-11b), the approximate k-value can be obtained in advance by connecting two temporal equations, and then through the above equations, the spatiotemporal effects and catalytic conversion rate in the nanoreactor can be analysed.

As shown in **Figure 3-18**, the nanoreactor did not show an actual correlation for linear equations without spatiotemporal effects. In contrast, for the equations with spatiotemporal properties, the nanoreactor exhibited a highly linear correlation. Combined with the study of the catalysis process, it can be seen that this conclusion confirmed that there were spatiotemporal effects in the AMPS@AM-Ag nanoreactor, so it can catalyse the uninterrupted tandem reaction process.

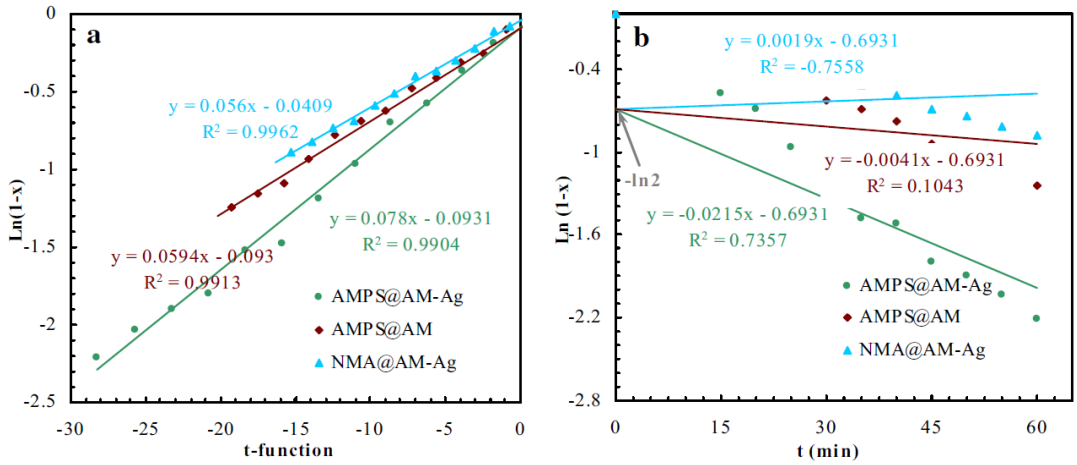

Figure 3-18 Spatiotemporal kinetic track from the prepared nanoreactors (a with substantial effect; b without spatiotemporal engagement).

3.6 Conclusion

In this experiment, a new type of tandem catalytic nanoreactor was prepared, which effectively ensured that tandem reactions were carried out in sequence and every step was independent of each other without interference. Inspired by the spatial independent and non-interfering catalysis within natural cells, this nanoreactor mainly used the core and shell two layers to separate different catalytic sites. The core layer contained acid sites, which were responsible for catalysing hydrolysis, while the shell layer contained metal reduction sites, which were responsible for the catalytic reduction. The two active sites together achieved the whole tandem catalytic processes.

Several different tests were used to clarify the composition and catalytic performance of the nanoreactor AMPS@AM-Ag. Firstly, SEM, TEM, and DLS tests proved the core-shell double-layer structure of the polymer, and then the FTIR, SPR, EDS, XRD tests were used to confirm the composition and the elements of the polymer reactor. Finally, the UV spectrum was used to track the entire catalytic process and compare the control samples, showing that only the polymer reactor AMPS@AM-Ag can complete the non-interference tandem reaction. At the same time, the interactions between the substrates and the core,

shell and core-shell structure of the polymer reactor were studied via electrochemical tests, proving the spatiotemporal separation effects. In this way, this core-shell nanoreactor AMPS@AM-Ag was able to achieve the desired tandem reactions in high efficiency and without interference. In addition, this spatiotemporal separation effect was further demonstrated by building a kinetic theory model, which proved that the novel nanoreactor can complete each step of the tandem reaction independently. This new type of nanoreactor provides inspirations for the development of new functional materials and also inspires the practical application of tandem catalysts in the future.

Chapter 4 Three-layer smart polymer reactor MIP-AgPRS and the tandem/non-tandem catalysis

4.1 Introduction

Tandem catalysis is of great importance for research and application in modern chemical industry [168-170]. Tandem catalytic reactors are able to catalyse complex reactions in sequence, enabling multi-step reactions to proceed in one pot, which simplifies the reaction steps and greatly improves synthesis efficiency. Therefore, several research groups worldwide have shown interests in it and have contributed to developing novel tandem catalysts [117, 171]. Among them, polymer reactors containing acidic and basic catalytic sites are the earliest endeavours to complete multi-step tandem catalysis [172, 173]. In this type of reactor, acidic and basic catalytic sites respectively catalyse different reactions, thus completing the complete tandem catalytic process together. However, it is likely to produce side reactions or even incompatible reactions during the process, limiting the application of tandem catalysis. [37, 174] Therefore, it is vital to ensure precise site control and reasonable site separation for the improvement of future catalytic reactors with multiple sites.

Humans have gained large amounts of inspiration and knowledge from nature to solve complex challenges. One of the challenges is developing enzyme-like molecularly imprinted polymers (MIPs) to enable catalysis with molecular recognition. As one of the hotspots of functional polymers, MIPs have many advantages, such as easy preparation and specific recognition [175, 176]. The molecular recognition function mainly comes from the unique preparation process of the polymers. Firstly, the functional monomer and template molecules are assembled through covalent or non-covalent bonds like hydrogen bonds. Then the functional monomer is synthesised in the presence of an initiator, a cross-linking agent under light or heat conditions, and the template is further removed after the polymerisation. After washing the templates, the cavities in the polymer could selectively rebind the target molecules, achieving recognition behaviours

[166, 177]. As a result, the MIP catalyst could be used as the carriers of multiple catalytic sites to permit tandem catalysis as well as avoid unnecessary side reactions. However, since there are various reactions and special requirements in practical applications, it is also necessary to control the process of tandem reactions in order to achieve a controllable catalytic reaction process.

Marine creatures such as mussels have strong adhesion abilities which can adhere to almost all solid surfaces, including stones, metals and even polytetrafluoroethylene (PTFE) surfaces [178, 179]. Moreover, the adhesive ability of mussel can adapt to a variety of external environmental conditions, such as different temperatures, different fluctuating humidity and salinity, the marine currents and environment [180]. So far, the molecular mechanism of mussel adhesion has not been completely clarified, but studies have shown that it is mainly derived from 3,4-dihydroxyphenylalanine (DOPA) and lysine amino acid fragments [181, 182]. Mussels can bond with its adhesion surface and reach cross-linking interactions because of the catechol component in DOPA. This cross-linking mainly derives from various interactions such as metal chelation, hydrogen bonding, and free radical coupling [183, 184]. Based on these strong interactions, the adhesive silk foot protein of mussels also showed significant self-healing ability. After cutting off the dopamine polymers, the injury site will heal spontaneously due to the self-assembly behaviours of dopamine and amino components [94]. The self-assembly ability of mussels in the aqueous environment provides inspiration for self-controlled catalysis. Also, it proposes a solution for the preparation of functional polymers applied in the aqueous environment.

In summary, inspired by the delicate structure of biological systems in nature, this experiment prepared a "sandwich" tandem reactor, in which the middle layer is the switch of the tandem reaction. The middle switch was prepared by introducing dopamine components, which can open and close in different temperatures to control the entire tandem process. In addition, to avoid some unnecessary reactions in tandem reactions, the top and the bottom layers of the catalyst were synthesised as MIPs, which can specifically recognise the substrates. As shown

in **Figure 4-1**, the first and third layers of the reactor were the MIP layers prepared by imprinting the initial substrate and the intermediate product respectively. The first layer was made of acidic monomers PAMPS that contained acidic sites for catalysing hydrolysis, and the third layer was a functional polymer PAM containing Ag nanoparticles to catalyse reduction process. In this way, the active sites in two layers were able to complete the tandem catalysis from hydrolysis to reduction. In this experiment, 4-nitrophenyl acetate (NPA) and 4-nitrophenol (NP) were chosen as examples for the initial template and intermediate product of the tandem reaction respectively because these two compounds are an excellent coupling pair for tandem reactions and could be catalysed under mild reaction conditions (such as room temperature) [124].

The second switchable layer in the middle consisted of polydopamine acrylamide (PDPA) and polyacrylamide (PAM), controlling the channel of intermediate products. It performed the "open" and "close" processes by the self-healing and dissociation of the hydrogen bonds between PDPA and PAM. The self-healing mechanism of hydrogen bonds has been explained in detail in many manuscripts reported in the literature [185, 186]. Essentially, the self-healing effect of hydrogen bonds originates from their conversion effects. At lower temperatures, the interaction between the hydrogen bonds causes the channel to close. When the temperature rises, the dissociation of the hydrogen bond causes the channel to open, allowing the polymer to act as a switch for the tandem reaction. As shown in Figure 4-1, when the temperature was low, the channel in the middle layer were closed, preventing the intermediate product for reaching the sites for the next step reaction, so there was only the simple hydrolysis catalysis. As the temperature rose, the channels of the intermediate layer opened, allowing the intermediate product to further contact the metal nanoparticles, completing the tandem reaction from hydrolysis to reduction. In addition, according to the repeated catalytic tests, there were still stable and tight connections between different layers because of the good adherence ability of the dopamine layer in the middle. This chapter aims to prepare a polymer catalytic reactor to achieve the "smart" tandem catalytic reaction process, so as to provide a solution to the modulation of the current tandem catalytic areas.

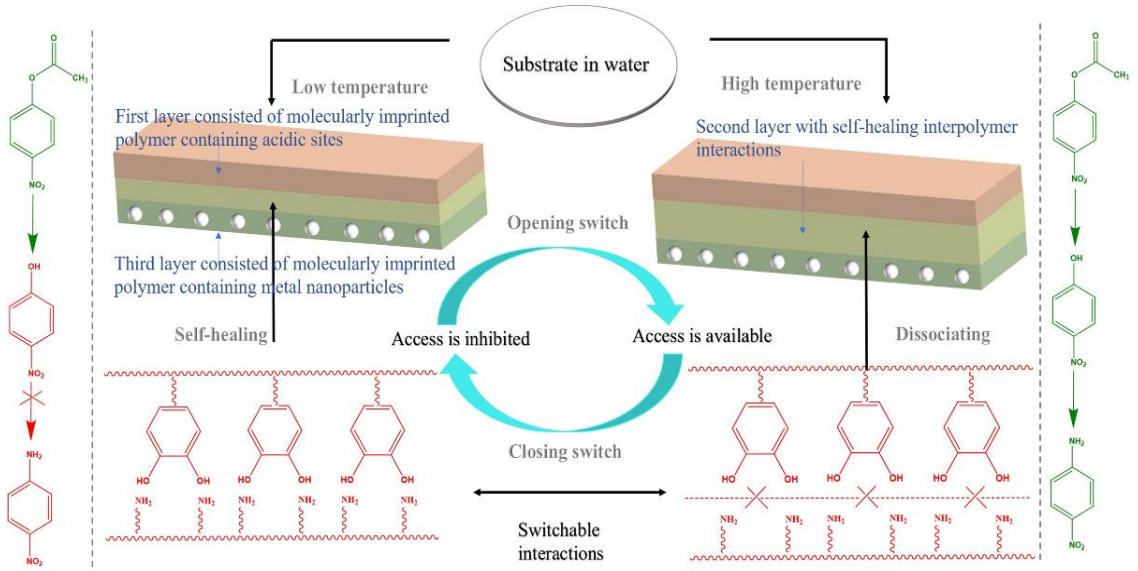

Figure 4-1 The mechanism of the "smart" tandem catalyst.

4.2 Experimental section

4.2.1 Experimental materials and equipment

The chemicals and equipment used in the experiment are shown in **Table 4-1** and **Table 4-2** below:

Table 4-1 Experimental materials

Chemicals	Purity	Company
4-Nitrophenyl acetate (NPA)	≥98%	Sigma-Aldrich Ltd
2,2'-Azobis(2-methylpropionitrile) (AIBN)	98.0%	Sigma-Aldrich Ltd
N, N'-Methylene bisacrylamide (MBA)	99.0%	Sigma-Aldrich Ltd
Divinylbenzene	80.0%	Sigma-Aldrich Ltd
Dimethyl sulfoxide (DMSO)	≥99.9%	Sigma-Aldrich Ltd
Sodium borohydride ($NaBH_4$)	≥98.0%	Sigma-Aldrich Ltd
2-Acrylamido-2-methylpropane sulfonic acid (AMPS)	99.0%	Sigma-Aldrich Ltd
Acrylamide (AM)	≥99.0%	Sigma-Aldrich Ltd
Silver nitrate ($AgNO_3$)	≥99.0%	Sigma-Aldrich Ltd
N- [2-(3, 4-dihydroxy phenyl) ethyl]-2-methylacrylamide	≥99.0%	Sigma-Aldrich Ltd
4-Nitrophenol (NP)	≥99.0%	Sigma-Aldrich Ltd

Table 4-2 Experimental equipment

Equipment	Company	Model
Vacuum oven	Yiheng Instrument, China	DZF-6020
Electronic balance	Sartorius, Germany	BS-210S
Electrochemical workstation	Chenhua instruments, China	CHI760E
UV-visible spectrophotometer	Shimadzu corporation, Japan	UV-2800
Transmission electron microscope	Hitachi, Japan	JEM-2100
Scanning electron microscope	JEOL, Japan	JSM-7800F
Fourier Transform Infrared Spectrometer	Thermo Fisher Scientific Inc., US	Nicolet MX-1E
Zetasizer	Malvern Panalytical, UK	Nano ZS90
X-ray diffractometer	Bruker Corporation, Germany	D8 discover
BET surface area and porosity analyser	Micromeritics, China	ASAP 2460
Temperature-programmed desorption device	Fantai, China	FINESORB-3010

4.2.2 The preparation of tandem catalytic reactor

As mentioned above, the catalytic reactor was composed of three polymer layers: the top and bottom MIP layers for tandem reaction (containing acidic sites and Ag metal nanoparticles) and the middle switch control layer (PDPA-PAM layer). In order to connect the three layers successfully, one layer was prepared firstly, and then part of this layer was immersed in the reaction solution of the next layer, so that a polymer interpenetrating network could be formed between the two layers. Similarly, in the next step, one side of the synthesised two-layer polymer was immersed in the solution of the next layer so that the interpenetrating network could be formed between the third layer and the other two layers [187].

Firstly, 2-acrylamide-2-methylpropane sulfonic acid (AMPS) (2.33 g), azobisisobutyronitrile (AIBN) (0.09 g), N, N'-methylenebisacrylamide (MBA) (0.35 g) and the initial substrate 4-nitrophenyl acetate (NPA) (0.407 g) were dissolved in dimethyl sulfoxide (DMSO) (10 ml) in a glass beaker. After ultrasonic dispersion and nitrogen deoxygenation, the mixed solution was transferred into a glass petri dish and then placed in a vacuum oven at 70° C for 3 hours to synthesise completely. As a result, the first MIP precursor was prepared.

In the second step, acrylamide (AM) (1.59 g), 3-methacrylamide dopamine (DPA) (0.5 g), the crosslinker divinylbenzene (0.11 g), and the initiator AIBN (0.11 g) were fully dissolved in dimethylformamide (10 mL) by ultrasonic dispersion. Then the solution of the second layer was transferred into the petri dish with the first polymer layer to form the interpenetrating network and incubated for 3 hours. Then, after nitrogen deoxygenation, the whole system (the first layer and the second layer solution) was put into the vacuum oven at 70°C for 5 hours to polymerise, obtaining the first two layers of the reactor.

The third step was to prepare the third MIP layer. Firstly, the intermediate product template NP (2.25 mmol) was added to the $AgNO_3$ solution ($AgNO_3$: 2.25 mmol; DMSO: 3 ml) to form the $[Ag(NP)_2]^+$ complex. Then the reaction monomer acrylamide (AM) (1.6 g), template complex $[Ag(NP)_2]^+$ solution, MBA (0.34 g) and AIBN (0.18 g) were dissolved in DMSO (7 ml). The mixed solution was dissolved completely by ultrasonic dispersion. Then the solution of the third layer

was transferred to the petri dish with the prepared first two layers to connect with them completely and incubated for 3 hours. After nitrogen deoxygenation, the whole system was put into the vacuum oven at 70°C for 2 hours to polymerise completely. Finally, an excess of sodium borohydride ($NaBH_4$) solution ($NaBH_4$: ten times the Ag ion content; solution: 200 ml deionised water) was used overnight to reduce the Ag ions in the polymer reactor. After the reduction, the residual $NaBH_4$ was washed away with excess deionised water. Then the template in the polymer reactor was washed with 500 ml ethanol containing 10% acetic acid to remove the imprinted components completely. FTIR tests were used to detect if the templates were removed completely. Thus, the polymer reactor with three-layer structure was synthesised (named "MIP-AgPRS"; "MIP" is molecularly imprinted polymer, "Ag" stands for Ag nanoparticles, and "S" stands for switchable characteristics) (**Figure 4-2**).

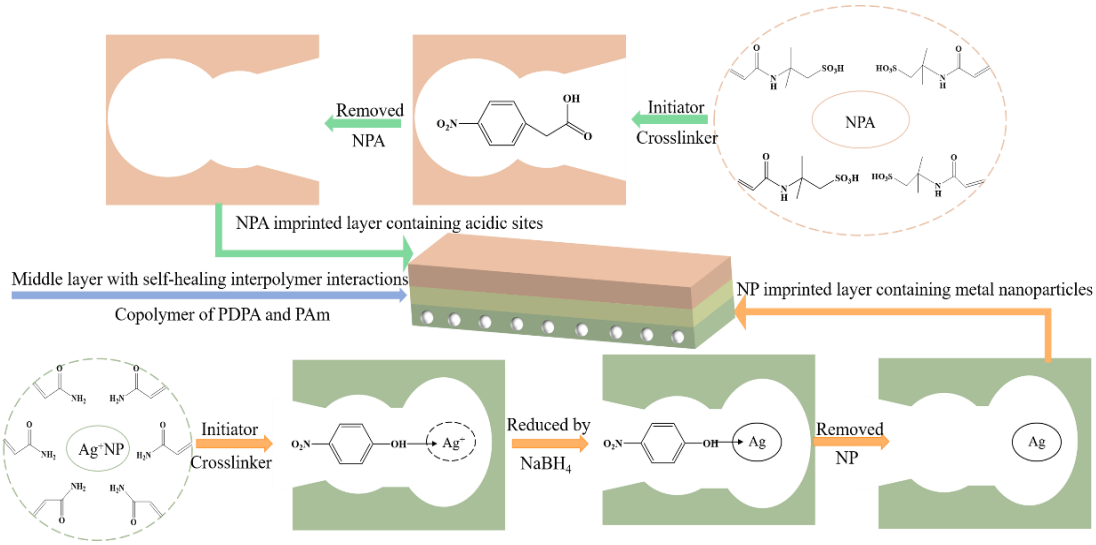

Figure 4-2 The preparation process of the three-layer polymer reactor.

In order to further investigate the switchable performance of the middle layer in the polymer reactor MIP-AgPRS, two controls were prepared under comparable conditions (MIP-AgPRO and MIP-AgPRC), as shown in **Figure 4-3**. The control MIP-AgPRO contained the same MIP top and bottom layers containing acidic sites and metal nanoparticles separately, but the middle switch layer was replaced by the polymer PAM, so it was always open ("O"). The other control MIP-AgPRC also contained the same MIP layers, but the middle layer was

replaced by the polymer PDPA and always remained "closed" ("C"). Therefore, one control (MIP-AgPRO) can complete the tandem reaction regardless of high and low temperature, and the other control (MIP-AgPRC) can only perform a single-step reaction regardless of high or low temperature. The prepared sample MIP-AgPRS can control the process of the tandem reaction at different temperatures. Thus, the polymer reactor and the controls were prepared.

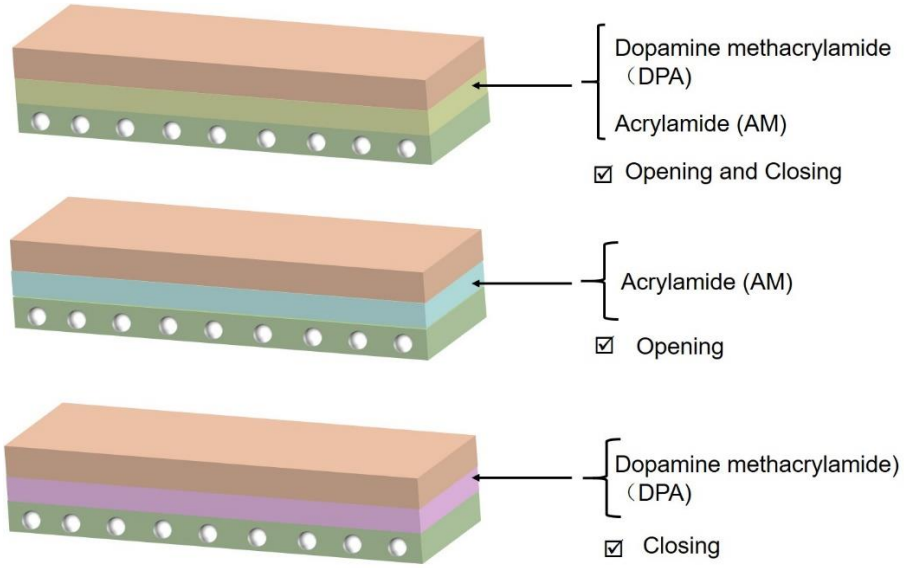

Figure 4-3 Different components of three reactors and controls.

4.3 Tests and characterisation

4.3.1 Fourier transform infrared spectrometer (FTIR) test

Fourier transform infrared spectroscopy (FTIR) was used to study the functional groups of the polymer reactor and the template removing processes of the MIP layers in the polymer reactor. A thin slice was taken from the three-layer polymer reactor (single layer and three layers together) and grounded to the size of ca. 60-mesh for tests. The powder samples of polymer reactors were mixed with potassium bromide (1:50-1:100), grounded and tableted for the tests.

4.3.2 Morphology, structure and elemental composition characterisation of polymer reactor

Several different tests were performed to characterise the morphology and elements of the polymer reactor. First of all, the macroscopic morphological

images of the three polymer layers were taken by a digital camera, and the morphology of the polymer reactor and its control group was compared and observed. A transmission electron microscope (TEM) was used to prove the presence and the dispersion of metal nanoparticles contained in the bottom layer of the polymer reactors. For the measurements, the powder samples from the bottom layer of the polymer reactor and controls were dispersed in ethanol (mass ratio: 1:300). A few drops of dispersion were added dropwise to the TEM copper mesh (carbon film) and dried for the tests.

The morphology of the MIP layer and the non-imprinted layer of the polymer reactor were characterised and compared by scanning electron microscope (SEM). The surface plasmon resonance (SPR) was used to evidence the characteristic absorption peaks of metal nanoparticles to examine their type. In addition, X-ray diffraction (XRD) spectroscopy was used to further confirm the existence and types of metal nanoparticles. At the same time, an energy dispersive spectroscopy (EDS) was used to determine the different elements in different samples to further study the compositions of the reactors. In these tests, samples were tested as powders.

4.3.3 BET surface area and porosity analyser tests

The specific surface area and porosity analyser (BET) test was conducted to study the specific surface area and pore size distribution of the MIP layers and the non-imprinted layer as comparison to further confirm the presence of molecularly imprinted components. The powder samples (0.1 g) from different layers were thoroughly dried, weighed, and placed in a long-necked flask for testing.

4.3.4 Temperature programmed desorption (TPD) tests

To analyse the molecular recognition properties, the temperature programmed desorption (TPD) test was used to characterise the interactions between the corresponding substrates and the molecularly imprinted components in the top and bottom layers. It is known that the polymer with corresponding imprinted component will show a higher desorption temperature when the substrate is

desorbed from the polymer. The powder samples (20 mg) were put into a U-shaped tube and 20 μl of the corresponding substrate (concentration: 0.5 μmol/mL acetonitrile solution) was added for complete adsorption. Then the sample was heated at the rate of 10 °C/min in a nitrogen gas until the substrate was desorbed from the samples. The final desorbing spectra were recorded and analysed by the data processing system.

4.3.5 Dynamic light scattering (DLS) tests

The temperature-responsive self-healing abilities of the polymer reactor were recorded and studied by dynamic light scattering (DLS) tests. The powder samples from the middle switchable layers of the polymer reactor MIP-AgPRS and two controls were firstly added in deionised water (mass ratio: 0.1%). After ultrasonic dispersion, the solution was left at a specific temperature for fifteen minutes to achieve equilibrium before measuring. During DLS tests, the samples were measured for the change of its the particle size (Rd) with different temperatures (from 20 °C to 65 °C).

4.3.6 Catalytic tests

The tandem catalytic processes were recorded by the batch test of different polymer reactors over time [134]. The initial concentration of the testing substrate NPA was 0.5 μmol/mL in acetonitrile solution, and the catalysts content in different samples for the tests was 0.1 mg/ml. The catalysis processes were recorded with an UV spectrophotometer, and each result was obtained by averaging three tests. The samples for the tests were respectively put in 25 °C and 50 °C (keeping in a hot bath) to maintain the temperatures in the testing processes. Then the solutions were transferred on the spectrophotometer for tests every 10 minutes up to a total time of 100 minutes.

In addition, due to the self-hydrolysis of the initial substrate NPA taking place during in the tests, the conversion rate without the catalyst was measured at the same time of each test and then deducted to obtain the conversion contributed only by catalysts. The second step of the reduction process in the tandem

reaction proceeded after the hydrolysis test with the reducing agent sodium borohydride (four times the molar amount of NPA).

4.3.7 Electrochemical tests

The self-healing catalytic mechanism between the polymer reactors and the catalytic substrates was characterised by electrochemical tests. The test was carried out through an electrochemical workstation equipped with a three-electrode device (Au plate working electrode, Pt wire counter electrode, and Ag/AgCl reference electrode). During the test, after having absorbed 2 μmol of the substrate solution (0.5 μmol/ml acetonitrile solution), the middle layer of the polymer reactor (10 mg), was placed in an electrolytic cell (electrolyte: 10 mL PBS; pH 7.0). The electrochemical tests were performed while samples were being dispersed with an ultrasonic instrument. The scanning range of the catalytic reactor was 0 V to -1 V, and the scanning rate was 1 mV/s.

4.4 Results and analysis

4.4.1 The analysis of FTIR tests

From the preparation processes explained in section 4.2.3, it can be seen that the middle switchable layer was a copolymer made of PDPA and PAM, while the top and the bottom MIP layers were composed of PAMPS and PAM containing Ag nanoparticles, respectively. First of all, FTIR was used to investigate the composition of the polymer reactor and the two control reactors. As shown in **Figure 4-4a**, four main absorption bands (2900-3700, 1600-1800, 1000-1200 and 1000-1400 cm^{-1}) can be seen in the spectra, corresponding to O-H/N-H, C=O, S=O and C-N/C-C stretching vibration peaks respectively [188, 189]. The appearance of these functional groups was mainly due to the common composition of the three polymer layers together and on the different polymer reactors. As shown in Figure 4-4a, the three polymer reactors all exhibited similar functional groups. To further explore the components of the polymer reactor, the spectra of the top (MIP-NPA), middle (NIP) and bottom (MIP-NP-Ag) layers in the polymer reactor MIP-AgPRS are presented in **Figure 4-4b**. It can be seen that

the top layer containing PAMPS exhibited extra S=O bonds (~1237 and 1050 cm^{-1}) compared with the other two layers, which was consistent with the structure of the reactor.

Moreover, in order to analyse the template-removing processes of the MIP layers on the top and bottom of the reactor, FTIR was used to compare the spectrum of the precursor (polymer reactor without washing the templates), the final MIP layer, and the two templates (NPA and NP) (**Figure 4-4c** and **Figure 4-4d**). As shown in Figure 4-4c, the precursor of the top layer MIP-NPA respectively contained the characteristic peaks of the final product MIP-NPA and the substrate NPA. However, as for MIP-NPA that has undergone the washing step to remove the template, there was no obvious characteristic peak of NPA displayed in the spectrum. Similarly, as for the bottom layer MIP-NP in Figure 4-4d, its precursor contained the corresponding characteristic peaks of both MIP-NP and template molecule NP, while MIP-NP did not contain the corresponding NP characteristic peak. Combined with the synthesis route in Figure 4-2, the existence of the MIPs can be confirmed. More analysis and characterisation about MIP are further discussed in 4.4.3 and 4.4.4.

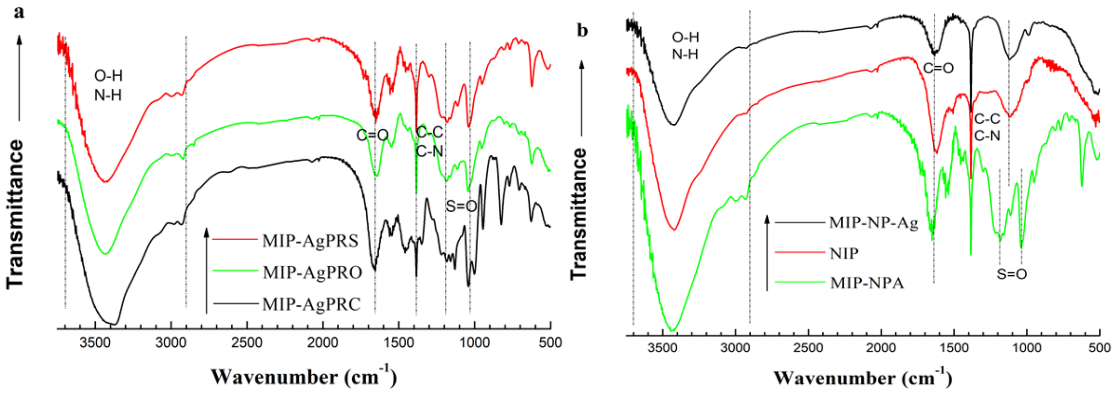

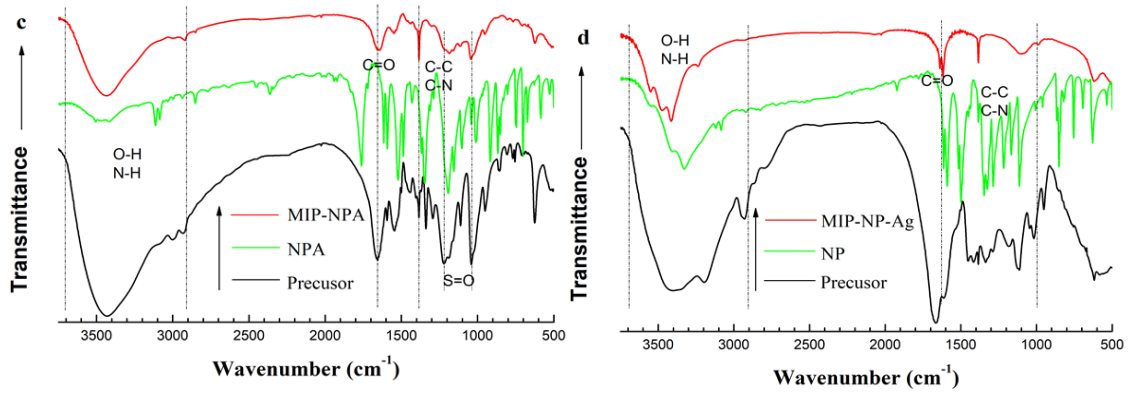

Figure 4-4 FTIR spectra of polymer reactors and imprinting processes (a: three different catalysts; b: three different layers of prepared reactor MIP-AgPRS; c: NPA imprinted layer; d: NP imprinted layer).

4.4.2 The analysis of morphology, structure and elements

Firstly, a digital camera was used to characterise the macroscopic morphology of the three-layer structure of the polymer reactor. **Figure 4-5** shows the macroscopic images of the polymer reactor MIP-AgPRS and the two control groups. It can be seen that all three groups of polymer reactors showed the corresponding three-layer structure. Unlike the top PAMPS layer, the bottom layers of the three samples were black polymer layers due to the presence of the metal nanoparticles. In addition, the reactor MIP-AgPRO exhibited a white polymer layer rather than the black layer like the other two samples because it did not contain PDPA.

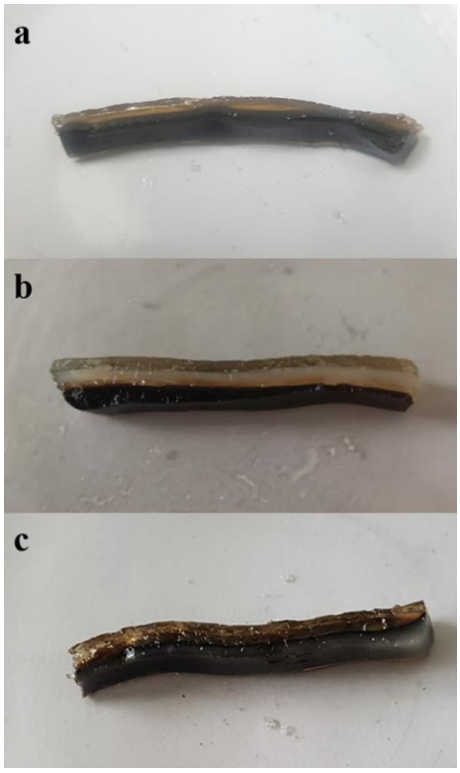

Figure 4-5 Digital images of the polymer reactor and two controls (a: MIP-AgPRS; b: MIP-AgPRO; c: MIP-AgPRC).

To further investigate differences in morphologies of the three-layer structure of the polymer reactor, especially to distinguish the different morphologies between the MIP layer and the middle non-imprinted layer, SEM tests were used to study the specific morphologies of the three layers in different samples. As shown in **Figure 4-6**, the two different imprinted layers in the top and bottom both exhibited a rougher surface morphology than the non-imprinted layer in the middle. This morphology was mainly caused by the washing step for templates removal during preparation. In addition, the distribution of metal nanoparticles can also be seen in the bottom MIP layers in Figures 4-6g, h, and i.

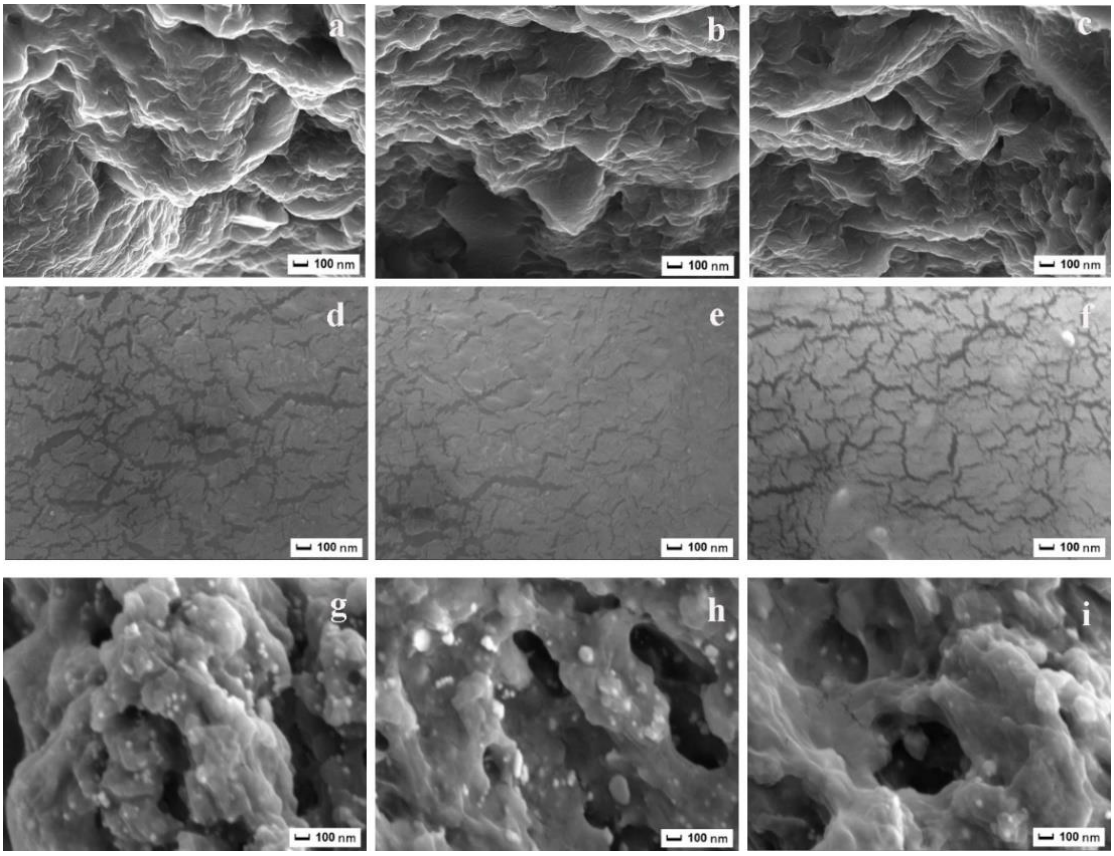

Figure 4-6 SEM images of the polymer reactor and two controls. (MIP-NPA layer: a MIP-AgPRS; b MIP-AgPRC; c MIP-AgPRO; NIP layer: d MIP-AgPRS; e MIP-AgPRC; f MIP-AgPRO; MIP-NP layer: g MIP-AgPRS; h MIP-AgPRC; i MIP-AgPRO).

To further explore the existence of metal nanoparticles in the polymer reactor, TEM images of the bottom MIP layers containing metal nanoparticles in different samples were taken. **Figure 4-7a, b and c** show the metal-containing imprinted layers in MIP-AgPRS and the two controls. It can be seen that the corresponding metal nanoparticles were well dispersed in the three samples and had a particle size of about 7-10 nm. Meanwhile, the middle layer of the polymer was presented as a comparison in **Figure 4-7d**. There was no obvious distribution of metal nanoparticles in this layer. The basic morphological structure of MIP-AgPRS was as expected.

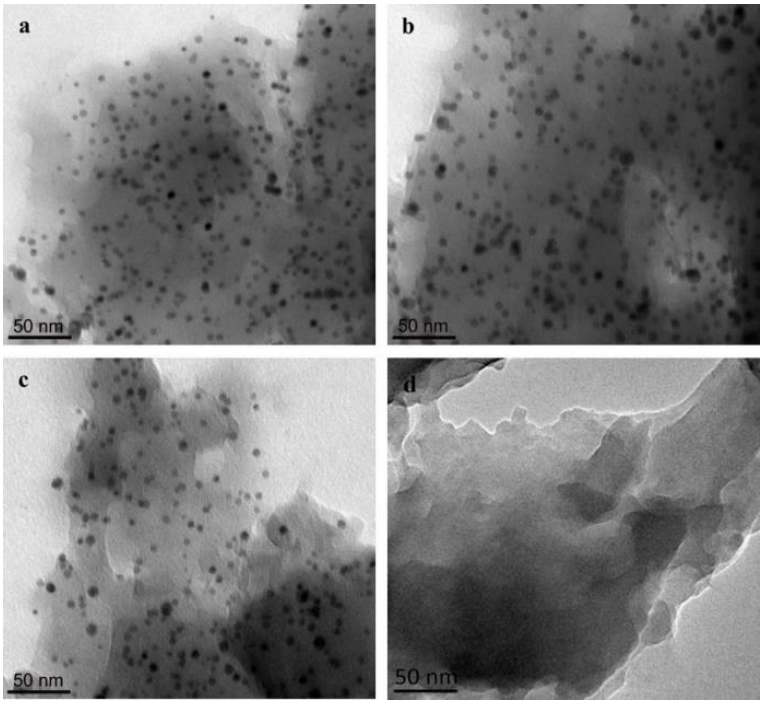

Figure 4-7 TEM images of metal nanoparticles in the polymer reactor and two controls. (a: MIP-AgPRS; b: MIP-AgPRO; c: MIP-AgPRC; d: middle layer in MIP-AgPRS).

To confirm the type of metal nanoparticles, further characterisations were conducted through surface plasmon resonance (SPR) and X-ray diffraction (XRD). SPR spectra are shown in **Figure 4-8**. The three samples in the figure all showed the characteristic peaks of Ag nanoparticles at around 410nm [190], while the other control group without Ag nanoparticles (MIP-PRS) did not show the corresponding characteristic peak. At the same time, the XRD pattern in **Figure 4-9** shows that the three polymer reactors contained the corresponding typical peaks of Ag nanoparticles, which exhibited the characteristics values at 2θ of 38.1, 44.3, 64.4, 77.5, and 81.6. The positions of several peaks were consistent with the XRD standard patterns of Ag, confirming the presence of Ag nanoparticles.

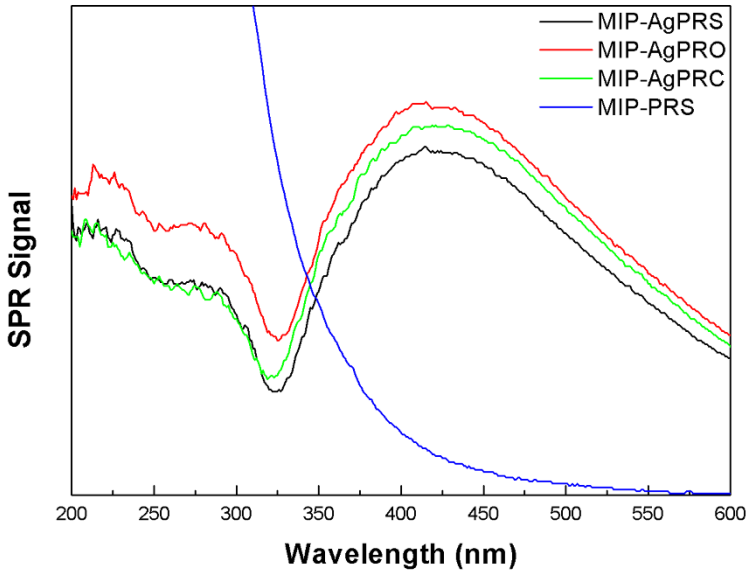

Figure 4-8 SPR spectra of polymer reactor and controls.

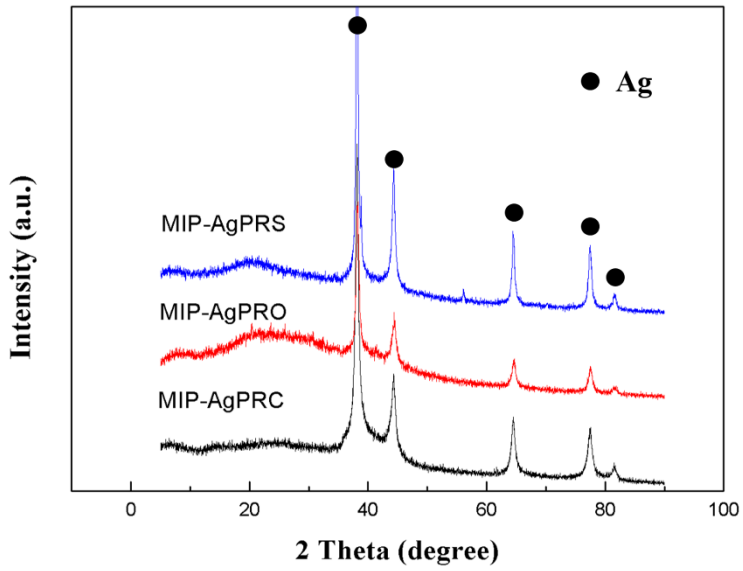

Figure 4-9 XRD patterns of the polymer reactor and controls.

In addition, the elemental compositions of the polymer reactor and the control groups were characterised by EDS tests. As shown in **Figure 4-10a**, the polymer reactor MIP-AgPRS and the other two control groups all showed the same basic element distribution of C, N, O, S, and Ag, which was consistent with the composition. The element S came from the polymer PAMPS, and the element Ag came from the Ag nanoparticles in the bottom layers. In addition, in order to confirm the different compositions in different layers in the polymer reactor,

Figure 4-10b shows the compositions of the elements of the three layers in MIP-AgPRS, respectively. It can be indicated that the intermediate layer of PDPA-PAM (NIP) contained only the three basic elements: C, N and O. In addition, the top MIP-NPA layer showed extra S element apart from C, N and O because of PAMPS, while the bottom layer MIP-NP showed extra Ag element. From the above tests, it can be proved that the three-layer structure MIP-AgPRS was prepared as expected.

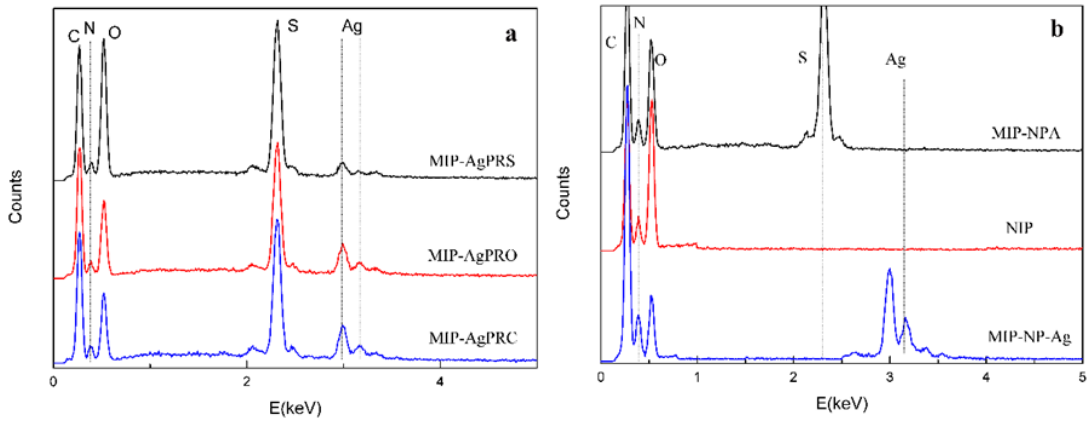

Figure 4-10 EDS spectra of the polymer reactors. (a: spectra of three polymer reactors; b: spectra of three layers of MIP-AgPRS).

4.4.3 The analysis of BET specific surface area and pore size

Figure 4-11 showed the BET adsorption isotherms of three different polymer layers in the polymer reactor MIP-AgPRS. It can be indicated that the two imprinted layers MIP-NPA and MIP-NP-Ag both exhibited certain pore size distributions (<10 nm) [191], but the non-imprinted layer in the middle did not show obvious pore size. The pore diameter of MIP-NPA was around 4nm and the pore diameter size of MIP-NP-Ag was around 5 nm. The difference in the pore size was related to the type of the templates and washing processes.

At the same time, the specific surface areas of the three layers of the samples are presented in **Table 4-3**. As for MIP-AgPRS, it can be seen that compared with the middle layer (11.4 m^2/g), the other two imprinted layers showed a much larger specific surface area (top: 109.5 m^2/g; bottom: 73.9 m^2/g). The surface

areas of other two controls showed similar results. The higher surface areas of the MIPs resulted from the repeated template washing processes in the synthesis procedures.

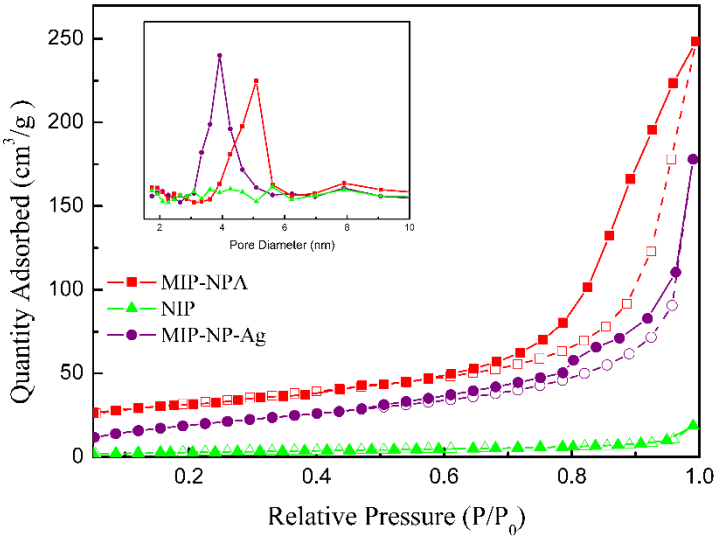

Figure 4-11 BET sorption isotherms of the polymer reactors MIP-AgPRS (closed symbols: nitrogen adsorption; open symbols: nitrogen desorption).

Table 4-3 BET analysis of the different layers of polymer reactors.

	Surface area ($m^2 g^{-1}$) of different samples		
Different layer	MIP-AgPRC	MIP-AgPRO	MIP-AgPRS
MIP-NPA	98.7	112.3	109.5
NIP	24.5	29.5	11.4
MIP-NP-Ag	68.2	74.4	73.9

4.4.4 The analysis of temperature programmed desorption (TPD) tests

The TPD test was used to further explore the interactions between the imprinting substrates and the corresponding MIP layers [36]: the stronger the interaction between the substrate and the polymer the higher the desorption temperature. **Figure 4-12a** shows the desorption curves of NPA desorbing from the three samples MIP-AgPRS, MIP-AgPRO and MIP-AgPRC. Moreover, the desorption curve of the analogue bis 4-nitrophenyl carbonate (BNPC) desorbing from MIP-AgPRS was also given as a template reference for comparison. It can be seen that the desorption temperatures of the different samples were 321, 326, 326 and 256 °C, respectively. The polymer reactor showed a higher desorption temperature for the corresponding imprinted substrate than the reference template analogue. Similar results were also observed for another imprinting substrate NP. **Figure 4-12b** shows the desorption curves of NP from MIP-AgPRS, MIP-AgPRO and MIP-AgPRC, with the desorption temperature of 272, 274 and 273 °C, respectively. The figure also shows the curve for the analogue 2-nitrophenol (2 -NP), which desorbed from the reactor MIP-AgPRS at 197 °C.

Figure 4-12 demonstrates that the three polymer reactors showed similar desorption temperatures for the template NPA, and comparable results were obtained for the other template NP. However, the two analogues, BNPC and 2-NP used as a reference, both showed lower temperatures than the corresponding templates. The interactions between the imprinted components and the substrates derived from the induced molecular memory (the imprinting process of the template molecule) [192], leading to a stronger interaction between the corresponding substrate and the polymer. Combined with the results of BET test presented in section 4.4.3, these results have further confirmed that the polymer reactor contained MIP components. The MIP components enabled the molecular recognition abilities of the polymer reactor, which would help it to complete the tandem catalysis with higher efficient for specific substrates.

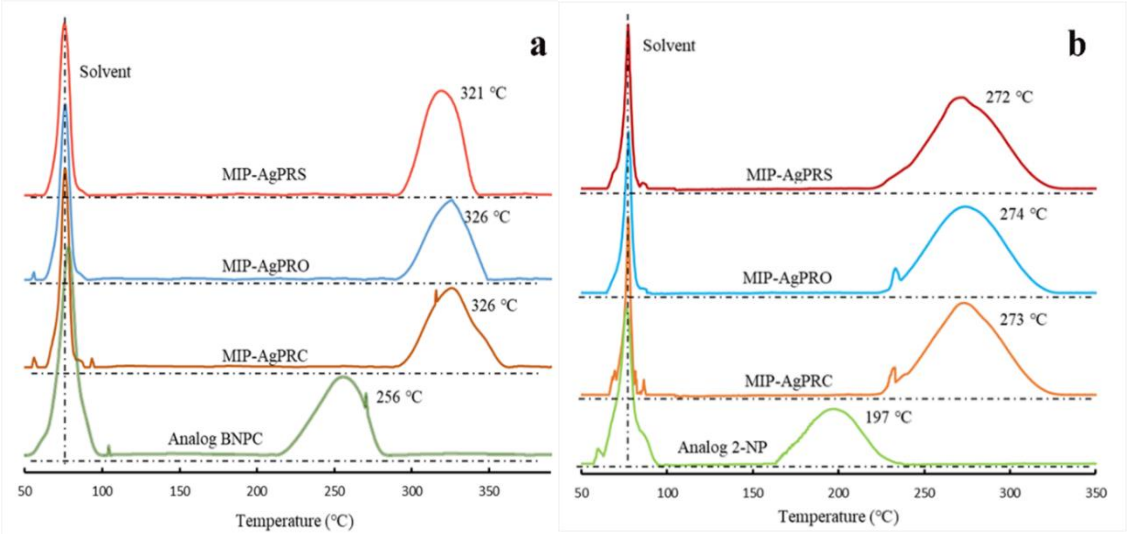

Figure 4-12 TPD desorbing profiles of NP, NPA and reference substrate (a: NPA and BNPC; b: NP and 2-NP).

4.4.5 The analysis of DLS tests

As shown in **Figure 4-13a** and **4-13b**, the temperature-responsive process (self-healing interaction) of copolymer PDPA-PAM was studied *via* the change of particle size of the polymer with the different temperature. The change of the hydrodynamic diameter Rd of the switchable polymer reactor MIP-AgPRS indicated a clear dependence on temperature changes. Nonetheless, as for the other two controls MIP-AgPRC and MIP-AgPRO, as the expansion change of the polymer network structure itself was very weak, no obvious correlation between Rd and changing temperatures was observed from the figure.

As for MIP-AgPRS, there was a dramatic increase of Rd in the temperature range from 35-50 °C as exemplified in Figure 4-13a. To figure out the transition point of the change, the differential form of the change was calculated, and it is shown in Figure 4-13b. It can be seen that the most significant change of Rd happened at 38 °C. When the temperature was lower than 38 °C, MIP-AgPRS exhibited smaller hydrodynamic diameters. This was due to the solid complementary interactions between PDPA and PAM, which formed the "closure" tandem reaction channel and obstructed the entry of the intermediate products (e.g.NP in

the experiment). At this time, the reactor only had the channel for the first simple reaction of hydrolysis. When the temperature rose above 38 °C, the interactions between PDPA and PAM was dissociated so that the catalytic channel was "opened", resulting in the bigger dynamic diameters. At this time, the intermediate products were able to pass through the channel, enabling the processes of tandem catalysis. The results indicated that there were self-healing interactions in the middle layer of the polymer reactor capable of “opening” and “closing” the channel of intermediate products, which were the reason for the switchable catalysis.

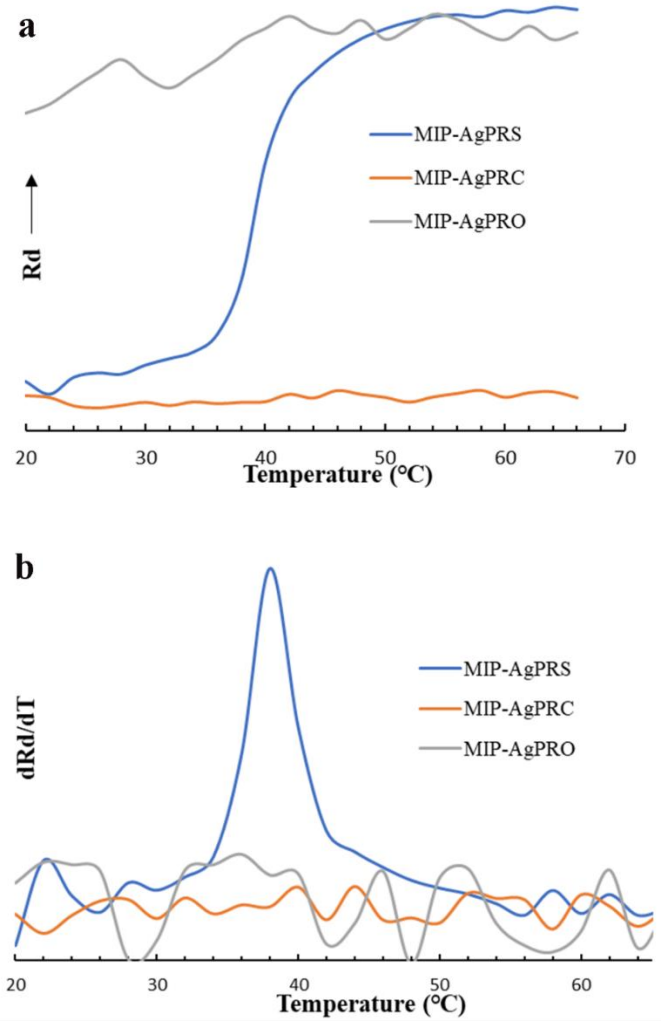

Figure 4-13 Changing DLS spectra of polymer reactor and controls in different temperatures (a normal; b differential).

4.4.6 The analysis of UV catalytic tests

In order to further study the self-controlled tandem catalytic process of the polymer reactor, the complete reaction processes at both low temperature and high temperature were recorded by UV spectrophotometer. Firstly, the UV spectra of the initial substrate 4-nitrophenyl acetate (NPA), the intermediate product 4-nitrophenol (NP) and the final product 4-aminophenol (AP) were collected and the results are presented in **Figure 4-14.** This was done to better understand the positions of the different products in each step of the reactions.

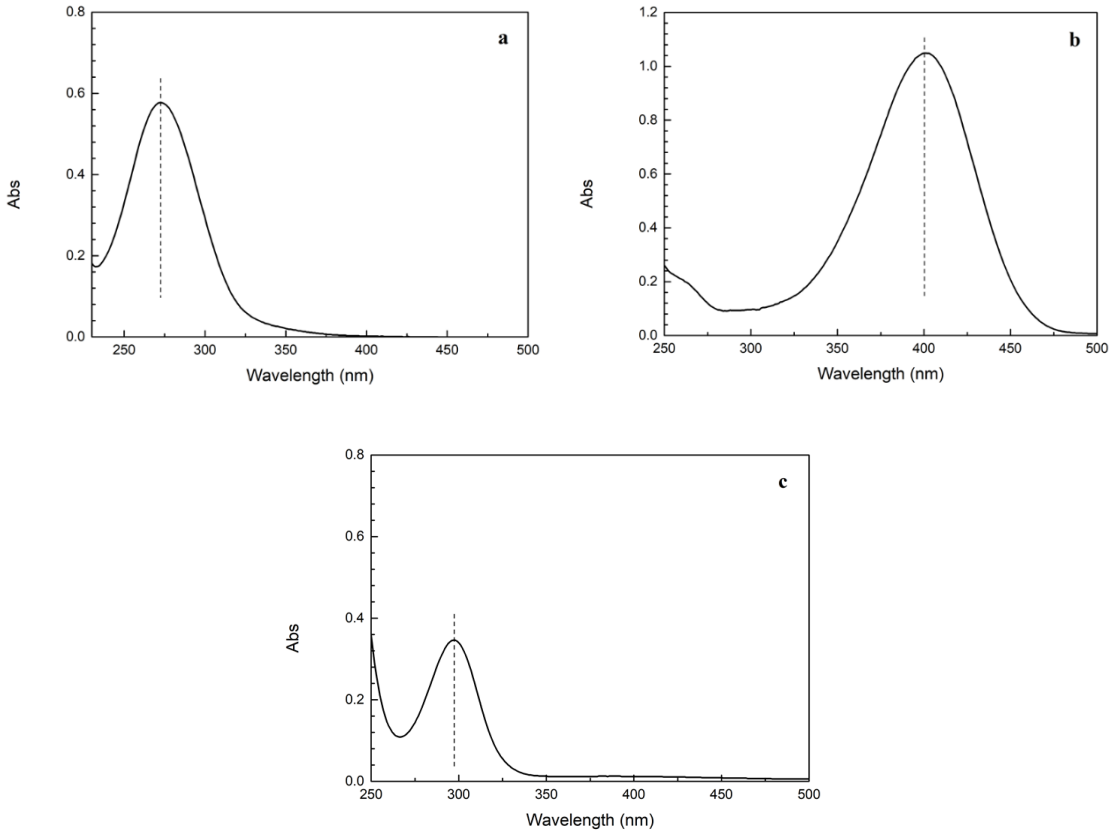

Figure 4-14 UV spectra of NPA (a), NP (b) and AP(c).

DLS test discussed before showed that the transition temperature of the switchable layer in the middle of the reactor was 38 °C. Hence, two temperatures, 25 °C and 50 °C, one lower and the other higher than 38 °C, were selected respectively as examples for the comparative study of the catalytic reaction.

As for the control MIP-AgPRC with the closed channel, the catalytic performance at two different temperatures is shown in **Figure 4-15a** and **Figure 4-15b**. It

shows in two figures that NPA (271 nm) decreased, and meanwhile, the hydrolysis product NP (400 nm) rose. The conversion efficiency of NPA was higher at 50 °C than that at 25 °C because of the high temperature, but the reactor only conducted the simple hydrolysis reaction at both temperatures because of the always closed channel in the middle. As for the control MIP-AgPRO with the open channel, the catalytic performance was more complicated. As shown in **Figure 4-15c**, at 25 °C, the initial product NPA decreased which resulted in the increase of the final product AP, while the intermediate product NP increased firstly and then decreased. The changing processes of the spectrum indicated the tandem reaction process of NPA from hydrolysis to reduction. At 50 °C (**Figure 4-15d**), the changing process was similar, which proved the open channel in the middle layer of MIP-AgPRO.

As for the smart polymer reactor MIP-AgPRS, at 25 °C (**Figure 4-15e**), the spectrum was similar to MIP-AgPRC, showing that a decrease of NPA resulted in the increase of NP. At this temperature, only the simple hydrolysis reaction is catalysed in the system by the acidic sites in the top layer, while no tandem reaction can occur due to the close channel of the PDPA-PAM middle layer. However, at 50 °C (**Figure 4-15f**), the spectrum of MIP-AgPRS became similar to that of MIP-AgRRO, in which the initial NPA was converted to the AP, and at the same time, NPA increased firstly and then decreased. In this process, NPA was hydrolysed to NP catalysed by the acidic sites in the top layer, and then NP was catalytically reduced to AP by the Ag nanoparticles in the bottom layer. At this temperature, MIP-AgPRS achieved tandem catalysis from hydrolysis to reduction because of the open channel of the PDPA-PAM layer.

In summary, the control group MIP-AgPRC could only complete the simple hydrolysis catalysis, while the control group MIP-AgPRO is able to carry out the tandem catalytic reaction but without self-controllable ability. Only the polymer reactor MIP-AgPRS can perform the controllable non-tandem/tandem catalysis reactions at different temperatures.

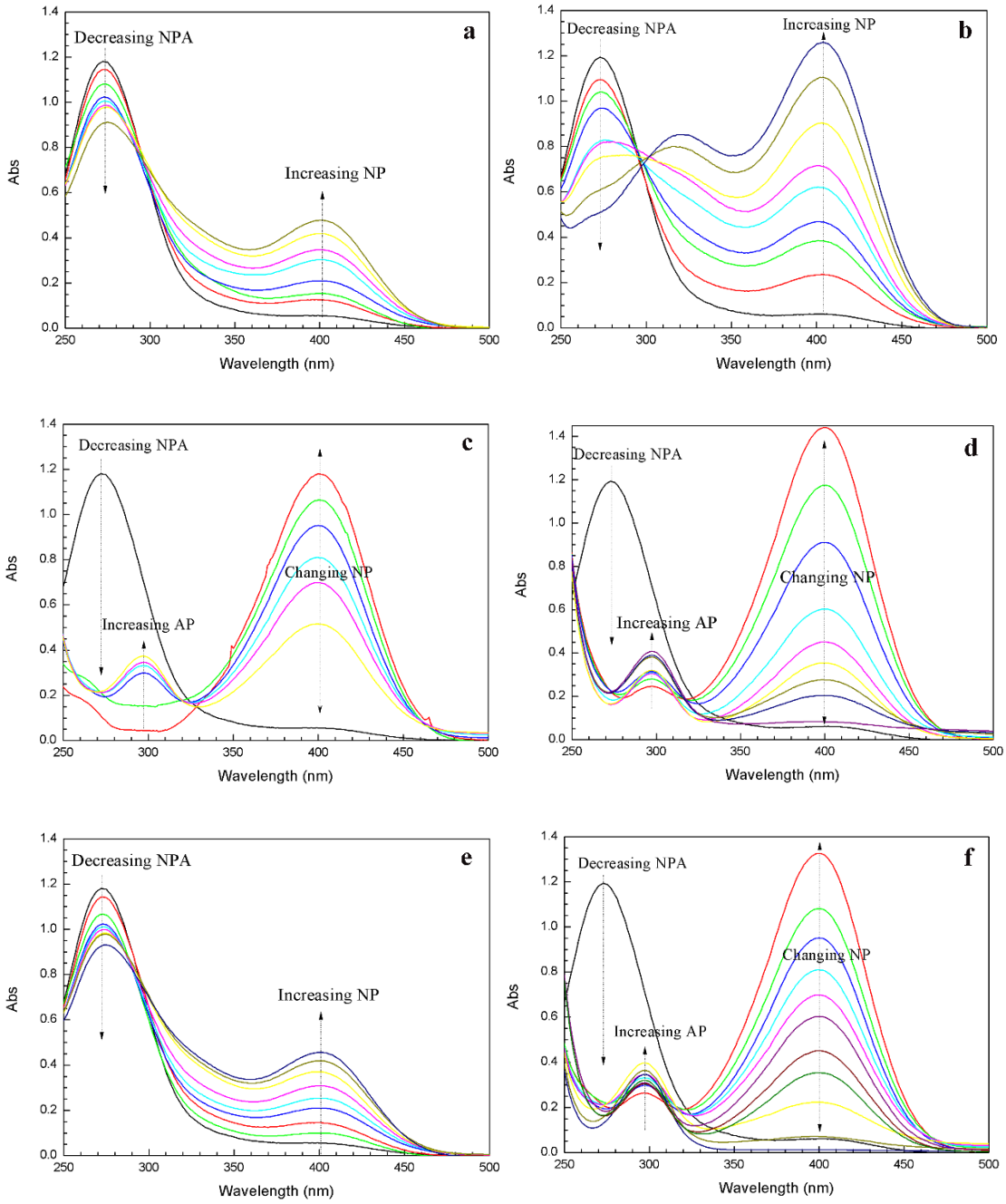

Figure 4-15 The changing UV spectrum of NPA of the polymer reactors at different temperatures (a: MIP-AgPRC at 25 °C; b: MIP-AgPRC at 50 °C; c: MIP-AgPRO at 25 °C; d: MIP-AgPRO at 50 °C; e: MIP-AgPRS at 25 °C; f: MIP-AgPRS at 50 °C).

4.4.7 The analysis of electrochemical test

Electrochemical testing was used to further explain the interactions between the polymer reactors and the substrate [135, 193]. As we known that the possibility to oxidise or reduce the substrate molecule relies on the binding force between the substrate molecule and the polymer reactors. A stronger force requires more energy to overcome the binding, resulting in a greater redox potential. The specific theory has been discussed in detail in section 2.4.4. As shown in **Figure 4-16** [142, 158], the substrate experiences the following processes in the whole reaction system: diffusion to the electrode surface, desorption, and the final oxidation-reduction process. As the influence of the diffusion process was offset by the ultrasonic dispersion, the final desorption process of the substrate molecule was mainly determined by the redox potentials. In this way, the changes of the potentials can be used to clarify the strength of the interactions between the substrate and the smart polymer reactor at different temperatures.

Figure 4-16 A complete electrochemical process of a substrate molecule B

According to the self-healing performance of the middle PDPA-PAM layer of the polymer reactor, 25 °C and 50 °C were respectively selected as two examples to study the interactions between the middle switchable layer and the substrate of the reactor and the controls. As for the reactor MIP-AgPRS, at 25 °C, the reactor exhibited a larger reduction potential value of 884 mV (**Figure 4-17a**), showing a strong interaction with the substrate. When the temperature increased to 50 °C, the reactor showed a relatively smaller reduction potential value of 842 mV (**Figure 4-17d**), showing a weaker interaction force with NPA. Combined with the DLS analysis presented previously, it was known that the stronger interaction at 25 °C derived from the self-healing behaviour between them while the weaker interaction at 50 °C was due to the dissociation of the self-healing effects. The results proved the switchable channel in the middle at different temperatures.

Compared with the self-healing smart polymer reactor MIP-AgPRS, the other two controls, MIP-AgPRO and MIP-AgPRC, did not show significant potential changes when the temperature changed. Under the two temperatures, the control MIP-AgPRO always kept the channel of the middle layer open so that the force between it and the substrate was weak, showing a smaller reduction potential value (25 °C: 812 mV; 50 °C: 804 mV) (**Figure 4-17b** and **Figure 4-17e**). On the other hand, as for the control MIP-AgPRC, it exhibited a greater reduction potential at different temperatures, showing stronger interactions with the substrate, which was due to the always closed channel at different temperatures (25 °C: 877 mV; 50 °C: 872 mV) (**Figure 4-17c** and **Figure 4-17f**). To compare the changes of potential more directly, **Table 4-4** showed the reduction potential value and the potential difference of the desorption of NPA from the three polymer reactors. The changes of the potential strongly proved that the self-healing middle layer of MIP-AgPRS performed different interactions with the substrate at different temperatures, enabling the non-tandem/tandem switchable reactions.

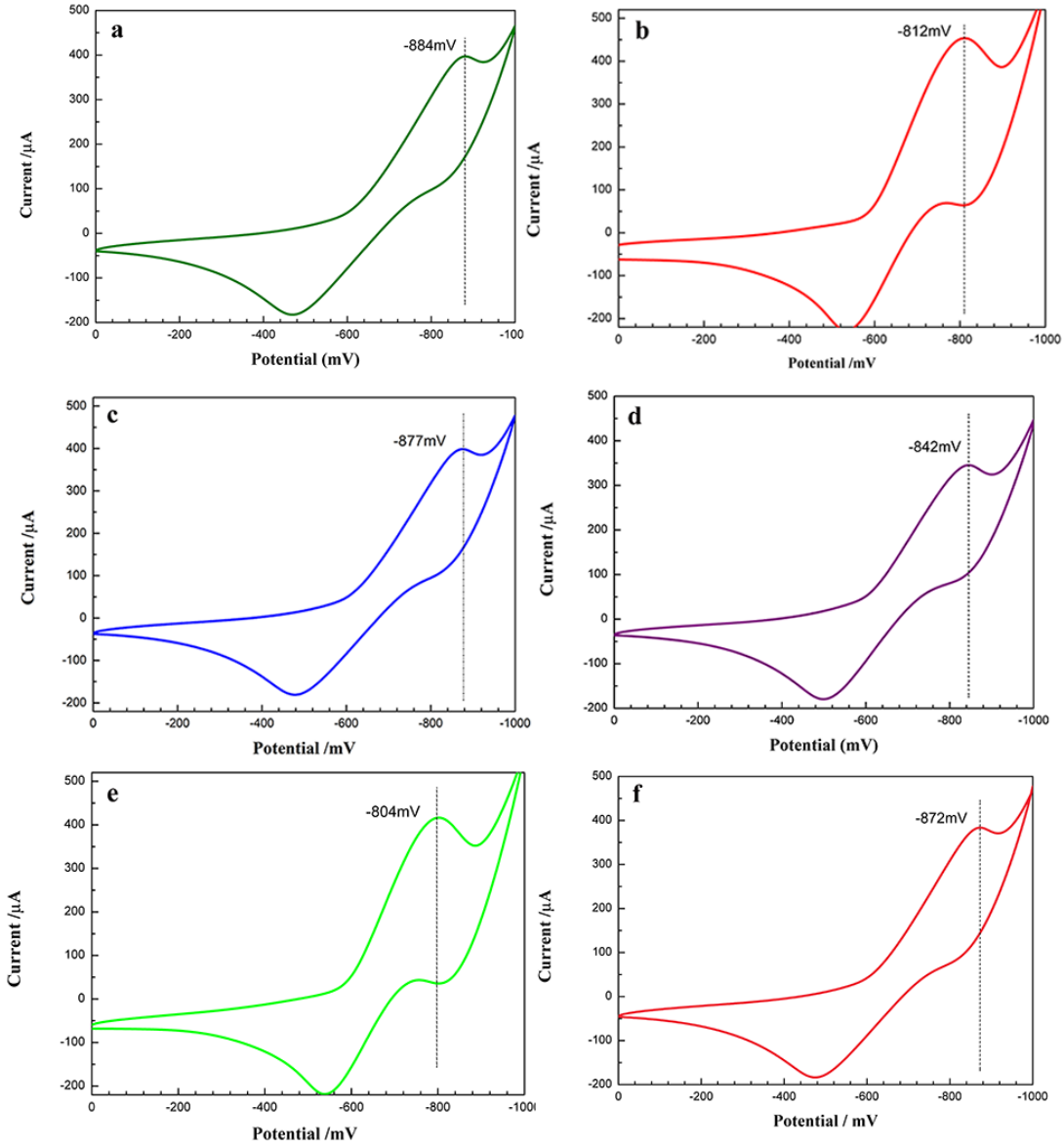

Figure 4-17 Reduction curves of substrates desorbing from all the polymer reactors (a: MIP-AgPRS at 25 °C; b: MIP-AgPRO at 25 °C; c: MIP-AgPRC at 25 °C; d: MIP-AgPRS at 50 °C; e: MIP-AgPRO at 50 °C; f: MIP-AgPRC at 50 °C).

Table 4-4 Reduction potentials (mV) with substrates desorbing from all the polymer reactors.

Catalytic Reactor	25 °C	50 °C	Delta
MIP-AgPRS	-884	-842	42
MIP-AgPRO	-812	-804	8
MIP-AgPRC	-877	-872	5

4.5 Conclusion

The work here reports the preparation of a polymer reactor MIP-AgPRS with three-layer structure, which can control the progress of the tandem catalytic reaction. The top and bottom layers of this smart reactor contained acidic and reductive Ag metal nanoparticles sites respectively, which were responsible for completing the tandem process from hydrolysis to reduction. In addition, MIPs were used as the carriers of the two active sites to obtain the separation of reaction sites and the selective catalytic reaction. The middle layer of the reactor was a controllable layer with self-healing interactions, which consisted of the copolymer of the mussel-like polymer PDPA and PAM. This layer performed as a molecular switch to control the transport of the intermediate product, thereby realising the control of the tandem reaction. When the temperature was low (lower than the responsive temperature of the intermediate layer 37 °C), the channel was closed due to the self-healing interaction between PDPA and PAM, preventing the transport of intermediate products. At this temperature, only the simple hydrolysis reaction can occur. When the temperature was higher than 37 °C, the channel of the middle layer opened because of the dissociation of the interactions, permitting the transport of the intermediate product to the bottom layer for the next reaction, enabling the tandem reaction. Hence, the polymer reactor can control the non-tandem/tandem processes at different temperatures.

Several different characterisations and tests were used to study the composition and the smart catalytic properties of the polymer reactor. FTIR was used to confirm the basic functional groups of the three-layer reactor. SEM test showed the different morphologies of the different layers, highlighting the differences between the MIPs and the middle layer. After confirming the dispersion of the metal nanoparticles in TEM images, SPR and XRD tests confirmed that the type of the metal nanoparticles was Ag. Moreover, EDS test showed the basic elements of the polymer reactor were C, N, O, S and Ag as expected. In order to study the MIP polymer layer and their recognition ability to the corresponding substrates, FTIR was used to compare the samples before and after the substrate

washing processes, confirming that the substrate had been completely removed from the sample. After using BET to investigate the surface area and pore size of the MIPs, TPD test was used to record the desorbing temperatures of NPA and NP from the corresponding MIP layers, which proved greater interactions between substrates and the MIPs.

After confirming the basic composition and morphology of the polymer reactor, then DLS test was used to study the changing particle size of the reactor with the temperature. The results indicated that the response temperature of the middle layer is 38 °C. Based on this response temperature, two different representative temperatures, 25 °C and 50 °C, were chosen as examples to study the catalytic processes by UV test. The results showed that at 25 °C, the reactor could only carry out a single hydrolysis reaction, while at 50 °C, the reactor could complete the tandem catalytic process from hydrolysis to reduction. At the same time, electrochemical tests confirmed that there were different interactions between the reactor and the substrate at different temperatures. Therefore, this work has presented a new catalyst that is able to control the tandem reaction, inspiring the development of functional catalysts in the future.

Chapter 5 Dual-responsive double-layer polymer reactor DPR and the tandem/non-tandem smart catalysis

5.1 Introduction

Tandem catalysis enables a series of complex reactions to proceed in sequence, achieving one-pot catalysis, which improves the utilisation of raw materials and the efficiency of the reaction [194, 195]. Due to the diversity and mechanisms of tandem catalytic processes, it is of great significance to obtain more control over the reaction processes [196, 197]. In order to achieve this goal, several research groups worldwide have been paying attention to the configuration-activity relationship of the catalyst, proposing new catalysts such as functional microspheres and multi-stage structures [34, 198]. These new catalysts are able to achieve specific regulation of the reaction channels based on the separation of different catalytic sites [160, 199]. Although a series of progress has been made, the practical applications of switchable tandem catalysts are still greatly restricted. One of the most significant challenges is the complexity of tandem reactions in practical situations. Sometimes this involves both simple reactions and multi-step tandem reactions at the same time. Therefore, novel tandem catalysts that are suitable for tandem/non-tandem reactions are needed.

As mentioned before, complex reactions in biological systems can proceed in separate compartments without interference [36]. Moreover, many living organisms (both animals and plants) in nature are able to respond quickly to the environment. They can precisely control access to different active sits through their soft shape and freely changeable stacking structure, so as to better adapt to different environments [187]. Inspired by this feature, a dual-responsive double-layer polymer catalyst was proposed here to achieve switchable simple/tandem reactions from low temperatures to high temperatures by responsive shape-changing.

In this experiment, a double-layer polymer catalyst DPR (double-responsive polymer reactor) was prepared. Each layer was copolymerised using two monomers and the temperature responsiveness was achieved by the interactions between the two monomers within the resulting copolymer. The first layer was copolymerised using two monomers which can establish 'weak' polymer forces (**Figure 5-1**). Herein, acrylamide (AM) and 2-acrylamido-2-methylpropanesulfonic acid (AMPS) were chosen as functional monomers in virtue of their good solubility in a variety of solvents. Also, the copolymer had weak hydrogen bond force between their functional groups, which would be broken at relatively high temperatures, resulting in responsiveness to temperatures [157]. The second layer was copolymerised using 1-vinlylimidazole (VI) and 2-trifluoromethacrylic acid (TFMA). Due to the strong nature of the interactions between these two monomers, their disruption in the resulting copolymer would be achieved at higher temperatures than the interactions between AM and AMPS [200]. Therefore, this second copolymer would responsive to higher temperature (**Figure 5-2**). The combination and disruption of the forces of the two copolymers are reversible, so the polymer catalyst can achieve repeatable switching processes. In addition, since the first layer contained acidic active sites for catalytic hydrolysis, Au nanoparticles were introduced into the second layer to perform the catalytic reduction process. Therefore, the double-layer polymer catalyst can realize the control of the tandem process from hydrolysis to reduction.

As shown in **Figure 5-1**, when the temperature is lower than the responsive temperature of both the two layers ($T < 37$ °C; low temperature), the channels of the upper and lower layers are closed, resulting in no obvious catalytic reaction at this condition. When the temperature rises above the responsive temperature of the first layer (37 °C $< T < 53$ °C; medium temperature) but lower than the responsive temperature of the second layer, the reaction channel of the first layer is open. At this time, the polymer catalyst is in a clearly curved and arched state, achieving the simple reaction of catalytic hydrolysis on the first polymer layer with acidic sites. When the temperature rises to the responsive temperature of the second layer ($T > 53$ °C; high temperature), both the double-layer channels are

open. At this time, the polymer reactor can perform a tandem catalytic process from catalytic hydrolysis to reduction. As a result, the reactor DPR can complete the “smart” catalytic process from simple reaction to tandem reaction from medium temperature to high temperature.

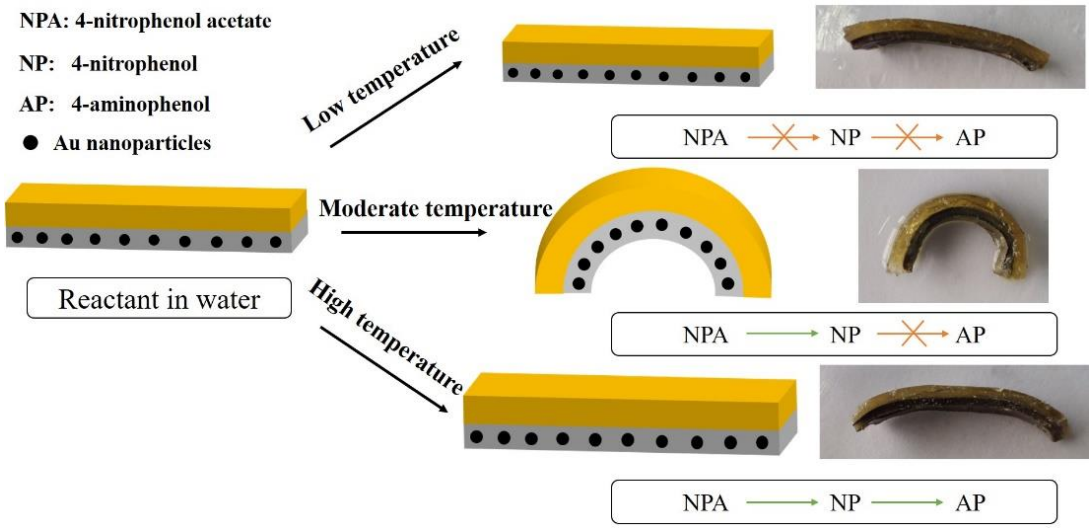

Figure 5-1 The switchable tandem catalytic processes of double-responsive polymer reactor

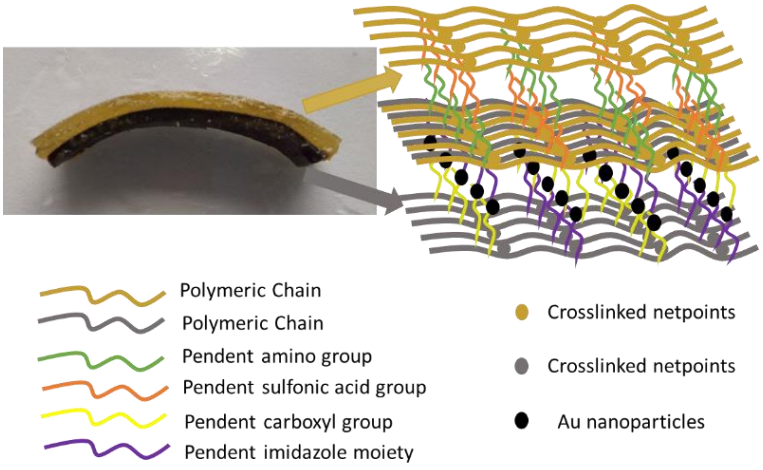

Figure 5-2 The mechanism of bilayer polymer reactor

5.2 Experimental section

5.2.1 Experimental materials and equipment

The chemicals and equipment used in the experiment are shown in **Table 5-1** and **Table 5-2** below:

Table 5-1 Experimental materials

Chemicals	Purity	Company
4-Nitrophenyl acetate（NPA）	≥98%	Sigma-Aldrich Ltd
2,2'-Azobis(2-methylpropionitrile) (AIBN)	98.0%	Sigma-Aldrich Ltd
N, N'-Methylene bisacrylamide (MBA)	99.0%	Sigma-Aldrich Ltd
Potassium chloride (KCl)	≥99.0%	Sigma-Aldrich Ltd
Dimethyl sulfoxide (DMSO)	≥99.9%	Sigma-Aldrich Ltd
Sodium borohydride ($NaBH_4$)	≥98.0%	Sigma-Aldrich Ltd
2-Acrylamido-2-methylpropane sulfonic acid (AMPS)	99.0%	Sigma-Aldrich Ltd
Acrylamide (AM)	≥99.0%	Sigma-Aldrich Ltd
1-Vinyl imidazole (VI)	≥99.0%	Sigma-Aldrich Ltd
Gold (III) chloride trihydrate ($HAuCl_4 \cdot 3H_2O$)	≥99.9%	Sigma-Aldrich Ltd
2-Trifluoromethylacrylic acid (TFMA)	98.0%	Sigma-Aldrich Ltd
4-Nitrophenol (NP)	≥99.0%	Sigma-Aldrich Ltd

Table 5-2 Experimental equipment

Equipment	Company	Model
Vacuum oven	Yiheng Instrument, China	DZF-6020
Electronic balance	Sartorius, Germany	BS-210S
Electrochemical workstation	Chenhua instruments, China	CHI760E
UV-visible spectrophotometer	Shimadzu corporation, Japan	UV-2800
Transmission electron microscope	Hitachi, Japan	JEM-2100
Scanning electron microscope	FEI, US	FEI NovaNano450
Fourier Transform Infrared Spectrometer	Thermo Fisher Scientific Inc., US	Nicolet MX-1E
Zetasizer	Malvern Panalytical, UK	Nano ZS90
X-ray diffractometer	Bruker Corporation, Germany	D8 discover

5.2.2 Preparation of double-layer polymer catalyst

As mentioned before, the two layers of the smart reactor are composed of copolymers with different temperature responsiveness. One of the two layers is the high temperature-responsive layer with Au nanoparticles. To synthesise it, first of all, the functional monomer VI (0.285 g; 3 mmol) and TFMA (0.372 g; 2.61 mmol) were dissolved in dimethyl sulfoxide (DMSO, 10 mL) and dispersed by ultrasound. Then the initiator azobisisobutyronitrile (AIBN) (0.092 g; 0.56 mmol), the crosslinker N, N'-methylenebisacrylamide (MBA) (0.177g; 1.15 mmol) and

gold (III) chloride trihydrate (0.34g; 1 mmol) were added and fully dissolved by ultrasound. The mixed solution was deoxygenated by N_2 for 30 min and put into the oven for 1 hour at 70 °C to fully synthesise. After polymerisation, the contained Au ions were reduced by excess sodium borohydride (10:1 to Au ions). After the reduction, the prepared polymer was thoroughly washed with plenty of deionised water continuously to remove the sodium borohydride and unreacted monomer. Thus, the first layer PVI-PTFMA-Au was prepared.

The second step was to prepare the medium temperature-responsive layer PAMPS-PAM. The functional monomer AMPS (0.94 g; 4.54 mmol) and AM (0.4 g; 5.63 mmol) were fully dissolved in 6 ml of deionised water. Then the crosslinker MBA (0.0375 g; 0.24 mmol), redox initiator system potassium persulfate (KPS) (0.053 g; 0.2 mmol) and sodium bisulphite (0.0247 g; 0.23 mmol) were added to the solution. After dissolving in an ice bath ultrasonically, the mixed solution was fully deoxygenated by nitrogen. Then the first prepared layer was partially immersed in the second layer to form the interpenetrating network between them. The mixed solution was placed in a vacuum oven at 30 °C for an hour. After complete polymerisation, the reacted polymer was rinsed with a large amount of deionised water to remove unreacted monomers. Thus, the dual-responsive bilayer polymer reactor (DPR) was prepared.

In order to study the temperature-responsive abilities of two different layers, two controls were also prepared for comparison. The two controls were prepared in comparable conditions but only one layer with a single temperature sensibility. The first one was a moderate-temperature responsive polymer reactor (MPR), which was composed of PAMPS and PAM with acidic catalytic sites. The second one is a high-temperature responsive polymer reactor (HPR), which was composed of PVI and PTFMA with Au nanoparticles encapsulated as reductive sites. By comparing with the two controls, the dual temperature responsive properties of DPR can be better investigated.

5.3 Tests and characterisation

5.3.1 The composition and morphology characterisation of the polymer reactor

Firstly, some basic tests were conducted to study the morphology and structure of the polymer reactor. FTIR test was first used to determine the functional groups in the polymer reactor. Herein, the sample powder was mixed with potassium bromide (1:50-1:100) and tested as a tablet. SEM imaging was used to characterise the morphology and bilayer structure of the polymer reactor.

As the high temperature responsive layer of DPR contained Au nanoparticles, a series of characterisations were used to confirm their presence and determine the type of metal nanoparticles. TEM was used to characterise the dispersion and size of the metal nanoparticles in the polymer reactor. SPR was used to determine the type of nanoparticles by measuring the metal resonance peak. XRD test was used to further confirm the existence and type of Au nanoparticles. The element distribution in the polymer reactor was also characterised by EDS. By comparing the elements contained in the reactor and the control group, the composition of the polymer reactor was found as expected.

5.3.2 Dual-temperature responsive property tests

UV titration was used to explore the optimal ratio of the two monomers in the copolymerisation. The titration of the two comonomers in the moderate-temperature responsive layer was performed by adding AM (2 μmol/ml; 0.3 mL; 10 μL per titration) with different concentrations to AMPS (0.25 μmol/ml; 3 mL). The titration of two comonomers in the high-temperature responsive layer were processed by gradually adding different concentrations of TFMA (2.5 μmol/ml; 0.35 mL; 20 μL per titration) to VI (0.3 μmol/ml; 3 mL).

The specific phase transition temperature of the two layers in the polymer reactor was confirmed by dynamic light scattering (DLS). The powder sample of DPR and two controls were put in deionised water for ten minutes at the starting temperature to reach kinetic equilibrium before the test. The concentration of the sample was 0.1 mg/ml. After the determination of phase transition temperature

of DPR, the reactor was placed in deionised water at low, medium and high temperatures respectively to observe the deformation with a digital camera.

5.3.3 Self-switchable tandem catalytic tests

The non-tandem/tandem self-switchable catalytic process of polymer reactor DPR was tested in PBS solution (pH: 7; 10% (v/v) methanol) [134]. The initial substrate NPA (0.02 μmol/mL, 10 mL PBS, pH 7.0) and $NaBH_4$ (ten times the concentration of NPA) were added to the reaction system firstly. As for the reactor DPR and controls, the concentration of each sample was 0.1 mg/mL. The catalytic process was tested with a UV-vis spectrophotometer, and the result of each test was obtained by averaging three tests. Because of the existence of self-hydrolysis of the initial substrate, NPA, in the test, the final conversion efficiency of the catalyst was obtained by deducting the conversion rate of the self-hydrolysis performance without the catalyst performed under the same conditions.

5.4 Results and discussion

5.4.1 The optimal ratio of the two monomers

As mentioned before, the thermal sensitivity of DPR comes from the interactions between two monomers within each polymeric layer. The interaction and dissociation processes between the two monomers used to prepare the two copolymer layers allowed DPR to control the channel of acidic and reducing active sites, achieving the self-switchable catalysis. As for the two copolymer layers, an excessive amount of any of the monomers would cause the dislocation of the steric structure of the copolymer, resulting in unsaturated interactions and reactivity defects, which can reduce the efficiency of the reactions. Hence, the two copolymers PAMPS-PAM and PTFMA-PVI can reach complete interaction and dissociation with the optimal stoichiometric ratio, thereby improving the thermal sensibility of the polymer reactor [201]. Since the complementary effects between different functional groups will lead to changes in electronic transitions (valence electrons) in the electron cloud, UV titration [157] can be used to record the change process to figure out the optimal ratio.

The UV titration spectrum of AMPS-AM and VI-TFMA are presented in **Figure 5-3a** and **5-3b**. As shown in Figure 5-3a, the spectrum shifted as AM with different concentrations were added to AMPS. However, the spectrum stopped shifting and only an increase in absorbance was observed when the ratio of PAM/PAMPS reached 1.24/1. Similarly, as shown in Figure 5-3b, the spectra kept shifting when TFMA with continuously changing concentration was added to VI. The optimal ratio of them was finally determined to be PVI/PTFMA of 1.12/1. Therefore, the copolymerisation of the two monomers were prepared in accordance with the optimal ratio.

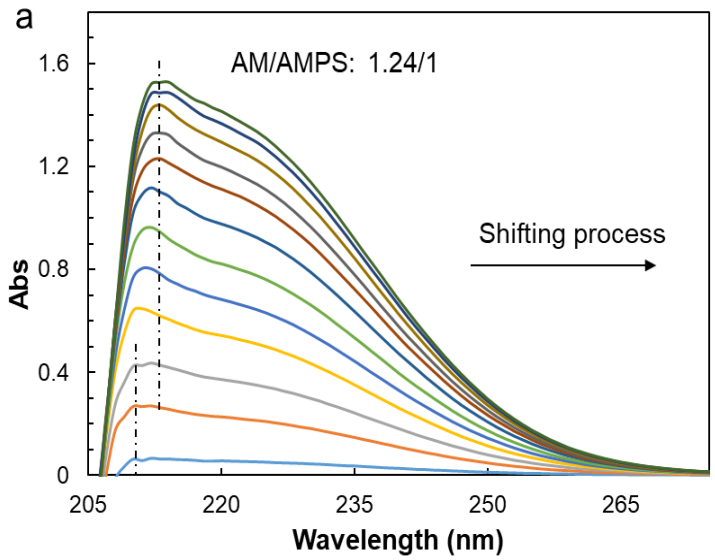

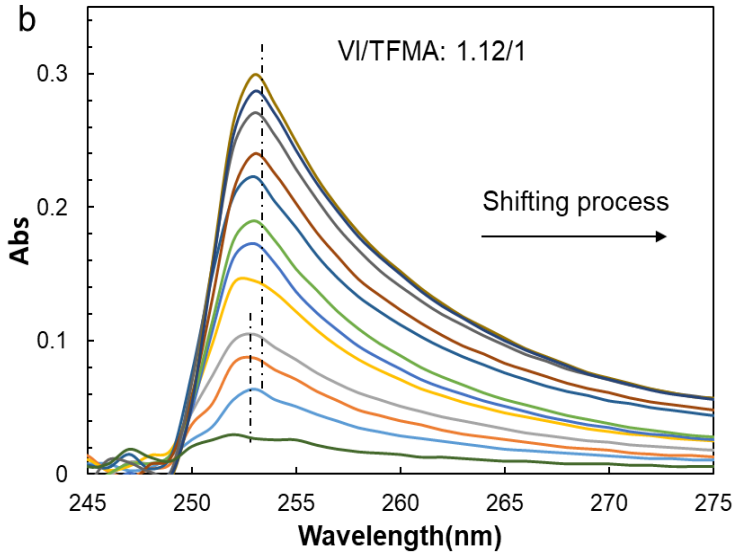

Figure 5-3 The changing UV titration spectra of polymer reactor (a PAMPS-PAM (adding AM to AMPS); b PTFMA-PVI (adding TFMA to VI)).

5.4.2 The analysis of FTIR test

FTIR test was used to analyse the functional groups of the dual-responsive polymer reactor DPR. As shown in **Figure 5-4**, there were three prominent peak bands in the spectrum (3000-3750 cm^{-1}, 1500-1750 cm^{-1} and 1000-1500 cm^{-1}), which corresponding to the stretching vibration of O-H/N-H, C=O and C-N/C-C respectively [188]. The presence of the three prominent peaks was ascribed to the composition of the two copolymers PAMPS-PAM and PTFMA-PVI in the reactor.

In order to confirm the composition of the copolymer, the spectra of two controls MPR and HPR were also presented in the figure. It is shown that the double-layer polymer reactor DPR contained all the main characteristic peaks contained in MPR and HPR. Therefore, it can be further confirmed that DPR was composed of the two copolymers as expected.

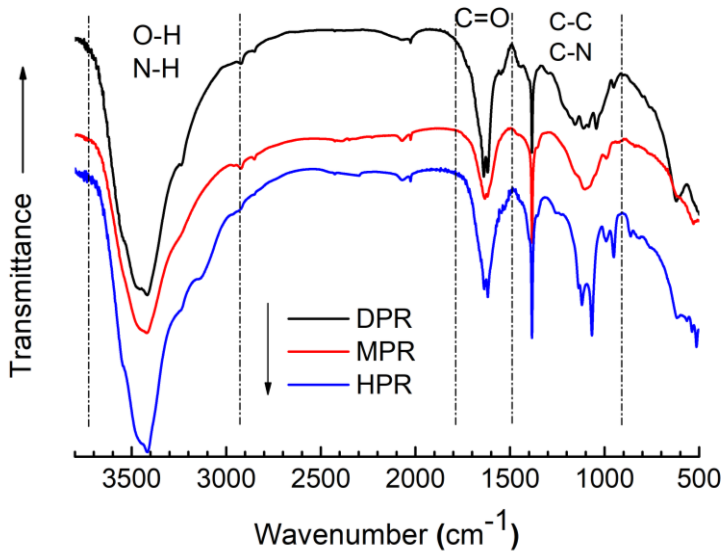

Figure 5-4 FTIR spectra of polymer reactor DPR and two controls

5.4.3 The analysis of macro structure and SEM morphology

The double-layer structure and the micro morphologies of the polymer reactor were observed through macroscopic photos and microscopic SEM images. **Figure 5-5** shows that DPR consisted of two polymer layers, while the two controls MPR and HPR were both single-layer reactors. The black layer in DPR was the copolymer PVI-PTFMA-Au and the other yellow one was the copolymer PAMPS-PAM. The black colour in DPR and HPR resulted from the presence of the Au nanoparticles.

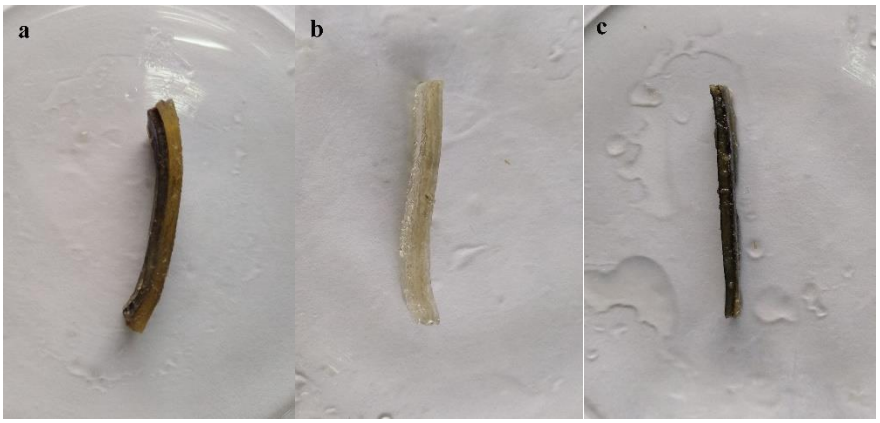

Figure 5-5 The digital images of polymer reactor DPR and the controls （a DPR; b MPR; c HPR）.

Figure 5-6 showed the SEM images of the double-layer reactor DPR. It is shown that compared with the layer PAMPS-PAM, the layer PVI-PTFMA-Au showed obvious dispersion of metal nanoparticles. In addition, it can be observed that the boundary between the two layers was very clear but tightly connected, which confirmed the double-layer structure as expected.

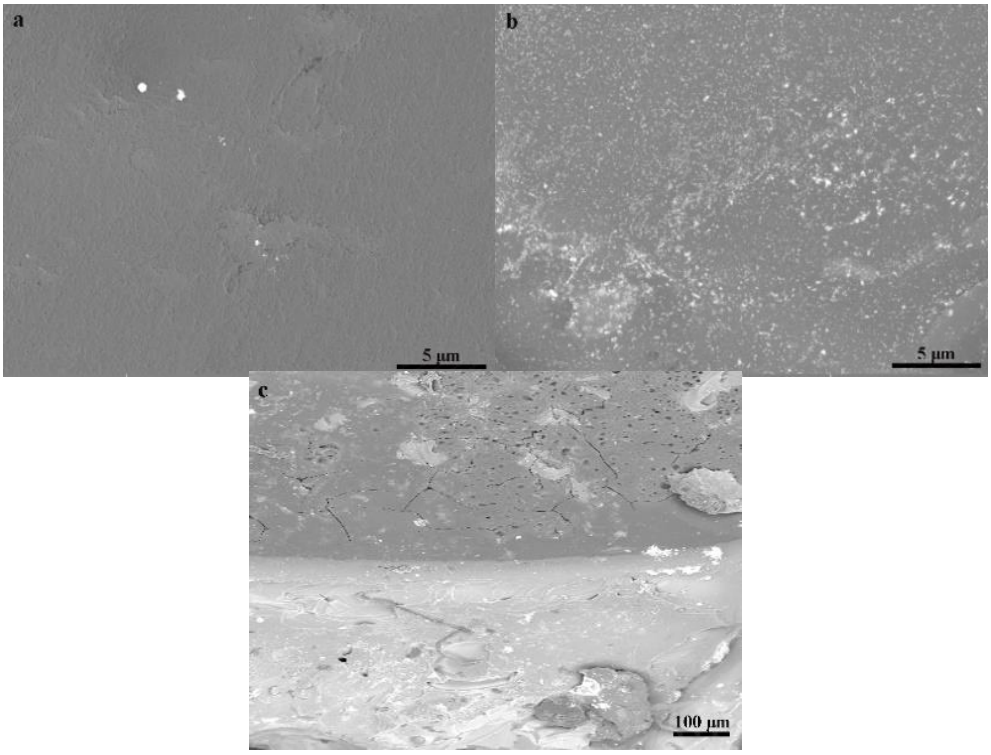

Figure 5-6 SEM images of polymer reactor DPR (a PAMPS-PAM; b PVI-PTFMA-Au; c the boundary of two layers).

5.4.4 The analysis of metal nanoparticles and elements in the polymer reactor

Firstly, the dispersion of metal nanoparticles was observed by TEM analysis. As shown in **Figure 5-7a**, the metal nanoparticles were dispersed on the DPR reactor uniformly with particles size of about 10 nm. Another control HPR also showed obvious dispersion of nanoparticles with a comparable size (**Figure 5-7b**). However, there was no obvious dispersion of metal nanoparticles in second control MPR (**Figure 5-7c**). Therefore, TEM results were consistent with the preparation processes.

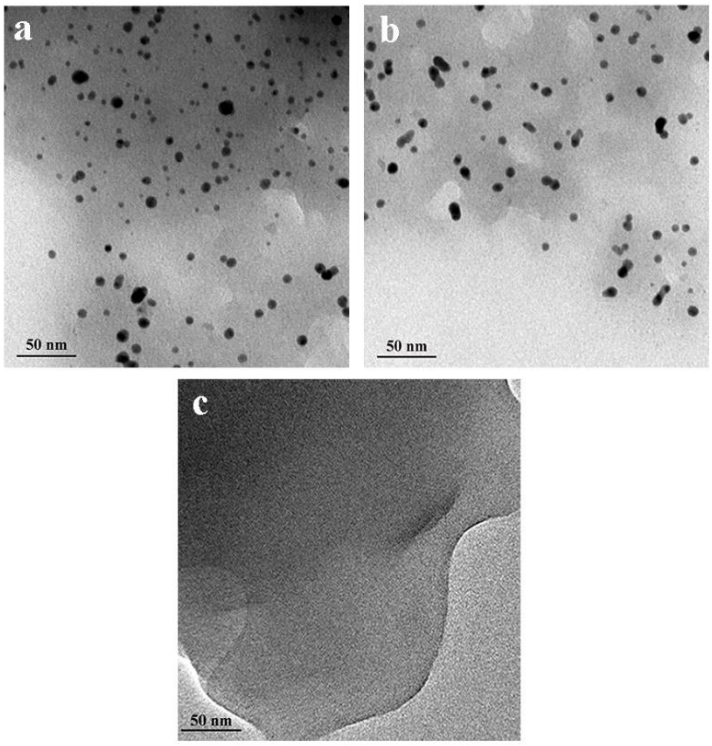

Figure 5-7 TEM images of polymer reactor DPR and two controls (a DPR b HPR c MPR).

After observing the size and dispersion of the nanoparticles in the polymer reactors, the type of metal nanoparticles was further studied by SPR and XRD tests. **Figure 5-8** shows that both the reactor DPR and the reactor HPR exhibited the metal plasmon resonance peak around 560 nm. Following the comparison of these results with similar studies reported in the literature [202], the presence of Au nanoparticles was confirmed. Since the reactor MPR only contained acidic sites, there was no obvious metal resonance peak in the figure. XRD results reported in **Figure 5-9** confirmed the existence of Au metal nanoparticles in the two reactors DPR and HPR. There were peaks at the positions of 38.3°, 44.4°, 64.6° and 77°, which indicated the existence of Au nanoparticles according to the standard XRD cards. However, the reactor MPR only showed a broad polymer peak around 20°, which also appeared in the other two samples and no obvious metal nanoparticles peaks were shown. Both the SPR and XRD tests demonstrated that the type of metal nanoparticles was Au.

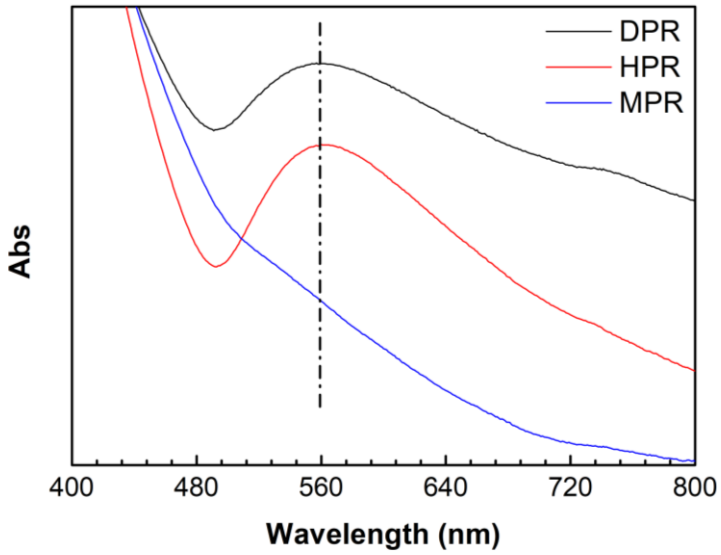

Figure 5-8 The SPR spectra of polymer reactor DPR and two controls.

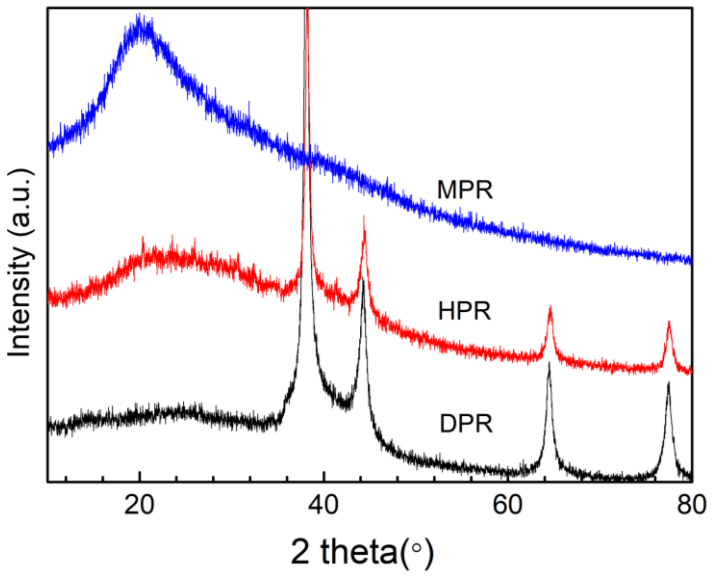

Figure 5-9 The SPR spectra of polymer reactor XRD and two controls.

The EDS test was used to characterise the different elements contained in the catalytic reactor and the controls. As shown in **Figure 5-10**, apart from the basic elements of C, N, and O, the moderate-temperature responsive reactor MPR had an extra S element than HPR, which was due to the presence of the acidic sites from polymer PAMPS. Compared with MPR, HPR contained Au and F elements due to the presence of PTFMA and Au nanoparticles. The double-layer reactor

DPR contained all the elements that appeared in the two controls. EDS results further proved that the composition of DPR was as expected.

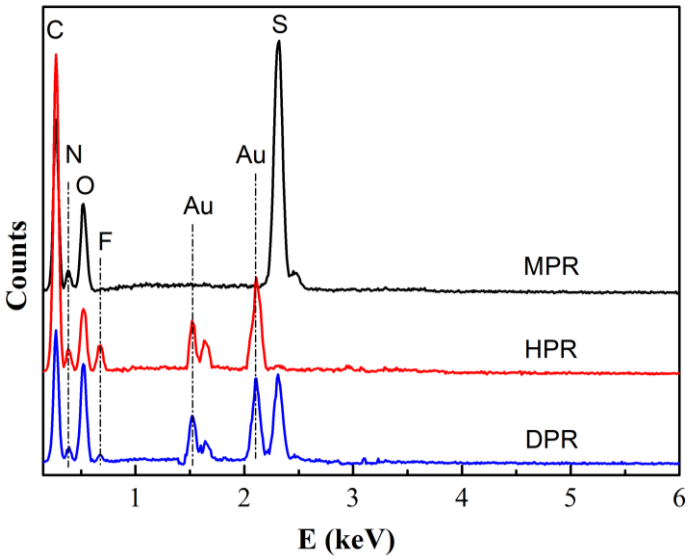

Figure 5-10 EDS spectra of polymer reactor DPR and two controls.

5.4.5 The analysis of dual-responsive thermal performance

To study the specific temperature responsive abilities of DPR, DLS tests were used to record the changing dynamic diameter Rd with the increasing temperatures to determine the responsive temperatures of the two polymer layers respectively. As shown in **Figure 5-11a**, the dynamic diameter Rd increased dramatically at 37 °C, which was because of the dissociation of the PAMPS-PAM interaction at medium temperature. At this temperature, the channel of this copolymer layer opened, so the particle size increased significantly, enabling the catalytic hydrolysis process. As for the high-temperature responsive reactor HPR, Rd increased significantly at 50 °C, which was the result of the dissociation of the interaction between PVI-PTFMA. At this temperature, the channel of this copolymer opened, enabling the catalytic reduction.

In contrast to MPR and HPR, which only respond to a single temperature, DPR showed a substantial increase in Rd at both medium and high temperatures, which was consistent with the dual-responsive characteristics of the double-layer

composition. **Figure 5-11b** shows the differential image of Figure a, demonstrating the temperature sensitivity in a more direct way. It can be seen that DPR experienced two significant dynamic diameters increases at 37 °C and 50 °C. Therefore, when the temperature was between 37 °C and 50 °C, the channel of the PAMPS-PAM layer was opened, achieving simple hydrolysis catalysis. When the temperature was higher than 50 °C, the channel of the PVI-PTFMA-Au layer was also opened, enabling the tandem catalysis from hydrolysis to reduction. Therefore, the two layers in DPR can act as switches enabling to control of the tandem catalysis.

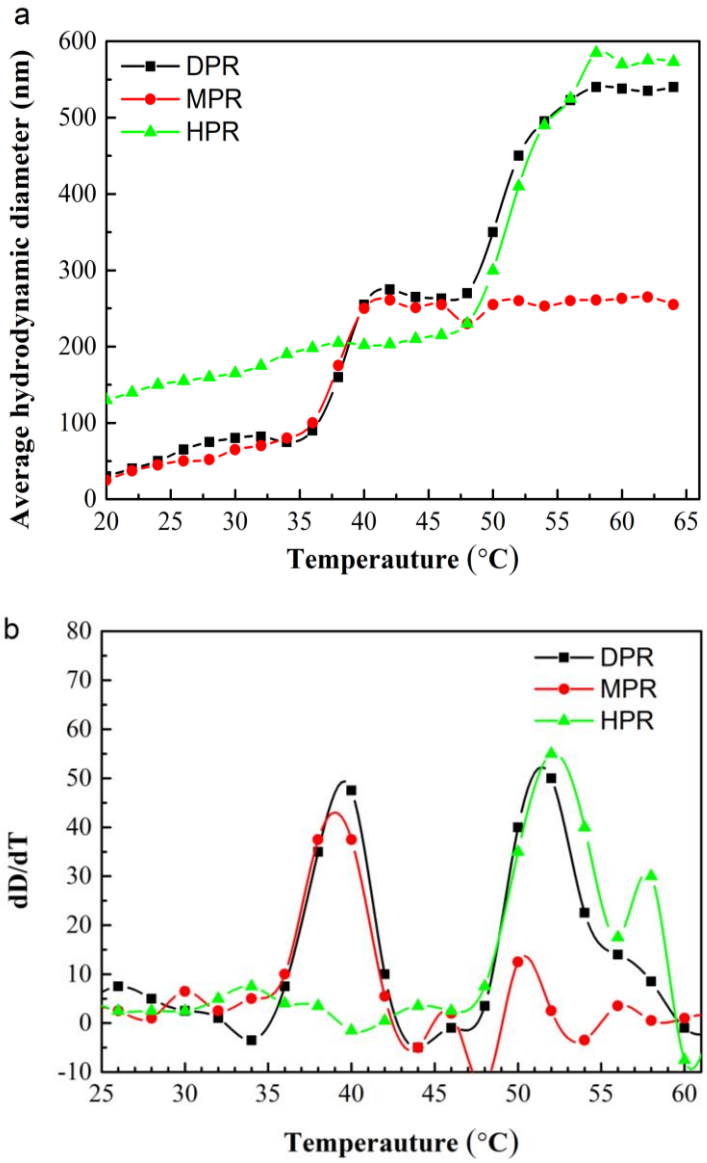

Figure 5-11 Changing DLS diameter of polymer reactor DPR and controls in different temperature (a normal; b differential)

After studying the temperature-responsive properties of DPR, the deformation of the reactor at different temperatures were recorded. According to the two responsive temperatures of 37 °C and 50 °C of DPR, three specific temperatures, 30 °C (below 37 °C), 45 °C (between 37 °C and 50 °C) and 60 °C (above 50 °C) were chosen for observation. As shown in **Figure 5-12a**, DPR was almost flat at 30 °C, which was due to no obvious reaction in two temperature-sensitive layers. When the temperature rose to 45 °C, it can be seen that DPR underwent a large deformation and became bent (**Figure 5-12b**). This was caused by the dissociation of the interaction between PAMPS-PAM above its responsive temperature. When temperature increased to 60 °C, DPR deformed into flat again because of the open channel of the other PVI-PTFMA-Au layer (**Figure 5-12c**). This deformation process was reversible with temperature, indicating that the DPR responded to different temperatures, resulting in the shape changes.

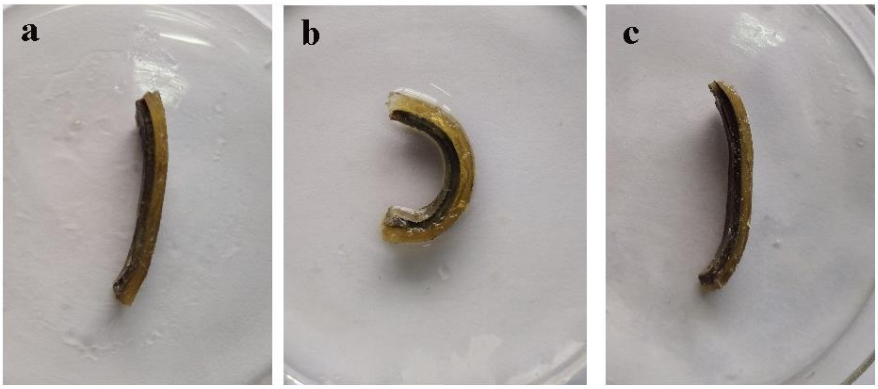

Figure 5-12 Shape changing of polymer reactor DPR in different temperatures (a 30 °C; b 45 °C; c 60 °C)

5.4.6 The analysis of non-tandem/tandem catalytic processes in different temperatures

UV spectrophotometer was used to investigate the reaction process of initial substrate NPA in different temperatures to study the non-tandem/tandem catalytic performance. Three temperatures (30 °C, 45 °C and 60 °C) were selected according to the two responsive temperatures. First of all, as for the control MPR that responded at moderate temperature, there was no apparent reaction at 30 °C because the channel was closed (**Figure 5-13a**). When the temperature rose to 45 °C (**Figure 5-13b**), the initial substrate NPA (271 nm) decreased while the intermediate product NP (400 nm) increased significantly, indicating that NPA was hydrolysed to NP. At 60 °C (**Figure 5-13c**), there was no further change of the spectrum. The results confirmed the channel for acidic sites of MPR opened at 45 °C. As for the control HPR that responded at high temperature, there were no distinct changes of the spectrum at 30 °C (**Figure 5-13d**) and 45 °C (**Figure 5-13e**), as these two temperatures were below the responsive temperature of the layer. However, when the temperature was 60 °C (**Figure 5-13f**), the decrease of NPA resulted in the increase of final product AP (295 nm). At this condition, the channel to the reductive sites Au nanoparticles were open and the imidazole group contributed to part of the hydrolysis performance, so that NPA could be converted to NP and then finally reduced to AP. The control HPR responded to the high temperature as expected.

As for the dual-responsive reactor DPR, the reaction situation was more complicated. When the temperature was 30 °C (**Figure 5-13g**), there was no obvious change in the spectrum because the temperature did not reach the responsive temperature of the two layers. At 45 °C (**Figure 5-13h**), it can be seen that NPA decreased while at the same time NP increased. This was due to the opening of the channel of the PAMPS-PAM layer, providing acidic sites to hydrolyse NPA to NP. The spectra were similar to the performance of MPR at 45 °C. At 60 °C (**Figure 5-13i**), the final product AP increased while NPA decreased, and the intermediate product NP increased firstly then decreased. The spectrum was comparable with the spectrum of HPR at 60 °C. Both spectra showed the tandem processes while the hydrolysis efficiency of DPR was higher.

Therefore, the double-layer polymer reactor can respond to medium and high temperatures respectively, completing the simple hydrolysis catalysis at medium temperature (between 37 °C and 50 °C) and the tandem catalysis from hydrolysis to reduction at high temperature (above 50 °C), permitting to achieve self-switchable catalysis processes.

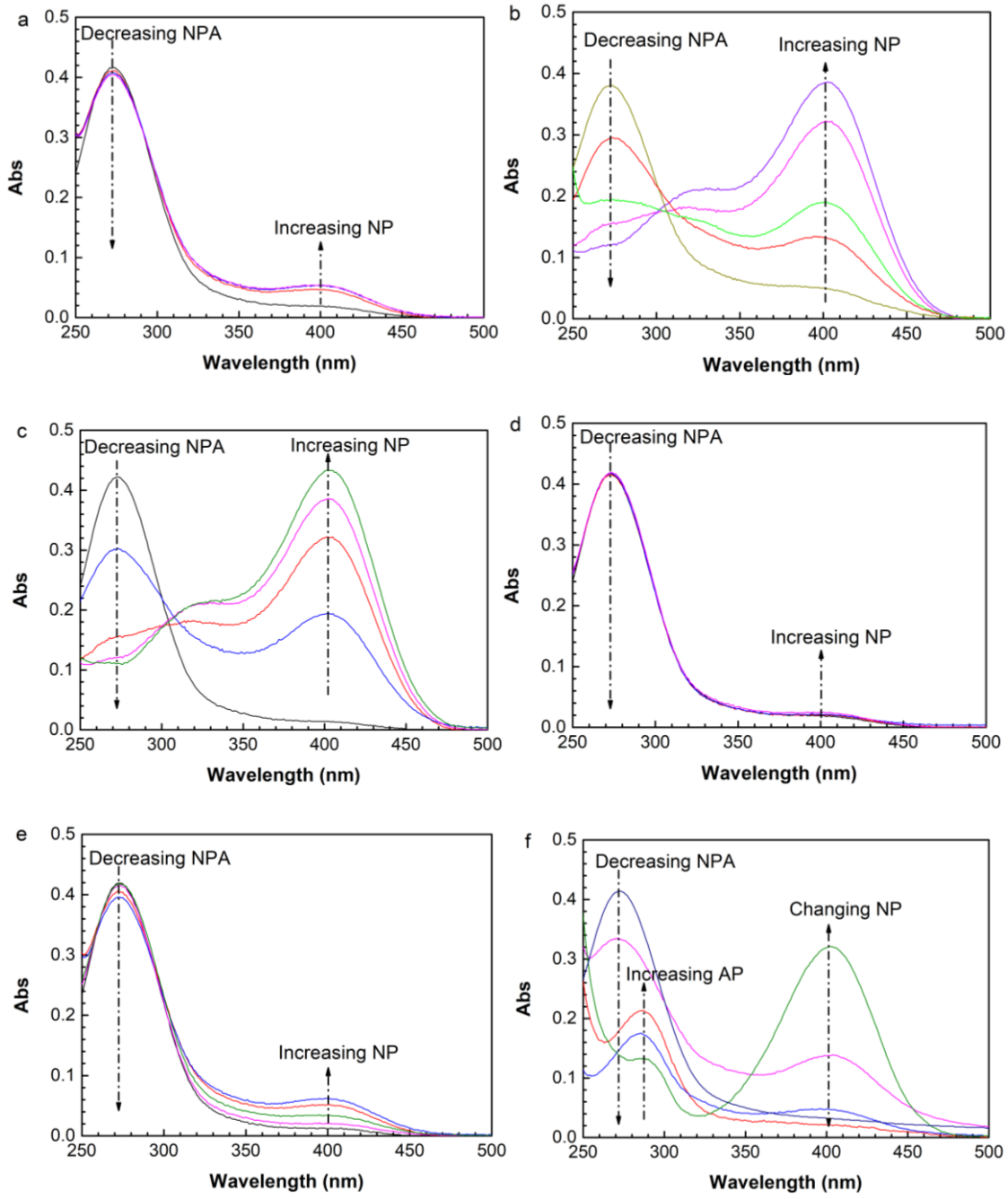

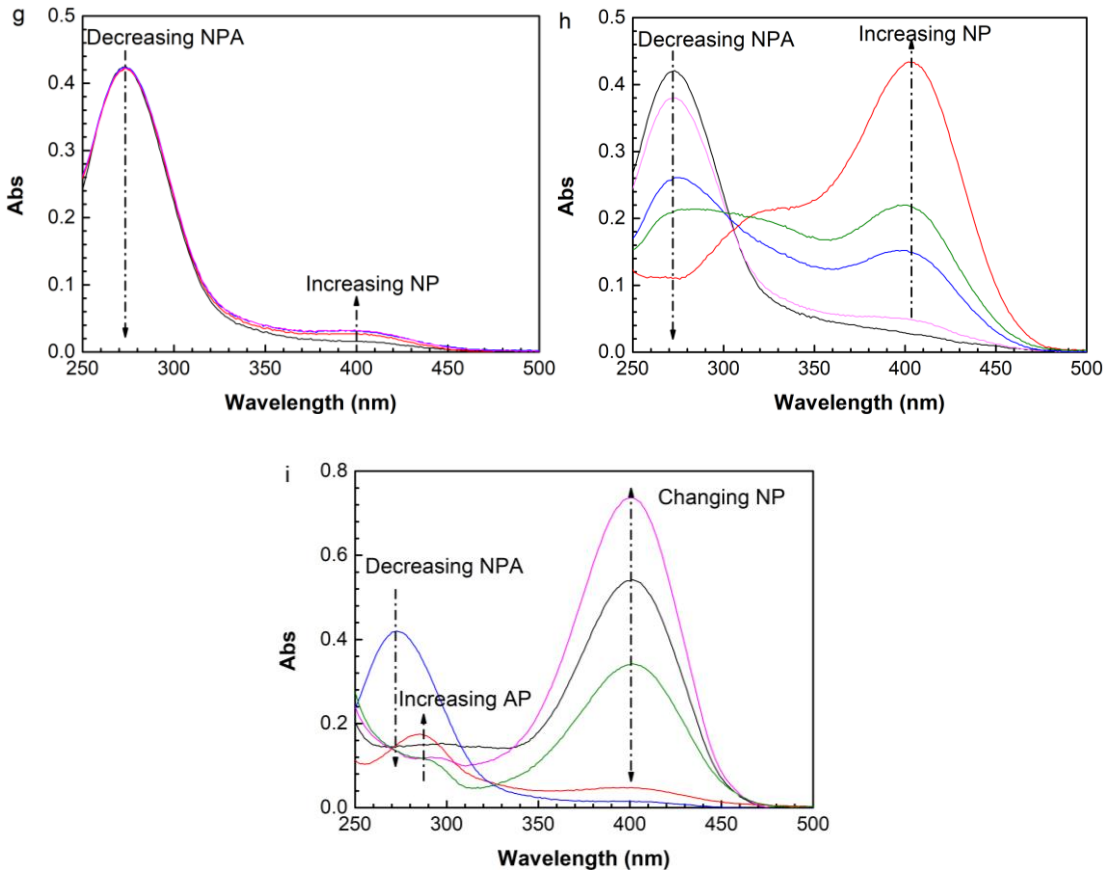

Figure 5-13 The catalytic behaviors in UV spectra of DPR and the controls in different temperatures (MPR: a 30 °C; b 45 °C; c 60 °C; HPR: d 30 °C; e 45 °C; f 60 °C; DPR: g 30 °C; h 45 °C; i 60 °C)

5.5 Conclusion

In this chapter, a dual-responsive double-layer catalytic reactor DPR was prepared to achieve the self-switchable catalysis from non-tandem to tandem. This smart catalytic reactor is composed of two thermal-responsive layers which would respond to medium temperature (37 °C) and high temperature (50 °C). At the same time, the two layers contained acidic sites and Au nanoparticles respectively, which are able to catalyse different reactions.

The first layer is the copolymer of PAMPS-PAM, which can respond to medium temperature of around 37 °C as a result of the presence of hydrogen bonds between the functional groups. When the temperature is higher than 37 °C, the

channel in this layer will open, enabling access to the acidic sites for the hydrolysis reactions. The second layer consisted of the copolymer PTFMA-PVI with Au nanoparticles encapsulated. The stronger polymer compounding interactions make it responsive to the temperature of around 50 °C. When the temperature is higher than 50 °C, the channel in this layer will also open, providing the access to Au nanoparticles for catalytic reduction. In this way, the double-layer polymer reactor DPR is able to catalyse the simple hydrolysis reaction at medium temperatures (between 37 °C and 50 °C), while it catalyses tandem reaction from hydrolysis to reduction at higher temperatures (above 50 °C), reaching smart control of tandem reaction processes.

In the experiment, the optimal ratio of the two monomers (PAM/PAMPS: 1.24/1; PVI/PTFMA: 1.12/1) was confirmed through the UV titration process to achieve the optimal responsive properties. After confirming the morphology and structure through a series of tests such as FTIR, SEM, and TEM, the temperature-sensitive performances of different layers were recorded by DLS test, and two responsive temperatures (37 °C and 50 °C) were obtained. Three specific temperatures (30 °C, 45 °C and 60 °C) based on these two responsive temperatures were chosen as examples to study the self-controlled catalysis processes. It can be seen from the UV test that at low temperature (30 °C), the reactor has no obvious catalytic effect; at medium temperature (45 °C), the catalytic hydrolysis process can be conducted due to the open channel in PAMPS-PAM layer; at high temperature (60 °C), the tandem catalysis from hydrolysis to reduction can be achieved because of the open channels of both layers. Thus, the polymer reactor DPR can realise the self-switchable processes of simple reaction at medium temperature and tandem reaction at high temperature.

Chapter 6 Self-switchable polymer reactor PRS with PNIPAM-PAM smart switch capable of tandem/simple catalysis

6.1 Introduction

Exploring novel methods to synthesise complex organic molecules has been an important goal in the area of catalysis for several years [30, 205]. Tandem catalysis is among the most effective solutions. In tandem catalysis, a series of catalytic processes proceed in sequence without interference, which not only saves time and energy but also decreases the loss of raw materials [168, 206]. However, because tandem reactors need to contain multiple active sites (catalysts), it is important to separate different sites and ensure that each step is performed separately [207, 208]. In the previous experiment, different molecularly imprinted polymers were introduced as the carriers of different active sites. Since the catalysts are dispersed in different imprinted polymers, the tandem process can be performed without interference. In addition, due to the unique recognition characteristics of MIP, the selectivity of the catalytic process can be achieved [55]. On the other hand, it is still necessary to control the catalytic reaction process effectively because of the multi-step and complex process.

Temperature-sensitive polymers can control and adjust their own state under different temperature conditions, which has always been a research hotspot in the field of smart polymers. Poly-N-isopropylacrylamide (PNIPAM) is one of the most successful and widely studied temperature-sensitive smart materials, which has been widely studied by researchers [209-211]. In solutions with different concentrations, PNIPAM exhibits a relatively stable lower critical solution temperature (LCST), generally around 31-33 °C [212]. As the temperature gradually increases to above the phase transition temperature, PNIPAM will undergo a significant phase transition from hydrophilic to hydrophobic, which is caused by the hydrophilic and hydrophobic units contained in its structure. PNIPAM has a repeating composition of hydrophilic amide groups and

hydrophobic isopropyl groups. When the temperature is below LCST, it is hydrophilic because of the strong hydrogen bond interactions between the amide group and water. When the temperature is above the LCST, because of the destruction of the hydrogen bond, the interaction between the main chain and the isopropyl group becomes predominant [213], causing the change of the linear chain from random coil chains to the collapsed globules. In this condition, it exhibits a hydrophobic state. Therefore, PNIPAM possesses a rapid and effective temperature response during temperature transitions. However, since PNIPAM is very soft in the hydrated state, it is critical to further improve its mechanical properties for better use in practical applications. There are many different ways to modulate its mechanical properties. One of the most commonly used methods is the introduction of a hydrophilic or hydrophobic copolymer in the polymerisation mixture composition obtaining a copolymer. Generally, the copolymer will also affect the LCST of PNIPAM. Adjusting the LCST of PNIPAM to a larger temperature range can achieve broader applications in different areas such as smart catalysis [214, 215]. For example, the random ratio copolymerisation of NIPAM and N, N-diethylacrylamide (DEA) produced response behaviours at different temperatures [216]. In addition, the copolymerisation of NIPAM and the hydrophilic monomer N, N-dimethylaminopropylacrylamide (DMAPAAm) caused an increase of LCST due to the strengthening of the hydrogen bonds between polymer chains and water molecules [217-219]. Among a lot of comonomers, acrylamide (AM) is one of the most commonly used ones. Although AM is not a thermally responsive polymer, due to its hydrophilic structure [220], it will increase the value of LCST of PNIPAM. Meanwhile, it can improve the mechanical stability of the material by forming a semi-interpenetrating polymer network with PNIPAM [221].

In this chapter, a three-layer polymer reactor was prepared, which was composed of two imprinted polymer as top and bottom layers and a self-controlled switchable middle layer. The top and bottom layers consisted of two MIPs, which acted as carriers for two different catalytic sites (acidic sites and metal nanoparticles sites). As a result, each step of the tandem catalysis can be carried out separately without unnecessary interference. In addition, the recognition

ability of imprinted polymers enabled the selective catalytic processes of the polymer reactor. As shown in **Figure 6-1**, the top layer was poly (2-acrylamido-2-methylpropanesulfonic acid) (PAMPS), which contained acidic sites, responsible for catalytic hydrolysis. The bottom layer was composed of polyacrylamide (PAM) with Ag nanoparticles encapsulated in it, responsible for the catalytic reduction process. As for the imprinted substrates, 4-nitrophenol acetate (NPA) and 4-nitrophenol (NP) were chosen as the two model substrates. As we know, NPA can carry out the tandem process from hydrolysis to reduction and NP is its hydrolytic intermediate [194].

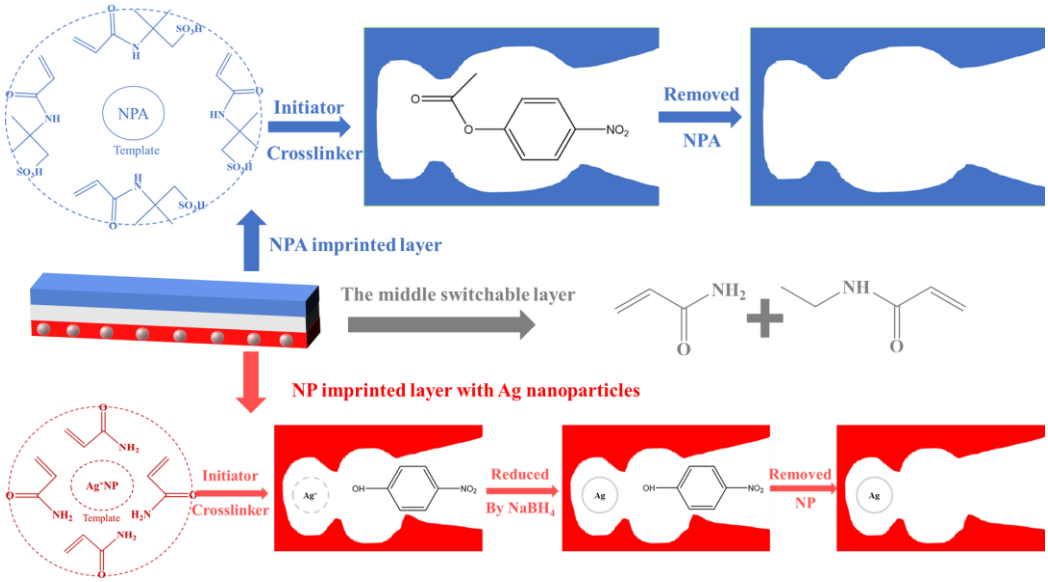

Figure 6-1 The preparation of the three-layer switchable polymer reactor.

In between these two imprinted layers, a switchable layer, composed of PNIPAM and PAM, was prepared. As a temperature-sensitive polymer, PNIPAM can act as a switch to open and close repeatedly at different temperatures to adjust the tandem process. At the same time, to enhance the mechanical stabilities of PNIPAM in the repeated catalysis process, and also to enhance the affinity between the intermediate layer and the top and bottom layers, AM was introduced to copolymerise with NIPAM to obtain the copolymer PNIPAM-PAM. It can be seen in **Figure 6-2** that the intermediate layer swells and becomes hydrophilic at low temperatures, allowing the intermediate to pass through. At these

temperatures, the tandem catalytic reaction process from hydrolysis to reduction is carried out. At higher temperatures, the intermediate layer will shrink and become hydrophobic, hindering the passing of the intermediate. Therefore, only a simple hydrolysis reaction will proceed. In this way, the reactor can exhibit the different catalytic performances from low to high temperatures. To further determine the switchable properties of the polymer reactor, two controls without the switchable ability and therefore with the middle layer always open (only PAM) or close (only polystyrene (PS)) were also prepared.

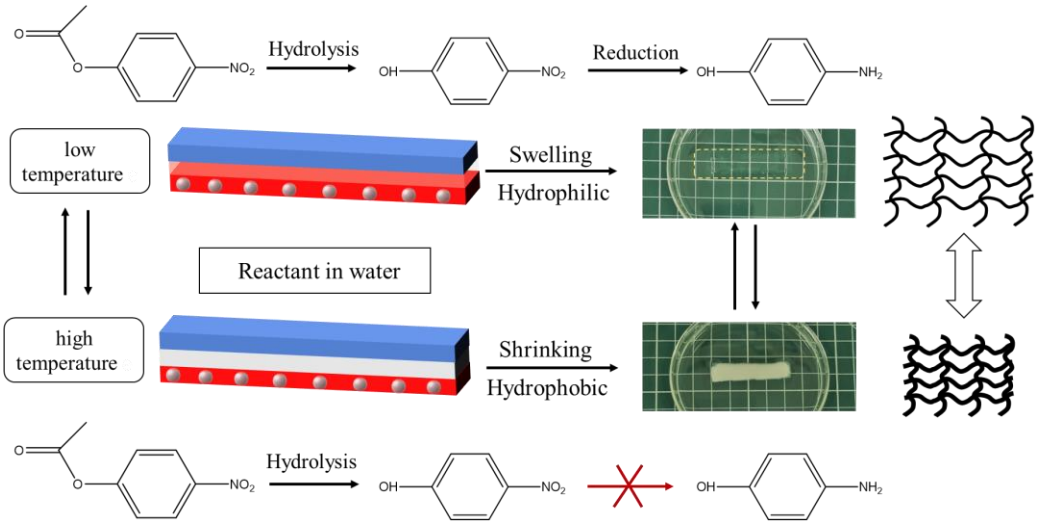

Figure 6-2 The switchable mechanism of the three-layer polymer reactor.

6.2 Experimental section

6.2.1 Experimental materials and equipment

The chemicals and equipment used in the experiment are shown in **Table 6-1** and **Table 6-2** below:

Table 6-1 Experimental materials

Chemicals	Purity	Company
Ammonium persulfate (APS)	99.0%	Sigma-Aldrich Ltd
N, N'-Methylene bisacrylamide (MBA)	99.0%	Sigma-Aldrich Ltd
Dimethyl sulfoxide (DMSO)	≥99.9%	Sigma-Aldrich Ltd
Sodium borohydride ($NaBH_4$)	≥98.0%	Sigma-Aldrich Ltd
N-isopropylacrylamide (NIPAM)	99%	Sigma-Aldrich Ltd
2-Acrylamido-2-methylpropane sulfonic acid (AMPS)	99.0%	Sigma-Aldrich Ltd
Acrylamide (AM)	≥99.0%	Sigma-Aldrich Ltd
Silver nitrate ($AgNO_3$)	≥99.9%	Sigma-Aldrich Ltd
4-Nitrophenol (NP)	≥99.0%	Sigma-Aldrich Ltd
4-Nitrophenyl acetate (NPA)	≥98%	Sigma-Aldrich Ltd
Acetic acid	≥99.9%	Sigma-Aldrich Ltd
Methanol	≥99.9%	Sigma-Aldrich Ltd

Table 6-2 Experimental equipment

Equipment	Company	Model
Vacuum oven	Binder GmbH, Germany	VD 23
Magnetic stirrer	Fisher Scientific, UK	Isotemp
Ultrasonic cleaner	JAMES products Europe	SONIC 6MX
UV-visible spectrophotometer	JASCO, Japan	Jasco V-6700
Electronic balance	OHAUS, US	Valor 2000
Scanning electron microscope	TESCAN, Czech Republic	TESCAN VEGA 3
Fourier Transform Infrared Spectrometer	JASCO, Japan	Jasco FT/IR-6200
Zetasizer	Malvern Panalytical, UK	Nano-S
X-ray diffractometer	Siemens, Germany	Siemens D5005
Differential Scanning Calorimeter	TA instruments, US	DSC Q200

6.2.2 Preparation of the polymer reactors

As mentioned in the first section, the top and bottom layers of the three-layer polymer reactor consisted of two molecularly imprinted polymer containing different catalytic sites (top: acidic site; bottom: Ag nanoparticles) and the middle layer was a temperature-responsive layer (PNIPAM-PAM) (as shown in **Figure 6-1**). In order to make the layers tightly connected during the preparation process, after completing the synthesis of the first layer in a glass petri dish, the solution of the middle layer was added to form an interpenetrating network in the boundary area. Similarly, after the completion of the polymerisation of the second layer, the two layers of polymer were partially immersed in the solution of the third layer to fully diffuse. Thus, in the three-layer polymer reactor, the polymer layers were closely bonded.

The first step was the preparation of the top imprinted layer. The monomer AMPS (2.33 g), the crosslinker MBA (0.35 g), the initiator APS (0.075 g) and the imprinted substrate NPA (0.36 g) were dispersed in 10 mL dimethyl sulfoxide (DMSO). Then the solution was completely dissolved by ultrasound and deoxygenated by nitrogen gas. Subsequently, the solution was put in a vacuum drying oven at 70 °C for 3 hours to complete the polymerisation (MIP-PAMPS).

The second step was the preparation of the middle layer. The monomer NIPAM (2.26 g) and AM (different molar ratios; see 6.4.1 analysis for details), crosslinker MBA (0.3 g) and initiator APS (0.075 g) were dispersed in the solvent DMSO (10 mL). Then the mixed solution was fully dissolved by ultrasound and deoxygenated by nitrogen gas. After polymerisation of the first layer, one side of the polymer was immersed in the reaction solution of the intermediate layer. Then it was put in a vacuum oven at 70 °C for 3 hours to synthesise (PNIPAM-PAM).

The third step was the preparation of the bottom imprinted layer. The monomer AM (1.6 g), the cross-linking agent MBA (0.34 g), the initiator (0.075 g) and the complex of metal ions and imprinted substrate $[Ag\ (NP)_2]^+$ (2.25 mmol $AgNO_3$ and 2.25 mmol NP mixed together in 2 mL DMSO for 30 minutes) were dispersed and dissolved in DMSO (10 ml). After deoxygenating with nitrogen gas, part of the intermediate layer was immersed in the solution to form an interpenetrating

network. Then the solution was put in a vacuum oven at 70 °C for 2 hours to fully polymerise (MIP-AgPAM).

After the synthesis of the three-layer polymer reactor, the Ag ions in the MIP-AgPAM layer in the reactor were fully reduced by a large amount of $NaBH_4$ solution (ten times the molar amount of Ag ions). After reduction, it was repeatedly rinsed with plenty of deionised water to remove the unreacted monomer and the excess $NaBH_4$. The last step was to remove the imprinted template by washing it repeatedly (36 hours; changing solution every 12 hours) with 250 mL methanol and acetic acid solution (10:1). The washing process was detected by UV-vis until they were removed completely. At last, a three-layer polymer reactor PRS (switchable polymer reactor) (**Figure 6-1**) was obtained.

To further investigate the controllable catalytic performance of the reactor PRS, two controls, PRO and PRC, were prepared under the same conditions for comparative studies. PRC refers to a control reactor that is always closed ("C"). PRC also has an acidic imprinted top layer and an imprinted bottom layer containing metal nanoparticles, but the middle switch layer is made of hydrophobic monomer styrene. Therefore, it can only be always closed preventing the substrate to pass through it. PRO is a control reactor that is always open ("O"). Like PRC, PRO has the same top and bottom molecularly imprinted layers like PRS while the middle layer is made of hydrophilic monomer acrylamide, which is open all the time. Therefore, the two control reactors can only have an open or closed configuration under different conditions, so that the adjustable catalysis of the switchable reactor PRS can be further studied.

6.3 Tests and characterisation

6.3.1 Structural and morphological tests of the polymer reactor

A series of basic characterisations were used to determine the morphology and structure of the reactor. Firstly, the macroscopic morphology and structure of the samples were recorded using a camera. SEM imaging was used to characterise the basic morphology of the three layers of the polymer and the layer-to-layer

boundary junction. Then FTIR tests were used to confirm the functional groups contained in the polymer and the molecular imprinting process. A sufficiently dried micro sample powder (10 mg) was taken for tests.

The MIP-AgPAM in the polymer reactor contained Ag nanoparticles, so a series of tests were used to determine the existence and type of metal nanoparticles. SEM was used to characterise the dispersion and particle size of the metal particles on the polymer reactor. XRD tests were used to further study the presence and type of metal nanoparticles. The element distribution in the polymer reactor was also characterised by EDS, and the composition of each layer of the reactor was confirmed by comparing the different elements contained in the reactor and the control groups.

6.3.2 Thermo-responsive behaviours

The thermo-response behaviours of the polymer reactor were clarified via different tests. In the experiment, the changing trend of hydrodynamic diameter with temperature was recorded by dynamic light scattering (DLS) to firstly study the optimal ratio of the copolymer in the middle layer. PNPAM-PAM samples with different copolymerisation ratios were dispersed in water with a solid content of 0.5% and then filtered using a syringe filter (Corning; 0.22 μm). After dispersing in water for 10 minutes and reaching an equilibrium state [222], the solution was set to the starting temperature to begin the test, and the test temperature range was between 25 °C and 60 °C.

Differential scanning calorimetry (DSC) was used to further confirm the temperature-sensitive behaviour of different sample ratios and determine the LCST value of different samples. The solid content of the sample in the test was 10% (w/v), the temperature range was also from 25 to 60 °C, and the scan rate was 2 °C /min.

After confirming the optimal ratio, the polymer switchable response was also characterised by DLS. The powders of the middle layer of PRS and the two control groups were used to study the change of particle size with temperature

using DLS. After determining the responsive temperature of the reactor by DLS, the samples were placed in deionised water in temperature lower and higher than the response temperature respectively. Then the morphological changes were observed and recorded with a digital camera.

6.3.3 Self-controlled tandem/simple catalytic tests

A UV spectrophotometer was used to study the time-varying self-controlled catalytic process in the catalytic system of the polymer reactor in a batch system [36, 223]. Firstly, the spectra of the initial substrate NPA (0.25 μmol/mL), the intermediate NP (0.1 μmol/mL) and the final product AP (0.1 μmol/mL) were recorded. In all tests performed with different samples at different temperatures (30 °C and 60 °C), the concentration of the polymer reactor was always maintained at 0.1 mg/mL. To carry out the measurements at a specific temperature, the reaction systems were placed on a constant temperature stirrer to maintain a stable temperature during the tests. The solution in the system was taken and measured every 10 minutes. The total test time of each sample was 90 minutes.

The initial concentration of the substrate NPA was 0.1 μmol/mL (20 mL PBS, pH 7.0). An excessive amount of reducing agent $NaBH_4$ (4 times the NPA concentration) was added to the catalytic system. In order to assess the reproducibility of the experimental results, the final conversion efficiency was the average of three experiments. Moreover, to offset the effects of the self-hydrolysis of NPA, the hydrolysis of NPA was carried out without a catalyst, and then the self-hydrolysis reaction of NPA was subtracted from the catalytic system. Therefore, the final catalytic performance of the polymer reactor could be studied without the influence of self-hydrolysis.

6.4 Results and discussion

6.4.1 The optimised ratio between PNIPAM and PAM

Although the PNIPAM layer has good temperature-sensitive properties, it is important to ensure a good connection among the different polymeric layers during the repeated switching catalytic reactions. Therefore, it is necessary to further improve the adhesion of the intermediate layer to other layers. Thus, AM was introduced to copolymerise with NIPAM. As AM is a hydrophilic monomer without temperature sensitivity, the increase of its content will affect the temperature sensitivity of PNIPAM. Hence, a series of copolymers of AM and NIPAM in different ratios (6:1, 5:1, 4:1, 3:1, 2:1 respectively) were prepared and the temperature-sensitive properties of the copolymer were analysed to find out the optimal copolymerisation ratio.

Firstly, DLS test was used to study the LCST and response sensitivity of different samples. **Table 6-3** demonstrated the LCST of copolymers with different ratios. It is shown that the LCST value of the PNIPAM-PAM copolymer increased from 33 °C to 53 °C with the increase of AM content which was ascribed to the formation of stronger hydrogen bonds between the functional groups of the hydrophilic monomer AM and water molecules [224]. However, when the copolymer ratio increased to 2:1, it did not show obvious LSCT, which meant that the content of AM should be controlled to less than 2:1 to ensure the temperature-sensitive performance of the intermediate layer. In order to analyse the LCST more directly, **Figure 6-3a** presents the DLS graphs of the hydrodynamic diameter (D) of several samples that changed with temperature. **Figure 6-3b** shows the results in a differential form. It can be seen that the LCST of pure PNIAM was at 33°C. As the content of AM increased, the LCST gradually increased while the sensitivity of the temperature response (the size of the phase change peak in Figure 6-3b) decreased. By comparison, it is demonstrated that when the ratio was further increased to 4:1, the sensitivity was significantly reduced. As 5:1 had a higher content of AM and similar temperature-sensitive performance compared to 6:1, 5:1, it was selected as the optimised ratio of the copolymer.

Table 6-3 LCST data of different ratios between PNIPAM and PAM collected by DLS and DSC.

Sample Name (PNIPAM/PAM)	LCST (°C)	
	From DLS curve	From DSC curve
Pure PNIPAM	33	33
6:1	43	42
5:1	47	48
4:1	51	51
3:1	53	54
2:1	N/A	N/A

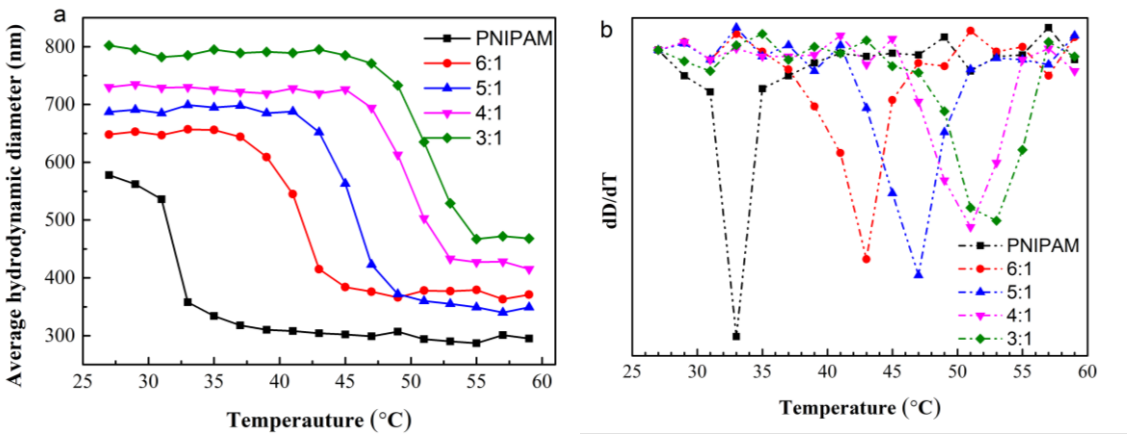

Figure 6-3 DLS spectra of different ratio samples of copolymer PNIPAM-PAM with hydrodynamic diameter changing as a function of temperature (a) Normal; (b) differential.

The temperature sensitivity of the copolymer was further studied by non-isothermal DSC (**Figure 6-4**). The smallest endothermic peak observed in the figure was the phase transition temperature (LCST) of the polymer. It can be seen from **Table 6-3** that the specific value was similar to the DLS result. As shown in Figure 6-4, the temperature sensitivity performance has decreased with the addition of AM. When the molar ratio PNIPAM/PAM reached 4:1 and 3:1, the

temperature sensitivity performance was significantly lower than that of 5:1. As a result, it can be confirmed that 5:1 is the optimal ratio between the two monomers in the copolymerisation. On one hand, the optimal polymerisation ratio was found through the characterisation of the temperature-sensitive properties of copolymers in different proportions. On the other hand, it can be seen that the response temperature of PNIPAM can be adjusted within a specific range (33 °C to 53 °C) by adding a comonomer, which can also provide new ideas for the application of PNIPAM-based temperature-sensitive polymers in a broader temperature range.

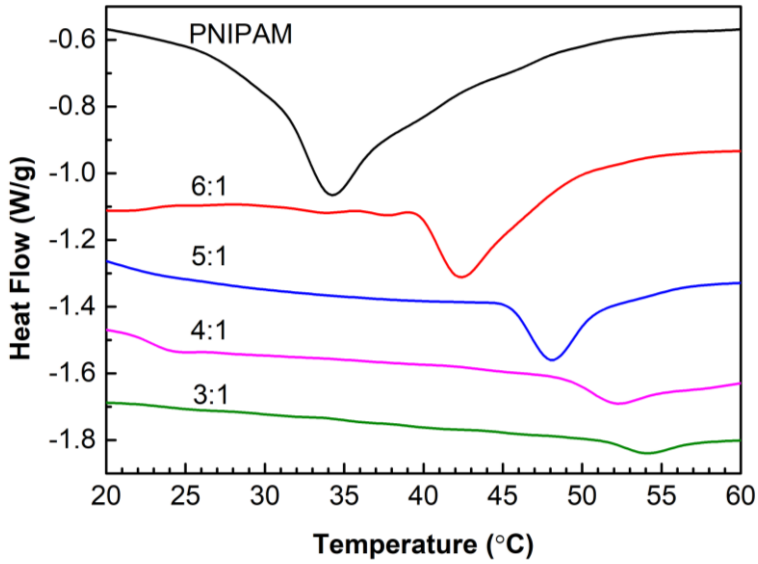

Figure 6-4 Non-isothermal DSC profiles at a heating temperature of 2°C min^{-1}.

6.4.2 The analysis of macro structure and SEM micro morphology

The basic morphology of the three-layer structure of the polymer reactor was observed through macroscopic photographs and microscopic SEM images. In **Figure 6-5** shows that three-layer structure of the polymer reactor PRS was seen clearly using the digital picture. The figure also shows that the presence of the metal nanoparticles in the bottom layer was responsible for its black colour.

Figure 6-6 presents the SEM image of the three layers of the polymer reactor. As shown in Figure 6-6a, the polymer exhibited an obvious three-layer structure and the connection between layers was tight. The boundary images between the two layers were further shown in Figure 6-6b and 6-6c. As shown in the figures, the boundary parts between the first layer and the second layer and between the second layer and the third layer not only exhibited a significantly different double-layer structure but also had a close connection. This was attributed to the formation of the polymer interpenetrating network structure in the double layer during the polymerisation process. The different specific morphologies of the three layers were shown in Figure 6-6d, 6-6e, and 6-6f respectively. It is demonstrated from the figure that the two imprinted layers MIP-PAMPS and MIP-AgPAM exhibited a rougher surface morphology than the middle layer, which was caused by the extensive template washing steps during the preparation processes. At the same time, in the image of the MIP-AgPAM layer (Figure 6-6f), a large number of evenly distributed metal nanoparticles with similar diameters can also be seen, which also proved the existence of nanoparticles in the reactor. Therefore, the macroscopic images and SEM images confirmed that the basic morphology and structure of the polymer reactor were as expected in the experiment.

Figure 6-5 The three-layer structure of polymer reactor PRS

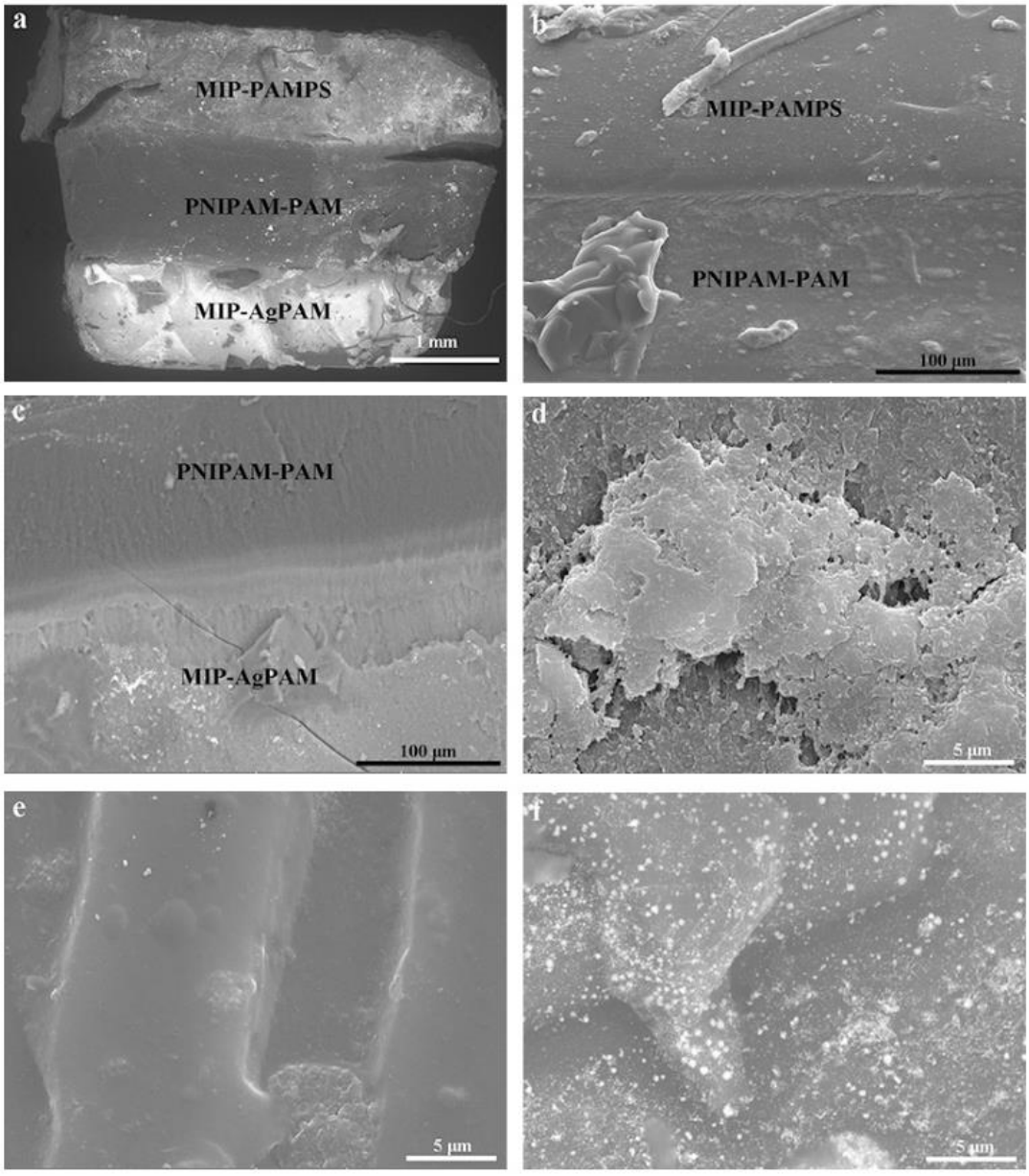

Figure 6-6 SEM images of PRS (a:three-layer structure of PRS; b: the boundary of MIP-PAMPS and PNIPAM-PAM; c: the boundary of PNIPAM-PAM and MIP-AgPAM; d: MIP-PAMPS layer; e: PNIPAM-PAM layer; f: MIP-AgPAM layer).

6.4.3 The analysis of functional groups and molecular imprinting process by FTIR

To study the composition of the three layers of the reactor, FTIR test was first used to analyse the functional groups of the reactor. The three-layer polymer

reactor PRS consisted of molecularly imprinted polymers in the top and bottom layers, and a temperature-sensitive response layer in the middle. From the synthesis process it was known that the top layer was composed of PAMPS, the bottom layer was composed of PAM with Ag nanoparticles, and the middle layer was the copolymer of PNIPAM and PAM. As shown in **Figure 6-7**, the spectra of PRS exhibited four prominent characteristic peaks (respectively at 1000-1200, 1200-1400, 1600-1800 and 2900-3700 cm^{-1}), which resulted from the compositions of the three-layer polymer, specifically the peaks corresponded to the stretching vibration of S=O, C-C/C-N, C=O and O-H/N-H bonds [188]. Figure 6-7 also showed the infrared spectra of each individual layers alone to further illustrate the specific composition of each layer. Compared with the other two layers, the MIP-PAMPS layer showed an extra S-O peak at 1025 cm^{-1}, mainly because of the presence of AMPS. Similarly, the same peak also appeared in the PRS spectrum. In addition, compared with the other two layers, the PNIPAM-PAM layer also showed a characteristic peak of isopropyl at 1370 cm^{-1} [225], confirming the existence of PNIPAM. Through the FTIR spectra of PRS and the three layers separately, it was proven that that the basic structural components of the polymer were as expected.

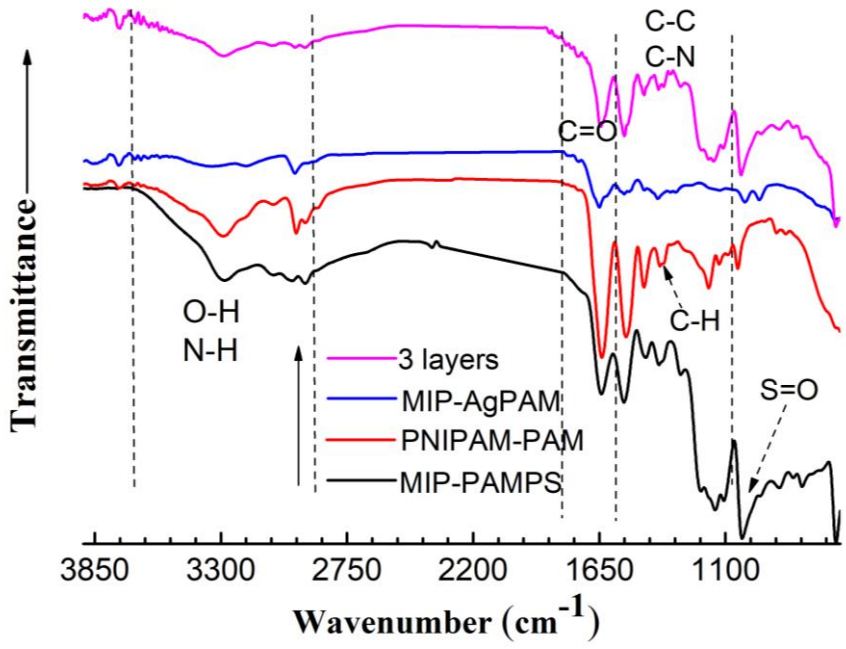

Figure 6-7 FTIR spectra of polymer reactor PRS and three layers respectively.

In addition, the elution processes of the imprinted molecule (the template) of the polymer were characterised by FTIR. As shown in the preparation route shown in Figure 6-1, in the synthesis steps of the imprinted polymer, the precursor containing the imprinted template (the substrate) was synthesised first and then the imprinted template was washed out to free the imprinted cavities. Therefore, in **Figure 6-8**, the two imprinted layers of MIP-PAMPS and MIP-AgPAM were compared with the spectra of their precursors and templates respectively (the unwashed imprinted polymers are identified here as “precursor”). As indicated in Figure 6-8a, the precursor spectrum contained the characteristic peaks of PAMPS and substrate NPA, respectively. As for the final sample MIP-PAMPS, most of the characteristic peaks of the substrate were not observed, confirming the elution process of the imprinted substrate. Similarly, in Figure 6-8b, the precursor showed the characteristic peaks of MIP-AgPAM and the substrate NP, while after the template washing process, the imprinted polymer did not show the characteristic peaks of the substrate. Hence, the FTIR spectra confirmed the imprinted structure of the polymer reactor and the success of the washing steps.

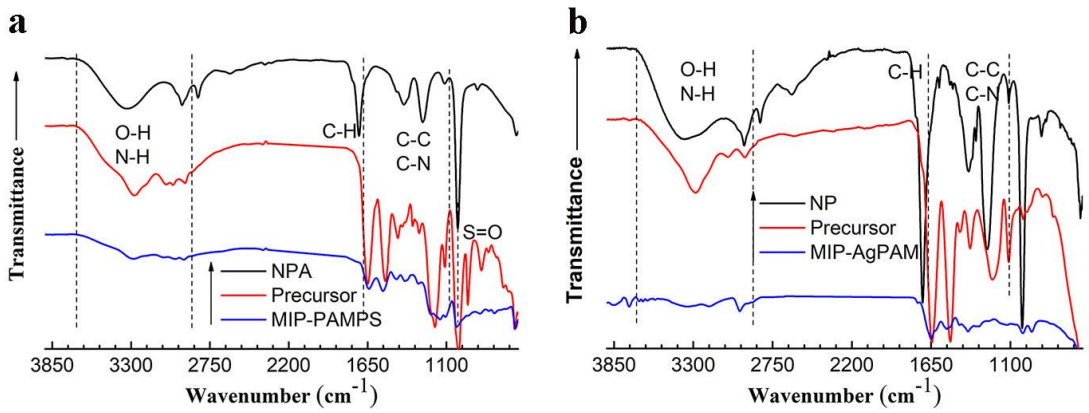

Figure 6-8 Imprinted behaviours of two different molecularly imprinted layers (a: MIP-PAMPS layer; b: MIP-AgPAM layer).

6.4.4 The analysis of metal nanoparticles and elements in the polymer reactor

After studying the specific morphology and structure of the polymer, XRD and EDS tests were used to confirm the types of metal nanoparticles in the reactor and the elemental composition of the reactor. **Figure 6-9** showed the XRD patterns of the reactor PRS and the three layers of it respectively. It can be seen from the different structural components of the three layers that the two layers of MIP-PAMPS and PNIPAM-PAM did not contain metal nanoparticles, while MIP-AgPAM contained Ag nanoparticles. As shown in Figure 6-9, the four samples all exhibited a broad peak band around 22°, which was mainly caused by the amorphous polymer components. In the MIP-AgPAM layer and the three-layer reactor PRS, there were also several sharper peaks appeared at 2θ of 38.7°, 44.4°, 64.4°, 77.5° and 82° respectively. By comparing with the XRD standard pattern, it can be confirmed that these are the characteristic signal peaks of Ag nanoparticles [226, 227].

After confirming the type of metal nanoparticles, the EDS tests were used to characterise the different elemental compositions in each layer of the reactor. As shown in **Figure 6-10**, in the MIP-PAMPS layer, apart from the basic elements of C, N, and O, there was an extra S element as compared to the other two layers. This was because of the presence of S in PAMPS. Compared with the other two layers, MIP-AgPAM additionally contained Ag elements. Combined with the synthesis diagram of the polymer reactor presented in Figure 6-1, it can be stated that the reactor PRS had the expected elements and the metal nanoparticles.

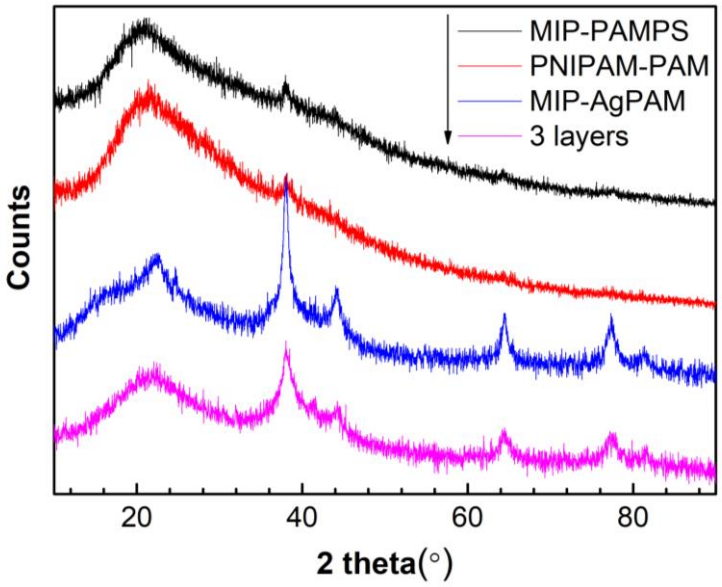

Figure 6-9 XRD spectra of polymer reactor PRS (three layers respectively and together).

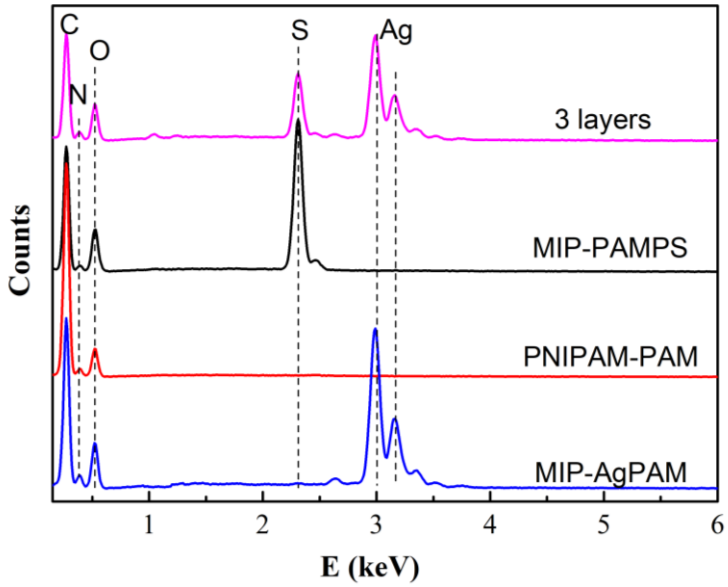

Figure 6-10 EDS spectra of PRS (three layers together and three different respectively).

6.4.5 The analysis of thermo-responsive transition behaviour

In section 6.4.1, the optimal ratio of 5:1 was obtained by analysing the temperature sensitivity of samples with different ratios, thereby preparing the reactor PRS. In this part, DLS was used to compare the PRS and the two control groups PRO and PRC to further explore the controllable temperature-sensitive behaviour of the polymer reactor. Through the preparation process, it is known that the middle layers of the two control groups PRO and PRC were PAM and PS respectively. One was hydrophilic and the other was hydrophobic, so they did not have temperature response properties.

As shown in **Figures 6-11a** and **6-11b**, the changes of the hydrodynamic diameter size (D) of PRC and PRO did not appear to be related to temperature changes. However, the size of polymer reactor PRS had a significant drop when the temperature was at 47 °C. In order to better confirm the LCST, Figure 6-11b shows the differential result of the particle size change. As shown in the figure, the maximum changing point (phase transition point) was at 47 °C, which determined the response temperature of the reactor. When the temperature was lower than 47°C, the reactor exhibited particles with a higher hydrodynamic diameter size. This was because the PNIPAM-PAM copolymer was in a hydrophilic state in this condition, so the reaction channel of the reactor was opened to allow the reactants to pass through. When the temperature was higher than 47°C, the particle size was relatively smaller due to the hydrophobic state of PNIPAM-PAM layer, closing the reaction channel and preventing the reactants. The three-layer polymer can achieve controllable tandem catalysis at different temperatures through the opening and closing switching performance.

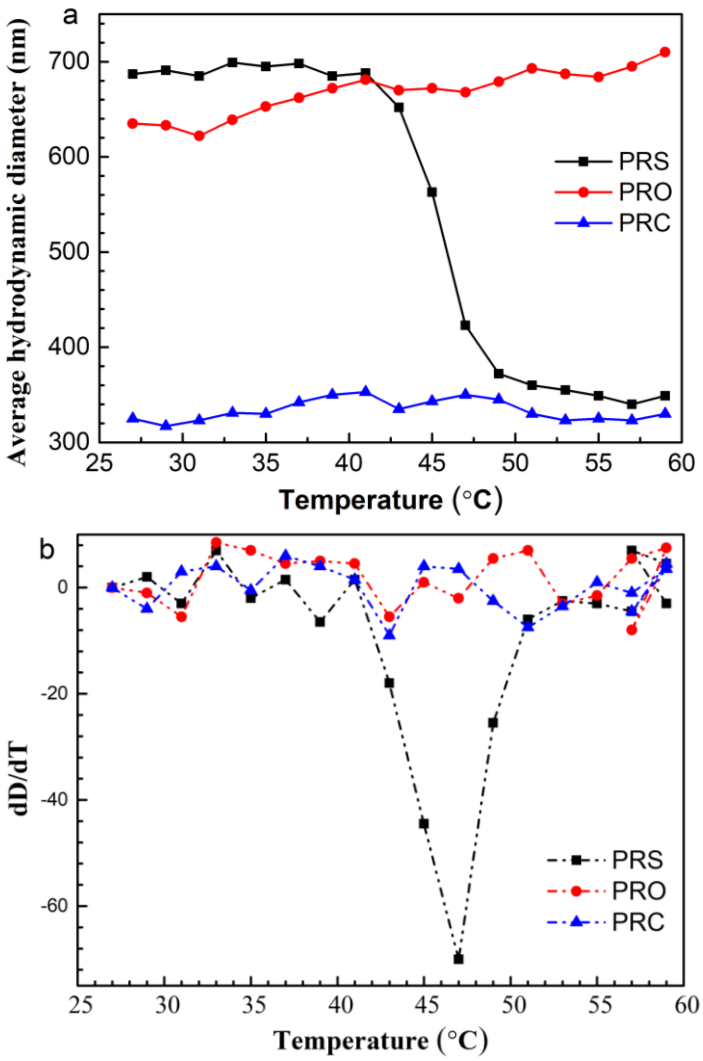

Figure 6-11 DLS spectra of three different polymer reactors with hydrodynamic diameter changing as a function of temperature (a) Normal; (b) differential.

After confirming the temperature-sensitive switching performance of PRS, the morphological changes of PRS at different temperatures were further observed. According to the response temperature of 47 °C, two temperatures, 30 °C (below 47 °C) and 60 °C (above 47 °C), were selected respectively. As shown in **Figure 6-12**, the middle layer of PRS underwent changes from transparent to opaque below and above the phase transition temperature [98]. Figure 6-12a and 6-12b showed the morphological changes of PRS. At 30 °C, it can be seen that the middle layer was transparent (hydrophilic), so the polymer reaction channel was open. As the temperature increased to 60 °C, the middle layer gradually became

opaque (hydrophobic) and the reaction channel was closed. To further understand the changing process of the middle layer, **Figure 6-13a** and **6-13b** show the specific changes of the middle layer from low temperature to high temperature. The changing processes were consistent with the temperature response behaviour studied by DLS.

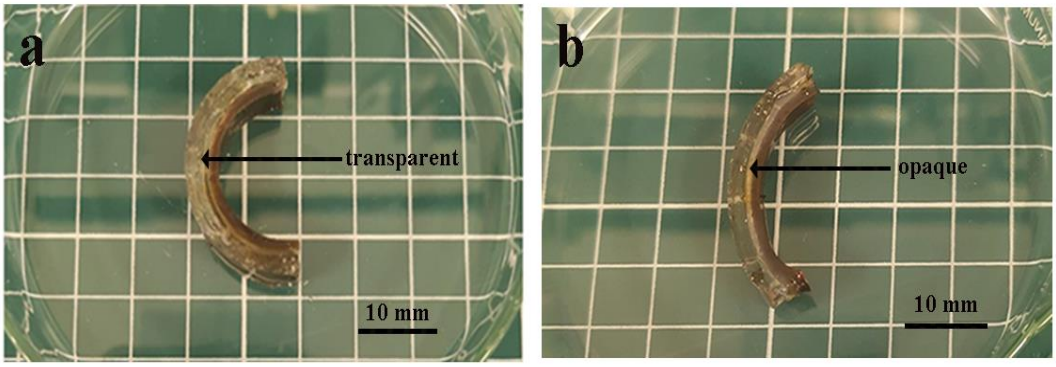

Figure 6-12 Digital images of polymer reactor PRS at different temperatures (a 30 °C; b 60 °C)

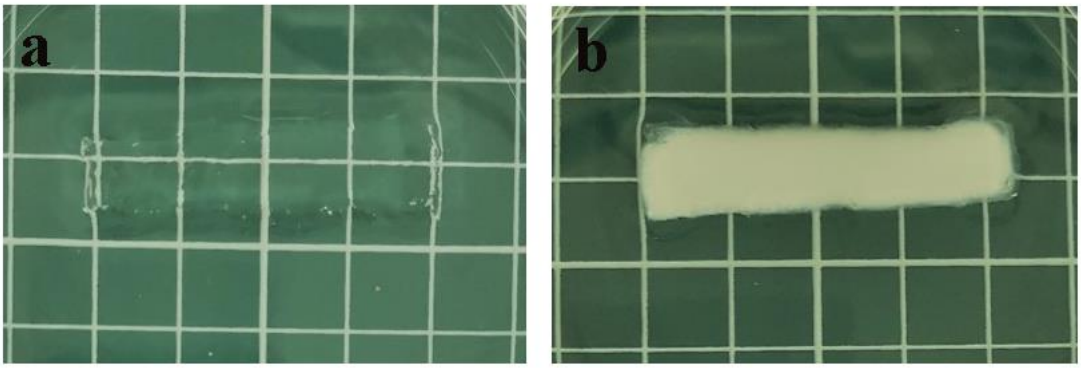

Figure 6-13 Digital images of PNIPAM-PAM layer at different temperatures (a 30 °C; b 60 °C)

6.4.6 The analysis of self-controlled catalytic processes in different temperatures

In order to study the specific tandem catalytic behaviours of polymer reactors, the reaction processes of the initial substrate NPA were recorded by UV spectrophotometer at different temperatures. To better study the catalytic process, firstly, the spectra of the initial substrate NPA (peak at 270 nm), the intermediate product NP (peak at 400 nm) and the final product 4-aminophenol (AP: peak at 295 nm) were obtained by UV as references (**Figure 6-14a**, **6-14b** and **6-14c**). In the discussion of temperature sensitivity in section 6.4.5, the LCST was determined at 47 °C, so a low temperature of 30 °C and a high temperature of 60 °C were selected as examples to compare and study the catalytic reaction process under different temperature conditions.

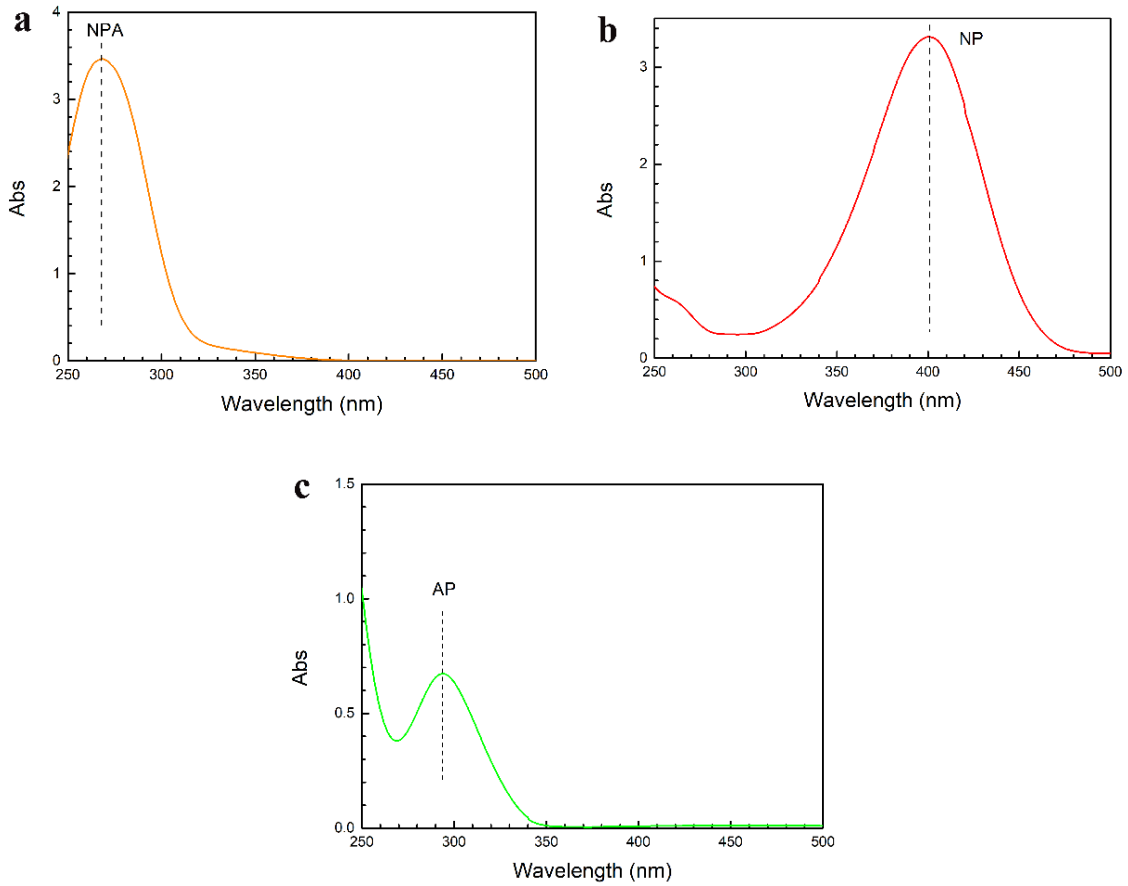

Figure 6-14 UV spectra of the initial substrate, intermediate product and final product (a 4-nitrophenol acetate; b 4-nitrophenol; c 4-aminophenol)

For the two control groups PRC and PRO without a temperature response layer, the reactors showed similar catalytic spectra at low and high temperatures respectively. As shown in **Figure 6-15a**, for the control reactor PRC, at 30 °C, the peak at 271 nm (NPA) dropped while the peak at 400 nm (NP) rose accordingly. It can be inferred that the NPA has experienced a hydrolysis process and converted to NP. As the temperature rose to 60 °C (**Figure 6-15b**), although the conversion rate of NPA increased, the whole process was still a single-step hydrolytic reaction, which was due to the closed channel of the middle layer of PRC, blocking the entry of intermediate products. As for the other control group PRO, it showed a more complicated reaction process. At 30 °C (**Figure 6-15c**), the initial product NPA at 270 nm decreased, the intermediate product NP (400 nm) first increased and then decreased, and the final product AP (295 nm) finally increased, which indicated the entire tandem catalytic process from hydrolysis to reduction. When the temperature rose to 60 °C, PRO can still achieve a similar tandem catalytic process (**Figure 6-15d**). This was because the middle layer of PAM was kept open due to its hydrophilicity, so the reactants could pass through freely, conducting tandem catalysis. It can perform tandem reactions, but cannot self-regulate the reaction process.

Both control groups only achieved single-step reactions or tandem reactions at two temperatures, but they did not permit the control of the reaction process at different temperatures. As for the polymer reactor PRS, at 30 °C (**Figure 6-15e**), the decrease of the initial substrate NPA (270 nm) leads to the increase of the final product AP (295 nm). The reaction process showed a similar spectrum to the control group PRO, demonstrating that PRS could complete the tandem catalytic process at this temperature. However, at 60 °C (**Figure 6-15f**), PRS showed a single-step hydrolysis reaction process similarly to PRC. Therefore, PRS achieved the catalytic process from the complex tandem reactions to the simple hydrolytic reactions from low to high temperature, completing the controllable tandem reactions.

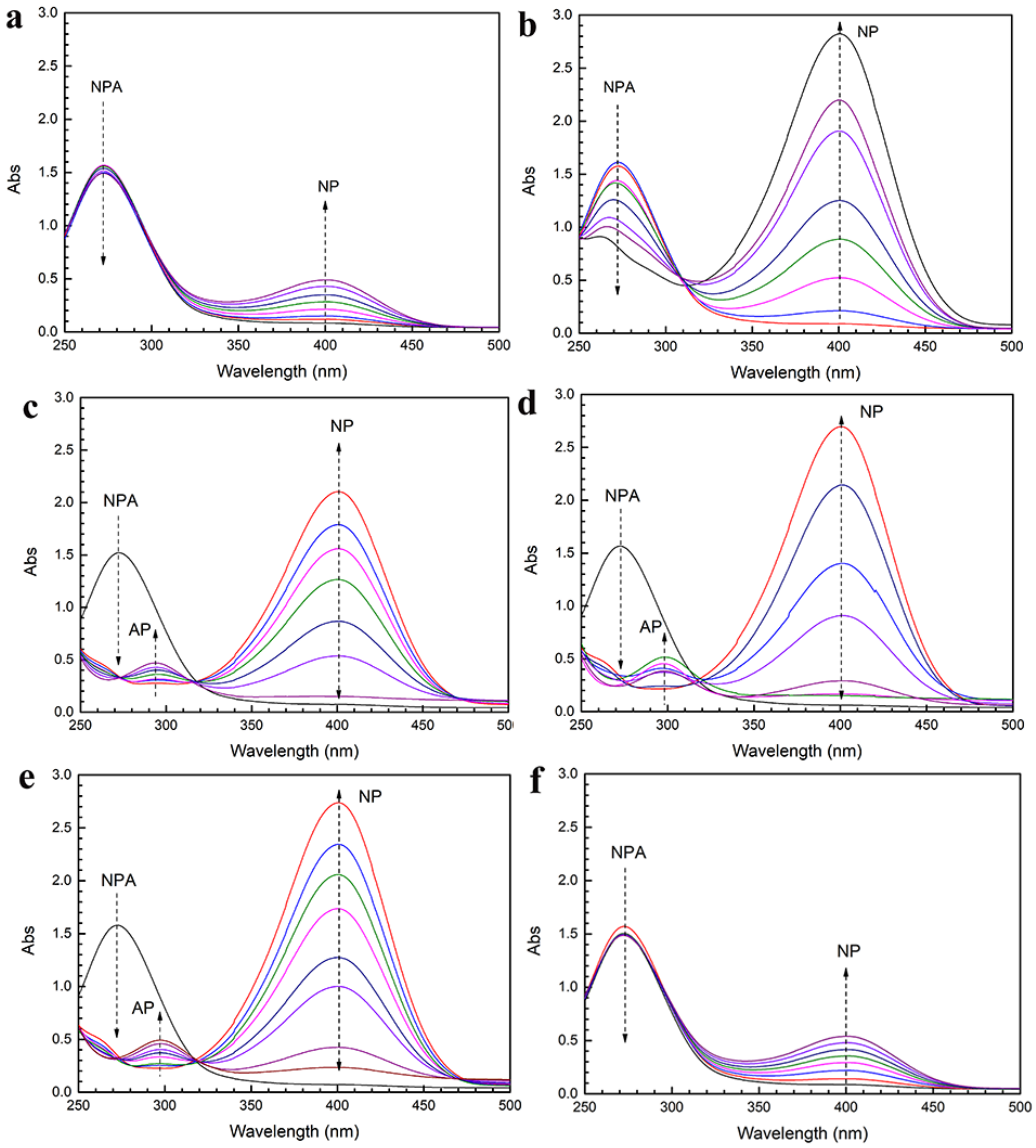

Figure 6-15 UV spectra of PRS and two controls in different temperatures (a PRC in 30°C; b PRC in 60°C; c PRO in 30°C; d PRO in 60°C; e PRS in 30°C; f PRS in 60°C)

Figure 6-16 demonstrated the changing efficiency during the repeated switching processes of the PRS. It is demonstrated from the figure that the polymer reactor maintained good catalytic efficiency (conversion rate of intermediate product NP) after several cycles from tandem reaction to single-step reactions. As the copolymerisation between PNIPAM and PAM with an optimal ratio improved the adhesion among the different layers, the three-layer polymer reactor kept a good

connection during repeated switching catalysis. In this way, PRS can repeatedly complete the controllable catalytic process from tandem reaction to simple reaction in water phase conditions with high catalytic efficiency.

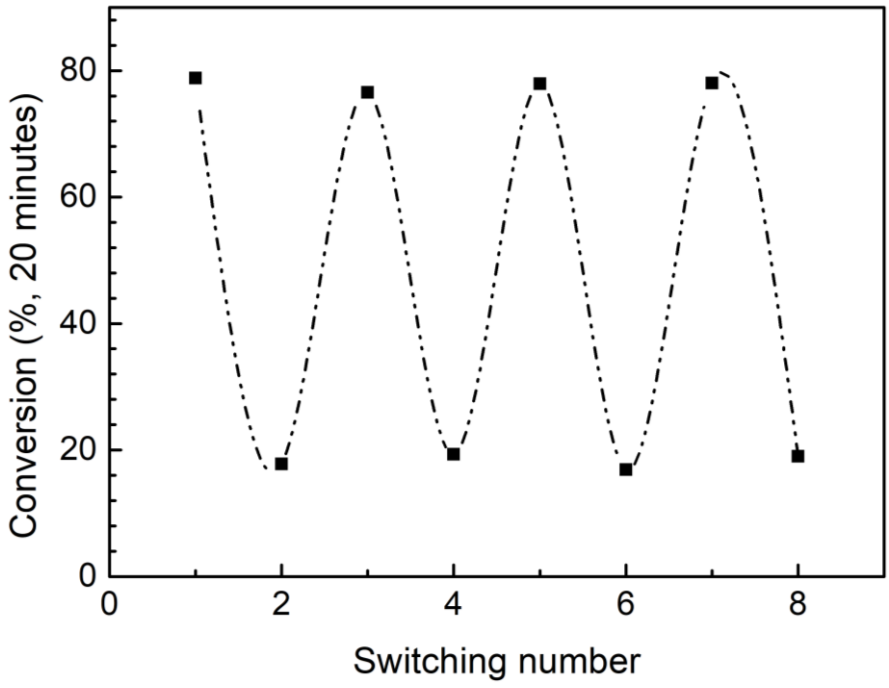

Figure 6-16 Repeating switchable performance of polymer reactor PRS

6.5 Conclusion

In the experiment described in this chapter, a self-controlled catalytic polymer reactor PRS was prepared. The reactor was made up of two molecularly imprinted polymer layers and a middle temperature-responsive layer. The top and bottom layers of molecularly imprinted polymers contained two different catalytical active sites respectively to ensure the two consecutive steps in tandem catalysis to be carried out without interference. Also, the molecularly imprinted properties of the polymer improved the selectivity of the reactions. The middle controllable layer was composed of PNIPAM and PAM, which can control the tandem or single-step reaction process according to different temperatures. When the temperature was lower than the LCST of the copolymer (< 47 °C), the

middle layer opened to allow the reactants to pass through, and then the tandem catalysis from hydrolysis to reduction could be carried out. When the temperature increased to above the LCST (> 47 °C), the middle layer was closed, inhibiting the entry of intermediates, so only the hydrolysis reaction could proceed. As a result, PRS permitted a controllable catalytic process. In addition, by adding an appropriate proportion of copolymer acrylamide (AM), the adhesion of the intermediate layer was significantly improved. While ensuring good temperature response characteristics, the high-efficiency catalysis process of repeated switching could be stably performed. The preparation of this new type of polymer reactor is able to realize the interference-free smart catalytic process. Meanwhile, by tailoring the composition of the middle smart layer, the potential for practical applications of functional catalysts in broader temperature ranges was demonstrated.

Chapter 7 Conclusion and future work

7.1 Conclusion

7.1.1 Conclusion and comparison

Tandem catalysis enables the multi-step reactions to be carried out in sequence, improving the reaction efficiency as well as the utilisation of raw materials, optimising the whole reaction process. However, given the multiple active sites involved in the reaction and the complex reaction process, the separation of active catalytic sites and the control over the processes are two major challenges in tandem catalysis. Aiming at addressing these two challenges, inspired by the biological system, several novel polymer reactors were proposed to obtain an interference-free smart tandem processes by combining a series of biomimetic polymers and active sites.

First of all, the catalytic process with site separation properties was achieved by an enzyme-like molecularly imprinted polymer reactor MIP-Au-NP-BNPC. The reactor was composed of functionally imprinted polymer PAMPS with Au nanoparticles encapsulated in it, containing both acidic sites and metal nanoparticle catalytic sites, which was able to carry out a tandem process from hydrolysis to reduction. At the same time, the polymer was imprinted with two template substrates: BNPC and NP. NP was the reduction product of BNPC. Due to the polymer recognition for the template, the reactor could selectively react with the substrate step by step, ensuring the tandem reactions in the desired direction. Several different tests were used to study the composition and catalytic properties of MIP-Au-NP-BNPC. FTIR, TEM, SPR and EDS tests were conducted to confirm the structure and composition of the reactor, as well as the existence and distribution of metal nanoparticles. SEM, BET and TPD tests were used to investigate the molecularly imprinted morphologies, pore size and the interactions between the sample and the substrate, clarifying the recognition to the two substrates BNPC and NP. Electrochemical tests were used to further confirm that there were strong interactions between the imprinted area and the

substrates. Then UV catalytic tests proved that MIP-Au-NP-BNPC was able to complete the whole tandem catalysis and it also achieved high efficiency and selectivity toward substrates. It was demonstrated from the tests that the reactor MIP-Au-NP-BNPC permitted to obtain the site separation and to improve the efficiency of the tandem reactions.

In subsequent experiment, it was demonstrated that the site separation could be achieved through a core-shell nanoreactor AMPS@AM-Ag. The core layer of the reactor was PAMPS containing acid sites, and the shell layer was PAM containing Ag nanoparticles. Due to the influence of mass transfer and the radial distribution of active sites, the reactor could perform sequential and interference-free tandem catalytic processes. In the experiment, the polymer composition of PAM/PAMPS was confirmed through FTIR tests. Then TEM, SEM and DLS tests proved that the reactor was a core-shell nanoreactor with a particle size of about 100nm, and it showed a narrow particle size distribution range and good dispersibility. SPR, EDS and XRD tests confirmed the existence of Ag nanoparticles. Finally, the tandem process of DNPO catalysed by AMPS@AM-Ag was recorded through the UV/vis spectroscopy, in which AMPS@AM-Ag completed the tandem processes successfully. At the same time, the interactions between the nanoreactor and the substrate were analysed through electrochemical tests. Combined with mass transfer and kinetic analysis, it was confirmed that the tandem process had spatiotemporal effects and could proceed without interference.

The above reactors permitted the separation of the catalytic sites and interference-free tandem reactions. Based on these results, the following experiments further achieved the smart control of the reaction process by introducing smart polymers to the system. The third reactor was a mussel-inspired three-layer smart polymer reactor MIP-AgPRS. The top and bottom layers of the reactor were made up of two molecularly imprinted polymers containing different catalytic sites to obtain the tandem catalysis. The middle layer was the switchable layer PDPA-PAM, which controlled the simple/tandem reaction process through the self-healing behaviours. A series of tests such as

FTIR, SEM, TEM confirmed the three-layer macro morphology, molecular imprinting basic structure, and encapsulated Ag nanoparticles inside MIP-AgPRS. Then the responsive temperature of the middle layer was obtained at 38 °C through the DLS tests by studying the changing particle size of the reactor with temperatures. Based on the responsive temperature, two different representative temperatures, 25 °C and 50 °C, were chosen to study the different catalytic behaviours to varying conditions by UV tests. It was demonstrated that MIP-AgPRS could only catalyse the simple hydrolysis reaction in low temperatures and it could complete the tandem reactions from hydrolysis to reduction in high temperatures. At the same time, electrochemical tests confirmed that there were different interactions between the reactor and the substrate at different response temperatures, proving the self-controlled abilities of the reactor.

The fourth experiment introduced two temperature-sensitive polymer layers as carriers for different catalytic sites to precisely control of the tandem reaction process. A double-layer polymer reactor DPR with dual-responsive abilities was synthesised for the experiments. The first layer of DPR was composed of the copolymer PAMPS-PAM. Due to the weaker hydrogen bonding between the two polymers, this switchable layer could respond to a moderate temperature. Another layer of DPR consisted of a copolymer PVI-PTFMA with Au nanoparticles, which had a stronger electrostatic force and responded to higher temperatures. In the experiment, the optimal ratio of the two monomers (PAM/PAMPS: 1.24/1; PVI/PTFMA: 1.12/1) was first confirmed through the UV titration process to achieve the optimal switchable response. Then a series of tests such as FTIR, SEM, TEM proved that the reactor morphology, structure and composition were as expected. The temperature-sensitive processes of different layers were recorded respectively and two response temperatures, 37 °C and 50 °C, were obtained through the DLS tests. Based on these two response temperatures, three representative temperatures, 30 °C, 45 °C and 60 °C, were chosen to observe the catalysis of the reactor. From the results of the UV tests, at low temperatures, the reactor had no obvious catalytic effect. At medium temperatures, the catalytic hydrolysis process could be conducted because of the opening of the PAMPS-PAM layer. At high temperatures, since both the PAMPS-

PAM and PVI-PTFMA-Au layers were opened, the tandem performance from hydrolysis to reduction was completed. In this way, the polymer reactor DPR was able to perform different catalytic behaviours at different temperatures, achieving the smart controlled processes.

The last experiment was a three-layer smart reactor PRS with self-controlled tandem/non-tandem catalytic abilities. Based on the previous three-layer polymer reactor MIP-AgPRS, PRS reactor was mainly prepared with different compositions of the middle switchable layer, changing the response mechanism and optimising the temperature sensitive abilities. The top and bottom layers of the reactor were molecularly imprinted polymers containing different catalytic sites and the middle layer was the copolymer PNIPAM-PAM. PNIPAM had a mild response temperature and an efficient response speed, acting as the switch of the catalytic reaction through the transition from hydrophilic to hydrophobic. The introduction of AM enhanced the mechanical strength and affinity of PNIPAM, enabling it to connect different layers more closely and achieving more stable repeated switching effects. In the experiment, several samples of PNIPAM-PAM with different ratios were polymerised to study the effects of different contents of PAM on the LCST of PNIPAM and the response sensitivity. The higher content of PAM increased the LCST and affected the temperature sensitivity of PNIPAM. Through DLS and DSC tests for the thermal properties, it was finally determined that 5:1 was the optimal ratio of the copolymer. The morphology and structure of the reactor were characterised by tests such as FTIR, SEM, EDS, and the response temperature of the reactor was obtained by DLS at 47 °C. Based on the thermal behaviour of the reactor, two temperatures, 30 °C and 60 °C, were chosen as examples to characterise the catalytic performance of PRS. As shown in UV tests, at 30 °C, the reactor could complete the tandem reactions from hydrolysis to reduction; at 60 °C, due to the phase change behaviour of the PNIPAM-PAM layer from hydrophilic to hydrophobic, only a single-step reaction could be conducted. In this way, PRS could achieve the self-controlled processes from tandem reactions to simple reactions. In addition, the catalytic conversion rate of the reactor has been maintained at a high level during the repeated switching tests, which meant the reactor allow a stable switching control

behaviour. At the same time, the investigation of the LCST for copolymers prepared with different monomers' molar ratio has also broadened the practical temperature ranges of the reactor.

In this research, several novel polymer reactors were proposed as the tandem catalysts. Firstly, the dual-template imprinted polymers and core-shell nanoreactor were used as the carriers of the active sites to reach the site separation of the tandem catalysis. Then several smart polymers were introduced as the self-controlled switch of the tandem catalysis, achieving the tandem/simple reactions at different temperatures. The research provides new ideas for the development of the catalysts used in multi-step complex reactions, so that tandem reactions can be carried out more concisely and efficiently. Moreover, it discussed different kinds of temperature-responsive polymers, inspiring the future development of functional polymers.

7.1.2 Comparison of different reactors

Among these reactors, the first reactor MIP-Au-NP-BNPC was able to solve the challenge of site separation by a dual-template imprinted polymer. It allows reactions to proceed one by one and also achieves selective catalysis toward specific substrates. The second reactor AMPS@AM-Ag can also separate the different active sites via the core-shell structure. The core-shell structure promotes the tandem catalysis in the desired direction. However, both reactors cannot reach smart control over the catalytic processes.

The double-layer reactor DPR was prepared based on the reactor AMPS@AM-Ag. Similar to AMPS@AM-Ag, it separates two different catalytic sites in two layers, but the layers are replaced with two temperature-responsive polymers. In this way, the reactor can also perform different catalysis from low to high temperatures as well as site separation.

As for the reactor MIP-AgPRS and PRS, both of them are prepared based on the first reactor MIP-Au-NP-BNPC but in addition they contained smart polymers as switches to control the catalytic processes. As a result, except for the selective tandem catalytic properties, they are also able to achieve the controllable

simple/tandem reactions in different conditions. The differences between the two reactors lie in the type of smart polymer in the middle layer. MIP-AgRPS contains the copolymer of PDPA and PAM with the UCST, which changes from the closed state to open state with the increasing temperature. However, PRS contains the copolymer of PNIPAM and PAM with LCST in the middle layer. It performs the opposite switchable behaviours from opening to closing as the temperature rises. Meanwhile, the changing temperature ranges and the sensitivity of the phase transition performances are also discussed. The last three reactors are designed based on the first two reactors to achieve successful smart tandem catalysis without interference.

7.2 Future work

In this research, several novel tandem catalytic reactors were prepared. On one hand, all of them allow the separation of catalytic sites, so that the catalyst could complete the continuous reaction efficiently, increasing the overall catalytic efficiency. On the other hand, some of them can also achieve a smart control of the catalytic process, improving the environmental adaptability of the reactors as well as broadening their application areas. Nevertheless, further improvement of this research work can have two directions:

The first one is the adjustment of the active sites. By changing the catalytic sites, such as using different types of metal nanoparticles or bimetallic systems, the efficiency of the catalytic reaction can be improved as much as possible for the same catalytic reactor. In addition, the reduction process of metal nanoparticles could be adjusted to improve the dispersion and particle size of metal nanoparticles by changing the reductive conditions such as the type of the reducing agents, the reducing time and stirring speed. Single variable method will be used to compare the effects of different conditions, so as to optimise the catalytic efficiency of the catalyst as much as possible.

The second one is the structural adjustment of the polymer reactor. For example, based on the core-shell nanoreactor AMPS@AM-Ag (Chapter 3), a novel smart

core-shell nanoreactor can be prepared by combining it with the smart carriers to enable self-controlled properties. Moreover, the structure of the multi-layer polymer reactor (Chapter 4, Chapter 5 and Chapter 6) can be adjusted to the multiple shell sphere or yolk-shell structure, etc. In this way, the catalytic reactions can be conducted in the desired directions, and the catalytic efficiency can also be improved owing to the increase of the specific surface area.

REFERENCES

[1] J. C. Wasilke, S. J. Obrey, R. T. Baker, G. C. Bazan, Concurrent tandem catalysis, Chemical Reviews, 2005, 105, 1001-1020.

[2] N. Shindoh, Y. Takemoto, K. Takasu, Auto-tandem catalysis: A single catalyst activating mechanistically distinct reactions in a single reactor, Chemistry A European Journal, 2009, 15, 12168-12179

[3] J. M. Lee, Y. Na, H. Han, S. Chang, Cooperative multi-catalyst systems for one-pot organic transformations, Chemical Society Reviews, 2004, 33, 302-312.

[4] S. T. Scroggins, Y. Chi, J. M. J. Fréchet, Polarity-directed one-pot asymmetric cascade reactions mediated by two catalysts in an aqueous buffer, Angewandte Chemie International Edition, 2009, 49, 2393-2396.

[5] Kanwal, A. Mujahid, N. Rasool, K. Rizwan, A. Malik, G. Ahmad, S.A.A. Shah, U. Rashid, N.M. Nasir, Palladium and copper catalyzed sonogashira cross coupling an excellent methodology for C-C bond formation over 17 years: A review. Catalysts, 2020, 10, 443.

[6] S. Cacchi, G. Fabrizi, A. Goggiomani, Palladium catalysis in the construction of the benzo[b]furan and furan rings from alkynes and organic halides or triflates, Heterocycles, 2002, 56, 613-632.

[7] J.-Q. Chen, J.-H. Li, Z.-B. Dong, A review on the latest progress of Chan-Lam coupling reaction, Advanced Synthesis Catalysis, 2020, 362, 3311-3331.

[8] H. E. Ho, T. C. Stephens, T. J. Payne, P. O'Brien, R. J. K. Taylor, W. P. Unsworth, Merging π-acid and Pd catalysis: Dearomatizing spirocyclization/cross-coupling cascade reactions of alkyne-tethered aromatics, ACS Catalysis, 2019, 9, 504-510.

[9] Arjona, A.G. Csάky, J. Plumet, Sequential metathesis in oxa- and azanorbornene derivatives, European Journal of Organic Chemistry, 2003, 611-622.

[10] B. Breit, Synthetic aspects of stereoselective hydroformylation, Accounts of Chemical Research, 2003, 36, 264-275.

[11] M. Vilches-Herrera, L. Domke, A. Börner, Isomerization-hydroformylation Tandem Reactions. ACS Catalysis, 2014, 4, 1706-1724.

[12] Z.-Q. Wu, W.-Z. Jia, K. Wang, J.-J. Xu, H.-Y. Chen, X.-H. Xia, Exploration of two-enzyme coupled catalysis system using scanning electrochemical microscopy, Analytical Chemistry, 2012, 84, 10586-10592

[13] S.F. Mayer, W. Kroutil, K. Faber, Enzyme-initiated domino (cascade) reactions, Chemical Society Reviews, 2001, 30, 332-339.

[14] S. I. Ikeda, Nickel-catalyzed intermolecular domino reactions, Accounts of Chemical Research, 2000, 33, 511-519.

[15] U. Díaz, D. Brunel, A. Corma, Catalysis using multifunctional organosiliceous hybrid materials, Chemical Society Reviews, 2013, 42, 4083-4097.

[16] M. Shibasaki, N. Yoshikawa, Lanthanide complexes in multifunctional asymmetric catalysis, Chemical Reviews, 2002, 102, 2187-2210.

[17] F. Alonso, F. Foubelo, J. C. González-Gómez, R. Martínez, D. J. Ramón, P. Riente, M. Yus, Efficiency in chemistry: from hydrogen autotransfer to multicomponent catalysis, Molecular Diversity, 2010, 14, 411-424.

[18] D. Yu, J. Wang, M. T. Reetz, Exploiting designed oxidase-peroxygenase mutual benefit system for asymmetric cascade reactions, Journal of the American Chemical Society, 141, 2019, 5655-5658.

[19] L. Lu, J. Chen, W. Xiao, Development of cascade reactions for the concise construction of diverse heterocyclic architectures, Accounts of Chemical Research, 2012, 45, 1278-1293.

[20] A.J. McCarroll, J.C. Walton, Programming organic molecules: Design and management of organic syntheses through free‐radical cascade processes, Angewandte Chemie International Edition, 2001, 40, 2224-2248.

[21] L. F. Tietze, Domino reactions in organic synthesis, Chemical Reviews, 1996, 96, 115-136.

[22] J. F. Rodríguez, K. I. Burton, I. Franzoni, D. A. Petrone, I. Scheipers, M. Lautens, Palladium-catalyzed hydride addition/C–H bond activation cascade: Cycloisomerization of 1,6-Diynes, Organic Letters, 2018, 20, 6915-6919.

[23] S.U. Son, K.H. Park, Y.K. Chung, Sequential actions of cobalt nanoparticles and palladium (II) catalysts: Three-step one-pot synthesis of fenestranes from an enyne and an alkyne diester, Journal of the American Chemical Society, 2002, 124, 6838-6839.

[24] B. Cornils, in: B. Cornils, W.A. Herrmann, R. Schlögl, C.-H. Wong, Catalysis from A to Z: A concise encyclopedia, Wiley, Toronto, 2000.

[25] S. A. Jagtap, S. P. Gowalkar, E. Monflier, A. Ponchel, B. M. Bhanage, Rhodium catalyzed selective hydroaminomethylation of biorenewable eugenol under aqueous biphasic condition, Molecular Catalysis, 2018, 452, 108-116.

[26] A.N. Thadani, V.H. Rawal, Multifunctional palladium catalysis. 2. tandem haloallylation followed by Wacker-Tsuji oxidation or sonogashira cross-coupling, Organic Letters, 2002, 4, 4321-4323.

[27] T. Ohmura, K. Yagi, S. Kusaka, M. Suginome, Tandem C-H transformations by a single iridium catalyst: Direct access to indoles and indolines from o-Alkyl-N-methylanilines. ACS Catalysis 2020, 10, 3152-3157.

[28] D. C. Leith, J. A. Labinger, J. E. Bercaw, Scope and mechanism of homogeneous tantalum/iridium tandem catalytic alkane/alkene upgrading using sacrificial hydrogen acceptors. Organometallics, 2014, 33, 3353-3365.

[29] D. C. Leitch, Y. C. Lam, J. A. Labinger, J. E. Bercaw, Upgrading light hydrocarbons via tandem catalysis: a dual homogeneous Ta/Ir system for alkane/alkene coupling, Journal of the American Chemical Society, 2013, 135, 10302-10305.

[30] T. L. Lohr, T. J. Marks, Orthogonal tandem catalysis, Nature Chemistry, 2015, 7, 477-608.

[31] A. Behr, A. J. Vorholt, K. A. Ostrowski, T. Seidensticker, Towards resource efficient chemistry: tandem reactions with renewables, Green Chemistry, 2014, 16, 982-1006.

[32] M. J. Climent, A. Corma, S. Iborra, M. J. Sabater, Heterogeneous catalysis for tandem reactions, ACS Catalysis, 2014, 4, 870-891.

[33] A. Schejn, A. Aboulaich, L. Balan, V. Falk, J. Lalevée, G. Medjahdi, L. Aranda, K. Mozet, R. Schneider, Cu^{2+}-doped zeolitic imidazolate frameworks (ZIF-8): efficient and stable catalysts for cycloadditions and condensation reactions, Catalysis Science & Technology, 2015, 5, 1829-1839.

[34] P. V. Dau, S. M. Cohen, A bifunctional, site-isolated metal-organic framework-based tandem catalyst, Inorganic Chemistry, 2015, 54, 3134-3138.

[35] L. M. Aguirre-Díaz, F. Gάndara, M. Iglesias, N. Snejko, E. Gutiérrez-Puebla, M.Á. Monge, Tunable catalytic activity of solid solution metal-organic frameworks in one-pot multicomponent reactions, Journal of the American Chemical Society, 2015, 137, 6132-6135.

[36] W. Wei, T. Zhou, S. Wu, X. Shen, M. Zhu, S. Li, An enzyme-like imprinted-polymer reactor with segregated quantum confinements for a tandem catalyst, RSC Advances, 2018, 8, 1610-1620.

[37] N. Xue, G. Zhang, X. Zhang, H. Yang, A reinforced Pickering emulsion for cascade reactions, Chemical Communication, 2018, 54, 13014-13017.

[38] H. Yang, L. Fu, L. Wei, J. Liang, B.P. Binks, Compartmentalization of incompatible reagents within Pickering emulsion droplets for one-pot cascade reactions, Journal of the American Chemical Society, 2015, 137, 1362-1371.

[39] M. Massaro, V. Schembri, V. Campisciano, G. Cavallaro, G. Lazzara, S. Milioto, R. Noto, F. Parisib, S. Riela, Design of PNIPAAM covalently grafted on halloysite nanotubes as a support for metal-based catalysts, RSC Advances, 2016, 6, 55312-55318.

[40] Y. B. Huang, J. Liang, X. S. Wang, R. Cao, Multifunctional metal-organic framework catalysts: synergistic catalysis and tandem reactions, Chemical Society Reviews, 2017, 46, 126-157.

[41] Z. Chen, Z.M. Cui, C.Y. Cao, W.D. He,L. Jiang, W.G. Song. L Jiang. Temperature-responsive smart nanoreactors: poly(N-isopropylacrylamide)-coated Au@mesoporous-SiO2 hollow nanospheres, Langmuir, 2012, 28, 13452-13458.

[42] S. Li, Y. Ge, A. Tiwari, S. Cao. A temperature-responsive nanoreactor, Small, 2010, 6, 2453-2459.

[43] J. Su, C. Xie, C. Chen, Y. Yu, G. Kennedy, G.A. Somorjai, P. Yang, Insights into the mechanism of tandem alkene hydroformylation over a nanostructured

catalyst with multiple interfaces, Journal of the American Chemical Society, 2016, 138, 11568-11574.

[44] H. Guo, J. Ma, Catalytic asymmetric tandem transformations triggered by conjugate additions, Angewandte Chemi International Edition, 2006, 45, 354-366.

[45] D. J. Ramón, M. Yus, Asymmetric multicomponent reactions (AMCRs): The new frontier, Angewandte Chemi International Edition, 2005, 44, 1602-1634.

[46] J. Zhu, Q. Wang, M. Wang, Multicomponent reactions in organic synthesis, Wiley-VCH, Weinheim, 2015.

[47] X. Yu, W. Wang, Organocatalysis: asymmetric cascade reactions catalyzed by chiral secondary Amines, Organic & Biomolecular Chemistry, 2008, 6, 2037-2046.

[48] C. Grondal, M. Jeanty, D. Enders, Organocatalytic cascade reactions as a new tool in total synthesis, Nature Chemistry, 2010, 2, 167-178.

[49] T. E. Nielsen, S. L. Schreiber, Towards the optimal screening collection: A synthesis strategy, Angewandte Chemie International Edition, 2008, 47, 48-56.

[50] W. Wilk, T. J. Zimmermann, M. Kaiser, H. Waldmann, Principles, implementation, and application of biology-oriented synthesis (BIOS), Biological Chemistry, 2010, 391, 491-497.

[51] K. Haupt, Molecularly imprinted polymers: the next generation, Analytic Chemistry, 2003, 75, 376 A-383A.

[52] K. Haupt, K. Mosbach, Molecularly imprinted polymers and their use in biomimetic sensors, Chemical Reviews, 2000, 100, 2495-2504.

[53] A. Poma, A. Guerreiro, M. J. Whitcombe, E.V. Piletska, A. P. F. Turner, S. A. Piletsky, Solid-phase synthesis of molecularly imprinted polymer nanoparticles with a reusable template- “plastic antibodies”, Advanced functional materials, 2013, 23, 2821-2827.

[54] G. Wulff, The use of polymers with enzyme-analogous structures for the resolution of racemates, Angewandte Chemie International Edition, 1972, 11, 341.

[55] J. Wackerlig, R. Schirhagl, Applications of molecularly imprinted polymer nanoparticles and their advances toward industrial use: A review, Analytical Chemistry, 2016, 88, 250-261.

[56] C. Alexander, H. S. Andersson, L. I. Andersson, R. J. Ansell, N. Kirsch, I. A. Nicholls, J. O'Mahony, M. J. Whitcombe, Molecular imprinting science and technology: a survey of the literature for the years up to and including 2003, Journal of Molecular Recognition, 2006, 19, 106-180.

[57] M. J. Whitecombe, N. Kirsch, I. A. Nicholls, Molecular imprinting science and technology: a survey of the literature for the years 2004-2011, Journal of Molecular Recognition, 2014, 27, 297-401.

[58] S. A. Zaidi, Recent developments in molecularly imprinted polymer nanofibers and their applications, Analytical Methods, 2015, 7, 7406-7415.

[59] S. Li, X. Huang, M. Zheng, W. Li, K. Tong, Molecularly imprinted polymers: Thermodynamic and kinetic considerations on the specific sorption and molecular recognition, Sensors, 2008, 8, 2854-2864.

[60] X. Zhang, M. Zhu, S. Li, “Key-vs.-lock”-like polymer reactor made of molecularly imprinted polymer containing metal nanoparticles, Journal of Inorganic and Organometallic Polymers and Materials, 2014, 24, 890-897.

[61] L. Chen, S. Xu, J. Li, Recent advances in molecular imprinting technology: current status, challenges and highlighted applications, Chemical Society Reviews, 2011, 40, 2922-2942.

[62] S. Subrahmanyam, A. Guerreiro, A. Poma, E. Moczko, E. Piletska, S. Piletsky, Optimisation of experimental conditions for synthesis of high affinity MIP nanoparticles, European Polymer Journal, 2013, 49, 100-105.

[63] M. Subat, A. S. Borovik, B. J. Konig, Synthetic creatinine receptor: Imprinting of a Lewis acidic zinc(II)cyclen binding site to shape its molecular recognition selectivity, Journal of the American Chemical Society, 2004, 126, 3185-3190.

[64] E. Byrne, E. Oral, J. Z. Hilt, N. A. Peppas, Networks for recognition of biomolecules: molecular imprinting and micropatterning poly(ethylene glycol)-Containing films, Polymers advanced technologies, 2002, 13, 798-816.

[65] A. Nematollahzadeh, W. Sun, C. S. A. Aureliano, D. Lütkemeyer, J. Stute, M. J. Abdekhodaie, A. Shojaei, B. Sellergren, High-capacity hierarchically imprinted polymer beads for protein recognition and capture, Angewandte Chemi International Edition, 2011, 50, 495-498.

[66] W. Chen, W. Lei, M. Xue, F. Xue, Z. H. Meng, W. B. Zhang, F. Qu, K. J. Shea, Protein recognition by a surface imprinted colloidal array, Journal of Materials Chemistry A, 2014, 20, 7165-7169.

[67] S. A. Zaidi, K. M. Han, S. S. Kim, D. G. Hwang, W. J. Cheong, Open tubular layer of S‐ofloxacin imprinted polymer fabricated in silica capillary for chiral CEC separation, Journal of Separation Science, 2009, 32, 996-1001.

[68] R. Jang, K. H. Kim, S. A. Zaidi, W. J. Cheong, M. H. Moon, Analysis of phospholipids using an open‐tubular capillary column with a monolithic layer of molecularly imprinted polymer in capillary electrochromatography‐electrospray ionization‐tandem mass spectrometry, Electrophoresis, 2011, 32, 2167-2173.

[69] A. Bhaskarapillai, N. Sevilimedu, B. Sellergren, Synthesis and characterization of imprinted polymers for radioactive waste reduction, Industrial & Engineering Chemistry Research, 2009, 48, 3730-3737.

[70] J. Wang, M. Xue, Z. Meng, Z. Xu, J. Luo, Application of molecularly imprinted polymers for the solid-phase extraction of hexanitrohexaazaisowurtzitane (CL-20) from soil samples, Analytical Methods, 2016, 8, 4413-4420.

[71] X. Su, X. Li, J. Li, M. Liu, F. Lei, X. Tan, P. Li, W. Luo, Synthesis and characterization of core-shell magnetic molecularly imprinted polymers for solid-phase extraction and determination of Rhodamine B in food, Food Chemistry, 2015, 171, 292-297.

[72] S. A. Zaidi, Recent advancement in various electrochemical and immunosensing strategies for detection of chloramphenicol, International Journal Electrochemical Science, 2013, 8, 9936-9955.

[73] S. A. Zaidi. J. H. Shin, Molecularly imprinted polymer electrochemical sensors based on synergistic effect of composites synthesized from graphene and other nanosystems, International Journal Electrochemical Science, 2014, 9, 4598-4616.

[74] R. Suedee, C. Jantarat, W. Lindner, H. Viernstein, S. Songkro, T. Srichana, Development of a pH-responsive drug delivery system for enantioselective-controlled delivery of racemic drugs, Journal of Controlled Release, 2010, 142, 122-131.

[75] H. Hiratani, A. Fujiwara, Y. Tamiya, Y. Mizutami, C. Alvarez-Lorenzo, Ocular release of timolol from molecularly imprinted soft contact lenses, Biomaterials, 2005, 26, 1293-1298.

[76] J. Damen, D. Neckers, Stereoselective syntheses via a photochemical template effect, Journal of the American Chemical Society, 1980, 102, 3265-3267.

[77] K. J. Shea, E. A. Thompson, S. D. Pandey, P. S. Beauchamp, Template synthesis of macromolecules. Synthesis and chemistry of functionalized macroporous poly (divinylbenzene), Journal of the American Chemical Society, 1980, 102, 3149-3155.

[78] G. Wulff, J. Vietmeier, Enzyme ‐ analogue built polymers, 25. Synthesis of macroporous copolymers from α ‐ amino acid based vinyl compounds, Macromolecular Chemistry and Physics, 1980, 190, 1717-1726.

[79] A. Leonhardt, K. Mosbach, Enzyme-mimicking polymers exhibiting specific substrate binding and catalytic functions, Reactive Polymers, 1987, 6, 285-290.

[80] D. K. Robinson, K. Mosbach, Molecular imprinting of a transition state analogue leads to a polymer exhibiting esterolytic activity, Journal of the Chemical Society, 1989, 969-970.

[81] R. Müller, L. I. Andersson, K. Mosbach, Molecularly imprinted polymers facilitating a β-elimination reaction, Die Makromolekulare Chemie, Rapid Communications, 1993, 14, 637-641.

[82] J. V. Beach, K. J. Shea, Designed catalysts. A synthetic network polymer that catalyzes the dehydrofluorination of 4-fluoro-4-(p-nitrophenyl) butan-2-one, Journal of the American Chemical Society, 1994, 116, 379–380.

[83] J. Matsui, I. A. Nicholls, I. Karube, K. Mosbach, Carbon-carbon bond formation using substrate selective catalytic polymers prepared by molecular

imprinting: An artificial class II Aldolase, The Journal of Organic Chemistry, 1996, 61, 5414-5417.

[84] N. Kirsch, J. Hedin-Dahlström, H. Henschel, M. J. Whitcombe, S. Wikman, I. A. Nicholls, Molecularly imprinted polymer catalysis of a Diels-Alder reaction, Journal of Molecular Catalysis B: Enzymatic, 2009, 58, 110-117.

[85] Z. Meng, T. Yamazaki, K. Sode, Enhancement of the catalytic activity of an artificial phosphotriesterase using a molecular imprinting technique, Biotechnology Letters, 2003, 25, 1075-1080.

[86] A. Reinecke, L. Bertinetti, P. Fratzl, M.J. Harrington, Cooperative behavior of a sacrificial bond network and elastic framework in providing self-healing capacity in mussel byssal threads, Journal of Structural Biology, 2016, 196, 329-339.

[87] C. Shao, M. Wang, L. Meng, H. Chang, B. Wang, F. Xu, J. Yang, P. Wan, Mussel-inspired cellulose nanocomposite tough hydrogels with synergistic self-healing, adhesive, and strain-sensitive properties, Chemistry of Materials, 2018, 30, 3110-3121.

[88] C.N.Z. Schmitt, Y. Politi, A. Reinecke, M.J. Harrington, Role of sacrificial protein-metal bond exchange in mussel byssal thread self-healing, Biomacromolecules, 2015, 16, 2852-2861.

[89] H. Zeng, D.S. Hwang, J.N. Israelachvili, J.H. Waite, Strong reversible Fe3+-mediated bridging between dopa-containing protein films in water, Proceedings of the National Academy of Sciences of the United States of America, 2010, 107, 12850-12853 (2010).

[90] J. Chung, A.M. Kushner, A.C. Weisman, Z. Guan, Direct correlation of single-molecule properties with bulk mechanical performance for the biomimetic design of polymers, Nature Materials, 2014, 13, 1055-1062.

[91] Z. Tang, J. Huang, B. Guo, L. Zhang, F. Liu, Bioinspired engineering of sacrificial metal-ligand bonds into elastomers with supramechanical performance and adaptive recovery, Macromolecules, 2016, 49, 1781-1789.

[92] X. Zhang, Z. Tang, B. Guo, L. Zhang, Enabling design of advanced elastomer with bioinspired metal-oxygen coordination, ACS Applied Materials & Interfaces, 2016, 8, 32520-32527.

[93] N. Holten-Andersen, G.E. Fantner, S. Hohlbauch, J.H. Waite, F.W. Zok, Protective coatings on extensible biofibres, Nature Materials, 2007, 6, 669-672.

[94] B.K. Ahn, D. W. Lee, J.N. Israelachvili, J. H. Waite, Surface-initiated self-healing of polymers in aqueous media, Nature Materials, 2014, 13, 867-872.

[95] H. Cho, G. Wu, J.C. Jolly, N. Fortoul, Z. He, Y. Gao, A. Jagota, S. Yang, Intrinsically reversible superglues via shape adaptation inspired by snail epiphragm, PANS, 2019, 116, 13774-13779.

[96] M. A. C. Stuart, W. T. S. Huck, J. Genzer, M. Müller, C. Ober, M. Stamm, G. B. Sukhorukov, I. Szleifer, V. V. Tsukruk, M. Urban, F. Winnik, S. Zauscher, I. Luzinov, S. Minko, Emerging applications of stimuli-responsive polymer materials, Nature Materials, 2010, 9, 101-113.

[97] E. Karjalainen, V. Aseyev, H. Tenhu, Upper or lower critical solution temperature, or both? Studies on cationic copolymers of N-isopropylacrylamide, Polymer Chemistry, 2015, 6, 3074-3082.

[98] Y. Okada, F. Tanaka, Cooperative hydration, chain collapse, and flat LCST behavior in aqueous poly(N-isopropylacrylamide) solutions, Macromolecules, 2005, 38, 4465-4471.

[99] X. Hu, Z. Tong, L. A. Lyon, Control of poly(N-isopropylacrylamide) microgel network structure by precipitation polymerization near the lower critical solution temperature, Langmuir, 2011, 27, 4142-4148.

[100] P. Zhang, F. Liu, Q. Liao, H. Yao, H. Geng, H. Cheng, C. Li, L. Qu, A microstructured graphene/poly(N-isopropylacrylamide) membrane for intelligent solar water evaporation, Angewandte Chemie International Edition, 2018, 57, 16343-16347.

[101] P. Kujawa, F. M. Winnik, Volumetric studies of aqueous polymer solutions using pressure perturbation calorimetry: A new look at the temperature-induced phase transition of poly(N-isopropylacrylamide) in water and D2O, Macromolecules, 2001, 34, 4130-4135.

[102] D. Crespy, R. M. Rossi, Temperature-responsive polymers with LCST in the physiological range and their applications in textiles, Polymer International, 2007, 56, 1461-1468.

[103] R. Liu, M. Fraylich, B. R. Saunders, Thermoresponsive copolymers: from fundamental studies to applications, Colloid and Polymer Science, 2009, 287, 627-643.

[104] Z. Song, K. Wang, C. Gao, S. Wang, W. Zhang, A new thermo-, pH-, and CO2-responsive homopolymer of poly[N-[2-(diethylamino)ethyl] acrylamide]: Is the diethylamino group underestimated? Macromolecules, 2016, 49, 162-171.

[105] E. Karjalainen, V. Aseyev, H. Tenhu, Influence of hydrophobic anion on solution properties of PDMAEMA, Macromolecules, 2014, 47, 2103-2111.

[106] T. Thavanesan, C. Herbert, F. A. Plamper, Insight in the phase separation peculiarities of poly(dialkylaminoethyl methacrylate)s, Langmuir, 2014, 30, 5609-5619.

[107] Y. Cao, X. Zhu, J. Luo, H. Liu, Effects of substitution groups on the RAFT polymerization of N-alkylacrylamides in the preparation of thermosensitive block copolymers, Macromolecules, 2007, 40, 6481-6488.

[108] N. V. Zakharova, M. A. Simonova, S. N. Zelinskii, V. V. Annenkov, A. P. Filippov, Synthesis, molecular characteristics, and stimulus-sensitivity of graft copolymer of chitosan and poly (N, N-diethylacrylamide), Journal of Molecular Liquids, 2019, 292, 11355.

[109] J. Seuring, S. Agarwal, Non-ionic homo- and copolymers with H-donor and H-acceptor units with an UCST in water, Macromolecular Chemistry and Physics, 2010, 211, 2109-2117.

[110] J. Seuring, F. M. Bayer, K. Huber, S. Agarwal, Upper critical solution temperature of poly (N-acryloyl glycinamide) in water: A concealed property, Macromolecules, 2012, 45, 374-384.

[111] J. Seuring, S. Agarwal, Polymers with upper critical solution temperature in aqueous solution: Unexpected properties from known building blocks, ACS Macro Letters, 2013, 2, 597-600.

[112] J. Seuring, S. Agarwal, First example of a universal and cost-effective approach: Polymers with tunable upper critical solution temperature in water and electrolyte solution, Macromolecules, 2012, 45, 3910-3918.

[113] L. Mäkinen, D. Varadharajan, H. Tenhu, S. Hietala, Triple hydrophilic UCST-LCST block copolymers, Macromolecules, 2016, 49, 986-993.

[114] F. Käfer, F. Liu, U. Stahlschmidt, V. Jérôme, R. Freitag, M. Karg, S. Agarwal, LCST and UCST in one: Double thermoresponsive behavior of block copolymers of poly (ethylene glycol) and poly(acrylamide-co-acrylonitrile), Langmuir, 2015, 31, 8940-8946.

[115] K. Wang, Z. Jia, X. Yang, L. Wang, Y. Gu and B. Tana, Acid and base coexisted heterogeneous catalysts supported on hypercrosslinked polymers for one-pot cascade reactions, Journal of Catalysis, 2017, 348, 168-176.

[116] M. Sankar, Q. He, S. Dawson, E. Nowicka, L. Lu, P. C. A. Bruijnincx, A. M. Beale, C. J. Kiely and B. M. Weckhuysen, Supported bimetallic nano-alloys as highly active catalysts for the one-pot tandem synthesis of imines and secondary amines from nitrobenzene and alcohols, Catalysis Science & Technology, 2016, 6, 5473-5482.

[117] Z.Jia, K. Wang, B. Tan and Y. Gu, Hollow hyper-cross-linked nanospheres with acid and base sites as efficient and water-stable catalysts for one-pot tandem reactions, ACS Catalysis, 2017, 7, 3693-3702.

[118] Z. Sun, S. Wang, X. Wang and Z. Jiang, Lysine functional heteropolyacid nanospheres as bifunctional acid-base catalysts for cascade conversion of glucose to levulinic acid, Fuel, 2016, 164, 262-266.

[119] Y. Wang, H. Lu and P. F. Xu, Asymmetric catalytic cascade reactions for constructing diverse scaffolds and complex molecules, Accounts of Chemical Research, 2015, 48, 1832-1844.

[120] M. Filice and J. M. Palomo, Cascade reaction catalyzed by bionanostructures, ACS Catalysis, 2014, 4, 1588-1598.

[121] Y. Hayashi, Pot economy and one-pot synthesis, Chemical Science, 2016, 7, 866-880.

[122] H. Tan, S. Guo, N. D. Dinh, R. Luo, L. Jin and C. H. Chen, Heterogeneous multi-compartmental hydrogel particles as synthetic cells for incompatible tandem reactions, Nature Communication, 2017, 8, 1-10.

[123] A. Küchler, M. Yoshimoto, S. Luginbühl, F. Mavelli and P. Walde, Enzymatic reactions in confined environments, Nature Nanotechnology, 2016, 11, 409-420.

[124] A. Zuo, W. Wei, Q. Zhou, S. Wu and S. Li, Artificial active nanoreactor with nature-inspired sequential catalytic ability, ChemistrySelect, 2017, 2, 6149-6153.

[125] R. P. P. Neves, P. A. Fernandes and M. J. Ramos, Mechanistic insights on the reduction of glutathione disulfide by protein disulfide isomerase, Proceeding of the National Academy of Sciences of the United States of America, 2017, 114, E4724-E4733.

[126] Y. Hamada, Y. Kanematsu and M. Tachikawa, Quantum mechanics/molecular mechanics study of the sialyltransferase reaction mechanism, Biochemistry, 2016, 55, 5764-5771.

[127] T. H. Fife and D. M. McMahon, Hydrolysis of bis(4-nitrophenyl) carbonate and the general base catalyzed hydrolysis of o-(4-nitrophenylene) carbonate, The Journal of Organic Chemistry, 1970, 35, 3699-3704.

[128] T. L. Huang, A. Székács, T. Uematsu, E. Kuwano, A. Parkinson and B. D. Hammock, Hydrolysis of carbonates, thiocarbonates, carbamates, and carboxylic esters of α-naphthol, β-naphthol, and p-nitrophenol by human, rat, and mouse liver carboxylesterases, Pharmaceutical Research, 1993, 10, 639-648.

[129] L. Chen, X. Wang, W. Lu, X. Wu and J. Li, Molecular imprinting: perspectives and applications, Chemical Society Reviews, 2016, 45, 2137-2211.

[130] J. Vicente, A. Arcas, M. Mora, X. Solans and M. Font-Altaba, Gold(I) and gold (III) ortho-nitrophenyl complexes. Crystal and molecular structure of ortho-nitrophenyltriphenylarsinegold(I), Journal of Organometallic Chemistry, 1986, 309, 369-378.

[131] K. Kuroda, T. Ishida and M. Haruta, Reduction of 4-nitrophenol to 4-aminophenol over Au nanoparticles deposited on PMMA, Journal of Molecular Catalysis A: Chemical, 2009, 298, 7-11.

[132] S. Li, Y. Ge and A. P. F. Turner, A catalytic and positively thermosensitive molecularly imprinted polymer, Advanced Functional Materials, 2011, 21, 1194-1200.

[133] X. Zhang, M. Zhu and S. Li, “Key-vs.-lock’’-like polymer reactor made of molecularly imprinted polymer containing metal nanoparticles, Journal of Inorganic and Organometallic Polymers, 2014, 24, 890-897.

[134] S. Li, Y. Ge, A. Towari, S. Wang, A. P. F. Turner and S. A. Piletsky, ‘On/off’-switchable catalysis by a smart enzyme-like imprinted polymer, Journal of Catalysis, 2011, 278, 173-180.

[135] Y. Han, X. Yuan, M. Zhu, S. Li, M. Whitcombe and S. A. Piletsky, A catalytic and shape-memory polymer reactor, Advanced Functional Materials, 2014, 24, 4996-5001.

[136] Y. Shi, C. Ma, L. Peng and G. Yu, Conductive “smart” hybrid hydrogels with PNIPAM and nanostructured conductive polymers, Advanced Functional Materials, 2015, 25, 1219-1225.

[137] H. özay, S. Kubilay, N. Aktas and N. Sahiner, Utilization of environmentally benign hydrogels and their networks as reactor media in the catalytic reduction of nitrophenols, International Journal of Polymeric Materials, 2011, 60, 163-173.

[138] A. M. Rosengren, B. C. G. Karlsson and I. A. Nicholls, Consequences of morphology on molecularly imprinted polymer-ligand recognition, International Journal of Molecular Science, 2013, 14, 1207-1217.

[139] R. J. L. Roy, LEVEL: A computer program for solving the radial Schrödinger equation for bound and quasibound levels, Journal of Quantitative Spectroscopy and Radiative Transfer, 2017, 186, 167-178.

[140] X. Antoine, E. Lorin and A. D. Bandrauk, Domain decomposition method and high-order absorbing boundary conditions for the numerical simulation of the time dependent schrödinger equation with ionization and recombination by intense electric field，Journal of Scientific Computing, 2015, 64, 620-646.

[141] A. Corichi, T. Vukašinac and J. A. Zapata, Polymer quantum mechanics and its continuum limit, Physical Review D, 2007, 76, 044016.1-044016.16.

[142] J. Wang, M. Zhu, X. Shen, S. Li, A cascade-reaction nanoreactor composed of a bifunctional molecularly imprinted polymer that contains Pt nanoparticles, Chemistry-A European Journal, 2015, 21, 7532-7539.

[143] Y. Ueda, H. Ito, D. Fujita, M. Fujita, Permeable self-assembled molecular containers for catalyst isolation enabling two-step cascade reactions, Journal of the American Chemical Society, 2017, 139, 6090-6093.

[144] S. Li, Y. Luo, M. Whitcombe, S.A. Piletsky, A successive-reaction nanoreactor made of active molecularly imprinted polymer containing Ag nanoparticles, Journal of Materials Chemistry A, 2013, 1, 15102-15109.

[145] F. Rudroff, M.D. Mihovilovic, H. Groger, R. Snajdrova, H. Iding, U.T. Bornscheuer, Opportunities and challenges for combining chemo- and biocatalysis, Nature Catalysis, 2018, 1, 12-22.

[146] C.M. Hong, R.G. Bergman, K.N. Raymond, F.D. Toste, Self-assembled tetrahedral hosts as supramolecular catalysts, Accounts of Chemical Research, 2018, 51, 2447-2455.

[147] B.C. Buddingh, J.C.M. van Hest, Artificial cells: Synthetic compartments with life-like functionality and adaptivity, Accounts of Chemical Research, 2017, 50, 769-777.

[148] S. Schmidt, K. Castiglione, R. Kourist, Overcoming the incompatibility challenge in chemoenzymatic and multi-catalytic cascade reactions, Chemistry-A European Journal, 2018, 24, 1755-1768.

[149] I. Wheeldon, S.D. Minteer, S. Banta, S.C. Barton, P. Atanassov, M. Sigman, Substrate channeling as an approach to cascade reactions, Nature Chemistry, 2016, 8, 299-309.

[150] J. Lu, J. Dimroth, M. Weck, Compartmentalization of incompatible catalytic transformation for tandem catalysis， Journal of the American Chemical Society, 2015, 137, 12984-12989.

[151] K. Motokura, N. Fujita, K. Mori, T. Mizugaki, K. Ebitani, K. Kaneda, An acidic layered clay is combined with a basic layered clay for one-pot sequential reactions, Journal of the American Chemical Society, 2005, 127, 9674-9675.

[152] Z. Dong, X. Le, X. Li, W. Zhang, C. Dong, J. Ma, Silver nanoparticles immobilized on fibrous nano-silica as highly efficient and recyclable heterogeneous catalyst for reduction of 4-nitrophenol and 2-nitroaniline, Applied Catalysis B: Environmental, 2014, 158, 129-135.

[153] L.C. Lee, J. Lu, M. Weck, C.W. Jones, Acid-base bifunctional shell cross-linked micelle nanoreactor for one-pot tandem reaction, ACS Catalysis, 2016, 6, 784-787.

[154] I.A. Smellie, J.K.D. Aldred, B. Bower, A. Cochrane, L. Macfarlane, H.B. McCarron, R. O'Hara, I.L.J. Patterson, M.I. Thomson, J.M. Walker, Alternative hydrogen peroxide sources for peroxyoxalate "glowstick" chemiluminescence demonstrations, Journal of Chemical Education, 2017, 94, 112-114.

[155] R.E. Morsi, R.A. Elsalamony, Superabsorbent enhanced-catalytic core/shell nanocomposites hydrogels for efficient water decolorization, New Journal of Chemistry, 2016, 40, 2927-2934.

[156] Y. Zhou, M. Zhu, S. Li, Self-switchable catalysis by a nature-inspired polymer nanoreactor containing Pt nanoparticles, Journal of Materials Chemistry A, 2014, 2, 6834-6839.

[157] D. Schwarz, J. Weber, Synthesis of mesoporous poly(melamine-formaldehyde) particles by inverse emulsion polymerization, Journal of Colloid and Interface Science, 2017, 498, 335-342.

[158] X. Zheng, R. Luo, M. Zhu, S. Li, Polymer nanoreactor with "mobility-recalling" domains for on/off switchable catalysis, ChemCatChem, 2015, 7, 814-818.

[159] W. Wei, M. Zhu, X. Shen, S. Wu, S. Li, Switchable polymer reactor composed of mussel-inspired polymer that contains Au nanoparticles, RSC Advances, 2016, 6, 42869-42875.

[160] B. Peng, X. Yuan, M. Zhu, S. Li, An "active" and self-switchable nanoreactor, Polymer Chemistry, 2014, 5, 562-566.

[161] X. Liu, D. Li, X. Sun, Z. Li, H. Song, H. Jiang, Y. Chen, Tunable dipole surface plasmon resonances of silver nanoparticles by cladding dielectric layers, Scientific Reports, 2015, 5, 1-7.

[162] R. Luo, M. Zhu, X. Yuan, S. Li, An autonomic and “off-on-off”- switchable polymer microreactor, RSC Advances, 2015, 5, 5598-5603.

[163] Y. D. Shikhmurzaev, Darcy's law for two-dimensional flows: Singularities at corners and a new class of models, American Institute of Chemical Engineers, 2017, 63, 5207-5214.

[164] T. Hayat, T. Ayub, T. Muhammad, A. Alsaedi, Flow of variable thermal conductivity oldroyd-B fluid with generalized Fourier’s and Fick’s laws, Journal of Molecular Liquids, 2017, 234, 9-17.

[165] C. Gong, D. Tao, K. Fu, J. Yang, Fick’s law assisted propagation for semisupervised learning, IEEE Transactions on Neural Networks and Learning Systems, 2015, 26, 2148-2162.

[166] Z. Xia, W. Wei, M. Zhu, S. Wu, X. Shen, S. Li, Artificial reactor containing polymeric bilayer architectures for the formation of self-controlled tandem catalytic-ability, Express Polymer Letters, 2020, 14, 12-25.

[167] Y. Lu, W, Wei, M. Zhu, S. Wu, X. Shen, S. Li, Polymer reactor with alterable substrate channeling for the formation of cascade/non-cascade-switchable catalytic ability, Journal of Inorganic and Organometallic Polymers and Materials, 2020, 30, 2039-2049.

[168] C. Robert, C. M. Thomas, Tandem catalysis: a new approach to polymers, Chemical Society Reviews, 2013, 42, 9392-9402.

[169] S. K. Raman, E. Brule, M. J. Tschan, C. M. Thomas, Tandem catalysis: a new approach to polypeptides and cyclic carbonates, Chemical Communications, 2014, 50, 13773-13776.

[170] A. Corma, J. Navas, M. J. Sabater, Advances in one-pot synthesis through borrowing hydrogen catalysis, Chemical Reviews, 2018, 118, 1410-1459.

[171] H. Yang, L. Fu, L. Wei, J. Liang, B. Binks, Compartmentalization of incompatible reagents within pickering emulsion droplets for one-pot cascade reactions, Journal of the American Chemical Society, 2015, 137, 1362-1371.

[172] H. Liu, F. Xi, W. Sun, N. Yang, E Gao, Amino- and sulfo-bifunctionalized metal-organic frameworks: one-pot tandem catalysis and the catalytic sites, Inorganic Chemistry, 2016, 55, 5753-5755.

[173] X. Zhang, L. Jing, F. Chang, S. Chen, H. Yang, Q. Yang, Positional immobilization of Pd nanoparticles and enzymes in hierarchical yolk-shell@shell nanoreactors for tandem catalysis, Chemical Communications, 2017, 53, 7780-7783.

[174] H. Peng, Y. Qin, X. He, W. Li, Y. Zhang, Epitope molecularly imprinted polymer nanoparticles for chemo-/photodynamic synergistic cancer therapy guided by targeted fluorescence imaging, ACS Applied Materials & Interfaces, 2020, 12, 13360-13370.

[175] R. Gui, H. Jin, H. Guo, Z. Wang, Recent advances and future prospects in molecularly imprinted polymers-based electrochemical biosensors, Biosensors and Bioelectronics, 2018, 100, 56-70.

[176] E. Abdollahi, A. Nezhad, A. Mohmadi, M. Abdouss, M. Kalajahi, Synthesis of new molecularly imprinted polymer via reversible addition fragmentation transfer polymerization as a drug delivery system, Polymer, 2018, 143, 245-257.

[177] S. Nishitani, T. Sakata, Potentiometric adsorption isotherm analysis of a molecularly imprinted polymer interface for small-biomolecule recognition, ACS Omega, 2018, 3, 5382-5389.

[178] G. Westwood, T. N. Horton, J. J. Wilker, Simplified polymer mimics of cross-linking adhesive proteins, Macromolecules, 2007, 40, 3960-3964.

[179] Y. Song, G. Ye, F. Wu, Z. Wang, S. Liu, M. Kopec, Z. Wang, J. Chen, J. Wang, K. Matyjaszewski, Bioinspired polydopamine (PDA) chemistry meets ordered mesoporous carbons (OMCs): A benign surface modification strategy for versatile functionalization, Chemistry of Materials, 2016, 28, 5013-5021.

[180] J. D. White, J. J. Wiker, Underwater bonding with charged polymer mimics of marine mussel adhesive proteins, Macromolecules, 2011, 44, 5085-5088.

[181] W. Wei, J. Yu, C. Broomell, Hydrophobic enhancement of dopa-mediated adhesion in a mussel foot protein, Journal of the American Chemical Society, 2013, 135, 377-383.

[182] S. Hong, Y. Na, S. Choi, I. Song, W. Kim, H. Lee, Non-covalent self-assembly and covalent polymerization co-contribute to polydopamine formation, Advanced Functional Materials, 2012, 22, 4711-4717.

[183] J. J. Wilker, Biomaterials: redox and adhesion on the rocks, Nature Chemical Bioloogy, 2011, 7, 579-580.

[184] Y. Liu, K. Ai, L. Lu, Polydopamine and its derivative materials: synthesis and promising applications in energy, environmental, and biomedical fields, Chemical Reviews, 2014, 114, 5057-5115.

[185] P. Cordier, F. Tournilhac, C. Solié-Ziakovic, L. Leibler, Self-healing and thermoreversible rubber from supramolecular assembly, Nature, 2008, 451, 977-980.

[186] C. Shao, H. Chang, M. Wang, F. Xu, J. Yang, High-strength, tough, and self-healing nanocomposite physical hydrogels based on the synergistic effects of dynamic hydrogen bond and dual coordination bonds, ACS Applied Materials & Interfaces, 2017, 9, 28305-28318.

[187] P. Xiao, S. Wu, X. Shen, M. Zhu, S. Li, Smart tandem catalyst developed with sundew's predation strategy, capable of catching, decomposing and assimilating preys, ChemCatChem, 2018, 10, 5231-5241.

[188] Q. Chen, D. Wei, H. Chen, L. Zhu, C. Jiao, G. Liu, L. Huang, J. Yang, L. Wang, J. Zheng, Simultaneous enhancement of stiffness and toughness in hybrid double-network hydrogels via the First, physically linked network, Macromolecules, 2015, 48, 8003-8010.

[189] C. Wang, J. Bai, Y. Liu, X. Jia, X. Jiang, Polydopamine coated selenide molybdenum: A new photothermal nanocarrier for highly effective chemo-photothermal synergistic therapy, ACS Biomaterials Science & Engineering, 2016, 2, 2011-2017.

[190] S. Link, M. A. Elsayed, Spectral properties and relaxation dynamics of surface plasmon electronic oscillations in gold and silver nanodots and nanorods, The Journal of physical chemistry, 1999, 103, 8410-8426.

[191] A. Pan, Z. Yang, H. Zheng, F. Liu, Y. Zhu, X. Su, Z. Ding, Changeable position of SPR peak of Ag nanoparticles embedded in mesoporous SiO_2 glass by annealing treatment, Applied Surface Science, 2003, 205, 323-328.

[192] J. Liu, H. Song, J. Liu, Y. Liu, L. Li, H. Tang, Y. Li, Preparation of molecularly imprinted polymer with double templates for rapid simultaneous determination of melamine and dicyandiamide in dairy products, Talanta, 2015, 134, 761-767.

[193] R. Luo, M. Zhu, X. Shen, S. Li, Polymer catalyst with self-assembled hierarchical access for sortable catalysis, Journal of Catalysis, 2015, 331, 49-56.

[194] W. Wei, P. Xiao, V.K. Thakur, I. Chianella, S. Li, Smart bilayer polymer reactor with cascade/non-cascade switching catalyst characteristics, Materials Today Chemistry, 2020, 17, 100279.

[195] K.C. Nicolaou, J.S. Chen, The art of total synthesis through cascade reactions, Chemical Society Reviews, 2009, 38, 2993-3009.

[196] P. Tanner, O. Onaca, V. Balasubramanian, W. Meier, C.G. Palivan, Enzymatic cascade reactions inside polymeric nanocontainers: a means to combat oxidative stress, Chemistry a European Journal, 2011, 17, 4552-4560.

[197] E. Raluy, I. Favier, A.M. Vinasco, C. Pradel, E. Martin, D. Madec, E. Teuma, M. G omez, A smart palladium catalyst in ionic liquid for tandem processes, Physical Chemistry Chemical Physics, 2011, 13, 13579-13584.

[198] W. Wei, S. Wu, X. Shen, M. Zhu, S. Li, Nanoreactor with core-shell architectures used as spatiotemporal compartments for “undisturbed” tandem catalysis, Journal of Inorganic and Organometallic Polymers and Materials, 2019, 29, 1235-1242.

[199] J. Yang, D. Shen, L. Zhou, W. Li, X. Li, C. Yao, R. Wang, A.M. Toni, F. Zhang, D. Zhao, Spatially confined fabrication of core-shell gold nanocages@mesoporous silica for near-infrared controlled photothermal drug release, Chemistry of Materials, 2013, 25, 3030-3037.

[200] S. Pandey, J.Y. Do, J. Kim, M. Kang, Fast and highly efficient catalytic degradation of dyes using k-carrageenan stabilized silver nanoparticles nano-catalyst, Carbohydrate Polymers, 2020, 230, 115597.

[201] Y. Cao, J. He, J. Sun, Fabrication of oriented arrays of porous gold microsheaths using aligned silver nanowires as sacrificial template, Materials Letters, 2009, 63, 148-150.

[202] F. Xu, J. Mei, M. Zheng, D. Bai, D. Wu, Z. Gao, K. Jiang, Au nanoparticles modified branched TiO2 nanorod array arranged with ultrathin nanorods for enhanced photoelectrochemical water splitting, Journal of Alloys and Compounds, 2017, 693, 1124-1132.

[203] D. Philip, Biosynthesis of Au, Ag and Au-Ag nanoparticles using edible mushroom extract, Spectrochimica Acta Part A: Molecular and Biomolecular Spectroscopy, 2009, 73, 374-381.

[204] C. Jayaseelana, R. Ramkumarb, A. A. Rahumana, P. Perumal, Green synthesis of gold nanoparticles using seed aqueous extract of Abelmoschus esculentus and its antifungal activity, Industrial Crops and Products, 2013, 45, 423-429.

[205] M. Rueping, K. Haack, W. Ieawsuwan, H. Sundén, M. Blanco, F. R. Schoepke, Nature-inspired cascade catalysis: reaction control through substrate concentration-double vs. quadruple domino reactions, Chemical Communications, 2011, 47, 3828-3830.

[206] J. Zhou, Recent advances in multicatalyst promoted asymmetric tandem reactions, Chemistry-An Asian Journal, 2010, 5, 422-434.

[207] A. R. Longstreet, D. T. McQuade, Organic reaction systems: Using microcapsules and microreactors to perform chemical synthesis, Accounts Chemical Research, 2013, 46, 327-338.

[208] M. Weitz, A. Mückl, K. Kapsner, R. Berg, A. Meyer, F. C. Simmel, Communication and computation by bacteria compartmentalized within microemulsion droplets, Journal of the American Chemical Society, 2014, 136, 72-75.

[209] M. Wei, Y. Gao, X. Li, M. J. Serpe, Stimuli-responsive polymers and their applications, Polymer Chemistry, 2017, 8, 127-143.

[210] J. Niskanen, H. Tenhu, How to manipulate the upper critical solution temperature (UCST), Polymer Chemistry, 2017, 8, 220-232.

[211] Y. C. Bae, S. M. Lambert, D. S. Soane, J. M. Prausnitz, Cloud-point curves of polymer solutions from thermooptical measurements, Macromolecules, 1991, 24, 4403-4407.

[212] K. Jain, R. Vedarajan, M. Watanabe, M. Ishikiriyama, N. Matsumi, Tunable LCST behavior of poly (N-isopropylacrylamide/ionic liquid) copolymers, Polymer Chemistry, 2015, 6, 6819-6825.

[213] C. Wu and S. Zhou, Laser light scattering study of the phase transition of poly (N-isopropylacrylamide) in water. 1. Single chain, Macromolecules, 1995, 28, 8381-8387.

[214] C. A. McFaul, M. F. Drenski, W. F. Reed, Online, continuous monitoring of the sensitivity of the LCST of NIPAM-AM copolymers to discrete and broad composition distributions, Polymer, 2014, 55, 4899-4907.

[215] A. Haleem, J. Chen, X. Guo, J. Wang, H. Li, P. Li, S. Chen, W. He, Hybrid cryogels composed of P(NIPAM-co-AMPS) and metal nanoparticles for rapid reduction of p-nitrophenol, Polymer, 2020, 193, 122352.

[216] Y. Maeda, M. Yamabe, A unique phase behavior of random copolymer of N-isopropylacrylamide and N, N-diethylacrylamide in water, Polymer, 2009, 50, 519-523.

[217] L. Tang, L. Gong, G. Zhou, L. Liu, D. Zhang, J. Tang, J. Zheng, Design of low temperature-responsive hydrogels used as a temperature indicator, Polymer, 2019, 173, 182-189.

[218] Y. Hiruta, M. Shimamura, M. Matsuura, Y. Maekawa, T. Funatsu, Y. Suzuki, E. Ayano, T. Okano, H. Kanazawa, Temperature-responsive fluorescence polymer probes with accurate thermally controlled cellular uptakes, ACS Macro Letters, 2014, 3, 281-285.

[219] A. Choe, J. Yeom, R. Shanker, M. P. Kim, S. Kang, H. Ko, Stretchable and wearable colorimetric patches based on thermoresponsive plasmonic microgels embedded in a hydrogel film, NPG Asia Materials, 2018, 10, 912-922.

[220] Y. Zhang, S. Furyk, D. E. Bergbreiter, P. S. Cremer, Specific ion effects on the water solubility of macromolecules: PNIPAM and the Hofmeister Series, Journal of the American Chemical Society, 2005, 127, 14505-14510.

[221] S. Liu, C. Y. Tso, Y. W. Du, L. C. Chao, H. H. Lee, T. C. Ho, M. K. H. Leung, Bioinspired thermochromic transparent hydrogel wood with advanced

optical regulation abilities and mechanical properties for windows, Applied Energy, 2021, 297, 117207.

[222] P. Xiao, S. Wu, X. Shen, M. Zhu, S. Li, Smart tandem catalyst developed with sundew's predation strategy, capable of catching, decomposing and assimilating preys, ChemCatChem, 2018, 10, 5231-5241.

[223] W. Wei, V. K. Thakur, Y. M. J. Chew, S. Li, Towards next generation “smart” tandem catalysts with sandwiched mussel-inspired layer switch, Materials Today Chemistry, 2020, 17, 100286.

[224] Z. Shen, K. Terao, Y. Maki, T. Dobashi, G. Ma, and T. Yamamoto, Synthesis and phase behavior of aqueous poly(N-isopropylacrylamide-co-acrylamide), poly(N-isopropylacrylamide-co-N, N-dimethylacrylamide) and poly(N-isopropylacrylamide-co-2-hydroxyethyl methacrylate), Colloid Polymer Science, 2006, 284, 1001-1007.

[225] A. Ortega, E. Bucio, G. Burillo, New interpenetrating polymer networks of N-isopropylacrylamide / N-acryloxysuccinimide: Synthesis and characterization, Polymer Bulletin, 2008, 60, 515-524.

[226] G. Yang, G. Gao, C. Wang, C. Xu, H. Li, Controllable deposition of Ag nanoparticles on carbon nanotubes as a catalyst for hydrazine oxidation, Carbon, 2008, 46, 747-752.

[227] D. Rajesh, C. S. Sunandana, Briefly brominated Ag thin films: XRD, FESEM, and optical studies of surface modification, Applied Surface Science, 2012, 259, 276-282